Doctoral Dissertation

A Study of Neutrons Associated with Neutrino and Antineutrino Interactions on the Water Target at the T2K Far Detector

(T2K

)

A Dissertation Submitted for the Degree of Doctor of Philosophy

December 2019

12   (   )

Department of Physics, Graduate School of Science, The University of Tokyo

Ryosuke Akutsu

Abstract

Neutrons production associated with neutrino interactions on water target in an energy region from sub-GeV up to a few GeV will be utilized to improve the physics program of neutrino experiments employing water Cherenkov detectors. To this aim, a precise prediction of such neutrons by Monte Carlo (MC) simulation is essential. However, current prediction is highly dependent on simulations due to large uncertainties related to the modeling of neutrino interactions in nuclear medium, hadronic final-state interactions in nuclei, and secondary interactions in detector medium. Therefore, it is worth studying these neutrons with beam neutrinos and evaluating the validity of simulations.

This thesis presents the first measurement of neutrons associated with neutrino interactions in water for accelerator neutrinos and antineutrinos at the T2K far detector.

The Tokai-to-Kamioka (T2K) experiment is a long-baseline ν oscillation experiment in Japan. A primarily ν_μ ($\bar{\nu}_\mu$) beam is produced at the J-PARC with a peak energy of $0.6\,\mathrm{GeV}$, and is detected by the Super-Kamiokande far detector, which is a $50\,\mathrm{kton}$ water Cherenkov detector located $295\,\mathrm{km}$ away from the beam source. The observed beam-neutrino events at the far detector can be used to study the neutron production.

In this thesis, the data collected at the far detector until 2018 are analyzed to measure neutrons associated with neutrino interactions on water target. By using Charged Current ν_μ and $\bar{\nu}_\mu$ enriched samples, mean neutron multiplicity is measured with a total systematic uncertainty of $\sim 8\%$. The measured mean neutron multiplicity is $1.00 \pm 0.17\,(\text{stat.})\,^{+0.07}_{-0.08}\,(\text{syst.})$ for the ν-mode operation and $1.40 \pm 0.26\,(\text{stat.})\,^{+0.10}_{-0.11}\,(\text{syst.})$ for the $\bar{\nu}$-mode operation. The equivalent expectation by the reference simulation is 1.50 (2.14) for the ν-mode operation ($\bar{\nu}$-mode operation), The deviation from the expectation is $2.75\,\sigma$ ($2.69\,\sigma$) for ν-mode operation ($\bar{\nu}$-mode operation) based on the total error of the measured value.

By using the measurement result, impact of uncertainty regarding the neutron production on a particular physics analysis is estimated based on experimental data for the first time, in context of Hyper-Kamiokande atmospheric neutrino oscillation analysis. From the estimation, this measurement provides the first demonstration that understanding of the neutron production is essential to utilize those neutrons in future experiments. As several experimental studies will be carried out, it is expected that a satisfactory level of understanding of those neutrons will be obtained.

Statement of Originality

This thesis and the results presented in it were produced as a result of my own original and independent research. However, this thesis contains the works that I performed as well as the works done by the past and present T2K collaborators. In a large experiment such as T2K, any analyses cannot be performed by a person and are always performed as part of the experiment. Indeed, the primary analysis of this thesis was performed within the T2K collaboration, with the works done by the other collaborators. In the following, this statement clarifies my contributions.

Chapter 1 presents an overview of neutrino physics associated with the primary analysis of this thesis based on both experimental and theoretical works, and gives the motivation of this thesis by reviewing relevant works. All the works done by others have been cited.

Chapter 2 and 3 describe an overview of the T2K experiment and the near detectors and the far detector to provide appropriate information in order to perform the primary analysis of this thesis. These chapters summarize the works done by the past and the present collaborators, and relevant documents have been cited.

Chapter 4 presents simulations used for this thesis. Almost all the works are done by others and relevant documents have been cited. However, I implemented neutron production processes into the far detector simulation, SKDETSIM, based on the work done by Tsui Ka Ming (ICRR, now Liverpool). He developed an interface which connects SKDETSIM with Gean4. I also made improvements on SKDETSIM such that systematic uncertainties on nucleon secondary interaction cross sections in HETC and MICAP can be studied. This is completely and independently done by myself.

Chapter 6 describes neutron tagging algorithm. Although the Super-Kamiokande collaboration has their own neutron tagging algorithms, the algorithm, that I developed newly and independently, is different from them. I wrote the codes of my algorithm from scratch. Moreover, part of my developments have been included into those algorithms. However, a recent study on random noise of the far detector's photosensors done by T. Mochizuki (ICRR, now graduated) within the Hyper-Kamiokande collaboration is adopted to this thesis. This Chapter also presents an analysis of low-energy neutron calibration. The analysis method presented in this thesis is based on the past Super-Kamiokande collaborators, and relevant documents have been cited. However, the estimation method of systematic uncertainty using the calibration data, which is presented in Chapter 8, was newly and independently

developed by myself in a completely different way compared to the past works done by the Super-Kamiokande collaboration. The effects of the far detector time variations were estimated by myself for the first time.

Chapter 7 describes the first application of neutron tagging to T2K data. This thesis uses the T2K data collected until 2018, which correspond to the Run 1-9 data taking periods. The data used in this thesis consist of two sets: primary neutrino interaction and neutron tagging. For the data set of primary neutrino interaction, part of the data was prepared by myself through the expert work of the data reduction, and the remaining data were prepared by the others. On the other hand, for the data set of neutron tagging, all the data were prepared by myself. The figure, tables, analysis methods presented in this chapter were produced by myself.

Chapter 8 presents the primary analysis of this thesis. In the first part, all the works related to MC simulations are done by myself, which includes the generation of the alternative Monte Carlo (MC) sets: GENIE and NuWro. I independently built a framework which enables full GENIE and NuWro MC sets for the first time at the far detector. For the neutron measurement part, I independently performed all the works from the generation of Monte Carlo events up to estimation of systematic uncertainties. However, for the systematic error estimation I used the works done by the T2K-beam working group for the neutrino beam fluxes, the T2K-neutrino interaction working group (NIWG) for the neutrino interaction cross sections, the T2K neutrino oscillation analysis groups for neutrino oscillation parameters, the T2K-SK working group for the neutrino event selection and the neutrino event reconstruction, the Super-Kamiokande collaboration for the discrepancy of the gain increase of photosensor between data and detector simulation. Although I used these inputs, all the methods to propagate these error inputs are developed by myself.

Chapter 9 summarizes this thesis, describes an impact of neutron production uncertainty based on the measurement result presented in Chapter 8, and presents future prospects. I made the estimation of the impact utilizing the atmospheric neutrino oscillation analysis tool, Osc3++, developed by R. Wendell (Kyoto) and other past Super-Kamiokande collaborators. In addition, in this estimation, I used an improved atmospheric neutrino oscillation analysis method developed by P. Menendez (UAM, now IFIC), which exploits information about tagged neutrons.

The primary analysis of this thesis, measurement of neutron associated with neutrino interactions in water, was officialized on 4 December 2019, and is now an official result of the T2K collaboration. The primary analysis is documented as the T2K technical note-371 and is credited to the T2K collaboration.

Acknowledgement

Contents

List of Figures

List of Tables

Chapter 1

Introduction

In the universe neutrinos are the second most dominant particles and their nature has not been fully understood yet. The remains of the unknown natures are not due to lack of study, but instead because of the significant feature of neutrinos that they interact extremely weakly with other particles. Although this feature still keeps neutrinos mysterious, it allows neutrinos to deliver unique information about the universe to us, which can not be obtained from other particles. In order to address such information, first of all neutrino interactions with matter need to be understood well.

This chapter begins with a brief history of neutrinos. Following this, neutrino oscillations and supernova relic neutrinos are described, which motivates the primary analysis of this thesis. Then, neutrons associated with neutrino interactions in water are introduced, and the motivation of the primary analysis and a thesis overview are given.

1.1 Neutrino physics

Neutrinos are accommodated by the Standard Model of particle physics that describes the fundamental forces between particles, except for the gravitational forces, and the elementary particles. In the original Standard Model, neutrinos are described as spin $1/2$ massless Dirac fermions and have three flavors: ν_e, ν_μ, and ν_τ. Each neutrino flavor has an associated charged lepton, which forms the three lepton generations, and electron, muon, and tau correspond to the first, second, and third generations, respectively. Neutrinos only interact with other particle via the weak interaction which separately conserves each generation's lepton number.

1.1.1 A brief history of neutrino physics

Neutrinos were originally postulated as "neutrons" by W. Pauli in 1930 [39] to remedy an apparent violation of energy conservation observed in β-decay. The modern neutron was discovered by J. Chadwick in 1932. In 1934, a theory of β-decay in which the neutrinos proposed by Pauli are included was developed by E. Fermi. However, it took another 22 years to prove the existence of neutrinos suggested by

Palui and Fermi. The first detection of neutrinos was made by C. Cowen and F. Reins in 1956 [40] and they detected $\bar{\nu}_e$ produced in a nuclear reactor via inverse β decay. Three years later, R. Davis and S. Harmer reported that ν_e and $\bar{\nu}_e$ are distinct particles [41].

In late 1950s, the Fermi's theory, which included only the vector component of the weak interaction, was modified. In 1956, T. Lee and C. Yang suggested that the parity of the weak interaction is not conserved [42]. Indeed, the parity violation was experimentally confirmed by C. Wu [43] and other experimentalists [44] in 1957. In 1958, M. Goldhaber *et al.* proved that neutrinos are always emitted with the same helicity from the electron capture processes [45]. In order to account for these experimental results, V-A theory was proposed by Sudarshan and Marshak, Feynman and Gell-Mann [46, 47] in 1958.

In the original V-A theory only one species of neutrino had been recognized, and only distinction was made between neutrinos and antineutrinos (*i.e.* ν_e and $\bar{\nu}_e$). In 1962, the AGS experiment at Brookhaven National Laboratory generated the first neutrino beam, and observed a second type of neutrino, the muon neutrino ν_μ, by detecting muons produced in ν_μ Charged-Current (CC) interactions [48].

In the late 1960s, the electroweak theory was established by A. Salam, S. Glashow and S. Weinberg [49, 50, 51]. The electroweak theory is combined with the Quantum Chromodynamics theory [52, 53], and the combined theory is known as "the Standard Model" of particle physics today. In the Standard Model, three gauge bosons, $W^\pm$ and Z^0, which are the mediators of the weak interaction, are predicted. Interactions which are accompanied by the $W^\pm$ bosons are regarded as CC interactions, whereas Neutral-Current (NC) interactions are interactions in which Z^0 boson is involved as the mediator. Figure 1.1 shows the vertices of CC and NC interactions. Electron neutrinos and muon neutrinos were observed via CC interactions, and NC interactions had never been observed before 1973. In 1973, the Gargamelle bubble chamber at CERN confirmed the existence of NC interactions.

(a) Charged Current interaction   (b) Neutral Current interaction
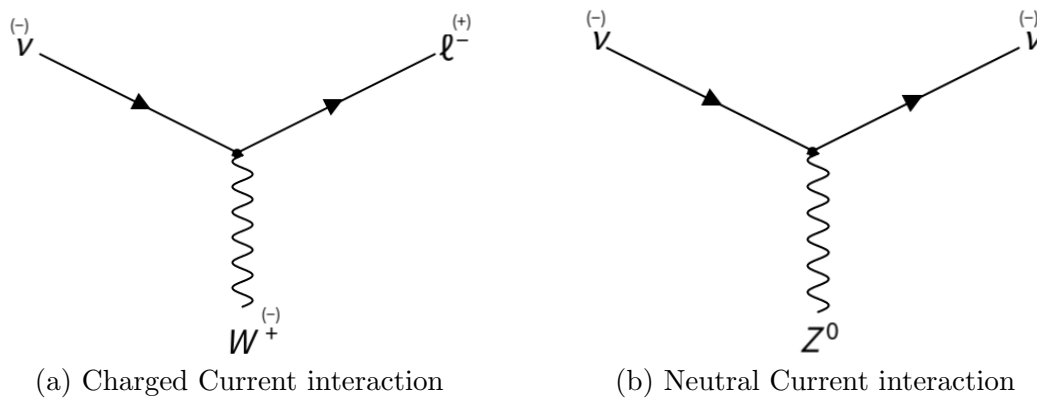
Figure 1.1: Feynman diagrams of neutrino interaction vertices

When the third charged lepton, τ, was discovered at SLAC in 1975 [54], a third generation of neutrino, ν_τ, was expected to exist. In 1989, the number of neutrino generations which are lighter than half the mass of Z^0 boson was determined

to be three by the Mark II experiment at the SLC [55] and other experiments at LEP [56, 57, 58], and existence of ν_τ was strongly indicated. Finally ν_τ was discovered by the DONUT experiment at Fermilab in 2001 [59].

These results established the nature of neutrinos as the particles of the Standard Model; In the Standard Model, ν_e, ν_μ, and ν_τ are neutral left-handed fermions, interact with matter only by the weak interactions, and are massless. However, the discovery of neutrino oscillation showed that neutrinos do have non-zero mass.

History of neutrino oscillation is very closely related to the "solar neutrino problem". However, neutrino oscillation was discovered by the observation of the atmospheric neutrinos.

The first indication of neutrino oscillation came from this problem. It was thought that neutrinos might be utilized to probe environments in which other particles can not penetrate. An attempt was made by R. Davis and J. Bahcall to study nuclear reactions occurring in the sun and test Bahcall's solar model, which is referred to as the standard solar model. To this aim, in 1968 Davis measured the electron neutrino flux from the sun at Homestake [60], and the observed flux was about three time smaller than the prediction of the standard solar model [61]. It was suspected that either there was a problem with the model or a problem with the measurement based on this discrepancy. However, in 1989 Kamikande [62] also observed a deficit of electron neutrino flux compared to the solar model with a direction information, which was consistent with the Homestake observation. The directional information which was unavailable at the Homestake experiment proved that electron neutrinos definitely come from the sun, but the measured flux was still smaller than the prediction. Observations of helioseismology showed agreement with the solar model's predictions by the early 1990s, whereas results from SAGE [63], GALLEX [64], and GNO [65] neutrino experiments still showed consistent results with the Homestake experiment. The answer to this solar neutrino problem was provided by Super-Kamiokande [66] and SNO [67]. Super-kamiokande precisely measured the flux of ^{8}B solar neutrinos only for the elastic scattering (ES) reaction by using a water target in 1998. In 2001, SNO detected all the three interactions, CC, ES, and NC, using a heavy water target to measure the total flux of ^{8}B solar neutrinos. The measured total flux by SNO with the constraint on ES from Superk-Kamiokande was consistent with the prediction of the standard solar model. Also, SNO translated the measured fluxes of CC, ES, and NC interactions into the flux of ν_μ and ν_τ under hypothesis of neutrino oscillations. The resultant flux of ν_μ and ν_τ was above $5.3\,\sigma$ from zero, which corresponds to transition between flavors.

The first observation of neutrino oscillations was obtained from atmospheric neutrinos. When primary cosmic rays, mostly protons, interact with nuclei in the atmosphere, (anti) muon and electron neutrinos are produced dominantly by pion and muon decays. A flux ratio of $(\nu_\mu + \bar{\nu}_\mu)/(\nu_e + \bar{\nu}_e)$ is expected to be $\sim$2 around at $1\,\text{GeV}$ of neutrino energies. However, Kamiokande observed about two times smaller than the expectation [68, 69]. Similar results were also reported by the IMB [70] and Soudan-2 experiments [71]. In 1998, Super-Kamiokande [72] measured zenith angle dependent fluxes of $\nu_e + \bar{\nu}_e$ and $\nu_\mu + \bar{\nu}_\mu$ separately. The zenith angle is a good proxy

of the distance that an incoming neutrino has traveled from its generation point. As will be described later, neutrino oscillation depends on the distance, and thus the zenith angle dependent fluxes are suitable to study neutrino oscillation. Both the observed electron neutrino and muon neutrino fluxes were consistent with the hypothesis of $\nu_\mu \to \nu_\tau$ oscillation, which became the discovery of neutrino oscillation. In 2006, the $\nu_\mu \to \nu_\tau$ oscillation was supported by the K2K long baseline neutrino experiment which used a muon neutrino beam [73]. K2K observed a deficit of the beam muon neutrinos, which is consistent with the observation of the atmospheric neutrinos by SK. Both SK and K2K observed the deficits of muon neutrinos by detecting muon neutrinos. Direct observation of $\nu_\mu \to \nu_\tau$ was made by OPERA [74] in 2014.

1.1.2 Neutrino oscillations

Neutrino oscillation was originally proposed by B. Pontecorvo in a context of ν - $\bar{\nu}$ oscillations in 1957 [75] although such oscillation has never been observed. In 1962, a full theory of two flavor oscillations was developed by Maki, Nakagawa and Sakata [76]. In the following, the standard three flavor neutrino oscillations are described.

The formalization of the theory of neutrino oscillations is built on the fact that the flavor eigenstates of the weak interaction, $|\nu_\alpha\rangle$ ($\alpha=e,\mu,\tau$), are different from the mass eigenstates, $|\nu_i\rangle$ ($i=1,2,3$). The flavor eigenstates in which neutrinos are always created are related to the mass eigenstates that neutrinos propagate as:

$$|\nu_\alpha\rangle = \sum_{i=1}^{3} U_{\alpha i}^* |\nu_i\rangle, \tag{1.1.1}$$

where $U_{\alpha i}$ are the elements of the 3×3 unitary matrix referred to as the Pontecorvo-Maki-Nakagawa-Sakata (PMNS) or Maki-Nakagawa-Sakata (MNS) matrix. In the modern parametrization [77], the matrix can be expressed in terms of four matrices as:

$$
\begin{aligned}
U &= \begin{pmatrix} U_{e1} & U_{e2} & U_{e3} \\ U_{\mu 1} & U_{\mu 2} & U_{\mu 3} \\ U_{\tau 1} & U_{\tau 2} & U_{\tau 3} \end{pmatrix} \\
&= \begin{pmatrix} 1 & 0 & 0 \\ 0 & c_{23} & s_{23} \\ 0 & -s_{23} & c_{23} \end{pmatrix} \begin{pmatrix} c_{13} & 0 & s_{13}e^{-i\delta_{CP}} \\ 0 & 1 & 0 \\ -s_{13}e^{i\delta_{CP}} & 0 & c_{13} \end{pmatrix} \begin{pmatrix} c_{12} & s_{12} & 0 \\ -s_{12} & c_{12} & 0 \\ 0 & 0 & 1 \end{pmatrix} \times \mathrm{diag}(1, e^{i\frac{\alpha_{21}}{2}}, e^{i\frac{\alpha_{31}}{2}}),
\end{aligned}
\tag{1.1.2}
$$

where $c_{ij}=\cos\theta_{ij}$ and $s_{ij}=\sin\theta_{ij}$. The U is parameterized by three mixing angles (θ_{12},

θ_{23}, θ_{13}), a Dirac CP-violating phase (δ_{CP}), and two Majorana CP-violating phases (α_{21},α_{31}), where CP stands for charge-parity. The Majorana CP-violating phases or the last matrix in the equation have physical meaning only if neutrinos are Majorana particle whose antiparticle is its own particle. It has not been shown whether or not neutrinos are Majorana particles yet. Whilst the Majorana nature of neutrinos is unknown, the Majorana CP-violating phases do not affect neutrino oscillation probability that can be studied experimentally since this probability depends on U^*U, in which case these phases are cancelled out.

Neutrino oscillations in vacuum

Neutrinos experimentally observed are created as the flavor states. Consider the time evolution of a neutrino which is produced in a flavor state $|\nu_\alpha\rangle$, in vacuum. Using the relation between the flavor eigenstates and the mass eigenstates, the state of the neutrino propagating in vacuum after time t, $|\nu_\alpha(t)\rangle$, can be written as (in natural units where c and $\hbar$ are set to 1):

$$
\begin{aligned}
|\nu_\alpha(t)\rangle &= e^{-i\hat{H}t}|\nu_\alpha\rangle \\
&= \sum_i e^{-iE_i t}U_{\alpha i}^*|\nu_i\rangle,
\end{aligned}
\tag{1.1.3}
$$

where $\hat{H}$ is the free particle Hamiltonian, E_i is the total energy of i-th mass state. The transition probability to flavor state $|\nu_\beta\rangle$ at time t is given as:

$$
\begin{aligned}
P(\nu_\alpha \rightarrow \nu_\beta) &= |\langle\nu_\beta|\nu_\alpha(t)\rangle|^2 \\
&= \sum_{i,j} U_{\beta i}^* U_{\beta i} U_{\alpha j} U_{\beta j}^* e^{-i(E_i - E_j)t}.
\end{aligned}
\tag{1.1.4}
$$

In the ultra-relativistic limit as is the case in neutrino oscillation experiments, the following approximation can be done:

$$
E_i - E_j = \sqrt{p_i^2 + m_i^2} - \sqrt{p_j^2 + m_j^2} \approx \frac{\Delta m_{ij}^2}{2E},
\tag{1.1.5}
$$

where m_i is the mass of i-th mass eigenstate, $E = |\boldsymbol{p}|$ is the neutrino energy in which case dependence of p_k and p_ℓ is neglected, p is the neutrino momentum, and

$$
\Delta m_{ij}^2 = m_i^2 - m_j^2.
\tag{1.1.6}
$$

Also, in this case the approximation $t \approx L$ is applicable, where L is the distance

that the neutrino traveled from its creation point. The transition probability can be written in terms of the neutrino energy E and the propagation length L:

$$P(\nu_\alpha \to \nu_\beta) = \sum_{i,j} U_{\alpha i}^* U_{\beta i} U_{\alpha j} U_{\beta j}^* \exp(-i\frac{\Delta m_{ij}^2 L}{2E}). \tag{1.1.7}$$

It may be instructive to express this as follows:

$$P(\nu_\alpha \to \nu_\beta) = \delta_{\alpha\beta} - 4\sum_{i>j} \mathrm{Re}\left[U_{\alpha i}^* U_{\beta i} U_{\alpha j} U_{\beta j}^*\right] \sin^2(\frac{\Delta m_{ij}^2 L}{4E})$$

$$+ 2\sum_{i>j} \mathrm{Im}\left[U_{\alpha i}^* U_{\beta i} U_{\alpha j} U_{\beta j}^*\right] \sin(\frac{\Delta m_{ij}^2 L}{2E}). \tag{1.1.8}$$

From the above equation and Equation 1.1.2, it can be seen that the probability can be described by the three mixing angles, the CP-violating phase δ_{CP}, and the squared mass differences. In addition, the probability varies periodically with a phase which is proportional to $\Delta m_{ij}^2 L/E$ ($\simeq 1.27 \times \frac{\Delta m_{ij}^2 L}{E} \left[\frac{\mathrm{eV}^2 \ \mathrm{km}}{\mathrm{GeV}}\right]$ in SI units), by which the phenomenon of this transition between flavor eigenstates is referred to as neutrino oscillation. It is worth noting that oscillations between different flavor eigenstates can happen only if the following two conditions are satisfied. One of the two condition is that the mixing matrix U is not diagonal, which means that the flavor eigenstates are different from the mass eigenstates. The other one is that at least one of the masses is different from others. Therefore, existence of neutrino oscillations is regarded as evidence of non-zero mass of neutrino.

For antineutrinos, the relation between the flavor and mass eigenstates is given as:

$$|\bar{\nu}_\alpha\rangle = \sum_{i=1}^{3} U_{\alpha i}|\bar{\nu}_i\rangle. \tag{1.1.9}$$

By following the same procedure as neutrinos, the oscillation probability is obtained as follows:

$$P(\bar{\nu}_\alpha \to \bar{\nu}_\beta) = \delta_{\alpha\beta} - 4\sum_{i>j} \mathrm{Re}\left[U_{\alpha i}^* U_{\beta i} U_{\alpha j} U_{\beta j}^*\right] \sin^2(\frac{\Delta m_{ij}^2 L}{4E})$$

$$- 2\sum_{i>j} \mathrm{Im}\left[U_{\alpha i}^* U_{\beta i} U_{\alpha j} U_{\beta j}^*\right] \sin(\frac{\Delta m_{ij}^2 L}{2E}). \tag{1.1.10}$$

The only difference between neutrinos and antineutrinos can be seen in the sign of

the third term from the above equation and Equation 1.1.10. If $\alpha=\beta$, the product, $U_{\alpha i}^* U_{\beta i} U_{\alpha j} U_{\beta j}^*$, becomes a real number. Thus, $P(\nu_\alpha \to \nu_\beta) = P(\bar{\nu}_\alpha \to \bar{\nu}_\beta)$ since the third term vanishes. On the one hand, for $\alpha \neq \beta$, oscillation probability differs between neutrinos and antineutrinos unless $\delta_{CP} = 0$ or π. Therefore, the value of δ_{CP} can be studied only via transition between different flavors (called "neutrino appearance").

As will be discussed later, it is practically sufficient to consider two flavor oscillations in many cases. The mixing matrix defined in Equation 1.1.2 reduces to a single rotation matrix as follows:

$$U = \begin{pmatrix} \cos\theta & \sin\theta \\ -\sin\theta & \cos\theta \end{pmatrix}. \qquad (1.1.11)$$

Accordingly, the oscillation probability given by Equation 1.1.8 reduces to

$$P(\nu_\alpha \to \nu_\beta) = \begin{cases} 1 - \sin^2 2\theta \sin^2\left(\frac{1.27\Delta m^2 L}{E}\right) & (\alpha = \beta) \\ \sin^2 2\theta \sin^2\left(\frac{1.27\Delta m^2 L}{E}\right) & (\alpha \neq \beta) \end{cases}. \qquad (1.1.12)$$

Neutrino oscillations in matter

When neutrinos propagate a dense matter such as the Sun and the Earth, the neutrino oscillation probability in vacuum is modified since they can interact with the matter via the weak interactions. This effect is known to be Mikheyev-Smirnov-Wolfenstein (MSW) effect [78, 79].

Propagation of neutrinos in matter is affected by effective potentials due to the forward CC and NC interactions. Since the NC interaction is independent on neutrino flavor, the resultant effect of the NC reaction is a common phase factor among the flavor states, and does not affect the vacuum oscillation probability. However, since only electrons and not muons and taus are contained in ordinary matter, the CC interaction affects electron neutrinos, whereas the other neutrino flavors do not undergo the interaction. This asymmetry introduces an additional potential V_{CC} which affects only electron neutrinos:

$$V_{\text{CC}} = \pm\sqrt{2}G_F n_e, \qquad (1.1.13)$$

where G_F is the Fermi coupling constant and n_e is the number density of electrons in the matter. In the equation, the positive and negative signs are applied to neutrinos

and antineutrinos, respectively.

In order to see how the matter effect modifies the vacuum oscillation probability, for simplicity, consider a case of two flavor oscillations between ν_e and ν_x in a constant matter, where ν_x is either ν_μ or ν_τ. In this case, the oscillation probabilities of $P(\nu_e \to \nu_x)$ and $P(\nu_e \to \nu_e)$ are obtained by replacing Δm^2 and $\sin^2 \theta$ in Equation 1.1.12 with Δm_M^2 and $\sin^2 \theta_M$, respectively. Δm_M^2 and $\sin^2 \theta_M$ are given as:

$$\sin 2\theta_M = \frac{\sin 2\theta}{\sqrt{\sin^2 2\theta + (\cos 2\theta - A/\Delta m^2)^2}} \tag{1.1.14}$$

$$\Delta m_M^2 = \Delta m^2 \sqrt{\sin^2 2\theta + (\cos 2\theta - A/\Delta m^2)^2}, \tag{1.1.15}$$

where $A = 2\sqrt{2} G_F n_e E$. Note that for $A \to 0$, $\sin 2\theta_M$ and Δm_M^2 reduce to the vacuum ones. From the above equation, it can be seen that the mixing angle and mass splitting are changed from the vacuum case by the matter effect.

Thanks to the matter effect, maximal mixing, $\sin \theta_M = 1$, can occur even for a very small vacuum mixing angle if the resonance condition is satisfied:

$$\cos 2\theta = \frac{A}{\Delta m^2}. \tag{1.1.16}$$

It is worth noting that the sign of A depends on neutrinos or antineutrinos. In addition, the condition is sensitive to the sign of Δm^2. Therefore, for positive value of $\cos 2\theta$, the resonance effect only happens for neutrinos if $\Delta m^2 > 0$, whereas it only happens for antineutrinos if $\Delta m^2 < 0$. In other words, the resonance effect can be utilized to determine the sign of Δm^2.

A full treatment of the matter effect within three flavor oscillations can be seen in [80].

Experimental status of neutrino oscillation parameters

The mixing angles θ_{12}, θ_{13}, θ_{23}, the Dirac CP-violating phase δ_{CP}, and the neutrino masses of the Standard Model need to be determined experimentally. Neutrinos oscillation experiments are sensitive to the angles, the phase, and the squared mass differences Δm_{21}^2 and Δm_{32}^2. Table 1.1 summarizes the current measurement results from various experiments. In the table, Normal hierarchy (NH) and Inverted hierarchy (IH) refer the ordering of neutrino eigen masses:

$$\text{NH}: \ m_3 \ > \ m_2 \ > \ m_1,$$
$$\text{IH}: \ m_2 \ > \ m_1 \ > \ m_3.$$

Table 1.1: Summary of the current measurements of neutrino mixing angles and squared mass differences. Values taken from [34] with 2019 update.

Parameter	Value
$\sin^2\theta_{21}$	0.307 ± 0.013
$\sin^2\theta_{13}$	$(2.18\pm0.07)\times10^{-2}$
$\sin^2\theta_{23}$	$0.536^{+0.023}_{-0.028}$ (IH) $0.512^{+0.019}_{-0.022}$ (NH) $0.542^{+0.019}_{-0.022}$ (NH)
Δm^2_{12}	$(7.53\pm0.18)\times10^{-5}$ eV^2
Δm^2_{23}	$(-2.55\pm0.04)\times10^{-3}$ eV^2 (IH) $(2.444\pm0.034)\times10^{-3}$ eV^2 (NH)

In reality, the relation, $|\Delta m^2_{23}| >> \Delta m^2_{21}$, is hold as shown in the table. Since the oscillation periods of neutrino oscillation probability depend on $\Delta m^2_{ij}L/E$, only oscillation parameters of interest can be studied experimentally by choosing relevant baseline L and neutrino energy E through the leading oscillation effect. In such case, the two flavor oscillations can be adopted, and a set of relevant mixing angle and square mass difference is extracted according to Equation 1.1.12.

In the following, the past and current neutrino oscillation experiments are briefly summarized.

θ_{12}, Δm^2_{12}:

> These parameters are related to the solar neutrino oscillations and have been measured by solar neutrino experiments[64, 65, 63, 81, 23, 82]. The preferred solution by these experiments, so called LMA solution [83], was confirmed by the KamLAND experiment [84], which uses a liquid scintillator to detect $\bar{\nu}_e$ produced in distant nuclear reactors.

θ_{23}, $|\Delta m^2_{23}|$:

> Atmospheric neutrinos and accelerator neutrinos are sensitive to these parameters. SK [85] and IceCube [86] have used atmospheric neutrinos while T2K [87, 88, 89], NovA [90, 91, 92], K2K [73], and MINOS [93] uses accelerator based neutrinos.

θ_{13}, Δm^2_{ee}:

In 2011, the first indication of non-zero value of θ_{13} was reported by T2K [94] which uses artificial ν_μ and $\bar{\nu}_\mu$ beams. Non-zero value of θ_{13} was measured in 2012 by nuclear reactor oscillation experiments: Daya Bay [95], RENO [96], and Double Chooz [97]. T2K also measured non-zero θ_{13} with a significance of more than 7 σ in 2014 [98]. In these reactor experiments, two neutrino mass splitting $|\Delta m_{31}^2|$ and $|\Delta m_{32}^2|$ needs to be taken into account, and these mass splitting can be studied via an effective squared mass difference: $\Delta m_{ee}^2 \simeq \cos^2\theta_{12}|\Delta m_{31}^2| + \sin^2\theta_{12}|\Delta m_{32}^2|$.

δ_{CP}:

The value has not been precisely measured yet so far and been still largely unknown. From an experimental point of view, measurements of $\nu_\mu \rightarrow \nu_e$ and $\bar{\nu}_\mu \rightarrow \bar{\nu}_e$ oscillations are the only possible way to study the parameter. T2K and NOνA which are ongoing experiments are designed to be sensitive to the parameter.

Importance of precision measurement of remaining neutrino oscillation parameters

Neutrino oscillations have been studied and related parameters have been measured by many experiments. However, the value of δ_{CP}, mass hierarchy (MH), and the octant of θ_{23} have not been understood yet.

One of questions which can not be answered by the Standard Model is the imbalance of matter (baryon) and antimatter (antibaryon) in the universe. To explain this asymmetry, in 1967 A. Sakharov proposed a set of three necessary conditions, one of which requires that in a theory both C- and CP-symmetries are violated [99]. The Standard Model contains such CP violation in the Cabbibo-Kobayashi-Masakawa (CKM) matrix [100, 101], which describes mixing between up- and down-type quarks. In the quark sector, the first CP violation was observed in measons via neutral K decays [102], and recently CP violation in baryons was discovered [103]. However, it is known that these observations of CP violation within the framework of the Standard Model are not sufficient to account for the matter and antimatter asymmetry, which naturally requires there be a theoretical model "beyond the Standard Model". From a theoretical point of view, non-zero value of δ_{CP} would motivate a model, which includes a heavy right-handed Majorana neutrino, has offered a scenario called "leptogenesis" [104]. In leptogenesis, first a lepton asymmetry is generated by the heavy neutrino decays if CP violation exists in the lepton sector, and the lepton asymmetry turns into the observed baryon asymmetry. Therefore, measurement of δ_{CP} is important to understand the matter-antimatter asymmetry.

Thanks to relatively large value of θ_{13}, a possibility for probing δ_{CP} has been opened. Among the current generation of neutrino oscillation experiments, T2K and NOvA have ability to study δ_{CP}. In 2019, T2K reported an indication of near

maximal violation by excluding $\delta_{CP} = 0$ with a significance of 3 σ [1] as shown in Figure 1.2. On the other hand, however, the NOvA's best estimation of δ_{CP} prefers CP conservation although statistical significance is very weak [105].
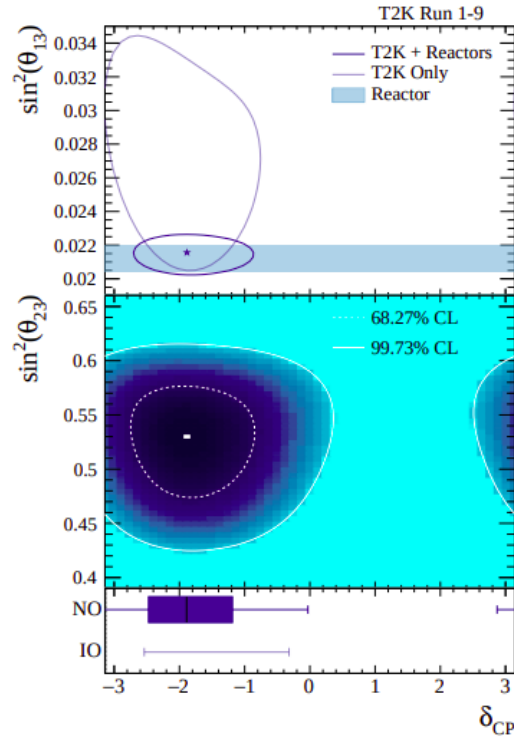
Figure 1.2: Experimental constraints on δ_{CP}, $\sin^2\theta_{13}$, and $\sin^2\theta_{23}$ by T2K. 2D confidence intervals for δ_{CP} vs $\sin^2\theta_{13}$ for NH (top), 2D confidence intervals for δ_{CP} vs $\sin^2\theta_{23}$ with reactor constraint for NH (middle), 1D confidence intervals on δ_{CP} with reactor constraint for both NH and IH (bottom). In the bottom figure, the error bars represent 3 σ allowed regions. Figure taken from [1].

Although the theoretical framework of mixing is similar between the neutrino and quark sectors, the matrix elements are very different between the CKM and PMNS matrices. Figure 1.3 visualizes the matrix elements of the two matrices, and clear difference can be seen. To account for this difference, theoretical models have been built [106, 107, 108, 109].
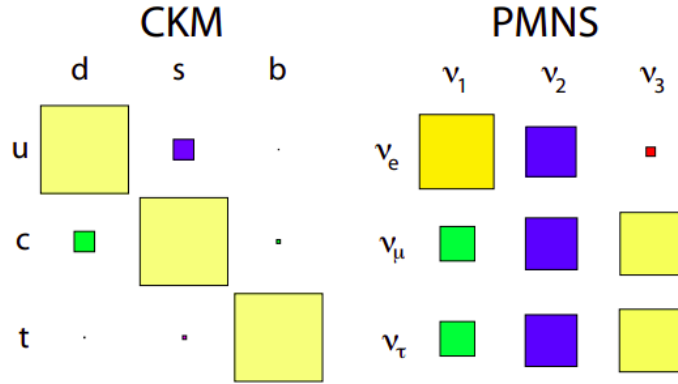
Figure 1.3: Size of matrix elements for the CKM matrix (left) and the PMNS matrix (right). Figure taken from [2].

In addition, from a theoretical point of view, understanding of the correct MH together with the neutrino mixing would provide information about how the neutrino mixing and masses are generated [110]. Thus, it is important to know the correct MH and the octant of θ_{23} as well as δ_{CP}. T2K, NOvA, and Super-Kamiokande are sensitive to MH due to the Earth's matter effect. Although statistical significance is still not sufficient, all the three experiments prefer NH. For the octant of θ_{23}, in both T2K and NOvA, the probabilities of $\nu_\mu \rightarrow \nu_e$ and $\bar{\nu}_\mu \rightarrow \bar{\nu}_e$ oscillations (called "bi-probability") can be sensitive to a term which is proportional to $\sin 2\theta_{23}$. Measurements of bi-probability distinguishes between the lower octant ($\theta_{23} < 45°$) and the upper octant ($\theta_{23} > 45°$). NOvA has weakly preferred the upper octant with a significance of 1.6 σ by comparing observed electron appearance events between the ν- and $\bar{\nu}$- modes of the beam neutrinos [105]. Figure 1.4 shows the measurement results by NOvA.
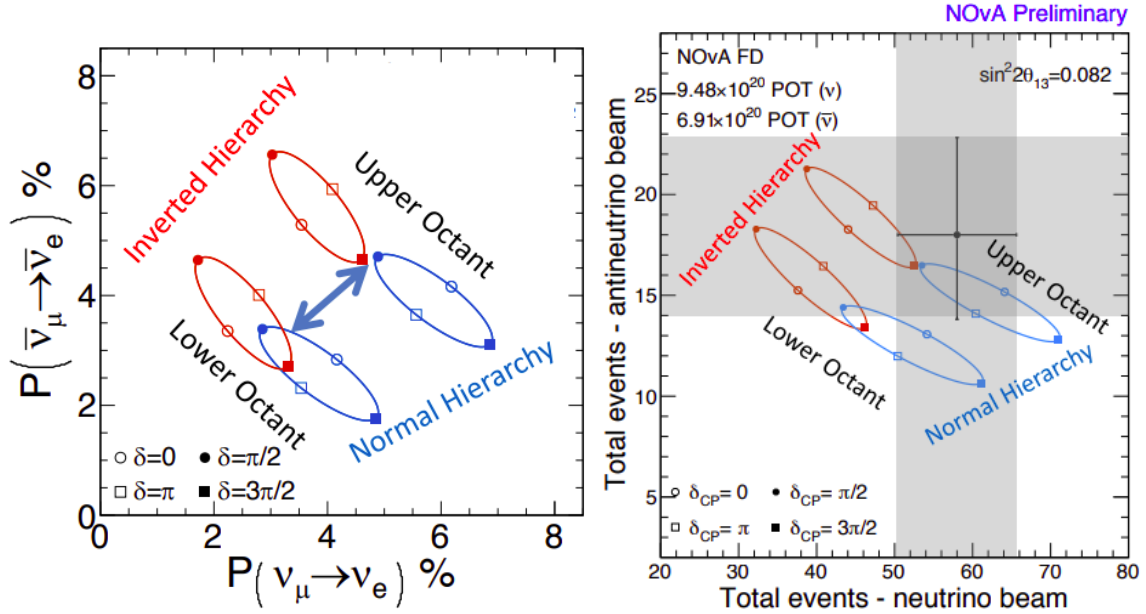
Figure 1.4: Probabilities of $\nu_\mu \to \nu_e$ and $\bar{\nu}_\mu \to \bar{\nu}_e$ oscillations for the NOvA experiment's setup (left) and the observed electron appearance events for the ν- and $\bar{\nu}$-beam operations (right). Figure taken from [3].

1.1.3 Supernova Relic Neutrinos

Neutrinos have offered themself as a probe to study the universe since the detection of the neutrinos [111, 112] from SN1987A, which is a core collapse supernova that occurred in the Large Magellanic Cloud. When the evolution of stars with mass of $M \gtrsim 8M_\odot$ reach to the final stages, core collapse supernovae eventually occur, which releases typical energies of $\mathcal{O}(10^{53})$ ergs. Since $\sim$99 % of the released energy is carried away as neutrino burst during a core-collapse explosion, detecting and studying these neutrinos experimentally may provide vital information to understand the mechanism of supernova explosion. Although the neutrino burst provides unique and interesting information, there has been no neutrino burst detected since SN1987, because expected supernova explosion rate in our galaxy is very small, $\lesssim 3$ per century [113, 114]. However, neutrinos emitted from all the past core-collapse supernovae should still exist at present because of the fact that neutrinos only weakly interact with matter. Indeed, flux of such neutrinos has been theoretically predicted and these neutrinos are called "supernova relic neutrinos" (SRN) and are referred to as "diffuse supernova neutrino background" (DSNB). Detailed experimental studies on SRN would provide information about the evolution of the universe.

The SRN flux is a superposition of each of all the past supernovae by taking into account the redshift effect by the expansion of the universe and the cosmochemical evolution. The differential SRN flux with respect to energies of SRN at the Earth is given by [115, 116]:

$$\frac{d\phi}{dE_\nu} = c \int_0^\infty R_{\text{SN}}(z)(1+z)\frac{dN(E'_\nu)}{dE_\nu}\left|\frac{dt}{dz}\right|dz, \qquad (1.1.17)$$

where R_{SN} is the core-collapse supernova rate at redshift z, E'_ν is defined as $E_\nu(1+z)$, and $dN(E'_\nu)/dE_\nu$ is the number spectrum emitted by one supernova explosion, where a neutrino received at energy E_ν was emitted at a higher energy E'_ν. The cosmic time t is related to the redshift z by Friedmann equation as follows:

$$\frac{dz}{dt} = -H_0(1+z)\sqrt{\Omega_{\text{m}}(1+z)^3 + \Omega_\Lambda}, \qquad (1.1.18)$$

where H_0 is the Hubble constant, Ω_{m} and Ω_Λ are the cosmic matter density and cosmological constant, respectively.

From an experimental point of view, large water Cherenkov detector is suitable to study SRN. Since typical average energy of SRN ranges from $\sim 10\,\text{MeV}$ to $\sim 20\,\text{MeV}$ [117, 118], SRN interacts with water via various reaction channels:

Inverse β decay (IBD): $\bar\nu_e + p(\text{free}) \rightarrow e^+ + n$

Electron elastic scattering: $\nu_e + e^- \rightarrow \nu + e^-$

CC interaction with oxygen: $\nu_e +^{16}O \rightarrow e^- +^{16}F,\ \bar\nu_e +^{16}O \rightarrow e^+ +^{16}N$

NC interaction with oxygen: $\nu_x +^{16}O \rightarrow \nu_x + \gamma + X,$

where x denotes all neutrino flavors (e, μ, τ) and X represents residual nuclei. Figure 1.5 shows the cross-sections for these interaction channels as a function of neutrino energy. As shown in the figure, the cross section of IBD is almost two orders of magnitude larger than those of the other reactions below $30\,\text{MeV}$. Therefore, SRN is dominantly detected through the IBD reaction.
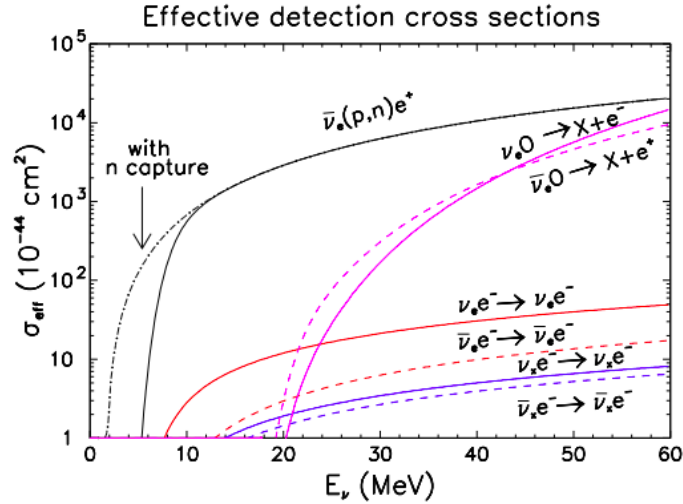
Figure 1.5: Effective cross section for SRN and water, which includes energy resolution and detector threshold effect based on Super-Kamiokand II. Figure taken from [4].

Present status of SRN searches

There have been many experimental SRN searches [119, 120]. However, SRN has never been observed. Super-Kamiokande [121, 122] and KamLAND [123] have set stringent upper limits on the SRN flux. Figure 1.6 shows a SRN flux prediction in comparison with the experimental limits. Although SRN flux prediction depends on theoretical model or assumption, the current experimental limits are close to prediction. Future experiments such as SK-Gd [124], Hyper-Kamiokande [125], JUNO [126], the Jinping neutrino experiment [127] may reach to various predictions, and thus aim to discover SRN.
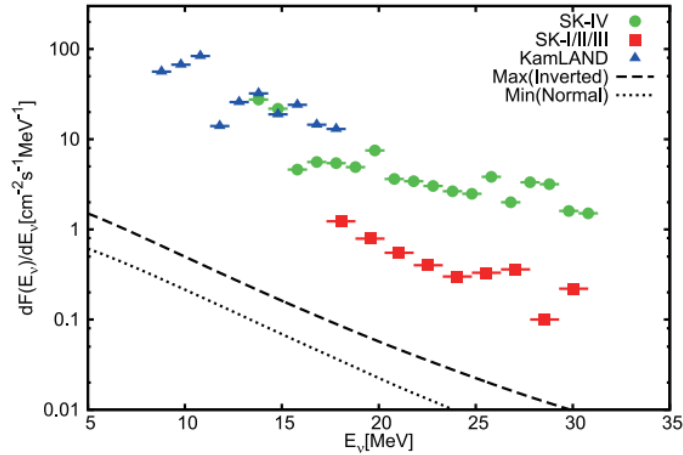
Figure 1.6: Experimental limits on SRN flux at 90% C.L. with flux predictions. Figure taken from [5].

1.2 Neutrons associated with ν-nucleus interactions on water

Neutrons associated with neutrino interactions on water target are expected to be of value to various important physics analyses: measurement of neutrino oscillations, SRN searches, and nucleon decay searches. It has also been suggested that information about these neutrons will improve neutrino oscillation analyses [128]. Indeed, in near future experiments employing water Cherenkov detectors such as SK-Gd [124] and Hyper-Kamiokande [125], utilization of such neutrons are planned in order to improve their physics analyses.

In this section, production of neutrons related to ν interactions on water target is outlined. Following this, benefits to physics analyses are described, and the current status of experimental studies on neutrons associated with ν interactions are overviewed, which emphasises the importance of the primary analysis presented in this thesis.

1.2.1 Neutron productions
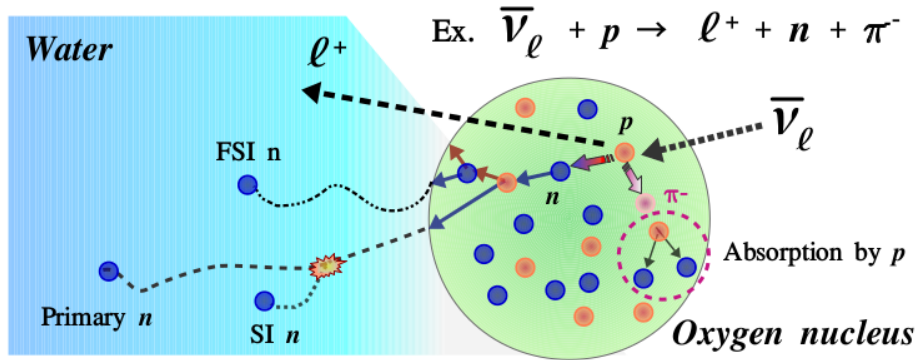
Figure 1.7: A schematic drawing of neutron productions by primary $\bar{\nu}$-nucleon interaction inside oxygen nucleus, hadronic-final-state interactions inside the nucleus, and hadronic secondary interactions in water. In this case, the primary reaction $\bar{\nu}_\ell + p \rightarrow \ell^+ + n + \pi^-$ is used.

When a neutrino interaction happens in water, the interaction often produce one or more neutrons. These neutrons are produced via three processes:

- Primary ν-nucleon interaction in nuclear medium,

    - *e.g.* $\bar{\nu}_\ell + p \rightarrow \ell^+ + n$

- Hadronic final-state-interaction (FSI) inside the target nucleus.

    - *e.g.* $p + p \rightarrow p + n + \pi^+$

- Hadronic secondary interaction (SI) in water.

  - *e.g.* $\quad n + ^{16}O \rightarrow n + n + ^{15}O^*$

Figure 1.7 shows a schematic drawing of neutron production by these three processes. These neutrons are quickly thermalized and then are captured by hydrogen nucleus, after which single 2.2 MeV γ ray is produced. By detecting this γ ray, the T2K far detector can tag neutrons of any energy. Details of the neutron tagging at the far detector will be described in Chapter 6.

For neutrino energies from sub-GeV up to several GeV, neutrinos scatter off a nucleon inside the target nucleus via various reaction channels. The resultant number of neutrons produced in the primary ν-nucleon interaction depends on interaction channel and whether it is neutrino or antineutrino. In the primary interaction, hadrons such as protons and charged pions as well as neutrons are also produced inside the target nucleus, and these hadrons have a considerable probability to undergo interaction inside the nucleus before they escape from it. This hadronic interaction inside nucleus is referred to as Hadronic final-state-interaction (FSI). After leaving the target nucleus, they propagate across the detector volume of an experiment, and they can interact with the detector's medium, which is known as hadronic secondary interaction (SI).
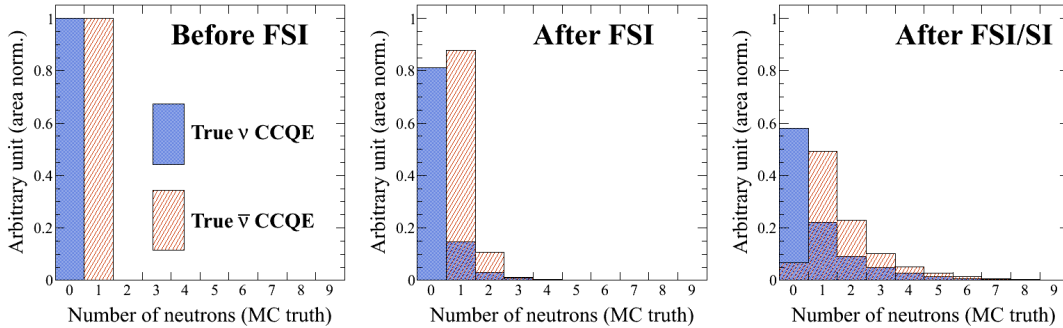
Figure 1.8: An example of neutron multiplicity using true CCQE ν (cyan) and $\bar{\nu}$ (orange) interactions in water. The left, middle, right correspond to neutron multiplicities after primary interaction, after FSI, and after SI, respectively. T2K beam neutrino flux is assumed.

Figure 1.8 shows an example of contribution from each process to neutron multiplicity in case of Charged Current quasi-elastic (CCQE) neutrino and anti-neutrino interactions on water target. In this case, neutrinos produce a proton, whereas antineutrinos produce a neutron as follows:

$$\nu_\ell + n \rightarrow \ell^- + p \tag{1.2.1}$$

$$\bar{\nu}_\ell + p \rightarrow \ell^+ + n. \tag{1.2.2}$$

The outgoing nucleons undergo FSI by they leave the target nucleus, and additional neutrons can be produced even for protons. For instance, a proton's FSI can produce a neutron via a single-pion production reaction: $p + p \rightarrow p + n + \pi^+$. As another example, a π^- produced by a single-pion production reaction of a neutron's FSI is often absorbed by a nucleon pair before it escapes from the nucleus, and the absorption can produce multiple neutrons. Due to the effects of FSI, neutron multiplicity is modified after FSI from that of the primary interaction as shown in the middle panel of the figure. Once particles produced in both the primary ν interaction and FSI leave the target nucleus, they undergo SI in water when propagating through the detector. In case of SI, negative muons produced in the primary neutrino interactions also contribute to the neutron production since these muons lose energies and are eventually captured on nuclei if they do not decay. As a consequence of SI, neutrons are further produced, which is illustrated in the right panel of Figure 1.8.

1.2.2   Benefits of utilization of neutrons

As explained above, the effects of FSI and SI largely modify the neutron multiplicity of the primary ν interaction. However, neutron multiplicity is still clearly different between neutrinos and antineutrinos even after FSI and SI. This difference, for instance, can be exploited to distinguish between neutrinos and antineutrons. Since water Cherenkov detectors are not magnetized (or can not be magnetized due to presence of photosensors), it is difficult to perform a ν-$\bar{\nu}$ separation although this is very important in order to improve sensitivities to the MH determination and δ_{CP} measurement. Similar difference in neutron multiplicity is also seen between CC interactions and NC interactions as shown in Figure 1.9, which is expected to be useful to reject one of main backgrounds for the MH determination by using the atmospheric neutrinos at SK.
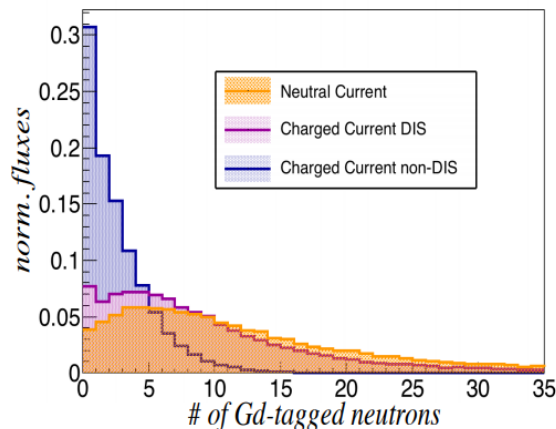
Figure 1.9: Distribution of tagged neutron multiplicity for different ν interaction channels in the SK atmospheric multi-GeV e-like sample assuming a 70% tagging efficiency, which corresponds to the full configuration of SK-Gd. Figure taken from [6].

Another way to utilize neutrons is about an improved energy estimation of neutrinos. It is desirable to reconstruct energies of neutrinos as precise as possible for any measurements of neutrino oscillations, because effects of neutrino oscillations depend on neutrino energy. In a water Cherenkov detector, only charged leptons and pions produced in ν interactions can be detected for most cases, and the energy which is transferred to the hadonic system at the primary ν interaction can not be seen. The resultant reconstructed neutrino energy is therefore highly biased, which smears effects of neutrino oscillations. Since the number of neutrons produced in FSI and SI are correlated with the unseen energy, estimate of neutrino energy is expected to be improved by counting these neutrons. Potential of such energy reconstruction has been studied in the context of the atmospheric neutrino analyses at SK-Gd [7]. Figure 1.10 demonstrates a significant improvement on the energy reconstruction of the atmospheric neutrinos. This idea can be applied to the atmospheric neutrino oscillation analyses in Hyper-Kamiokande, and a large improvement on the sensitivities to the δ_{CP} measurement and the MH determination has been expected as shown in Figure 1.11.
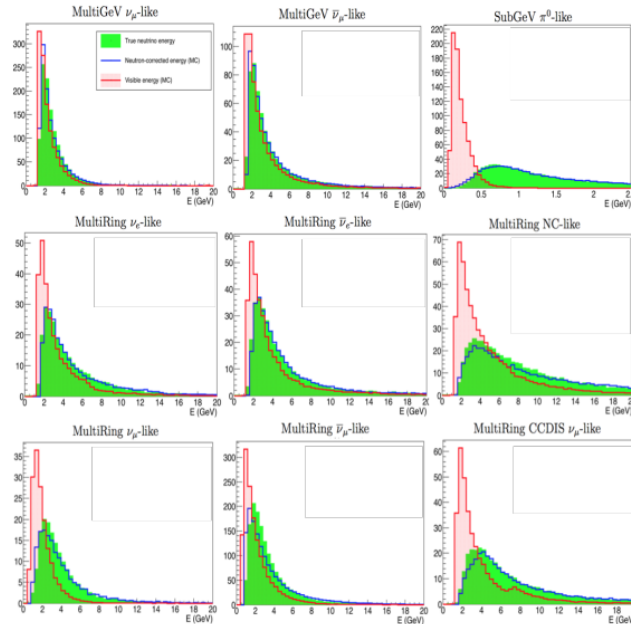
Figure 1.10: An example of MC simulation study on energy correction by counting number of tagged neutrons for the atmospheric neutrino samples in case of the SK-Gd's full configuration, in which a 70% neutron tagging efficiency is expected to be achieved. Green colored histograms represent true neutrino energies. Red and blue lines correspond to lepton energies and corrected lepton energies by counting the number of tagged neutrons, respectively. Figure taken from [7].
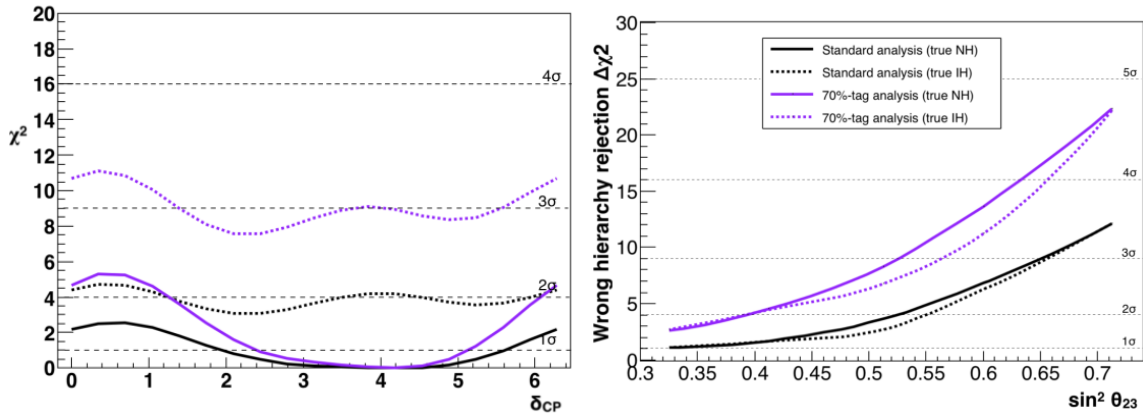
Figure 1.11: Sensitivities to δ_{CP} assuming true normal MH (right) and wrong MH rejection as a function of true $\sin^2 \theta_{23}$ for the atmospheric neutrino oscillation analyses at Hyper-Kamiokande. Black lines correspond to the conventional analysis method developed by the SK collaboration based on lepton energy. Magenta lines correspond to the improved analysis method in which case an energy correction and a better event selection using tagged neutrons are applied with an assumption of a 70% neutron tagging efficiency. Estimation for systematic uncertainties regarding neutron tagging (but, very rough) is taken into account for the magenta lines. Figure taken from [7].

Neutrons can also be utilized for neutrino astronomy and an improvement is expected in searching for SRN. As was mentioned in Section 1.1.3, IBD is the signal reaction of SRN in a water Cherenkov detector, and it can be efficiently identified by employing a coincidence of the prompt signal of e^+ and the delayed signal of n. In practice, this coincidence is made by requiring one tagged neutron for each reconstructed prompt event. To obtain an insight into an early stage of the universe, region of neutrino energies used for SRN search needs to be lowered as much as possible as shown in Figure 1.12. One of main background sources is produced by atmospheric neutrinos via NC quasi-elastic (NCQE) reaction: $\nu + ^{16}O \rightarrow \nu + ^{15}O^* + n$ and $\nu + ^{16}O \rightarrow \nu + ^{15}N^* + p$. The residual nuclei emit gamma rays according to de-excitation modes, which can mimic the prompt signal of SRN and the out-going nucleons produce neutrons via their FSI and SI. Therefore, the atmospheric NCQE background is an irreducible background even if one tagged neutron is required as shown in the left panel of Figure 1.13. However, energies of neutrons are quite different between the SRN and the atmospheric NCQE background. Neutrons produced by the SRN's IBD reaction have energies below a few MeV, whereas those of the NCQE background have much higher energies, more than several hundreds MeV, which results in a clear difference in the distance traveled of neutron from the primary ν interaction position as shown in the right panel of Figure 1.13. Further reduction of the atmospheric NCQE background may be achieved by exploiting this difference. Since the peak energy is similar between the T2K neutrinos and the Super-Kamiokande atmospheric neutrinos [129], studying the neutron travel distance by the T2K beam neutrinos may be useful.

21
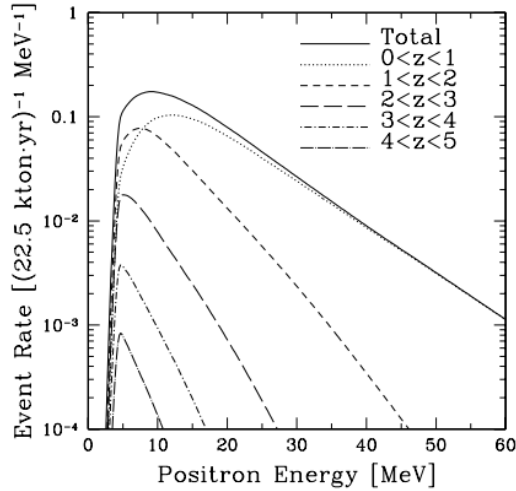
Figure 1.12: Expected SRN flux as a function of positron energy for different redshift at Super-Kamiokande. Figure taken from [8].
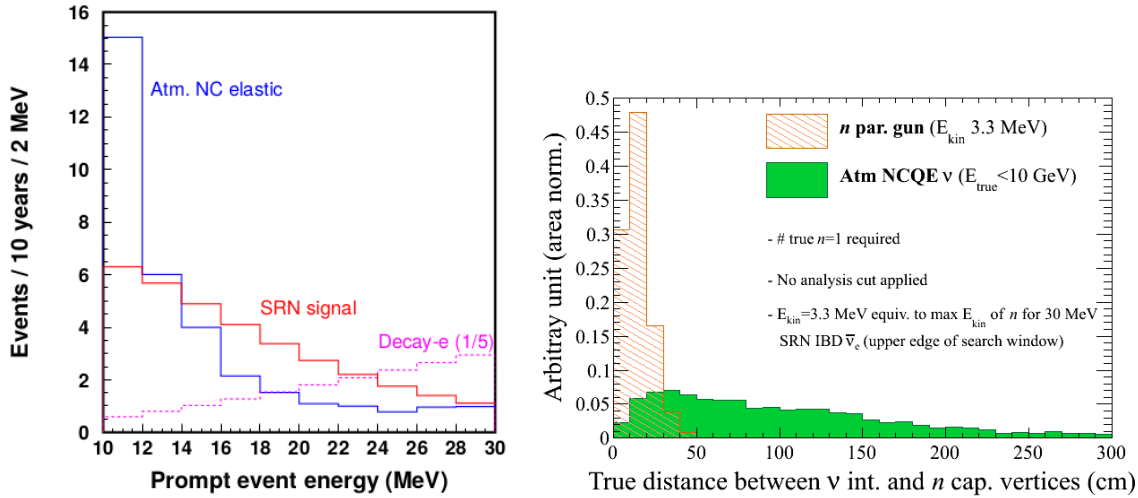
Figure 1.13: Expected positron energy spectrum at SK-Gd with an exposure of 10 years (left). The red, blue, and magenta lines represent the SRN signal, the atmospheric NCQE events, and the atmospheric CC decay electron events, respectively. A revised version of the LMA model [9] is used for the SRN flux. For the decay electron events, a reduction by a factor of five is assumed and is planned to be achieved by neutron tagging. Figure taken from [10]. Distribution of true distance from ν interaction to n capture vertices (right). The orange and green correspond to the inverse β decay signal of SRN and the NCQE atmospheric neutrino background, respectively.

Alongside the utilization of distance information for SRN searches, a possibility of similar utilization of neutron kinematics has been studied for estimation of neutrino direction and further ν-$\bar{\nu}$ separation in atmospheric neutrino oscillation analyses.
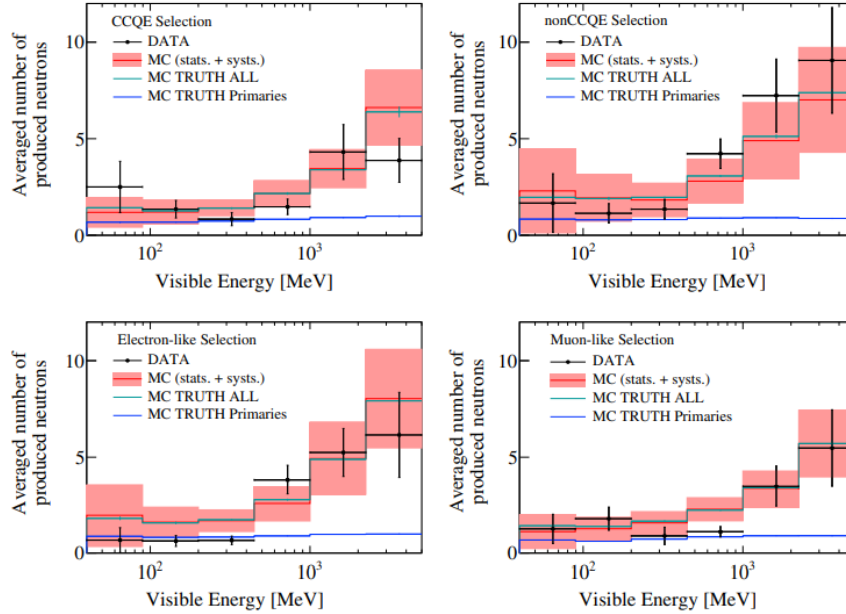
Figure 1.14: Mean neutron multiplicities as a function of visible energy for heavy water, measured by using atmospheric neutrinos at the SNO experiment. MC expectations are made from a combination of GENIE [11] and Geant4 [12]. The error bars of the data represent statistical errors and the envelopes of the MC expectations correspond to the assigned systematic uncertainties. Note that no systematic uncertainties due to hadronic SI are taken into account for the error envelopes. Figure taken from [13].

1.2.3 Current status of prediction of neutrons

Utilization of neutrons associated with neutrino interaction in water is able to produce promising improvements on various physics analyses as described above. In order to realize such improved analyses, the multiplicity and the kinematics of such neutrons need to be precisely understood with satisfactory control of related systematic errors. The SK collaboration has made only measurement of those neutrons by using the atmospheric neutrinos [130]. However, the measurement result does not have systematic uncertainty and, in addition, it is not compared with any MC predictions.

Although target material is not water, it is worth mentioning existing measurements of equivalent or similar neutrons to know the status of experimental studies on neutrons related to ν-nucleus interactions. The SNO collaboration has measured neutrons in the heavy water by using the atmospheric neutrinos [13]. As shown in Figure 1.14, the agreement between the data and their reference simulation varies over the visible energy and the analysis samples. In some regions overpredictions are seen despite the very large systematic uncertainties on the MC predictions. In the MINERvA experiment [131], a post-FSI enriched neutron sample in which neutrons produced in hadronic SI are reduced by applying analysis cut is prepared for the

antineutrino enriched mode of NuMI beam with a peak energy of $\sim 3\,\text{GeV}$ produced at Fermilab. By using the sample, neutron kinematics and multiplicity for antineutrino interaction on a hydrocarbon target are measured, and are compared between the data and their simulations [14]. A 15% overall overestimate was seen in their reference simulation, but further overestimates were found in a region of low energy deposition by neutron candidates as shown in Figure 1.15.
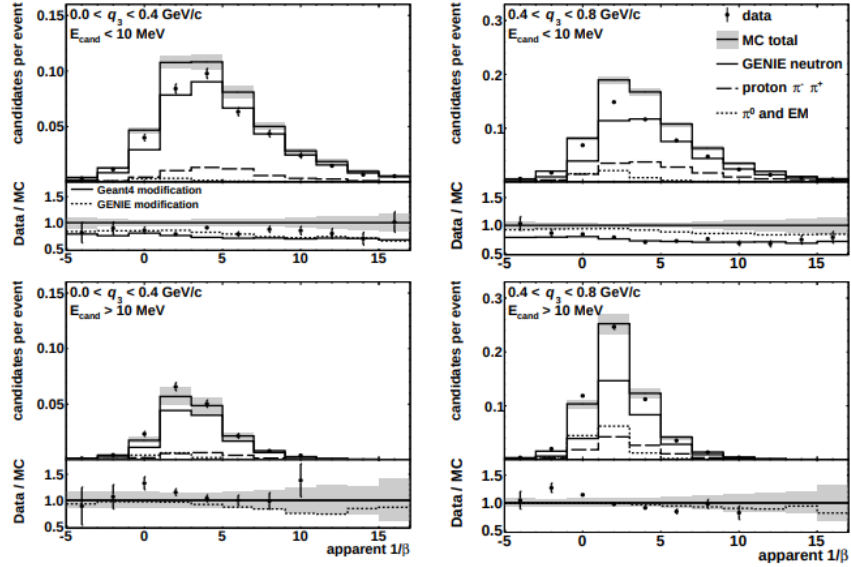
Figure 1.15: Distribution of measured apparent velocity for neutron candidates by the MINERvA experiment. The $\bar{\nu}$-mode of NuMI neutrino beam produced at Fermlab and a hydrocarbon target are used as neutrino source and target material, respectively. The data are shown with statistical error only and the gray bands represent the assigned systematic errors on the MC expectations. The MC expectations are produced by a combination of GENIE [11] and Geant4 [12]. Figure taken from [14].

Both SNO and MINERvA made their MC predictions by a combination of two MC simulations: GENIE [11] which simulates primary neutrino interaction and subsequent hadronic FSI and Geant4 [12] which handles simulation of particle propagation in detector medium (*i.e.* hadronic SI). For this combination, the SNO's result shows a large prediction uncertainty and the MINERvA's data show overprediction. Thus, it may be interesting to refer to another experimental study whose MC predictions are made from different MC simulations. The MiniBooNE experiment has studied NCQE ("NCE" in their paper) reaction with a mineral oil target [132], and their data have shown a $\sim 30\%$ of overprediction which is produced by two MC simulations: NUANCE [133] for primary neutrino interaction and FSI and GCALOR [134] for hadronic SI. Thus, MC simulations used in neutrino oscillation experiments utilizing atmospheric neutrinos and accelerator based neutrinos ranging from sub-GeV up to several GeV tend to overpredict.

Since the production process of protons related neutrino interactions are almost

the same as neutrons, it is worth discussing the current status of prediction of proton multiplicity. Figure 1.16 shows the proton multiplicity with kinetic energies above 500 MeV for a C_8H_8 target, measured by the T2K experiment [15]. As shown in the figure, the data shows less protons compared to several MC predictions, in which NEUT [135] and NuWro [136] are used for their simulation of the primary neutrino interactions and the FSI.
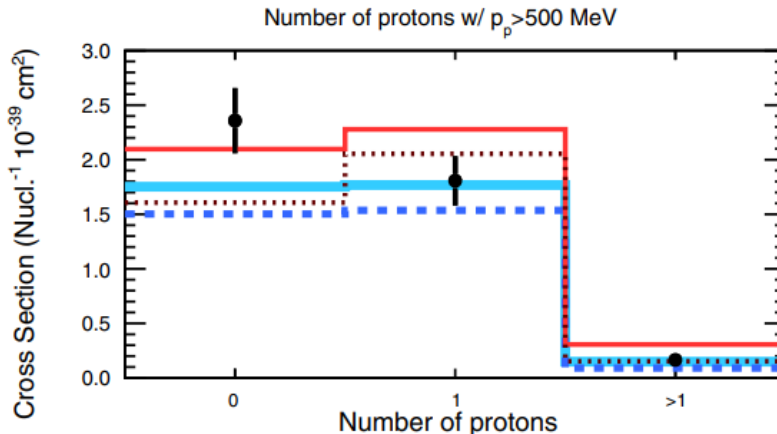
Figure 1.16: Proton multiplicity for CC ν_μ interactions on a C_8H_8 target with 0 pion in the final state, measured by the T2K experiment. Only protons with kinetic energies above 500 MeV are considered. The error bars of the data include both statistical and systematic uncertainties. Solid and broken lines represent predictions by different MC simulations with uses of various models. Figure taken from [15].

Another overprediction has been seen for both neutrino and antineutrino interactions on a liquid argon target in the ArgoNeut experiment at Fermilab [137], which is mentioned in Ref. [138].

1.3   Research motivation

In Section 1.1.2 and Section 1.1.3, neutrino oscillations, SRN, and their experimental status were described, and further improvement on these experimental studies needs to be done. To this aim, information about neutrons associated with neutrino interactions in water will be useful for various physics analyses. In order to utilize such information, these neutrons need to be precisely measured and that information can be used to improve MC predictions. However, as will described in Section 8.1, currently used MC simulations in neutrino oscillation experiments utilizing atmospheric neutrinos and accelerator based neutrinos produce different predictions of neutron production for water. In addition, no quantitative comparison of neutron multiplicity for water has been made although non-negligible difference in neutron multiplicity and proton multiplicity have been seen for different target materials as was described above. It is therefore quite valuable to measure those neutrons for water and understand how much level of agreement between data and simulations

can be realized. For this purpose, a well understood neutrino source is required.

T2K beam neutrino has advantages compared to other neutrino source such as atmospheric neutrinos:

- well known and peaked energy,

- well known neutrino flavour composition,

- known neutrino direction,

- two separate neutrino- and antineutrino-enriched fluxes.

Also, the SK far detector is capable of tagging neutrons on an event-by-event basis by detecting γ rays produced from neutron captures on hydrogen nucleus. Thus, T2K is suitable for studying those neutrons, and the primary analysis of this thesis presents the first measurement of neutrons associated with neutrino interactions in water for accelerator based neutrinos and antineutrinos.

1.4 Thesis overview

This thesis presents the first study on neutrons associated with neutrino interactions on water target for accelerator based neutrinos and antineutrinos using the data collected at the SK far detector of the T2K experiment.

An overview of the T2K experiment and a detail of the SK far detector are described in Chapter 2 and Chapter 3, respectively. Following this, simulations of the T2K beam neutrinos at the SK far detector are overviewed in Chapter 4. The data reduction and reconstruction of neutrino event at the far detector are the subjects of Chapter 5.

The original and independent works done by the author of this thesis are described from Chapter 6. Chapter 6 details the development of the neutron tagging algorithm and related analyses. The first application of the neutron tagging technique to accelerator neutrinos for water target is presented in Chapter 7. In Chapter 8, a measurement of mean neutron multiplicity associated with neutrino interactions in water is described, and the summary of this thesis and an outlook are given in Chapter 9 .

Chapter 2

The T2K experiment

The Tokai-to-Kamioka (T2K) experiment is a long baseline neutrino oscillation experiment in Japan [16]. It was originally designed to achieve the following goals:

- A precision measurement of Δm_{23}^2 and $\sin^2\theta_{23}$ with an accuracy of $\delta(\Delta m_{23}^2) \sim 10^{-4}\,\text{eV}$ and $\delta(\sin^2 2\theta_{23}) \sim 0.01$ by studies on muon neutrino disappearance.

- Observation of electron neutrino appearance from a muon beam neutrino if $\sin^2 2\theta_{13} > 0.008$.

The precision measurements of Δm_{23}^2 and $\sin^2\theta_{23}$ have been successfully done [139], although the accuracy continues to improve. The observation of ν_e appearance has also been achieved [98] in the ν_μ dominant mode, whereas $\bar\nu_e$ appearance has not been observed yet in the $\bar\nu_\mu$ mode. Since the value of θ_{13} has been measured by reactor based experiments, a possibility to probing δ_{CP} has been opened. Indeed, T2K is now moving to make a constraint on δ_{CP}, and has excluded the CP-conserving values ($\delta_{CP} = 0, \pi$) with a 90% C.L. for the first time [140, 139]. In addition, studies on the ν-nucleus interactions are also studied by the intensive beam neutrinos.
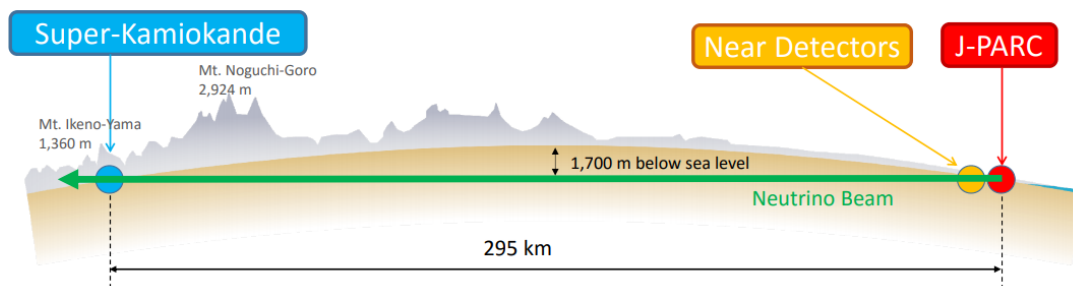
Figure 2.1: A schematic view of the T2K experiment.

Figure 2.1 shows a schematic layout of the T2K experiment. Predominantly muon neutrino and antimuon neutrino beams are produced at J-PARC (Japan Proton

Accelerator Research Complex) facility. They are detected by the INGRID and ND280 near detectors placed $\sim$280 m downstream from the production target of the neutrino beams before the beam neutrinos oscillate and the Super-Kamiokande far detector located 295 km further away after they oscillate. The near-far comparison of the detected neutrinos is the vital input to measure neutrino oscillation parameters. INGRID sits at the beam center to monitor the beam neutrinos. ND280 and SK are placed on an off-axis angle of 2.5° with respect to the beam center, which enables utilizing a relatively narrow band neutrino flux with a peak energy of 0.6 GeV. T2K has started taking physics data since January 2010.

This chapter describes the T2K beamlines, the off-axis beam method, and the T2K near detectors. Since the primary analysis of this thesis does use the data accumulated at the SK far detector only, details in SK will be described in Chapter 3.

2.1 Neutrino beam

The T2K neutrino beam [17] is produced at J-PARC in Tokai, Ibaraki, Japan. T2K adopts the off-axis approach to produce a narrow band muon neutrino beam with a minimal contamination of electron neutrinos and with a peak energy of 0.6 GeV. This beam configuration is determined in order to maximumize the oscillations of muon neutrinos at SK. The neutrino beam is produced by using two beam-lines: the J-PARC proton beam line and the neutrino beam line. In this section, first an overview of these beam lines are provided. Following this, the off-axis approach is described.

2.1.1 J-PARC proton beam line

A 30 GeV kinetic energy of proton beam is generated by the J-PARC proton beam line which consists of three accelerators: a linear accelerator (LINAC), a rapid cycling synchrotron (RCS), and the main ring (MR) synchrotron. The generation of the 30 GeV proton beam begins with LINAC by which an H$^-$ beam is accelerated up to a kinetic energy of 400 MeV. The accelerated H$^-$ beam is navigated to the RCS injection where an proton beam is created from the conversion of the H$^-$ beam by charge-stripping foils. The proton beam is then accelerated up to 3 GeV in kinetic energy by RCS whose the number of bunches are two per cycle. About 5% of these bunches are supplied to the MR to further accelerate the proton beam up to 30 GeV. For the T2K neutrino beamline which will be described in the following section, the accelerated protons are extracted as a spill which consists of eight proton bunches at the fast extraction point in MR and are supplied to the neutrino beamline.

Table 2.1 summarizes the machine design parameters of MR for the fast extraction mode. The beam power has been gradually increased. The continuous operation with a beam power of 480 kW was successfully achieved in 2018 [30]. Also, in 2018 the beam power of single shot reached to 520 kW [141], which is the highest beam power at the present moment.

Table 2.1: The parameters of the machine design of the J-PARC Main Ring for the fast extraction. [16]

Circumference	1567 m
Beam power	$\sim$750 kW
Beam kinetic energy	30 GeV
Beam intensity	$\sim$3$\times$10^{14} p/spill
Spill cycle	$\sim$0.5 Hz
Number of bunches	8/spill
RF frequency	1.67-1.72 Hz
Spill width	$\sim$5 μs

2.1.2 Neutrino beam line
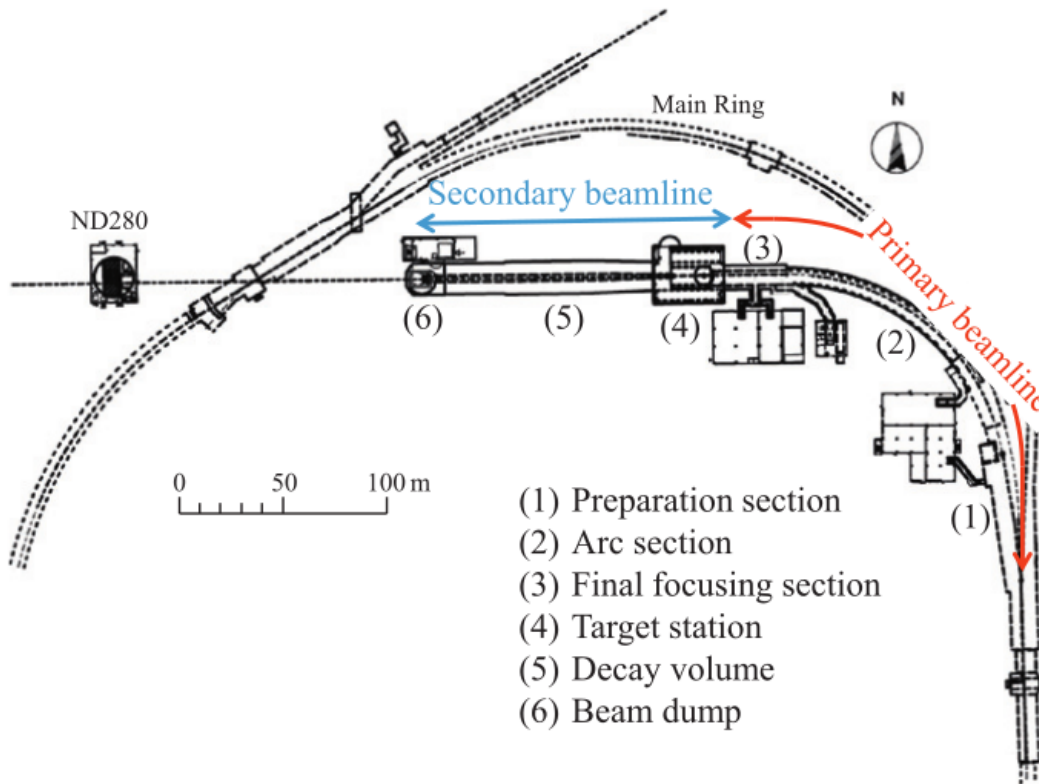
Figure 2.2: A schematic drawing of the neutrino beam line. Figure taken from [16].

The neutrino beamline consists of the primary and secondary beamlines as shown in Figure 2.2. In the primary beam line, the proton beam extracted from MR is directed toward Kamioka, and is transported through a series of beam monitors in the final focusing section: five current transformers (CTs), 21 electrostatic monitors (ESMs), 19 segmented secondary emission monitors (SSEMs) and 50 beam loss monitors (BLMs). Figure 2.3 shows the locations of these monitors.

29
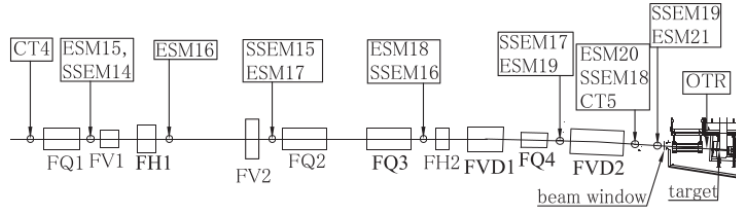
Figure 2.3: A schematic drawing of the neutrino beamline. Figure taken from [17].

By using these monitors, the beam intensity, position, profile, and loss are measured. In particular, CT5, which is placed on the most downstream, is used to measure Protons-On-Target (heareafter called "POT") on a buch-by-bunch basis. The measured POT is directly used to determine the beam neutrino flux.

Figure 2.4 shows a schematic drawing of the secondary beamline. Upon the injection from the primary beamline, the proton beam impinges a target ,which is a 91.4 cm long corresponding to 1.9 interaction length, 2.6 cm diameter and $1.8\,g/cm^3$ graphite rod, to produce secondary hadrons which are focused by three magnetic horns.
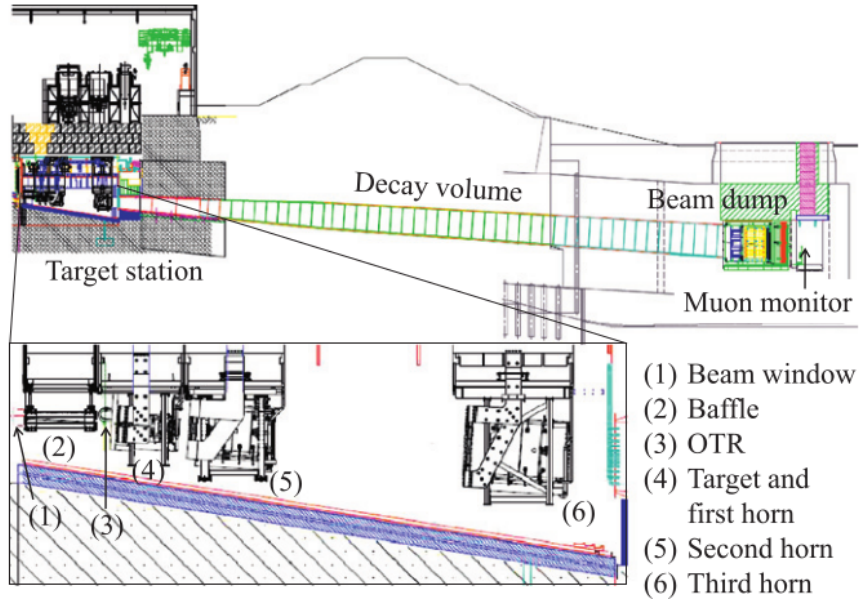
Figure 2.4: A cross-sectional view of the secondary beamline. Figure taken from [16].

The magnetic horns are operated with a 250 kA pulsed current whose polarity can be either positive or negative and are used to guide those secondary hadrons to a decay volume. The +250 kA operation predominantly focuses on π^+ and K^+ to produce a muon neutrino enriched beam as follows:

$$\pi^+ \to \mu^+ + \nu_\mu$$
$$K^+ \to \mu^+ + \nu_\mu.$$

30

In the -250 kA operation, on the one hand, π^- and K^- are focused on to create a high purity of muon antineutrino beam via the decays :

$$\pi^- \rightarrow \mu^- + \bar{\nu}_\mu$$
$$K^- \rightarrow \mu^- + \bar{\nu}_\mu.$$

A maximum filed of 1.7 T is produced in the ± 250 kA operation. The configurations of neutrino and antineutrino enriched beam are called forward-horn-current (hereafter called "FHC)" or reverse-horn-current (hereafter called "RHC") modes, respectively. Figure 2.5 shows an illustration of effects on the beam flux at SK for the operation with different horn currents, and the 250 kA operation increases the beam flux at the SK by a factor of ~ 17 at the peak energy compared to the case of 0 kA operation.
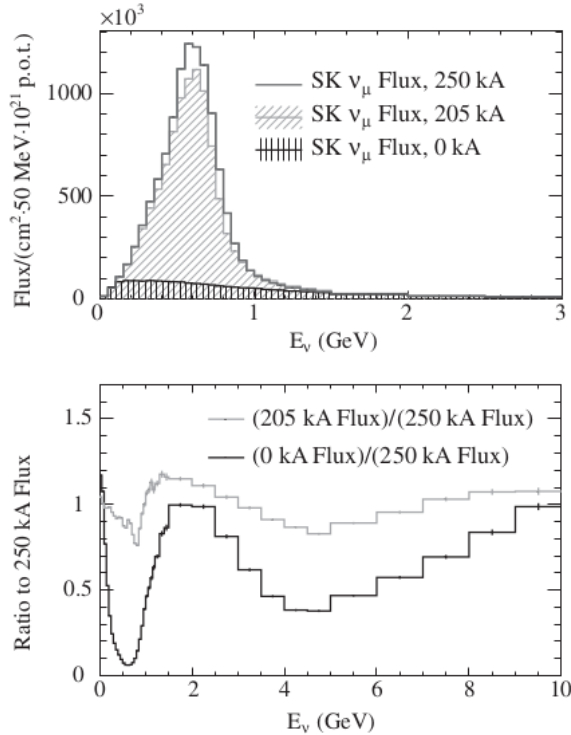
Figure 2.5: Muon neutrino flux at the SK for operation of different horn currents. Figure taken from [17].

Once the secondary hadrons are guided to the decay volume whose length is about 96 m, either muon neutrinos or muon antineutrinos are predominantly produced depending on the polarity of the horn magnets. However, there is a contamination of wrong-sign neutrinos which are produced by imperfect horn focusing, subsequent muon decays and another decay mode of the kaons:

$$\mu^+ \to e^+ + \nu_e + \bar{\nu}_\mu \quad \text{and} \quad K^+ \to \pi^0 + e^+ + \nu_e \quad \text{for FHC}$$

$$\mu^- \to e^- + \bar{\nu}_e + \nu_\mu \quad \text{and} \quad K^- \to \pi^0 + e^- + \bar{\nu}_e \quad \text{for RHC}$$

The length of the decay volume is determined to maximize the conversion rate from meason to muon neutrino, while minimizing the contamination of electron neutrinos in the beam. At the end of the decay volume, there is a beam dump which is made of 3.2 m long of graphite and 2.4 m long of iron. The protons, secondary hadrons, and measons below momenta of $\sim$5 GeV/c are absorbed by the beam dump.

A muon monitor [142, 143] is placed just downstream of the beam monitor in order to measure the beam intensity and direction on a bunch-by-bunch basis. Since muons are dominantly produced along with neutrinos from the two-body pion decay, these beam properties can be monitored by measuring the distribution profile of these muons. In addition, a detector consisting of nuclear emulsion is located just downstream of the muon monitor, by which the absolute flux and momentum distribution of those muons are measured.

2.1.3 Off-axis approach

ND280 and SK do not sit on the beam center, instead these detectors are placed on 2.5 $^\circ$ off-axis from the beam center. This approach is referred to as the "off-axis configuration" [144]. It utilizes the fact that, in the laboratory frame, the energies of neutrinos produced from the two-body decay of pions do depend only weakly on the energies of the parent pions in a energy region above scattering angle dependent threshold. This can be quantitatively explained by considering the energy conservation of the relativistic kinematics of the two-body pion decay, and the energy of outgoing neutrino E_ν in the laboratory frame is given as:

$$E_\nu = \frac{m_\pi^2 - m_\mu^2}{2(E_\pi - \sqrt{E_\pi^2 - m_\pi^2} \cos\theta)}, \tag{2.1.1}$$

where m_π is pion mass, m_μ, is muon mass, E_π is the parent pion energy, and θ is the scattering angle of the outgoing neutrino with respect to the parent pion's momentum direction. Figure 2.6 shows E_ν for different θ, and the weak dependence on E_π can be clearly seen above some E_π, which depends on θ.
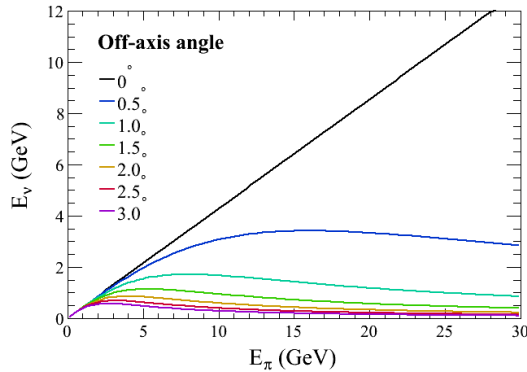
Figure 2.6: Neutrino energy from two-body decay of pion in Lab. frame as a function of parent pion energy for different off-axis angles. T2K uses an off-axis angle of $2.5°$.

By exploiting the effect of off-axis, a quasi-monochromatic neutrino beam flux can be produced. However, such beam intensity quickly decreases as the off-axis angle increases. The $2.5°$ off-axis angle of T2K is therefore determined by considering a balance between beam intensity and beam energy spread while keeping a peak energy of ~ 0.6 GeV for the oscillation maximum at SK. Figure 2.7 shows an illustration, in which the $2.5°$ off-axis maximize the T2K's sensitivity to the oscillation maximum.
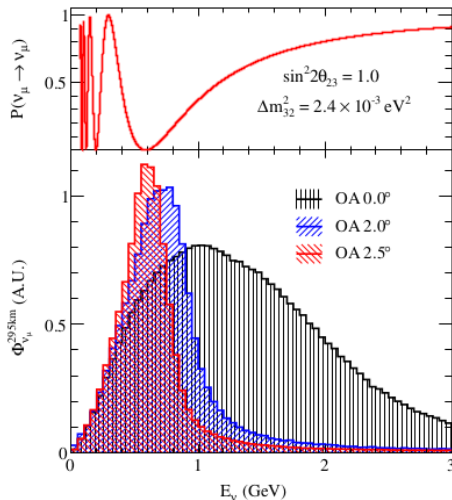
Figure 2.7: Survival probability of moun neutrinos with a baseline of 295 km (top) and neutrino beam fluxes at 295 km away from neutrino production target for three different off-axis angles (bottom). Figure taken from[17].

2.2 Near detectors

The T2K near detector complex, which is located 280 m downstream from the production target of the beam neutrinos, is used to monitor the profile of the neutrino beam and measure neutrino interaction rates in order to constrain uncertainties in

the measurements of neutrino oscillations. As shown in Figure 2.8, the near detector complex consists of two detectors: an on-axis detector, Interactive Neutrino Grid (INGRID), and an off-axis detector, Near Detector at 280 m (ND280). In this section, each component of these detectors is described.
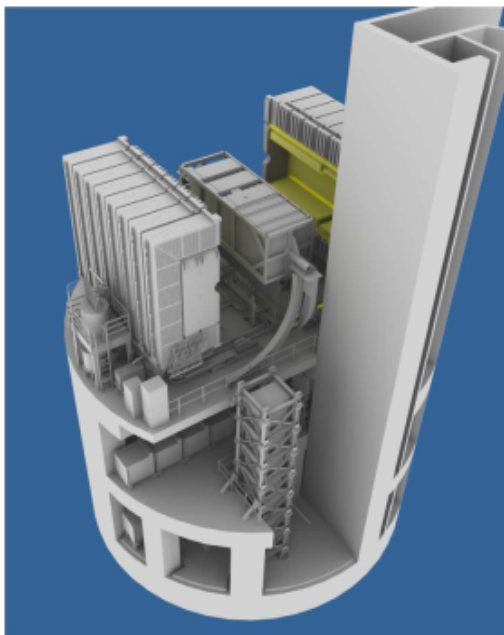
Figure 2.8: A schematic drawing of the near detector complex. Figure taken from [16].

2.2.1 On-axis near detector

INGRID is a separate array of iron and scintillator detector placed on the on-axis. The detector is designed to daily monitor the beam direction and intensity using neutrino interactions on its iron target. Also, the beam direction can be accurately measured within 0.4 mrad. INGRID consists of 16 identical modules as shown in Figure 2.9. The cross shape of INGRID whose center corresponds to the beam center is formed by 14 modules. The remaining two modules are separately placed on off-axis directions and used to check the axial symmetry of the neutrino beam.
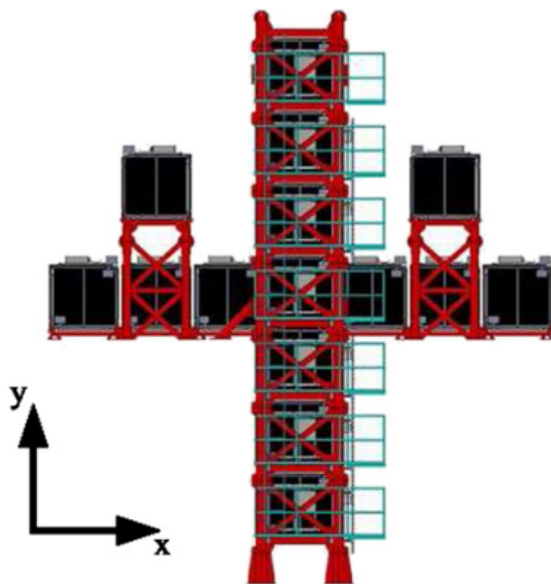
Figure 2.9: INGRID on-axis detector. The direction of the beam neutrinos is parallel with the z-axis. Figure taken from [16]

An INGRID module is made of 9 iron plates and 11 tracking scintillator planes. These iron plates and tracking planes are arranged in a sandwich structure and are surrounded by veto scintillator planes as shown in Figure 2.10. Each iron plate serves as a neutrino target and the total iron mass of one module is 7.1 ton. Each tracking plane consists of 24 scintillator bars. Also, each of veto plane is made of 22 scintillator bars which are different from the ones used in the scintillator plane. For both of the scintillator plane and veto plane, a wave-length shifting fiber (WLS) is inserted to each scintillator bar for light collection. The signal from a WLS are read out by an multi-pixel photon counter (MPPC) [145, 146] attached to the end of WLS.
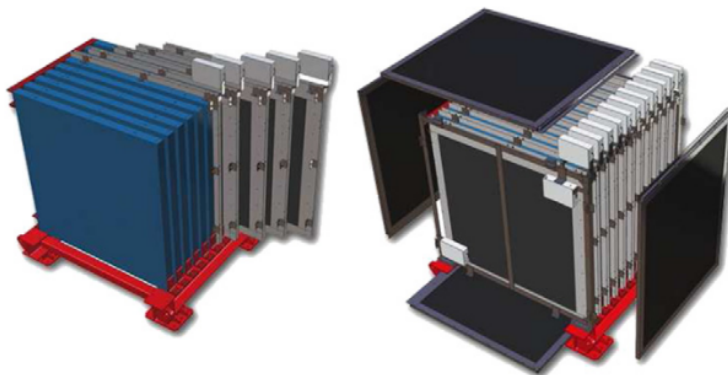
Figure 2.10: A schematic diagram of the INGRID module. Figure taken from [16]

INGRID is calibrated by using cosmic ray data. The measured mean light yield which is larger than 10 p.e./cm for MIP tracks satisfies the requirement.

2.2.2   Off-axis near detector

ND280 is a large, fine grained, and magnetized off-axis detector. Since the detector is placed on the same off-axis as SK, it is designed to achieve the following goals in order to accurately predict event rates at SK:

- Measure the energy spectrum of ν_μ to predict the event rate at SK.

- Measure the ν_e component which is the main background in ν_e appearance search at SK.

- Measure the cross sections of ν_μ interactions to reduce systematic uncertainties on ν-nucleus interaction models.

The detector design is determined by considering these requirements.
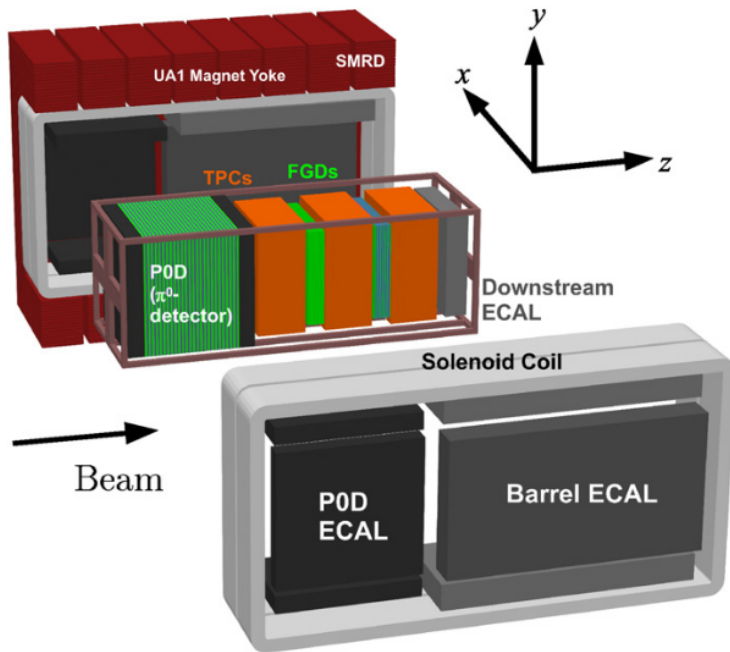
Figure 2.11: A simplified schematic view of ND280. Figure taken from [16].

ND280 is composed of a series of specialized detectors: 2 Fine Grained Detectors (FGDs), 3 gaseous Time Projection Chambers (TPCs), and a π^0 detector (P∅D). These subdetectors are contained in a metal frame container and are surrounded by Electromagnetic Calorimeters (ECals), which are contained within a magnet instrumented with side muon range detector (SMRD). Figure 2.11 shows a schematic drawing of ND280. To magnetize these detectors, a magnet (UA1) is used.

UA1 Magnet

The ND280 detecor uses the magnet which was previously used in the UA1 experiment. The magnet provides a horizontally oriented dipole magnetic field of $0.2\,\mathrm{T}$ and consists of water-cooled aluminium coils and a $850\,\mathrm{ton}$ flux return yoke.

Side Muon Range Detector (SMRD)

The SMRD [147] detector is incorporated into the yoke of the magnet surrounding ND280 and consists of 440 scintillator modules which are inserted into the $1.7\,\mathrm{cm}$ air gaps between $4.8\,\mathrm{cm}$ thick steel plates inside the yoke. It is purposely used to measure the momenta of muons escaping from the inner detectors at a large angle with respect to the neutrino beam. Also, it can act as a veto for entering particles such as cosmic ray muons and particles produced by beam-related events that happen in the cavity walls and iron of the magnet.

Pi -Zero detector (P∅D)

Since the π^0 produced in the neutral current interaction on water $\nu_\mu + N \rightarrow \nu_\mu + N + \pi^0 + X$ can mimic the signal event of ν_e appearance at SK, P∅D [148] is designed to measure this process. The detector consists of three components: the central section, "upstream ECal", and "central ECal". The central section is made of alternating scintillator plane, brass sheets, and water bags as show in Figure 2.12. The water bags can be filled with water or empties, which enable us to perform a subtraction method to extract the cross-section of the interaction process. The upstream ECal and central ECal are used to veto events entering from outside and consist of alternating scintillator planes and lead sheets and have not water bags.

Each scintillator plane is made of two perpendicular arrays of triangular scintillator bars, each of which has a hole filled with a WLS fiber. The signal from a WLS fiber is read out by a MPPC attached to one end. P∅D has 40 scintillator plates with 10,400 readout channels and 50 water bags. The total detector mass is $16.1\,\mathrm{ton}$ and $13.3\,\mathrm{ton}$ for the water-in configuration and water-out configuration, respectively.
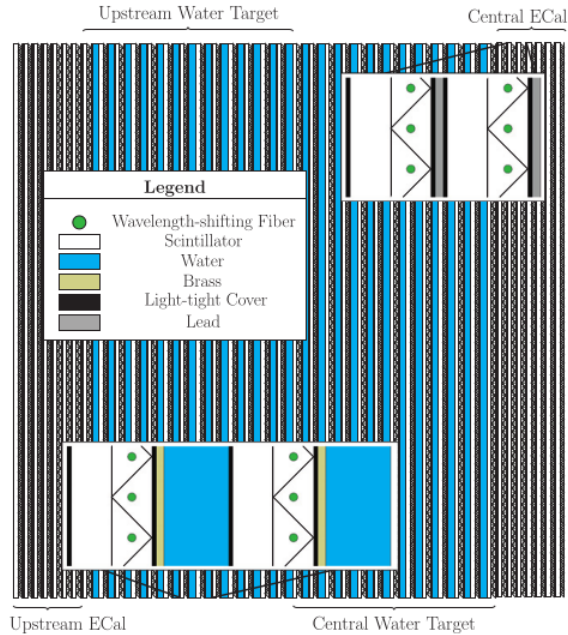
Figure 2.12: A schematic cross sectional view of P∅D. Figure taken from [16].

Time Projection Chamber (TPC)

Three TPCs [149] are separately placed just downstream of P∅D. TPCs are designed to have good resolution in reconstruction of charged particle tracks, momentum determination, and particle identification such that the event rate of muon and electron neutrinos as a function of energy can be measured.

Each TPC has an inner box filled with an argon based drift gas, which is contained within an outer box that holds CO_2 as an insulating gas. An 11.5 mm pitch copper strip pattern is accurately formed on the inner box panels such that an uniform electric field of around 280 V/cm is produced in the active volume of TPC. The magnetic field by the UA1 magnet is roughly parallel to the electric field. Figure 2.13 schematically shows a simplified TPC.

The argon atoms are ionized as charged particles traverse TPCs. The ionization electrons produced along the trajectories of those charged particles drift away from the central cathode towards one of the readout planes. Upon reaching the readout plane, the drifting electrons enter an amplification region by an electric filed of 27 kV/cm over a distance of 128 μm and are read out by bulk micromegas detectors [150].
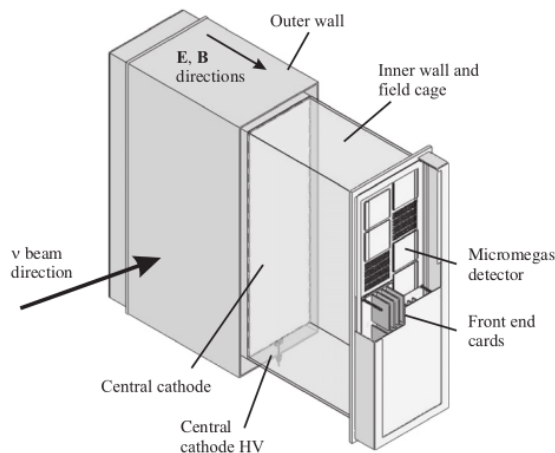
Figure 2.13: A schematic drawing of TPC. Figure taken from [16].

Fine Grained Detector (FGD)

The two fine grained detectors (FGDs) [151] have two functionalities: target mass of neutrino interaction and reconstruction of charged particle tracks. The outer dimension of FGDs are 2300 mm in width, 2400 mm in height, 365 mm in depth with 1.1 ton of target material. FGDs are made of layers of scintillator bars which are arranged in the direction perpendicular to the beam direction. Each scintillator bar has the dimension with a width of 9.61 mm, a height of 9.61 mm, and a depth of 1864.3 mm and has a WLS fiber whose one end is connected to a MPPC. The scintillator bars are arranged into modules, each of which contains a layer of 192 scintillator bars in the horizontal direction glued to 192 bars in the vertical direction.

The first FGD consists of 15 scintillator modules, whereas the second FDG has 7 scintillator modules and 6 water target modules. By comparing the neutrino interaction rates between FGDs, cross sections on carbon and water can be measured.

Electromagnetic calorimeter (ECal)

ECal [152] is a lead-scintillator sampling electromagnetic calorimeter, which surrounds the inner detectors: P$\emptyset$D, TPCs, and FDGs. It is utilized to complete the event reconstruction of the inner detectors fully by detecting photons and charged particles, which escape from the inner detector, and measuring the energies and directions of them. In particular, ECal plays a key role to reconstruct π^0 produced by ν interaction inside the inner detectors.

Chapter 3

Far detector Super-Kamiokande

Super-Kamiokande (SK) [18] is a 50 kton scale water Cherenkov detector located in Gifu Prefecture, Japan. SK consists of two key components: a tank filled with 50 kton of ultra pure water and roughly 13,000 photomultiplier tubes (PMT). When charged particles traverse the water, the Cherenkov light emitted by the charged particles is detected by the PMTs. In order to suppress the cosmic ray muon background, the detector is placed in the Kamioka mine under near the top of Mt Ikenoyama with 1000 m of overburden (2700 meter water equivalent). Figure 3.1 shows a diagram of the SK detector. SK started its operation in April 1996 with the primary purposes to search for nucleon decay and observe neutrinos from a variety of sources: solar neutrinos, astrophysical neutrinos, atmospheric neutrinos, and accelerator neutrinos. SK has also been used as the T2K far detector since January 2010. In this chapter, first the operation principle of the detector is described. Following this, the remaining parts describe the detector design and detector calibration.
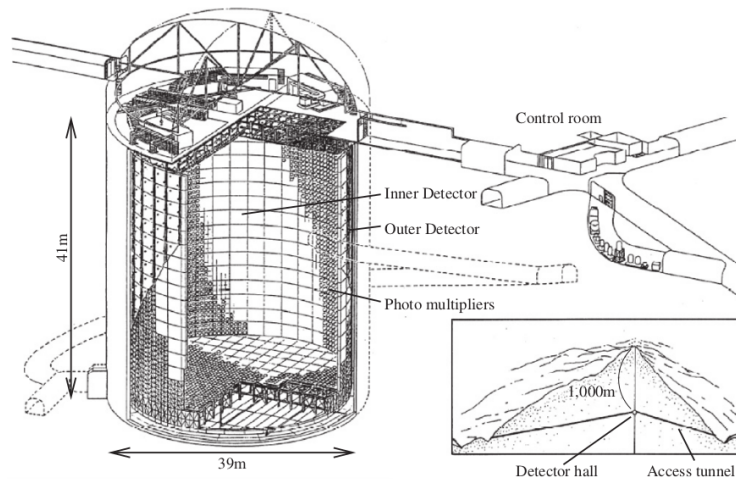
Figure 3.1: A schematic view of the Super-Kamiokande. Figure taken from [16].

3.1 Cherenkov radiation

Water Cherenkov detectors utilize the Cherenkov light emitted in the water to detect charged particles. When an object travels faster than the speed of sound, a shock wave is produced. Analogously, an electromagnetic shock wave referred to as "Cherenkov radiation" is produced if a charged particle traverses a dielectric medium faster than that of the phase velocity of light in the medium [153]:

$$v \geq \frac{c}{n}, \tag{3.1.1}$$

where v is the velocity of the charged particle, c is the speed of light in vacuum, and n is the refractive index of the medium. In Cherenkov radiation, photons are emitted as a cone with an opening angle θ_C called "Cherenkov angle" with respect to the direction of the motion of the charged particle:

$$\cos \theta_C = \frac{1}{n\beta}, \tag{3.1.2}$$

where $\beta = v/c$. The number of emitted photons per unit travel distance per unit wavelength of a charged particle with the electric charge z is given as:

$$\frac{d^2 N}{dx d\lambda} = \frac{2\pi z^2 \alpha}{\lambda^2} \left(1 - \frac{1}{n^2 \beta^2} \right), \tag{3.1.3}$$

where $\alpha \simeq 1/137$ is the fine structure constant.

In the environment of SK, the refractive index of the water is ~ 1.34 in a wave length region where the photosensors used for SK are sensitive. The momentum threshold for Cherenkov radiation is calculated to be approximately 0.57 MeV/c for an electron, 118 MeV/c for a muon, 156 MeV/c for a charged pion and 1052 MeV/c for a proton. Cherenkov light is emitted with the $\theta_C \sim 42°$ for a charged particle moving with $\beta \simeq 1$.

3.2 Detector design

The SK detector is made of a cylindrical stainless-steel tank with the diameter of 39 m and a height of 42 m. The tank is filled with 50 kton of ultra pure water and a cylindrical PMT supporting structure that optically separates the tank into two concentric cylinders: the inner detector (ID) and the outer detector (OD). ID has a cylindrical volume containing 32 kton of the water with 33.8 m in diameter and 36.2 m in height, and is used as the main detector. OD surrounding ID has a cylindrical shell volume with the thickness for the barrel side of 2.2 m and the thickness for the

top and bottom sides of 2.5 m. OD serves as an active veto counter for incoming particles such as cosmic ray muons originating from outside of the detector. OD is also used as a passive shield against neutrons and gamma rays which emanate from the surrounding rock. The PMT supporting structure defining ID is made of "super-module" frames whose dimensions are 2.1 m in height, 2.8 m in width and 0.55 m in thickness. Each of the super-modules houses twelve 20-inch PMTs for ID and two 8-inch PMTs for OD as shown in Figure 3.3. The inner side of the supporting structure is mounted with 11,129 inward-facing 20-inch PMTs and the outer side is mounted with 1,885 8-inch outward-facing PMTs. This detector design "ID and OD installed with PMTs" enables SK to be used as a Cherenkov-ring imaging detector. Figure 3.2 shows an event display of a "muon-like" event induced by T2K beam neutrinos. As shown in Figure, a clear ring which is produced by Cherenkov light emitted by the muon candidate can be found.
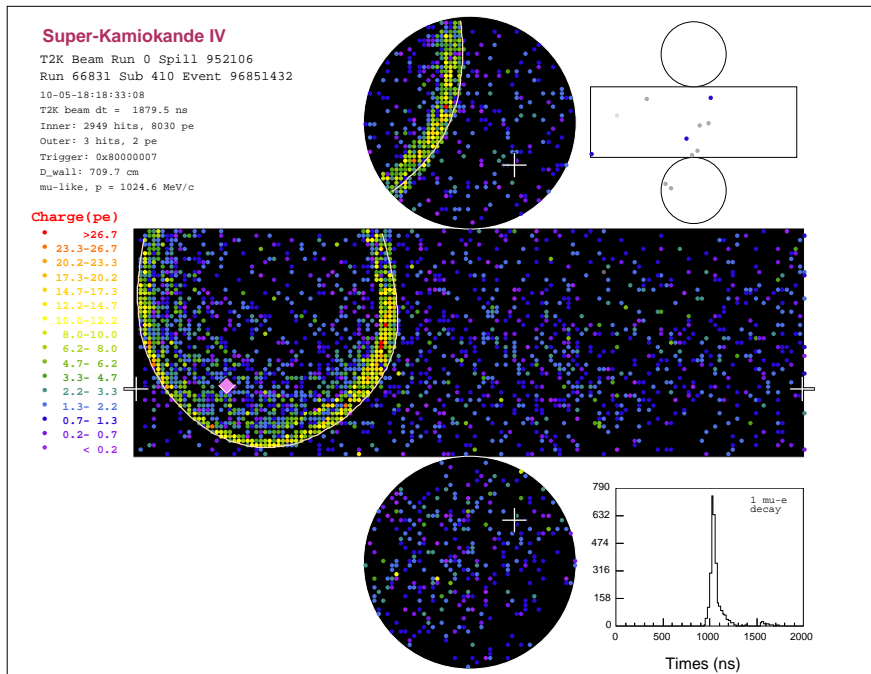
Figure 3.2: An unrolled event display of a typical single-ring muon-like data event of the T2K beam neutrino. Each dot corresponds to a PMT and color represents the number of observed photoelectrons.

Since the performance of the PMTs depend on magnetic field, 26 sets of horizontal and vertical Helmholtz coils line the inner wall of the tank. In the operation of these coils, the residual magnetic field is measured to be about 50 mG on average.
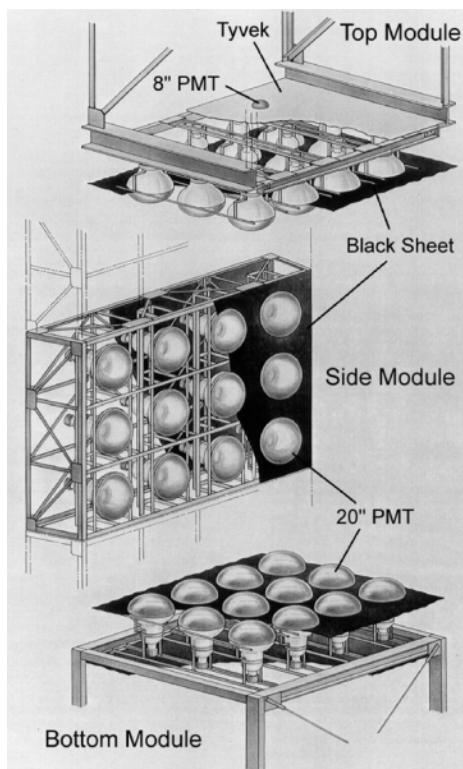
Figure 3.3: A schematic drawing of a super-module instrumented with the ID and OD PMTs. Figure taken from [18].

3.2.1 Experimental phases

The fourth-phase of SK(IV) started in September 2008 by upgrading its readout electronics [154, 19], and the T2K experiment began in Jan. 2010. Since this thesis is related only to SK-IV, this phase is described in the following.

3.2.2 Inner detector

In ID, 11,129 Hamamatsu R3600 20-inch PMTs, which were developed for the SK [155], are used. Figure 3.4 shows a schematic drawing of a PMT. All the PMTs are evenly placed 70 cm from each other on the wall of ID, which realizes that 40% of the surface area of ID is covered by the photocathodes. This enables detecting Cherenkov photons emitted by charged particles with a high efficiency and with an excellent resolution for observed geometrical pattern of PMT signals. The remaining 60% of the surface area is covered with black polyethylene sheets (hereafter called "black sheets") to prevent light leaks between ID and OD.
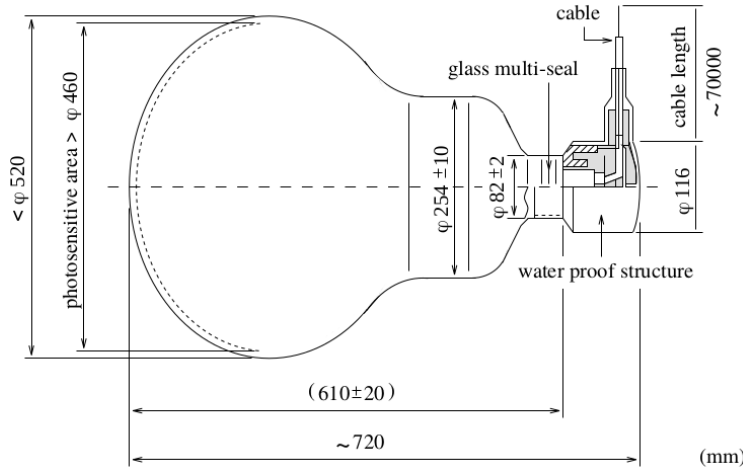
Figure 3.4: A cross-sectional view of an ID PMT. Figure taken from [18].

Photocathodes which are composed of a bialkali (Sb-K-Cs) material are sensitive to photons in a wavelength region from 300 nm to 600 nm and have the quantum efficiency (QE) with a maximum value of 22% around at 390 nm as shown in the left panel of Figure 3.5. When a photon reaches the photocathode of an ID PMT, a photoelectron (p.e.) is produced in accordance with the quantum efficiency. The p.e. is then amplified by the 11-stage dynodes inside the PMT with a gain of 10^7 at a supply high-voltage ranging from 1700 V to 2000 V. The collection efficiency for a p.e. at the first dynode is higher than 70%. The right panel of Figure 3.5 shows the transit time spread (TTS) of the PMTs for a p.e. signal and the TTS is evaluated to be ∼2.2 ns. The dark rate for the SK-IV is about 6 Hz on average when setting threshold on the signal to ∼0.25 p.e.
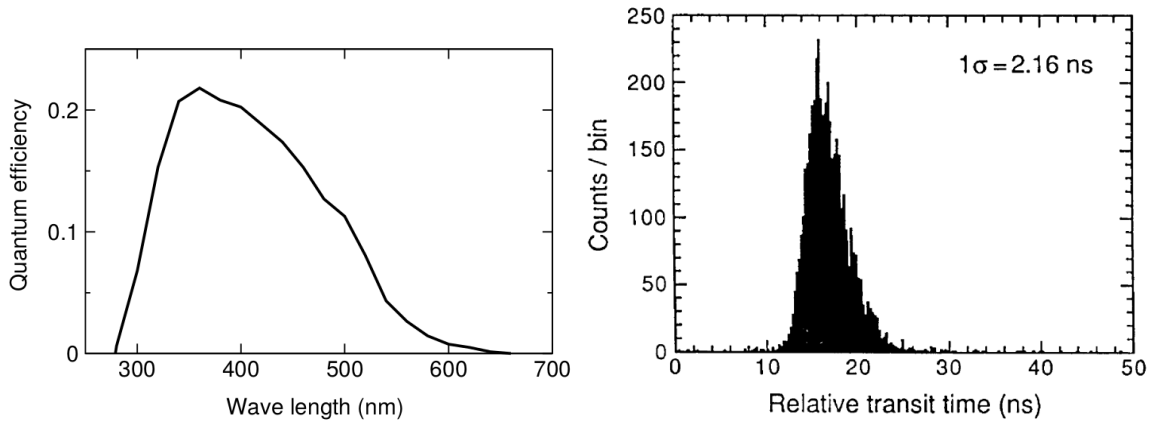
Figure 3.5: The wavelength dependence of the quantum efficiency of R3600 20-inch PMT (left). Distribution of the transit time of R3600 20-inch PMT (right). Figures taken from [18].

In 2001, SK had an accident by which about half of the ID PMTs were broken due to the implosion of an ID PMT. After the accident, PMT cases which are made of

a fiber reinforced plastic shell (FRP) at the base and an acrylic case were developed to protect implosions as happened in the accident. All the PMTs are encased by the FRP shell with an acrylic front window.

3.2.3 Outer detector

In OD, 1,885 8-inch PMTs [156] are evenly distributed on the inner surface of OD. Since the primary role of OD is to veto entering backgrounds such as cosmic ray muons, the ability of light collection need to be enhanced. For this purpose, reflective sheets made of Tyvek$^{\circledR}$ whose reflectivity is about 90 % at the wavelenght of 400 nm are used to cover all the surface of OD. Also, each of the OD PMTs is attached to a 50 cm square acrylic plate which absorbs ultraviolet light and remits the light with blue-green wavelengths that the PMT can detect.

3.2.4 Water and air purification

The underground water in the mine is utilized to supply the 50 kton of the ultra pure water inside the detector. Many impurities such as tiny dust, ions, radioactive isotopes, and bacteria are contained in the underground water. Those impurities attenuate Cherenkov light emitted by light absorption or scattering before the light reaches the PMTs of the detector. In addition, the radioactive isotopes originating from the uranium or thorium produce electrons and gamma-rays by their decay chains, which affect low energy analyses such as neutron tagging. Therefore, the underground water needs to be purified as much as possible before injecting it to the detector. The water purification system of SK basically consists of nine sequential processes as follows:

1. Water filter is used to remove large particles in the water.

2. Heat exchanger cools the water down to 13 $^{\circ}$C to prevent variations in the dark noise of the SK PMTs, water convection inside the tank, and the growth of bacteria.

3. UV light is used to kill bacteria in the water.

4. Metalic and carbonate ions and ^{218}Po and the daughter nuclei are removed by ion exchanger.

5. Radon-less air is dissolved into the water to improve the capability of the radon removal for later process.

6. Organic compounds down to a molecular weight of 100 are removed by a high-performance membrane.

7. Dissolved radon and oxygen gases are removed in vacuum de-gasifier system.

8. Ultra filter removes small particles with size down to 10 nm.

9. Remaining radon and oxygen dissolved in the water are further removed by membrane de-gasifier.

The purification processes suppress the radon concentration to a level of 10^{-3} Bq/m^3 and enable the attenuation length of the water inside the inner detector to reach about 90 m.

As the SK experimental area is surrounded by the rock in the mine, the concentration of radon contained in the air housing the experimental area is naturally very high. Therefore, the radon, which emanates from the rock, can contaminate the water in the detector, and needs to be removed. In order to reduce the radon concentration, the rock surrounding the experimental area is covered with a mine-guard (polyurethane). In addition, radon-free air produced in a hut outside of the mine by using compressors and activated charcoal filters is continuously provided to the experimental area.

3.3 Data acquisition for SK-IV

3.3.1 DAQ system

Once photoelectron is produced in a PMT by incident photon(s), the photoelectron is amplified through the dynodes inside the PMT and then is outputted as an analog signal. The analog signal is fed into a charge-to-time converter (QTC) which is a custom ASIC purposely designed for SK-IV [157]. If the signal from a PMT exceeds the threshold of a build-in discriminator in QTC (hereafter called "hit"), then QTC integrates the charge of the signal over the following 400 ns, and produces a square-wave pulse whose front edge corresponds to the time when the input signal exceeded the threshold and the width of the pulse is proportional to the integrated charge of the input signal. After integrating the charge of an input signal over 400 ns, QTC discharges the integrated charge with a constant current in the next ∼400 ns, which results in the total processing time of 900 ns for a hit. The output pulse of QTC is then digitized by a time-to-digital converter (TDC). The digitized data from the TDCs are eventually sent to readout front-end PCs by using Ethernet which enables the needed high rate of data transfer.

There are 20 front-end PCs to collect digitized information of all the ID and OD PMTs. Each front-end PC collects the digitized PMT hits from 30 ID and 20 OD fron-end boards QBEEs (QTC-Based Electronics with Ethernet), and then sorts the information of these PMT hits in order of time. The time-ordered PMT hit information from all the front-end PCs is then sent to another group of PCs, called Marger PCs, in order to make a time-order list of the PMT hits. Using the list, Margers apply a set of software triggers to select event candidates by using the variable N_{200} which is the number of PMT hits in a 200 ns time window. When N_{200} exceeds the threshold of a trigger type, the trigger is issued to select an event candidate. For each event candidate, a time window is defined around the time the trigger is issued, and all the PMT hit information inside the window is sent to a single Organizer PC. The Organizer PC collects all the event candidates from all the

Marger PCs, and writes them on disks. The data written on disks are eventually used in physics analyses in offline. Figure 3.6 shows a schematic drawing of the flow of the online data processing.
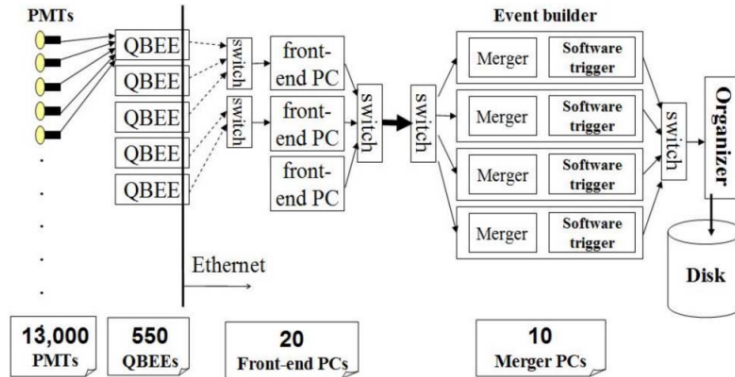
Figure 3.6: A schematic drawing of the online data process. Figure taken from [19].

3.3.2   T2K data acquisition at the far detector

As was described above, all the PMT hits are continuously sent to online PCs. The software trigger program running on online PCs is then applied to these hits to extract events. In order to avoid possible biases by the software trigger in online, first, PMT hits induced by the T2K beam neutrinos are stored on disks based on the absolute arrival time of the T2K beam neutrinos, and later the same software trigger program used in online is applied to the stored hits to extract events in offline.

Since the SK DAQ buffer can hold all the PMT hit information for a few second, T2K beam spill information needs to be available at SK before the buffer resets the temporally stored hit information. To make this possible, beam spill information containing spill timing data is transferred from the Neutrino beam-line at J-PARC to the SK control room via a VPN network in real-time, which is then immediately sent back to the J-PARC side to check for data corruption. For each beam spill, the absolute time when the first bunch of the spill arrives at the graphite target in the secondary beamline is measured by using the GPS system at J-PARC. Then, the absolute arrival time of a T2K beam spill at SK is calculated by adding the neutrino time-of-flight of $985.134\,\mu$s to the absolute time measured at J-PARC ($295.336\,\mathrm{km} \div 299792.458\,\mathrm{km/s} = 985.134\,\mu$s, where $295.336\,\mathrm{km}$ is the distance from the target of the proton beam to the SK detector center). The transferring time of the spill information is also monitored by measuring the round trip time (RTT) between Tokai-Kamioka-Tokai. The typical RTT is 30-50 ms, which is short enough to save the PMT hit information for each individual beam spill. Figure 3.7 shows a schematic drawing of the data acquisition using the beam arrival timing. A time window of $\pm 500\,\mu$s from the absolute beam arrival time is defined on a spill-by-spill basis, and all the PMT hits within the windows are stored on disks. The extraction of events from the PMT hits in the 1 ms time windows and classification of the

47

extracted events will be described in Section 5.2.
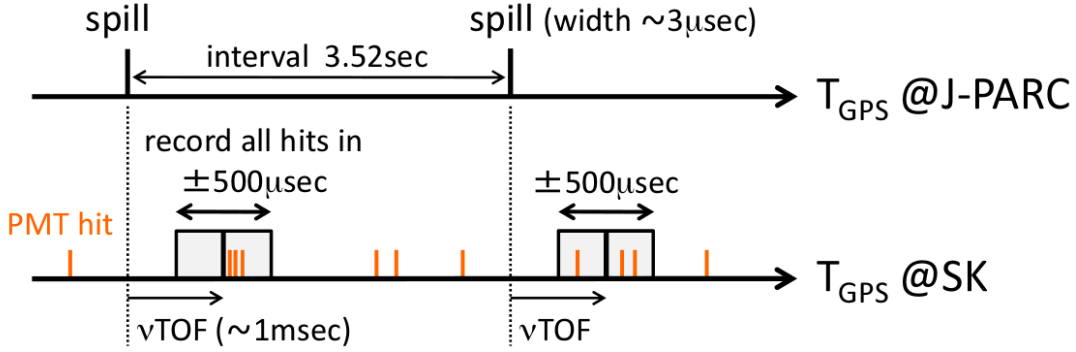
Figure 3.7: A schematic drawing of the data acquisition at SK. The spill interval and the width of one spill has been changed from 3.5 s and $\sim 3\,\mu$s to 2.4 s and $\sim 5\,\mu$s, respectively. Figure taken from [20].

Since the events induced by the T2K beam neutrinos are identified based on timing information, the absolute time needs to be precisely determined. The absolute time of a PMT hit is calculated based on the GPS clock. One pulse per second (1PPS) signal from the GPS receiver is sent from the main entrance to a local time clock (LTC) by an optical fiber with a length of about 1.8 km. Both all of QBEEs and the LTC are synchronized by a 60 kHz trigger clock which is distributed by a master clock module. The synchronization enables calculating the time difference between the 1PPS signal and the PMT signals recorded by the QBEE modules. The TDC count of QBEE is reset to 0 when QBEE receives a 60 kHz trigger. Therefore, the absolute time of each PMT hit T_{Abs}(PMT hit) can be obtained by using both of the TDC count of the QBEE and the LTC count as follows:

$$
\begin{aligned}
T_{Abs}(\text{PMT hit}) = \ & T_{Abs}(\text{GPS 1PPS}) \\
& + \left(\text{LTC count(60 kHz trigger)} - \text{LTC count(GPS 1PPS)}\right)/\text{LTC frequency} \\
& + \text{TDC count/TDC frequency} \\
& + 10008 \text{ ns} \\
& - 972.1 \text{ ns},
\end{aligned} \tag{3.3.1}
$$

where the factor $+10008$ ns accounts for the propagation of the 1PPS through the optical fiber and the factor -972.1 ns takes into account timing delay due to various sources:

- Time delay due to internal processing in LTC.

- Time delay due to internal processing in TDC.

- Difference in arrival time of trigger between LTC and QBEE.

- PMT's transit time and propagation time between PMT and signal cable.

The timing delay from each source is determined by calibration measurements [20].

For this determination of the absolute PMT hit time, the stability of the GPS system at SK is essential. In order to stably obtain the timing information from the GPS system, SK is equipped with two independent GPS modules (called "GPS1" and "GPS2"). In addition, a rubidium clock is installed, which is auxiliarily used if the timings of the two GPS modules are inconsistent. The GPS1 and GPS2 are consistent with each other within 200 ns. From comparisons with the Rb clock, however, the GPS2 shows more stable operation than that of the GPS1, and the GPS2 is used as the default clock. In the case where neither the GPS1 nor GPS2 works properly, the Rb clock is used for the absolute arrival time of the beam spills at SK.

3.4   Detector calibration

Since the precision of a measurement depends on how well the detector used in the measurement is calibrated, calibration works are the vital component in experiment. In this section, the procedures of the calibrations conducted in SK are summarized based on [21].

In SK, event is reconstructed using the timing and observed charge of PMTs. Therefore, timing and observed charge responses of PMT need to be well calibrated for each individual PMT. In addition, the optical properties of the water and other materials used in the detector need to be measured. The resultant PMT's responses and optical properties are also used as the ingredients for building the detector simulation.

3.4.1   Adjustment of high-voltage setting

The high-voltage setting for each individual PMT is adjusted so that all the PMTs produce approximately the same amount of charge for a given light intensity. For this adjustment, an isotropic light source was placed at the center of the detector. Since the shape of the detector is cylindrical, there is no position from which the distance between the light source and each PMT is the same. This makes the light attenuation effect in the water to be different on each PMT, and thus each PMT can not receive the same amount of light from a light source. In order to avoid the effect of the different in distance light attenuation, pre-calibrated reference 420 PMTs are used. All the ID PMTs including these reference PMTs are grouped based on geometrical relation with respect to the light source. For each group, PMTs, which belong to it, receive geometrically the same light intensity. The high-voltage of PMTs are then adjusted so that all the PMTs in the group observe the same charge as the reference PMTs.

3.4.2 Relative gain calibration

After determining the high-voltage setting for each PMT, all the PMTs produce roughly the same charge for a given light intensity, but each PMT still has residual variation in its PMT gain. This is regarded as the relative gain and is measured with calibration using a nitrogen-laser-driven dye laser. The laser is located roughly at the center position of the inner detector and emits light isotropically. In order to avoid the difference between the PMTs due to the SK tank's cylindrical geometry, two sets of measurement are conducted. In the first measurement, the laser is operated at a high intensity so that every PMT receive multiple photons. For each individual PMT, average observed charge Q_i^{obs} is measured and is expressed as follows:

$$Q_i^{obs} \propto I_H \times a_i \times \varepsilon^{QE} \times G_i, \tag{3.4.1}$$

where I_H is the light intensity, a_i is the angular acceptance of i-th PMT, ε^{QE} and G_i denote the quantum efficiency and gain of i-th PMT, respectively.

In the second measurement, the light intensity is set to a low intensity I_L such that only a few ID PMTs are hit by single flash. This low intensity enables making a reasonable assumption that each PMT hit is made by single photon and the hit does negligibly depend on the PMT gain. Therefore, the number of hits for each PMT counted in the second measurement can be expressed as:

$$N_i^{obs} \propto I_L \times a_i \times \varepsilon^{QE} \tag{3.4.2}$$

Using Equation 3.4.1 and 3.4.2, a quantity which is proportional to gain can be obtained for each PMT:

$$G_i \propto \frac{Q_i^{obs}}{N_i^{obs}} \tag{3.4.3}$$

The relative gain can be obtained by averaging the quantity over all the ID PMTs, since the proportional constant is common among all the ID PMTs. After obtaining the relative gain for each PMT, distribution of the relative gain is made using all the ID PMTs. From that distribution, the difference in the gain across all the ID PMTs has a standard deviation of 5.9%. The obtained relative gain is used to accurately convert observed charge to number of observed p.e. on a PMT-by-PMT basis when data is analyzed.

3.4.3 Absolute gain calibration

When photons reach the photocathode of a PMT, p.e. are produced by the photo-electric effect and the PMT eventually observes charge. The absolute gain relates the produced p.e. within observed charge, and is called single-p.e. distribution. To

convert observed charge to produced p.e. (or equivalently detected photons) and perform detector simulation, the single-p.e. distribution needs to be measured.

A nickel source, which contains a ^{252}Cf source providing neutrons, is utilized to create the single-p.e. distribution. The nickel source emits γ rays isotropically with total energy of $\sim$9 MeV via the reaction of ^{58}Ni(n;γ)^{59}Ni. In this measurement the nickel source is placed at the central position of ID and the γ rays are detected by all the ID PMTs. The observed number of p.e. is 0.004 per event on average for each PMT, meaning that more than 99% of produced PMT hits are due to a single-p.e. The observed charges of all the PMT hits produced by the nickel source are used to make the single-p.e. distribution by considering the relative gain difference among all the ID PMTs described in the previous subsection. Figure 3.8 shows the observed charge distribution.

From the charge distribution, the average of the charge is obtained and then the average is used as the conversion factor from pC to single-p.e. The conversion factor is found to be 2.658 pC/p.e. and is used to obtain the single-p.e. distribution which is used for the detector simulation.
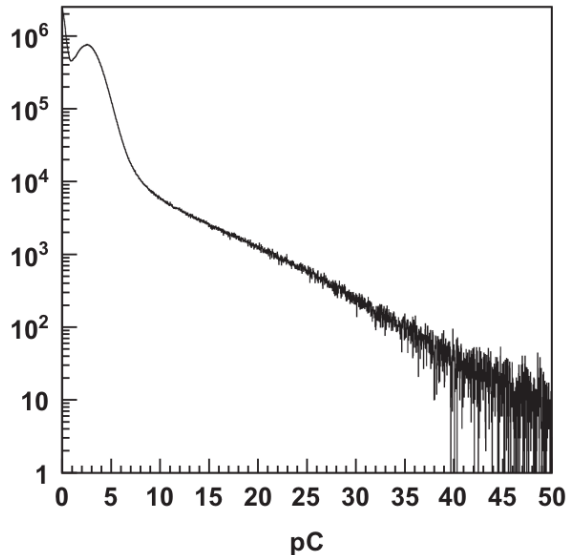
Figure 3.8: The measured single-p.e. distribution in unit of pC. Figure taken from [21].

3.4.4 Measurement of relative quantum efficiency

QE is different between the ID PMTs, and thus relative variation in the quantum efficiency (called "relative QE") needs to be measured for each individual ID PMT. As expressed in Equation 3.4.2, number of hits for a PMT is proportional to its QE when the intensity of a light source is low enough. The same nickel source as used in the measurement of the single-p.e. distribution is therefore used for relative QE determination. In order to measure the relative QE, the light intensity, the light propagation in water, and the geometrical acceptance need be taken into account, which is not easy in an analytic way. A detector simulation of the nickel calibration

is therefore performed by simulating the γ rays emitted from the nickel source. In the simulation, a common QE value is used among all the ID PMTs to predict the number of hit for each PMT. In addition, convection is artificially set such that the water quality is uniform across ID. The simulated number of hits are then compared to the data for each individual PMT and the resulting ratio between the simulation and the data is regarded as the relative QE. The relative QE obtained for each PMT is tabulated and is used for detector simulation.

3.4.5 Timing calibration

Since event reconstruction such as determination of vertices and track directions of particles produced by the T2K beam neutrinos aggressively utilizes timing of PMT hit. Time response, which is the time interval from the time, that photons reach a PMT, to the time, when the signal of the PMT is registered as a hit, needs to be precisely calibrated. The time response can differ between the ID PMTs, which originates from differences in the transit time of the PMTs, the lengths of the PMT signal cables, and the processing time of the readout electronics. In addition, a hit is registered when the analog signal of a PMT exceeds the threshold of hit discriminator, and the time to cross the threshold depends on the pulse height of the signal which is correlated with the observed charge of the signal. Therefore, the time response can also vary depending on the observed charge.

To calibrate the time response for each PMT, a nitrogen laser is used to inject a fast enough pulsed laser light a diffuser ball placed near the center position of ID. The timing of the laser light injection is provided by using a 2-inch monitor PMT. The laser light is flashed by varying its intensity. For each PMT hit, the timing of the fired laser, which is obtained from the monitor PMT, and time-of-flight (TOF) from the diffuser ball are subtracted. Using the TOF subtracted timings and the observed charges of the PMT hits, a two-dimensional distribution (hereafter called "TQ distribution") is made for each ID PMT as shown in Figure 3.9. In the TQ distribution, the observed charges in pC are divided into 180 bins defined as Q bins in order to obtain the observed charge dependence of the time response. The peak timing and standard deviation are obtained for each Q bin at which an asymmetric Gaussian function is fitted to the corresponding timing distribution. Once the timing distributions are fitted for all the Q bins, the obtained peak timing and standard deviations are fitted by a combination of polynomial functions. The resulting fit parameters are stored as TQ-map for each PMT and are used to correct hit timing as a function of the observed charge on a PMT-by-PMT basis.
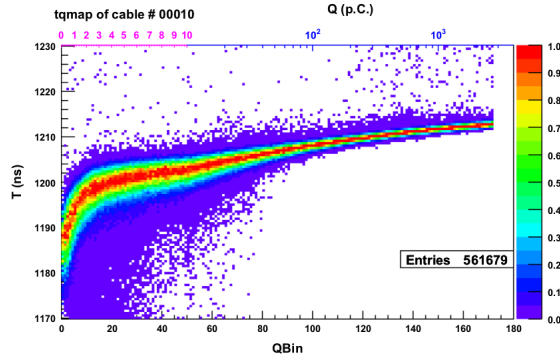
Figure 3.9: An example of the TQ distribution for an ID PMT. The horizontal axis is the observed charge (pC) binned into the Q bin whose binning is a linear scale up to 10 pC, and then becomes a log scale. The vertical axis represents the observed timing with the TOF correction from the diffuser ball and the laser firing timing. In the vertical axis, larger values correspond to earlier timing. Figure taken from [21].

The PMT timing resolution is also evaluated by using the same calibration data as for the TQ-map production above. All the PMT hits from all the ID PMTs are corrected by their TQ-maps, and the TQ-corrected hits are used to produce residual timing distribution for each Q bin. In each Q-bin, the residual timing distribution is fitted with an asymmetric Gaussian function to extract σ_t and σ_t' which are timing resolutions for before and after the peak timing of the residual timing distribution, respectively. Figure 3.10 shows the resultant timing resolution as a function of the observed charge, which is used for the detector simulation.
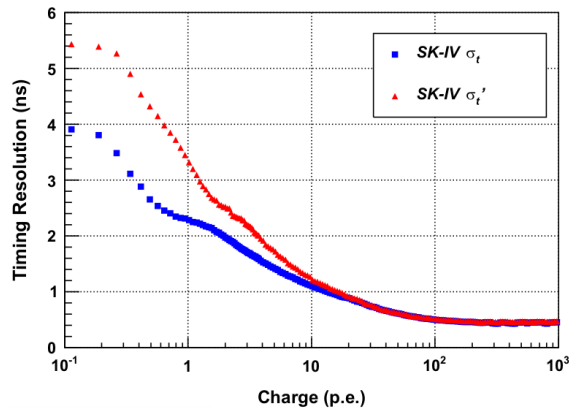
Figure 3.10: Timing resolution as a function of observed charge in p.e. The PMT hit timing of ID is modeled by an asymmetric Gaussian function whose parameters depend on observed charge. The σ_t and σ_t' are the timing resolutions for before and after the peak timing of the function, respectively. Figure taken from [21].

3.4.6 Measurement of water properties with laser light

In the detector, the water attenuates Cherenkov light by scattering and absorbing the light. The light whose wavelength is λ after traveling a distance l is attenuated

exponentially as $exp(-l/L(\lambda))$. $L(\lambda)$ is the light attenuation length of the water and is characterized by Equation 3.4.4.

$$L(\lambda) = \frac{1}{\alpha_{sym}(\lambda) + \alpha_{asym}(\lambda) + \alpha_{abs}(\lambda)}, \qquad (3.4.4)$$

where $\alpha_{sym}(\lambda)$, $\alpha_{asym}(\lambda)$, and $\alpha_{abs}(\lambda)$ are amplitudes for symmetric scattering, asymmetric scattering, and absorption, respectively. The $\alpha_{sym}(\lambda)$ parameter is modeled based on the Rayleigh scattering and symmetric component of the Mie scattering and has an angular dependence of $1 + \cos\theta^2$, where θ is angle between the incoming and the scattered directions of a photon. The $\alpha_{asym}(\lambda)$ parameter consists of the asymmetric Mie scattering which has a $\cos\theta$ dependence only for forward direction and has no amplitude for backward direction (*i.e.* 0 for $\cos\theta <0$). $\alpha_{abs}(\lambda)$ takes into account the effect of light absorption.

Each amplitude separately and the sum of thereof (*a.k.a* $L(\lambda)$) need to be precisely measured in order to accurately reconstruct an event and perform detector simulation. If the fraction of these amplitudes is different between data and simulation, it can make different observed light pattern even for same attenuation length. This is done by a calibration using an apparatus which can inject collimated laser light.

The calibration setup is shown in the left panel of Figure 3.11. In this calibration, a collimated laser light is vertically injected from the detector top to bottom. The direct light of the laser light is detected by the PMTs located around the target position of the laser beam. On the one hand, the scattered light by the water and the reflected light by the bottom PMTs and the black sheet are detected by the PMTs positioned on the top and barrel regions of ID. As the timing of light associated with the laser beam has a spacial dependence, the detector is vertically divided into five regions as schematically shown in the left panel of the figure: B1, B2, B3, B4, and B5. Then, for each region TOF-subtracted distribution, which is PMT hit time distribution after subtracting time-of-flight from the beam target position to each hit PMT, is made. A typical TOF-subtracted distribution is shown in the right panel of the figure. As shown in the panel, the broad structures of the PMT hits in earlier timing are produced by the scattered photons, whereas the peaks after 1800 ns originate from the photons reflected by the PMTs and the black sheets.
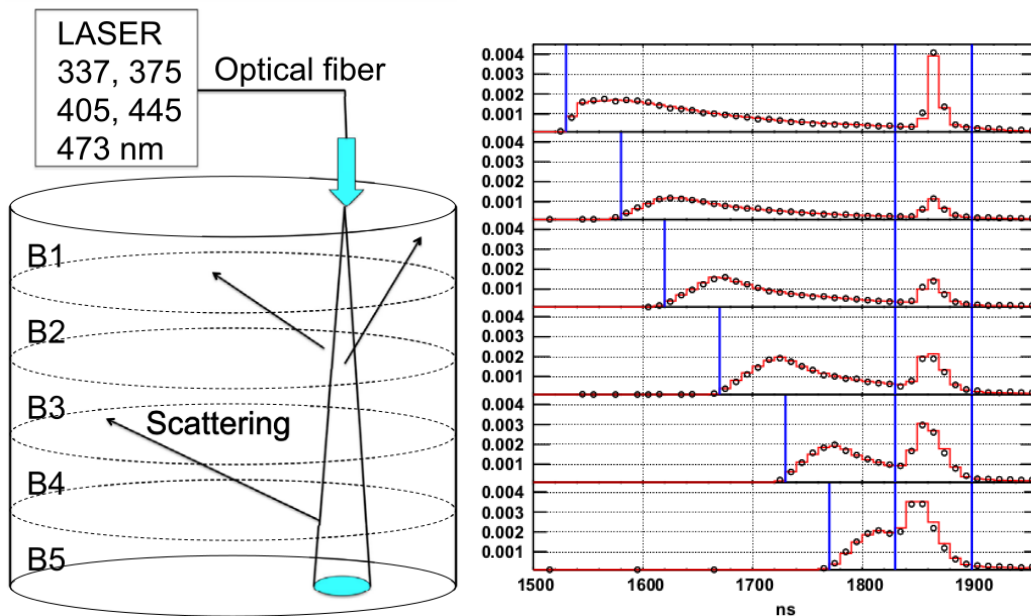
Figure 3.11: A schematic drawing of the laser calibration system for the measurement of the water properties (left). Distributions of the TOF-subtracted hit timings for the five different tank regions (right). Figures taken from [21].

In order to extract the scattering and absorption amplitudes, the left region enclosed by two lines in the right panel of Figure 3.11 is used. Since the total number of scattered photons and the shapes of the distributions in the region are sensitive to these amplitudes, a number of MC sets are generated by varying these amplitudes, and then a χ^2 fit is performed. This procedure is performed for five different wavelengths ranging from 365 nm to 445 nm. Figure 3.12 shows typical amplitudes obtained by the χ^2 fit.
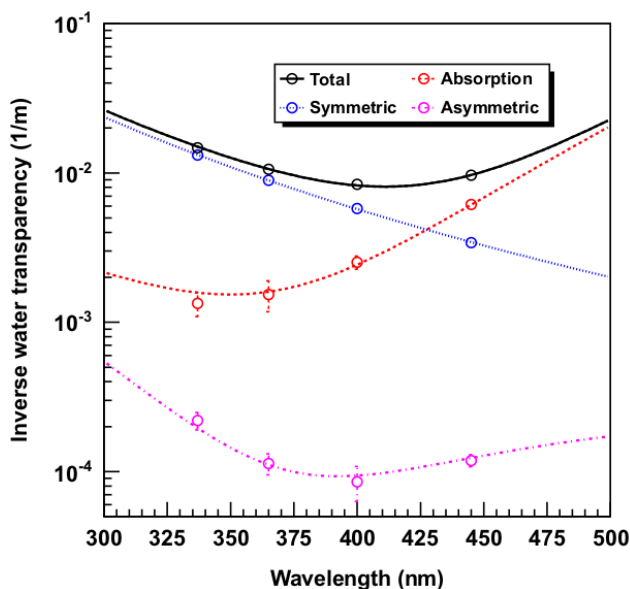
Figure 3.12: Typical fitted amplitudes. The points present the data taken in April 2009. The black, blue, red, and violet lines correspond to the fitted functions of total amplitude, symmetric scattering, asymmetric scattering, and absorption, respectively. Figure taken from [21].

3.4.7 Time variation of water transparency

The amplitudes of the light absorption and the light scattering extracted using the collimated laser light described above are continuously monitored. The time dependencies of these coefficients are shown in Figure 3.13. As shown in the figure, relatively large time variations in the absorption and the asymmetric scattering amplitudes are seen, which causes a time variation in the light attenuation length of the water. Since the asymmetric scattering coefficient is about one order of magnitude smaller than that of the absorption, the time variation of the light attenuation length is dominated by the light absorption.
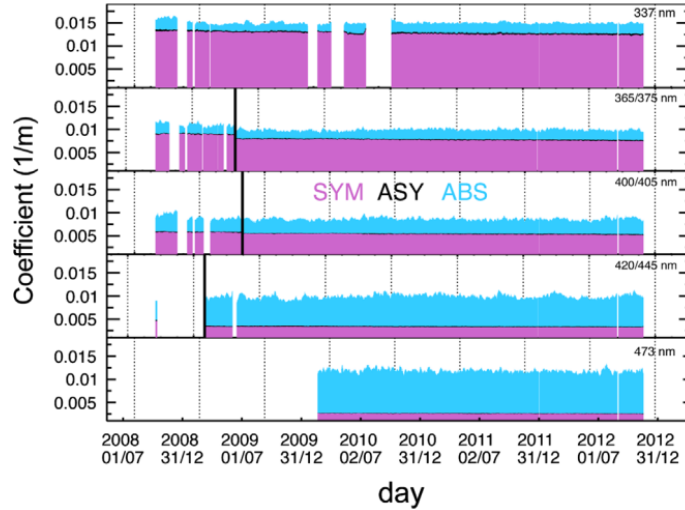
Figure 3.13: Time variations of the fitted amplitudes for various wavelengths. The violet, black, and cyan correspond to the amplitudes of symmetric scattering, asymmetric scattering, and light absorption. Three laser units were replaced during this data taking period, and the black vertical lines represent the time when the replacement was conducted. Figure taken from [21].

In order to relate the variation of absorption with the attenuation length, decay-electrons from cosmic ray muons are utilized. By using these electrons, an attenuation length averaged over the Cherenkov photon spectrum and the wavelength dependence of the PMT's QE (hereafter called "effective attenuation length" in this subsection) can be measured.

To measure the effective attenuation length, first a deacy-e event sample is prepared as follows:

- Select cosmic ray muons which stop inside the inner detector.

- For each selected muon, deacy-electron is searched for, and the time difference between the primary muon and the decay-electron, Δt, is within a time window: $3\,\mu s < \Delta t < 8\,\mu s$.

- The nearest distance from the reconstructed vertex of the decay-electron to the ID wall is $> 2\,m$.

- The distance between the reconstructed decay-electron vertex and the stopping position of the primary muon is $< 2.5\,m$.

After applying the cuts, there are about 1,500 decay-electron events per day [158]. To obtained the effective attenuation length, the azimuthal symmetry of Cherenkov radiation with respect to the momentum direction of a charged particle is exploited. With this symmetry, it is extracted by using distance from reconstructed decay-electron vertex to hit PMT position and observed charges. Each deacy-electron event in the sample has a number of PMT hits, and a distance r from the reconstructed its

vertex to each individual hit PMT position is calculated. Once r is calculated for all the PMT hits in the sample, they are filled into a histogram with bins of r. Then, the distribution of the logarithm of the mean observed charge, $\ln Q_{ave}$, in bins of r is calculated. The left panel of Figure 3.14 shows a typical $\ln Q_{ave}$ as a function of r.
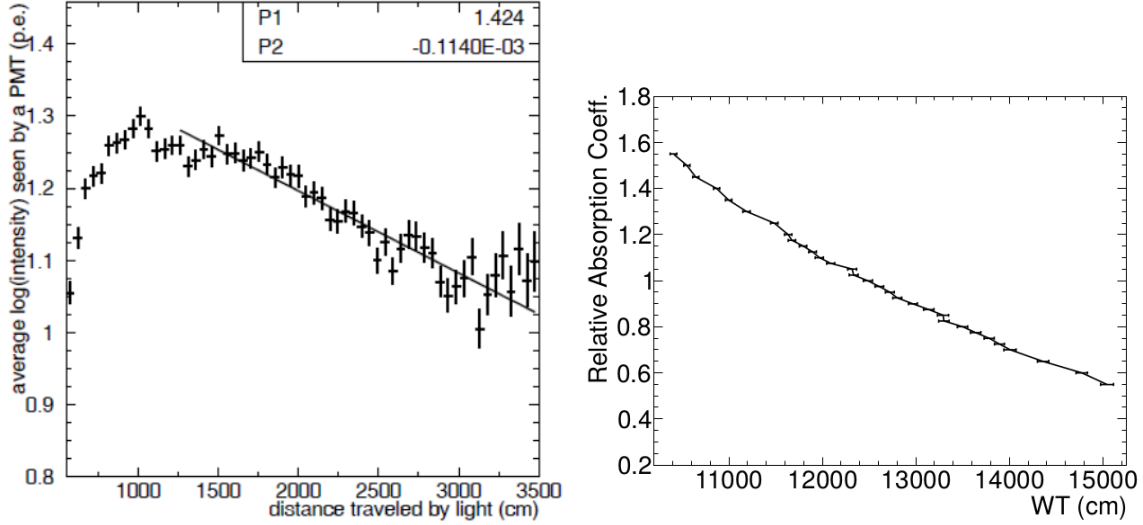
Figure 3.14: Typical $\ln Q_{ave}$ distribution (left) and the relation between the relative absorption amplitude and the effective attenuation length (right). In the left, the slope of the fitted linear function corresponds to the effective attenuation length. The left and right side figures taken from [22] and [23], respectively.

Since the slope of $\ln Q_{ave}$ distribution corresponds to the effective attenuation length, a linear function is fitted. The measured effective attenuation length is then converted to a scaling factor that scales the nominal absorption amplitude used in the detector simulation. The relationship between the effective attenuation length and the scaling factor is obtained by generating electrons with different absorption amplitudes in the detector simulation. The right panel of Figure 3.16 shows the obtained relation.

3.4.8   Position dependence of water transparency

The ultra pure water is supplied from the bottom part of the tank, and is returned to the water circulation system in the top region. This water flow makes a temperature gradient with respect to the vertical direction in the detector tank. Figure 3.15 shows a typical vertical dependence of the water temperature in the tank.
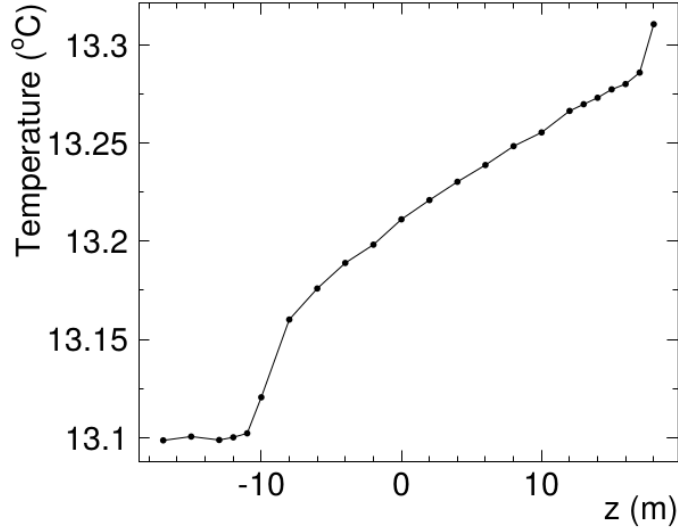
Figure 3.15: A typical vertical position z dependence of the water temperature inside the tank. Figure taken from [23].

As shown in the figure, the region with a vertical position z below -11 m does not have clear temperature variation, whereas for z >-11 m the temperature monotonically increases as a function of z. The temperature variation introduces a vertical position dependence of the light attenuation length, which causes an asymmetry of PMT's hit probability between the top and bottom regions. The vertical position dependence of the light attenuation length is modeled using the nickel calibration data obtained by monthly data taking and the real-time calibration data using the light produced by a Xe lamp. In the nickel calibration, the asymmetry of the PMT hit probability is quantified as follows:

$$\alpha_{TBA} = \frac{< N_{top} > - < N_{bottom} >}{< N_{barrel} >}, \tag{3.4.5}$$

where $< N_{top} >$, $< N_{bottom} >$, and $< N_{barrel} >$ are the mean hit rates of the PMTs located on the top, bottom, and barrel regions of the inner detector, respectively. In the case of the Xe calibration, the mean hit rates are replaced with the corresponding mean observed charges. Figure 3.16 shows the measured α_{TBA}s by the nickel and Xe calibrations, and there is a 3~5 % level of asymmetry.

59
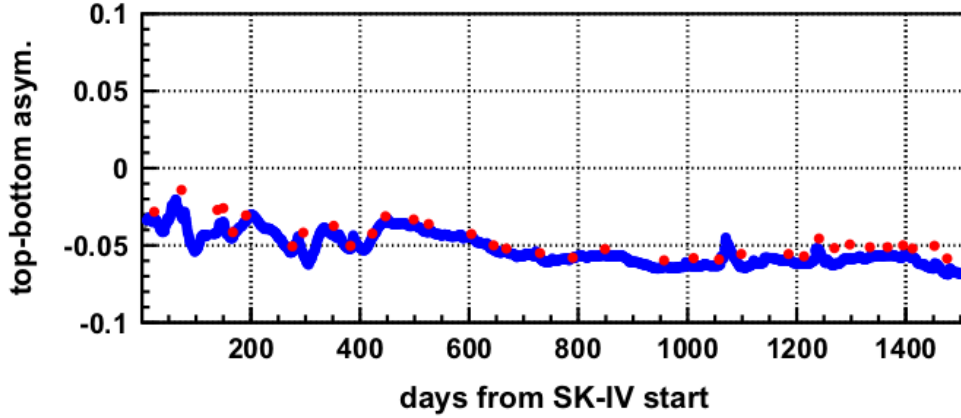
Figure 3.16: Time variation of the measured α_{TBA} with the daily calibration using Xe light source (blue) and the monthly nickel calibration (red). Figure taken from [21].

In order to account for the observed asymmetry, a vertical position dependence of the light absorption is modeled by introducing a time dependent parameter $\beta(t)$ into the detector simulation. The $\beta(t)$ parameter converts the measured α_{TBA} into the strength of the vertical position dependence. The resultant absorption coefficient, which depends on wavelength λ, time t, and vertical position z in the detector, is given as:

$$\alpha_{abs}(\lambda, Z, t) = \begin{cases} \alpha_{abs}(\lambda, t)(1 + \beta(t)Z) & \text{(for } Z \geq -11m) \\ \alpha_{abs}(\lambda, t)(1 - \beta(t)11) & \text{(for } Z \leq -11m) \end{cases} \qquad (3.4.6)$$

The relation between the β and α_{TBA} is derived by comparing the nickel calibration data and the corresponding MC samples, which are generated by varying the β parameter. The relation is found to be [159]:

$$\beta = (-0.164\alpha_{TBA}^2 - 3.676\alpha_{TBA}) \times 10^{-3}. \qquad (3.4.7)$$

3.4.9 Measurement of reflectivity for PMT and black sheet

The reflectivity of the ID PMT surfaces is also tuned by using the same laser calibration used for the extraction of the amplitudes of the water attenuation length as described in Section 3.4.6. The reflectivity is parametrized in an inclusive way as the complex refractive index of the PMT's photocathode: $n_{real} + in_{imag}$. Using the right region shown in Figure 3.11, n_{real} and n_{imag} are extracted similarly to the fitting of the absorption and scattering coefficients.

The reflectivity of the black sheets is also measured and is tuned. For this tuning, an in situ measurement is conducted as schematically drawn by Figure 3.17. As shown in the figure, laser light is injected toward the black sheet attached to

the experimental apparatus by varying incident angle at three wavelengths: 337 nm, 400 nm, and 420 nm. Then, the observed charges of the PMT hits due to the reflected light Q_{ref} are measured. The laser light is also injected without the black sheet to measure the intensity of the direct light, and the observed charges for the direct light Q_{dir} are measured. The reflectivity of the black sheets is then tuned by using the ratio between Q_{ref} and Q_{dir}.
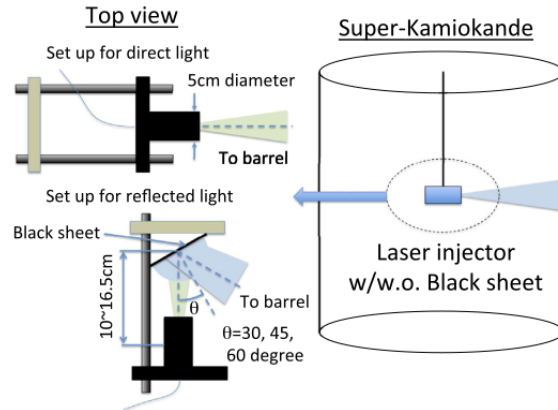
Figure 3.17: A schematic drawing of the setup for the reflectivity measurement of the black sheets. Figure taken from [21].

Chapter 4

Event simulation

In order to measure physical quantity of interest, measurement often needs "efficiency correction". In general, efficiency is dependent on particular experimental configuration such as performance of event reconstruction and analysis sample used for the measurement. As a consequence, it is often impossible to express efficiency in closed form. Similarly, expectation which includes effect of detector response can not be expressed analytically in many cases. Therefore, these quantities are obtained from results of Monte Carlo (MC) simulations.

This chapter describes MC event simulation at the T2K far detector which mainly consists of two parts: simulation of neutrino interactions in water and detector simulation for the particles produced in the neutrino interaction simulation. Section 4.1 overviews the simulation of the T2K beam neutrino fluxes which produces vital input to perform simulation of neutrino interactions. Following this, simulation of ν-nucleus interaction and detector simulation are described in Section 4.2 and Section 4.3, respectively. Then, modifications on the detector simulation which enables performing analyses with neutron tagging is described in Section 4.4. Section 4.5 summarizes the MC sets used for the primary analysis of this thesis.

4.1   T2K neutrino beam flux

The prediction of the T2K neutrino beam fluxes begins with the simulation of an upstream part of the primary proton beamline as shown in Figure 4.1. Protons with a kinetic energy of $30\,\mathrm{GeV}$ are injected to the target, which is simulated including the hadronic interactions by FLUKA [160]. The particles which have left the target material are stored with their kinetic information, and these particles are fed into another simulation JNUBEAM which is a Geant3 [161] based simulation with GCALOR for hadronic interactions.
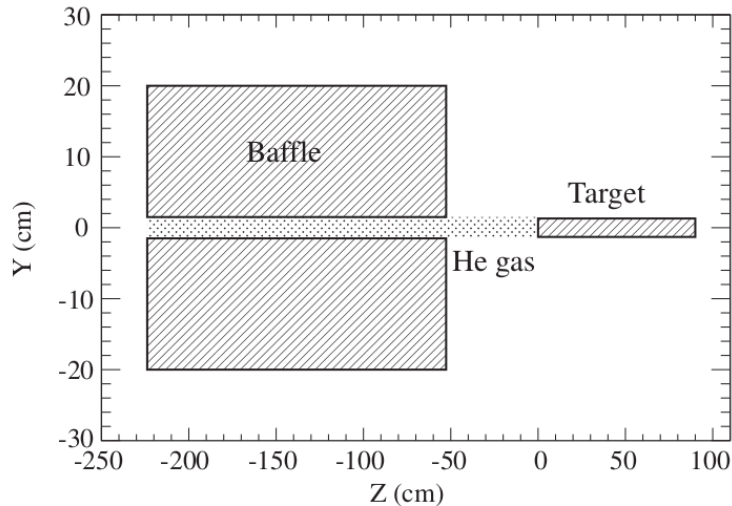
Figure 4.1: A schematic of the geometrical setup considered in the FLUKA simulation of the proton injection. Figure taken from [17].

In JNUBEAM, the geometrical setup of the horn and decay volume is considered. Particles are propagated through the setup, and these particles are simulated until they interact or decay. In order to save computational time, directions of neutrinos produced from particle decays are artificially set to either the far detector direction or the direction from its production point to a randomly selected point in the near detector plane. In the primary proton simulation by FLUKA and JNUBEAM, truth information such as the kinematics of the initial proton, full interaction chain of the neutrinos, the kinematics of the neutrinos, and the probability density in the decay phase-space are stored. Using the saved information, the neutrino flux and energy spectrum are made from the simulated events by weighting.

For the weighting in the hadron interactions which happen inside the target, several external measurements are used to accurately predict the flux. Since the flux prediction strongly depends on yields of pions and kaons, the results of pion and kaon differential yields for same proton energy as T2K measured by NA61/SHINE [162] [163] are used. In addition, other experimental data [164] [165] are also used to tune the region where the data of NA61/SHINE do not cover. Figure 4.2 shows the prediction of T2K fluxes at the far detector.
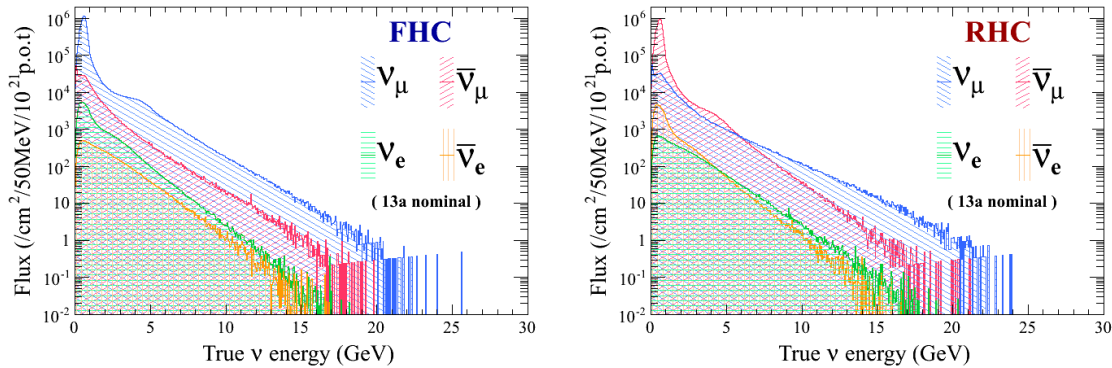
Figure 4.2: Beam neutrino non-oscillated fluxes for the FHC (left) and RHC (right) modes. These fluxes are used for event simulation at the far detector.

Recently the NA61/SHINE published the hadron yields for a replica target of the target used in T2K [166], and the analysis to use the results inside T2K has completed. In this thesis, the fluxes tuned by using the measurement of the replica target [31] are therefore used.

4.2 Neutrino interaction

In the energies of the T2K beam neutrinos up to $30\,\mathrm{GeV}$, neutrinos interact with nucleus, and a variety of reactions can occur in very different ways depending on energy. For instance, a neutrino can interact with whole an atomic nucleus coherently, whereas it can interact with a constituent quark inside a nucleus. Due to the complexity of neutrino interactions in the energy region, interaction cross sections are calculated by MC technique. In addition, since neutrino interaction often happen inside a nucleus, resultant outgoing particles are also produced inside the nucleus. Therefore, rescattering of these particles inside the nucleus needs to be taken into account.

In T2K, both neutrino interaction and subsequent rescattering of particles produced by the interaction are simulated by NEUT MC event generator [135]. In NEUT, the following processes are considered:

CC/NC (quasi-) elastic scattering

CC multi nucleons scattering

CC/NC single meason production

CC/NC coherent scattering

CC/NC deep inelastic scattering

Figure 4.3 shows the CC cross sections for neutrinos and antineutrinos, calculated by NEUT. In the figure, "MEC" and "RES" corresponds to CC multi nucleons scattering and CC single meason production, respectvely. CC deep inelastic scattering is divided into "Multi-pi" and "DIS".

64
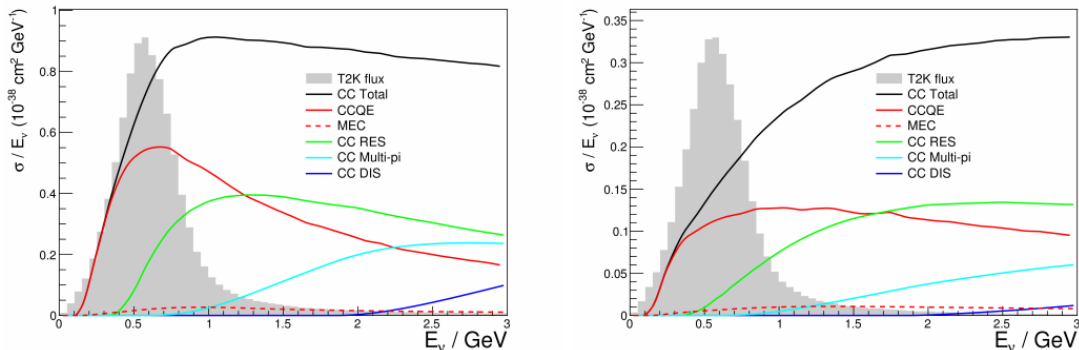
Figure 4.3: Cross-sections for interactions calculated by NEUT 5.3.2. Left and right correspond to ν_μ and $\bar{\nu}_\mu$. The gray histograms represent T2K fluxes, which are shown with arbitrary units. Figure taken from [24].

Elastic and quasi-elastic scattering

NC elastic scattering is a process in which an incoming neutrino scatters off a target nucleon. The reaction is given as:

$$\nu_\ell + N \rightarrow \nu_\ell + N \tag{4.2.1}$$

where ν_ℓ is either neutrino or antineutrino and N is either neutron or proton. In this process, only momentum is transferred to the target nucleon and no additional particles are produced.

In case of CCQE reaction which was mentioned in Section 1.2.1, a W boson is exchanged between an incoming neutrino and a target nucleon. Consequently, the neutrino and the target nucleon are converted to a charged lepton and other nucleon, respectively. In neutrino energies below ~ 1.5 GeV, CCQE is the dominant interaction process.

Since nucleon is not an elementary particle and an extended object, calculation of such interactions is difficult. For this calculation, the Llewellyn Smith model [167] is used for free protons. The model contains a set of parameters which need to be determined experimentally. Most of the parameters are accurately determined by experimental data for β-decay and electron-nucleus scattering. The axial form factor in the model which characterizes the axial charge distribution inside nucleon has a parameter called M_A^{QE}. Since M_A^{QE} can not be determined by those experimental data, it is set to 1.2 GeV/c^2 based on the results of K2K [168] and MiniBooNE [169].

For bound nucleon in nucleus, Fermi motion, Pauli blocking, and a nuclear screening effect are taken into account. Fermi motion is the initial movement of the target nucleon inside the nucleus before it interacts with neutrino and the relativistic Fermi gas (RFG) model [170] is used. Pauli blocking forces the out-going nucleon to have its momentum above the Fermi surface. Since the mediator of a weak interaction propagates through the nuclear medium, there is a screening effect on the propagator

due to long-range correlations between the nucleons inside the nucleus. This effect is taken into accunt by the random phase approximation [171, 172].

Multi-nucleon interaction (2p2h)

The CCQE reaction for bound nucleon described above is modeled under an assumption. In the assumption, direct correlation among nucleons in the target nucleus is ignored, and an incoming neutrino interacts with a bound nucleon without consideration of such direct correlation. However, the results of the ν_μ and $\bar{\nu}_\mu$ CCQE interaction for a carbon target by MiniBooNE [169, 173] suggest that existence of an interaction process (hereafter called "2p2h") in which an incident neutrino interacts with two nucleons simultaneously as a result of such direct correlation.
In NEUT, the 2p2h interaction modeled by Ref. [171, 174] is implemented. In this simulation, a neutrino interacts with a pair of nucleons inside the target nucleus as follows:

$$\nu + N + N' \to \ell + N'' + N''', \tag{4.2.2}$$

where N and N' is the incoming pair and $N'' + N'''$ is the outgoing pair. In NEUT, the incoming np pair is allowed for both neutrino and antineutrino interactions and is selected with a probability of $\frac{1}{3}$. If the selected incoming pair is not np, then nn and pp pairs are selected for neutrino interaction and antineutrino interaction, respectively.

Single meason production

Once the center of mass energy in a neutrino-nucleon interaction exceeds the mass of a delta baryon, the interaction can produce a baryon resonance excitation. The subsequent baryon decay produces a single meason as follows:

$$\nu + N \to \ell + N^* \to \ell + N' + m \tag{4.2.3}$$

where N and N' are the nucleon in the initial and the final state, respectively, N^* is the intermediate baryon resonance, ℓ is the outgoing lepton, and m is a meson such as π, K and η. In this reaction, any interaction channel is allowed if it conserves electric charge. For instance, single pion production has three CC neutrino interaction channels:

$$\nu_\ell + n \to \ell^- + p + \pi^0, \tag{4.2.4}$$
$$\nu_\ell + n \to \ell^- + n + \pi^+, \tag{4.2.5}$$
$$\nu_\ell + p \to \ell^- + p + \pi^+, \tag{4.2.6}$$

three CC antineutrino interaction channels:

$$\bar{\nu}_\ell + p \rightarrow \ell^+ + n + \pi^0, \tag{4.2.7}$$

$$\bar{\nu}_\ell + p \rightarrow \ell^+ + p + \pi^-, \tag{4.2.8}$$

$$\bar{\nu}_\ell + n \rightarrow \ell^+ + n + \pi^-, \tag{4.2.9}$$

and four NC neutrino (antineutrino) interaction channels:

$$\bar{\nu}_\ell + p \rightarrow \bar{\nu}_\ell + p + \pi^0, \tag{4.2.10}$$

$$\bar{\nu}_\ell + p \rightarrow \bar{\nu}_\ell + n + \pi^+, \tag{4.2.11}$$

$$\bar{\nu}_\ell + n \rightarrow \bar{\nu}_\ell + n + \pi^0, \tag{4.2.12}$$

$$\bar{\nu}_\ell + n \rightarrow \bar{\nu}_\ell + p + \pi^-. \tag{4.2.13}$$

It is worth noting that in case of CC interaction channels antineutrinos produce more neutrons compared to neutrinos. In NEUT, this reaction is simulated by the Rein and Sehgal's model [175] with some modifications and is considered for $W <$ $2\,\mathrm{GeV}/c^2$, where W is the invariant mass of the hadronic final state.

Coherent pion production

Coherent pion production reaction is also considered in NEUT, in which an incoming neutrino interacts with entire an oxygen nucleus producing a pion:

$$\nu_\alpha + {}^{16}O \rightarrow \ell_\alpha + {}^{16}O + \pi. \tag{4.2.14}$$

The outgoing lepton ℓ_α is a charged lepton for CC interaction while it is a neutrino for NC. The charge of the pion is the same charge as the incoming weak-current. Since four momentum transfer to hadronic system is low and the incoming momentum is carried by the pion produced, outgoing lepton and resultant pion tend to be peaked in forward direction. The simulation is performed according to the model by Rein and Sehgal [176].

Deep inelastic scattering

Once hadronic invariant mass W exceeds $1.3\,\mathrm{GeV}/c^2$, NEUT considers deep inelastic scattering (DIS), in which case an incoming neutrino interacts with a constituent quark in the target nucleon, and then hadrons are produced. The nucleon structure function used in NEUT is a model based on the GRV98 [177] for the parton distribution function, with the corrections in the low Q^2 region by Bodek and Yang [178].

Since the DIS interaction has an overlap with the single pion production described earlier for $W < 2\,\mathrm{GeV/c}^2$, only the processes producing more than one pion are considered in this region in order to avoid the overlap. In a region of W above $2\,\mathrm{GeV/c}^2$, production of heavier mesons such as K and η are taken into account and the outgoing hadrons in the final state are modeled based on PYTHIA/JETSET [179].

4.2.1 Hadronic final-state-interactions (FSI)

After primary neutrino interactions described above, the outgoing hadrons produced in the interactions may eventually exit the target nucleus by propagating through nuclear medium. The outgoing hadrons have considerable chance to undergo re-interaction with the nuclear medium, which is known to be hadronic final-state-interactions (FSI) as was mentioned in Section 1.2.1. These hadrons have their kinematics altered, can be absorbed, can produce more hadrons via FSI. Therefore, the resultant particles which just left the target nucleus are often different from the particles produced in the primary neutrino interaction.
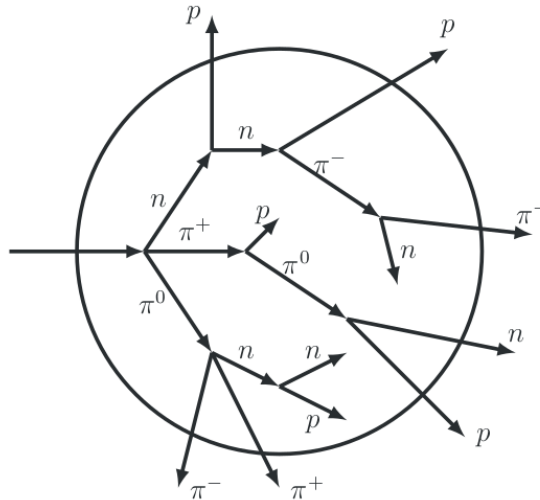
Figure 4.4: A schematic drawing of hadronic final-state-interactions by an intranuclear cascade model. Figure taken from [25].

In most neutrino event MC simulations including NEUT, FSI is simulated within framework of an intranuclear cascade model since modeling of FSI is quit difficult. The concept of intranuclear cascade model was proposed by R. Serber in l947 [180]. Then, a statistical calculation of cascade model based on his idea was made by M. Goldberger [181], and in 1958 most complete computation of the M. Goldberger calculation using MC technique was performed by N. Metropolis *et al*. [182, 183]. Currently widely adopted framework of cascade model was established by H. Bertini [184, 185].

Within cascade model, hadrons are treated as classically, and are linearly propagated through the nucleus from their generation points in finite steps. At each step, interaction probabilities are calculated for all the allowed reactions by taking into

account local nuclear density. Then it is determined whether or not an interaction happens at the step based on the calculations. This hadron transportation continues until hadrons exit the nucleus. Figure 4.4 shows a schematic drawing of intranuclear cascade model.

In the NEUT's cascade model, hadron FSI is simulated as follows. When a ν interaction happens, its interaction position inside the target nucleus is determined based on the Woods-Saxon nuclear density profile [186]. If the primary ν interaction was not DIS, then the hadrons produced in the interaction share the above interaction position as their production positions. In case of DIS, the production positions of hadrons are shifted due to the effect of formation zone. The concept was originally introduced by [187] and applied to hadron production for the first time by [188]. The distance between the primary ν interaction and the hadron production vertices is parametrized by p/μ^2, where p is the momentum of the hadron and μ^2 is a free parameter. The value of μ^2 is estimated based on the results of the SKAT experiment [189]. From the production position, each hadron is transported linearly through the nucleus step-by-step. Each step has a size of $x_{\text{step}} = R_N/100$ [190], where R_N is the size of the nucleus. This size is chosen to be small enough to be able to approximate constant nuclear density. For each step, the probability that a hadron passes a distance x (hereafter called "free path") without any interaction is calculated as:

$$P(\lambda) = e^{-x/\lambda}, \tag{4.2.15}$$

where $\lambda = (\sigma\rho)^{-1}$ is the mean free path and σ is the total interaction cross sections and ρ is the nuclear density. By generating a random number, the free path at a step is sampled as follows:

$$x = -\lambda \ln(\xi), \tag{4.2.16}$$

where ξ is a random number distributed uniformly between 0 and 1. If $x_{\text{step}} > x$, then an interaction happens. Otherwise, the hadron is linearly transported to the next step. When an interaction occurs, the Pauli blocking effect is taken into account, which requires the nucleon after the interaction to have a momentum larger than the Fermi momentum. If the requirement is not satisfied, the interaction is withdrawn, and the hadron moves to the next step. This transportation between steps is repeated until the hadron disappears by an interaction or it escapes from the nucleus.

For pion FSI, the model by Oset *et al* [191] is used for calculating cross sections of elastic scattering, single charge exchange, absorption. In a momentum region above $500\,\text{MeV/c}$, pions have high enough energies to produce multiple hadrons or perform double charge exchange. These reactions are modeled based on the results of fits to the data of pion scattering off from free proton and deuteron compiled

by [192].The model in NEUT has been tuned using various pion-nucleon and pion-nucleus data [26]. Figure 4.5 shows the tuned cross sections calculated by for $\pi^{\pm}$-^{12}C scattering.
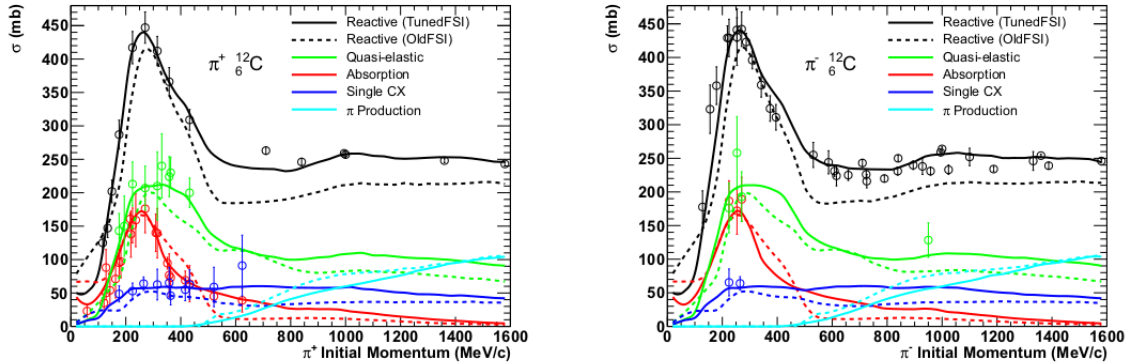
Figure 4.5: A schematic drawing of hadronic final-state-interactions. Figure taken from [26].

For nucleon FSI, the interaction probabilities are calculated based on the free nucleon-nucleon scattering by [193]. Elastic scattering, single pion production, and double pion production are considered. The cross sections are also used in GCALOR [134] by which hadronic interactions in the detector simulation are simulated. Figure 4.6 shows the cross sections used in NEUT and GCALOR.
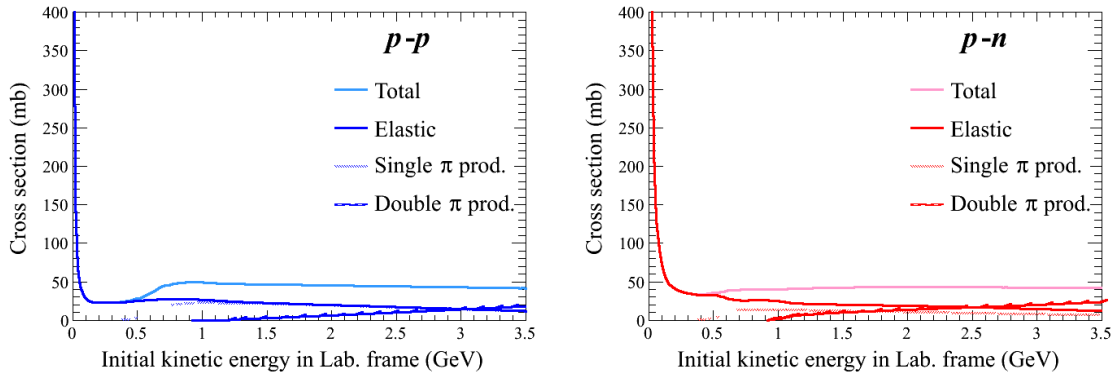
Figure 4.6: Cross sections of free N-N scattering used in NEUT and GCALOR. The left and right plots corresponds to pp scattering and pn scattering, respectively. The cross sections are retrieved from GCALOR.

4.3 Detector simulation

The resultant particles of NEUT, which are leptons and hadrons escaping from the nucleus, are fed into a detector simulation called SKDETSIM in order to simulate the detector response to these particles. SKDETSIM is a GEANT3 [161] based MC simulation and simulates particle interactions and decays including generation and

propagation of Cherenkov photons by considering the geometry of the SK detector. In addition, PMT's response to generated Cherenkov light and resultant response of the electronics are simulated. The detector parameters used in SKDETSIM such as the water property are tuned by using various calibration data described in Section 3.4. Output of SKDETSIM is formatted in the same as real data, and thus same analysis chain can be applied to both real data and output of SKDETSIM.

Hadronic interaction processes are simulated by GCALOR package [134], with an exception for charged pions below $500\,\mathrm{MeV}/c$ for which NEUT is used. GCALOR is a collection of different MC simulation models, which is summarized in Table 4.1. Note that in the energy region associated with the primary analysis of this thesis (also, most of the T2K beam neutrinos), FLUKA is not called in GCALOR.

Table 4.1: Summary of MC simulation models used in GCALOR. The energies are given by kinetic energy.

Criteria	MC simulation package
Hadrons $> 10\,\mathrm{GeV}$	FLUKA [194]
Hadrons $< 10\,\mathrm{GeV}$	HETC [195, 196]
Neutrons $< 20\,\mathrm{MeV}$	MICAP [197]

For nucleons with an energy below $3.5\,\mathrm{GeV}$ and charged pions with an energy below $2.5\,\mathrm{GeV}$, HETC (High Energy Transport Codes) uses NMTC (Nucleon Meson Transport Code) [198] which uses an intranuclear cascade evaporation model based on Bertini [185, 193]. The simulation procedure of the model is divided into two steps: fast cascade and subsequent evaporation of particles. In the first step, a cascade simulation is performed in a similar way described in Section 4.2.1. After the first step, the residual nucleus can be altered from the target nucleus before the cascade process, and can emit particles when deexciting. The evaporation process is handled by EVAP-4 [199] which is based on a MC calculation [200]. In this intranuclear cascade evaporation model, a nuclear density profile is used for both protons and neutrons [184]. It consists of three concentric sphere regions in order to approximate a charge distribution obtained from electron scattering data [201].

For neutron energies below $20\,\mathrm{MeV}$, MICAP (Monte Carlo Ionization Chamber Analysis Package) [202] is adopted. It uses ENDF/B-V (Evaluated Nuclear Data File version B) which consists of neutron scattering cross sections modeled based on experimental data. Various neutron-nucleus reactions are considered by MICAP and are summarized in Figure 4.7. Figure 4.8 shows the macroscopic cross section of water which is used to calculate interaction probability in MICAP. Within MICAP thermalization of neutrons and neutron capture are simulated.

Type of Reaction	final state particles
elastic scatt.	n
(nA,n'A)	n
(nA,2n'A')	2n
(nA,n'αA')	n, α
(nA,2n'αA')	2n, α
(nA,n'pA')	n,p
(nA,n'3αA')	n, 3α
(nA,γA)	γ
(nA,pA')	p
(nA,DA')	D
(nA,TA')	T
(nA,^3HeA')	^3He
(nA,αA')	α
(nA,2αA')	2α
(nA,3αA')	3α
(nA,2pA')	2p
(nA,pαA')	p,α
(nA,T2αA')	T, 2α
(nA,D2αA')	D, 2α
fission	n, p , α

Figure 4.7: Summary of neutron-nucleus reactions considered in MICAP. Figure taken from [27].
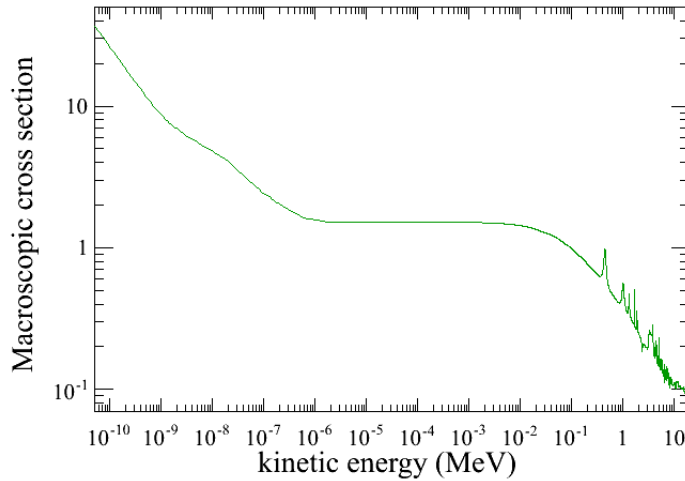
Figure 4.8: The macroscopic cross section for water used in MICAP.

Emission and propagation of Cherenkov photons in water are handled by custom codes. Attenuation of Cherenkov light in water due to absorption, Rayleigh scattering, and Mie scattering are taken into account. Light reflection by PMT, blacksheet, and Tyvek® are also considered. The timing and charge response of the SK PMTs and the subsequent response of electronics are simulated.

4.4 Hybrid neutron MC

As was described in the beginning of this chapter, MC simulation of the far detector mainly consists of two parts: simulation of neutrino interactions in water and detector simulation. The currently used MC sets in T2K (called "14a T2K-SK MC sets") do not include sufficient information in order to perform analyses which use information about neutron tagging. In addition, some neutron productions had not been simulated in SKDETSIM. Therefore, it was modified for the primary analysis of this thesis. As a result, another MC sets (hereafter called "hybrid neutron MC sets") were generated by using the modified SKDETSIM. In the following, modifications made for hybrid neutron MC are described.

For very low energy analysis such as neutron tagging, PMT hits related to low energy random background sources (e.g. radioactive decay products) have non-negligible impacts. However, an accurate simulation of these background sources is extremely difficult. Indeed, they have never been simulated in SKDETSIM. Although they can not be simulated easily, the PMT hits originating from them (hereafter called "noise hits") can be obtained from T2K dummy spill data. Since T2K dummy data is taken with the T2K trigger during T2K beam-off periods, the data contains noise hits produced by all the low energy background sources in the far detector as well as the dark noise of the ID PMTs. Thus, the first modification is to merge noise PMT hits into simulated ones which originate from neutrino interactions. This was done by author [203] and is as follows:

- In SKDETSIM, the energy threshold of the neutron simulation is reduced to 10^{-4} eV, which enables simulating 2.2 MeV γ ray emitted by neutron capture on hydrogen nucleus.

- The record time of PMT hit information is extended up to $+535\,\mu$s from trigger time, because thermal neutron capture has a capture time constant of $\sim200\,\mu$s.

- The dark noises of the ID PMTs are simulated only until $+18\,\mu$s, after which the PMT hits of dummy spill data are merged into the simulated hits which are produced by particles originating from neutrino interaction.

Figure 4.9 shows a schematic diagram describing how noise PMT hits of dummy spill data are added to simulated PMT hits. The $+18\,\mu$s at which noise PMT hits in dummy spill data are started to be merged with simulated hits is chosen due to the fact that PMT hit by PMT's after pulse has not been implemented in SKDETSIM. For the ID PMTs, PMT hits are also produced by their after pulses, which are peaked around $+15\,\mu$s later after primary hits due to neutrino interactions. Since after pulses are not simulated, they may produce additional background events in the neutron tagging only for real data if a time region before $\sim15\,\mu$s is included. In order to avoid such possible background events which can not be modeled by dummy spill data, the value of $+18\,\mu$s is determined.
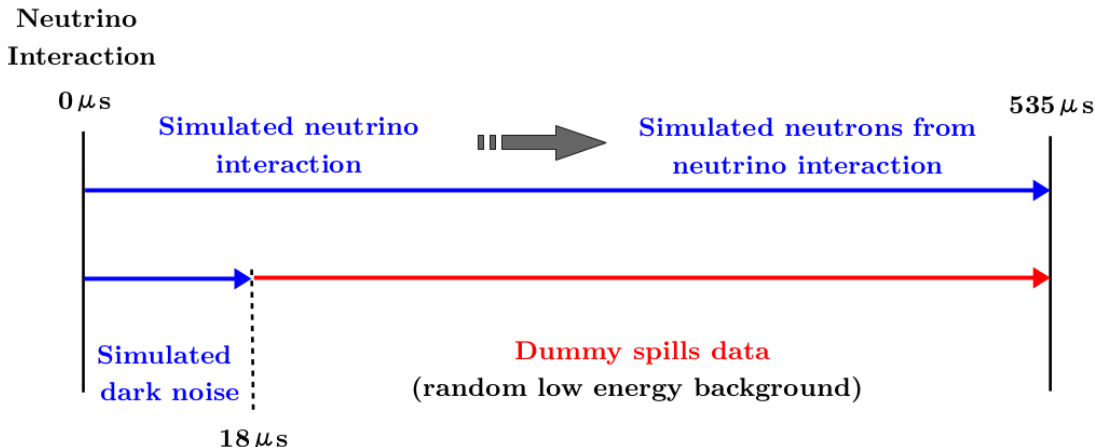
Figure 4.9: A schematic diagram of the procedure that merges noise PMT hits of dummy spill data into simulated PMT hits.

In addition to the above modification, another modification was made in SKDET-SIM. Neutron productions by μ^- and π^- captures on oxygen nucleus had never been simulated although contribution from these captures to total number of neutrons associated with neutrino interactions is not negligible. To implement neutron productions by these captures, Geant4.9.6 is used since these productions are not available in SKDETSIM. Technically `G4MuonMinusCaptureAtRest` and `G4PiMinusAbsorptionAtRest` which are the classes of Geant4.9.6 and are used as the default models, are directly called from SKDETSIM via an interface which connects SKDETSIM with Geant4.9.6. The resultant neutron multiplicity, their energy spectrum, and impact on the analysis samples used in the primary analysis of this thesis are summarized in Appendix A.

4.5 Summary of MC sets

The primary analysis of this thesis uses three hybrid neutron MC sets, each of which consists of simulated events for both FHC and RHC modes. The first set is generated based on NEUT and used as "default MC set" by which MC expectations and neutron tagging efficiency are calculated. For the other two sets, GENIE [11] and NuWro [136] are used as alternative MC ν event generators in order to study dependence of ν event generators on neutron tagging algorithm and compare neutron productions by neutrino interactions and FSI between the three generators. Although ν event generator is different for each MC set, the same detector simulation, SKDETSIM, is used for all the three sets.

The procedure of the MC generations is tricky due to very different energy scale between primary neutrino interactions ($\mathcal{O}(1)\,\mathrm{GeV}$) and γ rays from neutron captures ($\mathcal{O}(10^{-2})\,\mathrm{GeV}$). Since the beginning of the T2K data taking in January 2010, the far detector has been stably running, although there have been several time variations in

74

the detector. For primary neutrino interactions, effects of the detector time variations are negligibly small, whereas these effects can not be ignored for neutron tagging. Therefore, the detector simulation was run twice for each MC set in order to take into account the time variation effects. The first run was done with the same set of the detector parameters (or "generation point") as used for the generation of the 14a T2K-SK MC set (i.e. official T2K MC), which ensures that there is no systematic different in the part of primary neutrino interactions between the hybrid MC and the 14a T2K-SK MC sets. For the second run, different set of detector parameters was used, which were chosen in terms of neutron tagging. The generation point was determined by considering the following two factors. To take into account the time variations, one of the best representative generation point may be the point of a T2K Run where 50% of POT for the primary analysis of this thesis was accumulated. In addition, since the hybrid neutron MC uses dummy spill data to model noise PMT hits for neutron tagging, the limited statistics of dummy spill data needs to be taken into account. The generation point for the second detector simulation was chosen to be the far detector DAQ run#74222 which is in December 2015. Accordingly, the PMT hits of the dummy spill data taken from Nov. 2015 to Feb. 2016 were added to the simulated PMT hits of the second simulation. In case of the first detector simulation, its generation point is in August 2009. More details in the MC productions can be found in [204].

Note that in the analysis of this thesis the results of the first simulation are used for the neutrino event selection described in Section 7.2 and computing the MC expectation for quantities that use reconstructed muon kinematics, whereas the results of the second simulation are used only for the neutron tagging related.

Chapter 5

Data reduction

This chapter describes the data reduction of the T2K beam neutrinos at the SK far detector. The selection of the beam data is described in Section 5.1. Extraction of "events" induced by the T2K beam neutrinos, and the subsequent classification on the extracted events are overviewed in Section 5.2. Then, Section 5.3 describes neutrino event reconstruction. Information about the data taking until 2018 and the data set used for this analysis is summarized in Section 5.4.

5.1 Good spill selection

The reduction processes of the T2K event at the far detector begins with the selection of "good spills" by requiring the following conditions on a spill-by-spill basis. Only good spills are used for physics analyses. The criteria [20] are as follows:

1. **DAQ alive**

   The DAQ of the far detector must be running when taking the beam data.

2. **Bad subrun cut**

   The subrun of a spill collected should not be a bad subrun. A subrun is a unit of the far detector data, which roughly corresponds to one minute long of data taking. Each subrun is determined whether or not the subrun is suitable for physics analyses based on various information regarding the detector status. In order to assign good or bad to a subrun, the same definition used for the SK atmospheric analyses is utilized. Bad subruns are primarily caused by flashing PMTs that emit light from internal corona discharge inside.

3. **Incomplete data/GPS error cut**

   Since the rates of dark noise hits of the ID and OD PMTs are approximately constant for ~1 ms window which is equivalent to a T2K window, the number of hits within the $\pm\,500\,\mu$s of a spill is required to be greater than 4,8000 and 6000, respectively. The cut intends to reject the case where part of the detector is not working properly. These thresholds are

determined based on looking at dummy spill data in which the beam neutrino data are not included. The threshold for the OD hits has been changed from 6000 to 5400 during the Run 1-9 data taking periods mainly due to increase of number of dead-OD PMTs. In addition, the GPS system at the far detector is required to be stable by imposing the condition on the GPS time stamp: $|\text{GPS1} - \text{GPS2} - \text{offset}| < 100\,\text{ns}$.

4. **Special data block cut**

    Information about all the PMT hits is recorded by the DAQ system of the far detector in a unit of 17 μs long data block. The pedestal block which stores the pedestal data for all the channels of the front-end electronics module and TDC rest block which is for resetting some counters in the TDC chips are generated once per 4096 and 65536 blocks, respectively. These special blocks are mandatory for the data taking of the DAQ system, which causes an unavoidable loss of spills. The cut criterion is that a spill does not contain a special data block.

5. **Pre-activity cut**

    The final cut is designed to reject event produced by non-T2K beam neutrinos such as electrons by decays of cosmic-ray muons. The cut therefore require no activities in the 100 μs before the beam arrival timing in order to avoid contamination of such events in the beam window.

Table 5.1 summarizes the good spill selection at the far detector for the Run 1-9 data. The overall inefficiency of the spills during the Run 1-9 data taking periods is ~1% as shown in the table.

Table 5.1: Summary of the good spill selection at the far detector for the Run 1-9 data. Numbers taken from [31].

	Number of spills	Inefficiency
Beam good spills	20,122,743	0 %
(1) DAQ alive	20,085,525	0.18 %
(2) Bad subrun cut	20,039,874	0.23%
(3) Incomplete data/GPS error cut	20,030,596	0.05%
(4) Special data block cut	20,014,244	0.08%
(5) Pre-activity cut	19,915,932	0.49 %
Total SK good spills	19,915,932	1.03%
Total POT ($\times 10^{20}$)	31.2836	-

5.2 FC event selection

As was described in Section 3.3.2, a $\pm\,500\,\mu$s time window surrounding the expected time called "T2K window" are defined for each beam spill. The information about all the PMT hits in a T2K window is stored. Then later "events" induced by the T2K beam neutrinos are extracted and classified. In the following, the selection of the fully-contained (FC) events which is the primary sample of the T2K analyses is described.

5.2.1 Event classification

The software trigger program of the DAQ system is used to extract events contained in a T2K window by searching for clusters of PMT hits. In this program, the variable N_{200} which is number of PMT hits in a 200 ns sliding time window is calculated for the ID and OD PMT hits separately. The trigger thresholds of the ID and OD PMT hits are set to 47 hits, which roughly corresponds to a 5 MeV electron, and 22 hits, respectively. If either the ID's N_{200} or the OD's N_{200} exceeds the thresholds, a trigger is issued. For each issued trigger, the PMT hits within a time window from -5 μs to $< +35\,\mu$s surrounding the trigger time is defined as an event.

All the events extracted from T2K windows are then classified into five types of events: calibration events, OD events, Low Energy (LE) events, flasher events, and FC events. The classification is sequentially performed. Figure 5.1 schematically shows the flow of the classification.
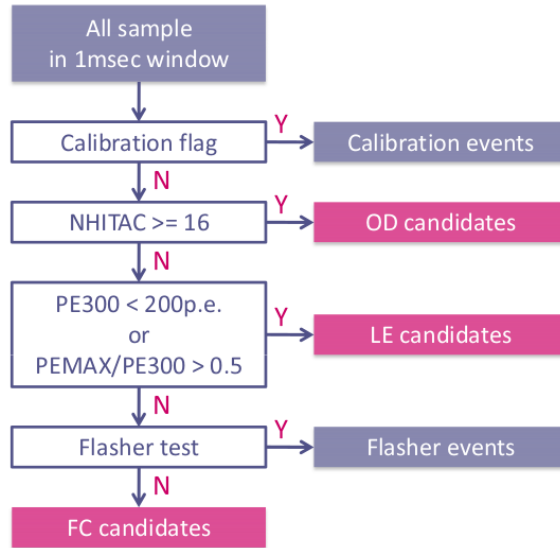
Figure 5.1: A schematic drawing of the flow of the FC event selection. Figure taken from [20].

The flow of the classification is as follows:

1. **Rejection of calibration events**

An event is required not to be a calibration event by checking a flag which identifies calibration events.

2. **OD events classification**

   NHITAC is calculated, where NHITAC is the number of OD PMT hits in the largest hit cluster. If NHITAC > 15, then the event is classified as an OD event.

3. **LE events classification**

   PE300 is computed, where PE300 is the total charge of the ID PMT hits within a 300 ns window. If PE300 < 200 p.e. which roughly corresponds to a 20 MeV electron, then the event is classified as a LE event. In addition, further reduction of LE events which are likely to be caused by radioactive decay products is performed. For such LE events, a very large fraction of PE300 is occupied by a single hit PMT. To detect such events, PEMAX is calculated, where PEMAX is the maximum charge of a PMT hit used for the calculation of PE300. If PEMAX/PE300 > 0.5, then the event is classified as a LE event.

4. **Rejection of flasher events**

   Sudden flashing PMT which emits light from its internal corona discharge can produce an event mimicking a FC event. Events caused by such PMTs called "flasher PMTs" are referred to as "flasher" events. Flasher events tend to have broader distribution of PMT hit timing compared to that of neutrino events. Also, flasher PMT tends to repeatably produce flasher events with similar geometrical pattern of PMT hit charge among them. By using the above two features, flasher events are distinguished from neutrino events.

   The broader feature is parameterized by MIN_{100} which is the minimum number of hits in a sliding 100 ns window from $+300$ ns to $+800$ ns after the trigger timing of the event.
   Flasher events tend to have larger MIN_{100} than that of neutrino events due to its broader feature. If $MIN_{100} > 20$, then the event is classified as a flasher event.

   Geometrical distribution of PMT hit charge is used to construct a statistical test (hereafter called "flasher scan"), and flasher events which are produced by same flasher PMTs are rejected by the test. To this aim, the ID wall is divided into 1450 regions called "patches", each of which contains 6 or up to 9 PMTs. For each patch, the total charge is computed. In addition, a database which consists of atmospheric neutrino data collected at the far detector is used to perform flasher scan. For a tested event, which will be judged as a flasher event or a FC event, the procedure of flasher scan are as follows. (1) A number of scanned events are sampled from the database to form a statistical ensemble; (2) The above total charges are calculated for the test event and all the sampled

events; (3) For each combination of a scanned event and the tested event, a Pearson correlation coefficient r and Kolmogorov-Smirnov distance d are calculated by using the total charges calculated above. Note that if a scanned event is similar to the tested events, then r and d tend to be large and the small, respectively. (4) The highest 10 rs and and smallest 10 ds are picked up, and a likelihood function is constructed. (5) If the likelihood exceeds a threshold, then the tested event is classified as a flasher event.

After this selection, the selected FC events are passed to event reconstruction.

5.3   Event reconstruction

After the FC event selection described above, event reconstruction is performed, in which number of particles contained in a FC event, their particle types, and their kinematics are reconstructed based on information about time and charge of PMT hit. At the far detector, this event reconstruction is done by a maximum likelihood based algorithm, called "fiTQun". The basics of fiTQun was originally developed in the MiNiBooNE experiment [205]. The main feature of fiTQun makes full use of both "unhit" PMTs and "hit" PMTs inside the SK ID (*i.e.* all the ID PMTs). Since fiTQun employs maximum likelihood technique, the event reconstruction is equivalent to find the best particle hypothesis. However, neutron tagging is out of scope of fiTQun, and it is fully separated from fiTQun. The algorithm of the neutron tagging is described in Chapter 6.

The event reconstruction by fiTQun is divided into four steps:

1. Event vertex pre-fitting,

2. PMT hit clustering (finding subevents),

3. Single-ring fit,

4. Multi-ring fit.

In the following, thees steps are briefly described. Details of fiTQun can be found in [28].

Vertex pre-fitting and finding subevents

Since a FC event contains PMT hit information in $\sim 40\,\mu$s, the event reconstruction begins to divide an event into "subevents" by clustering PMT hits in time. For instance, in case of a ν_μ CCQE reaction, a muon is created and produces PMT hits via Cherenkov radiation. Then, the muon eventually decays, and the resultant electron also produce PMT hits after a time scale of $\sim 2\,\mu$s from the creation of the parent muon on average. Therefore, in this case there are well separated two PMT hit clusters in time, each of which forms a subevent.

To define subevents, first the subevent algorithm performs a quick fit to roughly estimate the vertex of a event, which is done by finding the vertex position $\boldsymbol{x}$ and the vertex time t that maximize the following metric, called "goodness":

$$G(\boldsymbol{x}, t) = \sum_{i}^{\text{PMT hits}} \exp\left(-\frac{1}{2}\left(\frac{T_{\text{res}}^i}{\sigma}\right)^2\right),\qquad(5.3.1)$$

where T_{res}^i is residual time defined as $T_{\text{res}}^i = t_i - t - |\boldsymbol{R}_{\text{PMT}}^i - \boldsymbol{x}|/c_n$, t_i is hit time of i-th hit PMT, $\boldsymbol{R}_{\text{PMT}}^i$ is the position of i-th hit PMT, c_n is the group velocity of light in water, and σ is set to $4\,\text{ns}$. Form the above equation, it can be found that maximization of goodness is equivalent to minimize residual time.

After obtaining the vertex position $\hat{\boldsymbol{x}}$ and time $\hat{t}$ which maximize goodness, subevents are searched for. Consider the example of the above ν_μ CC reaction, in which case there are a muon and a decay-electron. For the PMT hits induced by the muon, their residual time may distribute around zero when using $\hat{\boldsymbol{x}}$ and $\hat{t}$. At zeroth-order approximation, it is reasonably assumed that the vertex positions of the second and later subevents are close to the first one. Under the assumption, in this case the residual time of PMT hits induced by the decay-electron can distribute near zero if $\hat{t}$ is changed to a suitable value. Therefore, subevents can appear as large peaks in goodness by scanning goodness with respect to t while keeping $\hat{\boldsymbol{x}}$. Figure 5.2 shows an example of the scanned goodness with respect to t for an event which contains a muon and a decay-electron. As shown in the figure, two clear peaks can be found, which corresponds to two subevents.

Since the number of subevents is a good proxy for the number of decay-electrons in an event, the number of decay-electrons is computed by using the number of subevents. The number of decay-electrons calculated in this way is used to make the analysis samples of the primary analysis in this thesis.
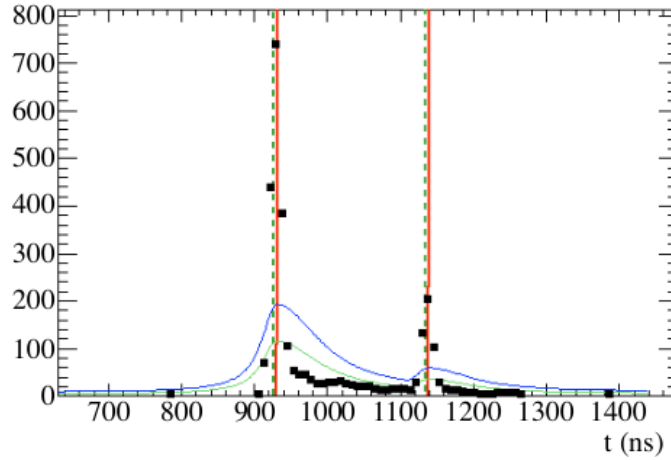
Figure 5.2: The goodness $G(\boldsymbol{x}, t)$ as a function of t for a MC event consisting a primary muon and a decay-electron (black dots). The vertical broken lines represent the true particle creation time. The orange solid lines denote the peak time of the subevents. The blue and green curves represent the threshold used for selecting subevent peaks. Figure taken from [28].

Sing-ring and Multi-ring fits

Once an event is divided into subevents, next process is applied to each subevent. Since fiTQun employs a maximum likelihood algorithm to reconstruct particles contained in an event, for each subevent the following likelihood function given a particle hypothesis is constructed:

$$\mathcal{L}(\boldsymbol{x}) = \prod_i^{\text{unhit}} P_i(\text{unhit}|\mathbf{x}) \prod_j^{\text{hit}} \{(1 - P_i(\text{unhit}|\mathbf{x}))\} f_q(q_j|\mathbf{x}) f_t(t_j|\mathbf{x}), \qquad (5.3.2)$$

where $\mathbf{x}$ parametrizes a hypothesis, which includes particle type, vertex, direction, and momentum. The likelihood function defined in the above equation mainly consists of two different kinds of PMTs: "unhit PMT" and "hit PMT". Unhit PMTs are PMTs that did not have a real hit, whereas hit PMTs are PMTs which did have a hit. In the above equation, the index i and j run over unhit PMTs and hit PMTs, respectively. The unhit probability $P(\text{unhit}|\boldsymbol{x})$ that is the probability not to make a hit for a given hypothesis $\boldsymbol{x}$ is calculated for each individual PMT. For unhit PMTs, only the unhit probability is considered. On the one hand, for hit PMTs, in addition to the hit probability $P(\text{unhit}|\boldsymbol{x})$ which can be computed from the unhit probability, probability for observed timing t and charge q are considered. The charge likelihood $f_q(q_j|\boldsymbol{x})$ is the probability density for observing q_j at j-th PMT for a given hypothesis $\boldsymbol{x}$. Similarly, the timing likelihood $f_t(t_j|\boldsymbol{x})$ is the probability density for observing a hit by j-th PMT at t_j for a given hypothesis.

It may be worth explaining how fiTQun gains the ability that enables performing particle identification. The presence of $f_q(q_j|\boldsymbol{x})$ in the above equation means that the likelihood function takes into account the charge pattern of a subevent in the SK tank. To construct $f_q(q_j|\boldsymbol{x})$, predicted charge is computed for each PMT, which

82

consists of the direct light due to Cherenkov radiation and the indirect light from light scattering in water and light reflection by the ID wall and the ID PMT surfaces. The prediction of the direct light strongly depends on given hypothesis, and uses Cherenkov emission profile which describes the average number of Cherenkov photons emitted per unit track length per unit solid angle by a particle with an initial momentum. Figure 5.3 shows the Cherenkov emission profile for an electron and a muon. As shown in the figure, electron produces broader angular distribution than that of muon, which is caused by the fact that electrons tend to undergo more multiple electromagnetic scattering compared to muons. Therefore fiTQun can perform a particle identification with an excellent performance by exploiting difference in emission of Cherenkov photons among different particle types.
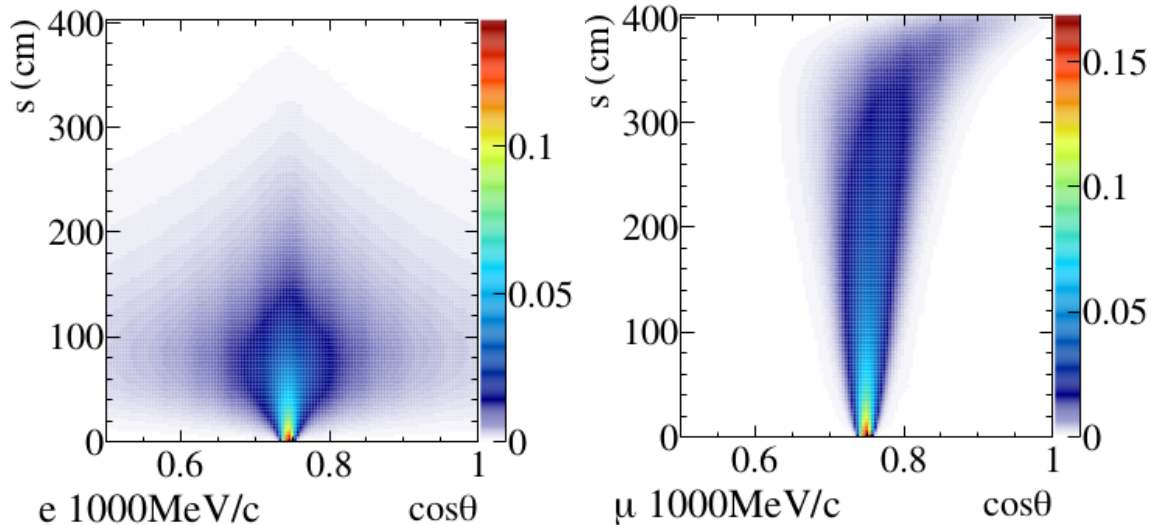
Figure 5.3: Cherenkov emission profile for electron (left) and muon (right) with initial momenta of $1000\,\mathrm{MeV}/c$. The vertical axes represent the distance traveled from the initial position of the particle. The horizontal axes show the cosine of the angle between the particle direction and the photon emission direction. Figure taken from [28].

The maximization of the likelihood function begins with "single-ring fit" which considers a particle track. The current single-ring fit supports three different particle hypotheses: electron, muon, and charged pion. For each particle hypothesis, the likelihood function is maximized to obtain the best estimates of parameters $\mathbf{x}$ describing the particle track. In practice, the maximization is performed by minimizing $-\ln\mathcal{L}$. Once the best parameters are obtained for all the single-ring hypotheses, the particle type is determined by the minimized $-\ln\mathcal{L}$.

For instance, the particle identification (PID) between electron and muon is performed based on the likelihood ratio $\ln(\mathcal{L}_e/\mathcal{L}_\mu)$, where $\mathcal{L}_e$ and $\mathcal{L}_\mu$ are the maximized likelihood function with respect to single-ring electron and muon hypotheses, respectively. Figure 5.4 shows distribution of $\ln(\mathcal{L}_e/\mathcal{L}_\mu)$ for electron events and muon events. As shown in the figure, the likelihood ratio is well separated around at zero, but there is a clear reconstructed momentum dependence. Therefore, in this case

PID is practically performed as follows:

$$
\text{PID} =
\begin{cases}
e-\text{like} & \text{if } \ln(\mathcal{L}_e/\mathcal{L}_\mu) > 0.2 \times p_{1\text{R}-e} \; [\text{MeV}/c] \\
\\
\mu-\text{like} & \text{otherwise}
\end{cases}
, \qquad (5.3.3)
$$

where $p_{1\text{R}-e}$ is the reconstructed momentum under single-ring electron hypothesis. In a similar way, other PID such as μ v.s. charged pion is performed.
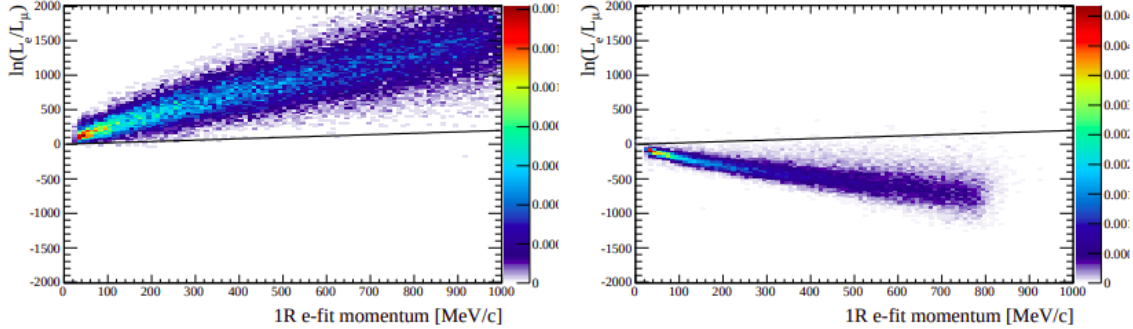
Figure 5.4: Two-dimensional distribution of single-ring $\ln(\mathcal{L}_e/\mathcal{L}_\mu)$ and reconstructed momentum under electron hypothesis for electrons (left) and muons (right). The distributions are made from particle gun MC events simulated by SKDETSIM. The solid lines indicate the cut criterion for single-ring electron and muon separation. Figure taken from [29].

Since in the energies of the T2K beam neutrinos, a primary ν-nucleon interaction often results in production of more than one visible charged particles which radiate Cherenkov photons. Therefore, after the single-ring fits, fiTQun moves to trying to find additional particle tracks by performing the "Mluti-ring" fit in which event hypothesis consisting of more than 1 particle track is considered.

Among the Multi-ring fits, a dedicated fit is performed for π^0. π^0 almost always decays into two γ rays, and these γ rays produce electromagnetic shower via a pair production of e^- and e^+ after they traveled some distance. Therefore, π^0 is observed as the two electromagnetic shower like tracks which originate from the decay vertex of the π^0. As a consequence, in π^0 hypothesis common vertex position and time are used for the two tracks.

Except for π^0 fit, a generic Multi-ring fit is performed only for the first subvent. The Multi-ring fit begins with two-ring hypotheses, and increase the number of particle tracks (or Cherenkov rings) one-by-one. During the fit, the two hypotheses, electron-ring hypothesis and "upstream-track π^+" hypothesis, are considered. The first one treats Cherenkov ring produced by electron or γ ray (i.e. "shower-like"), whereas that of charged pion or muon (i.e. "non-shower-like") is fitted by the other one.

Figure 5.5 shows the flow of the generic Multi-ring fit for an example in which case the best single-ring hypothesis is electron's one. As shown in the figure, the

Multi-ring fit tries all the possible combinations of the two hypotheses for a given number of particle tracks. However, the number of tracks considered is increased by one-by-one. In this case, first, an electron ring or a π^+ ring is added, and the best two-ring hypothesis is obtained. If the likelihood ratio between the $-\ln\mathcal{L}$ of the best two-ring hypothesis and that of the best single-ring hypothesis exceeds a certain threshold, the two-ring hypothesis is accepted, and another particle track is added in order to move to three-ring hypothesis. By following similar procedure, the algorithm continues to add a ring one-by-one up to six rings. Since this Multi-ring fit often contains fake rings, each ring found in the above procedure is refitted to improve the fit result and obtain the final result.
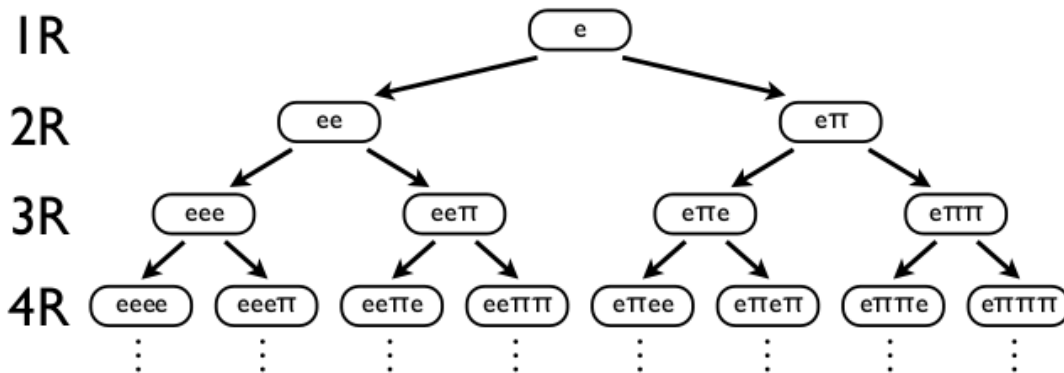
Figure 5.5: A schematic drawing of the flow for performing the Multi-ring fit for the case where the best first-ring fit is electron's one. Figure taken from [28].

Basic performance

As will be mentioned in Section 7.2, the analysis samples used in the primary analysis of this thesis, called "1Rν_μ samples", are based on single-ring μ-like events and contain a high fraction of CCQE interaction described in Equation 1.2.2. Therefore, it may be interesting to see the performance of the single-ring fit using muons produced by CCQE interaction. Figure 5.6 summarizes the resolutions of vertex position, momentum, and direction and misidentification probability that a true single-ring muon is misidentified as a single-ring electron. For the vertex resolution, first distribution of distance between true and reconstructed vertices is made. Then, the 68 percentile of the distribution is defined as the vertex distribution. Similarly, the direction resolution is estimated from distribution of angle between true and reconstructed directions. In case of the momentum resolution, first distribution of fractional variation from true momentum is made, and is fitted by a Gaussian. The fitted σ of the Gaussian is regarded as the momentum resolution. Misidentifiaction probability is estimated by following the criterion of electron-muon separation in Equation 5.3.3. Although the performance is dependent on the true momentum, it is good enough to study lepton kinematics dependence on the neutron production. Indeed, the primary analysis of this thesis measures such kinematics dependence in Chapter 8.
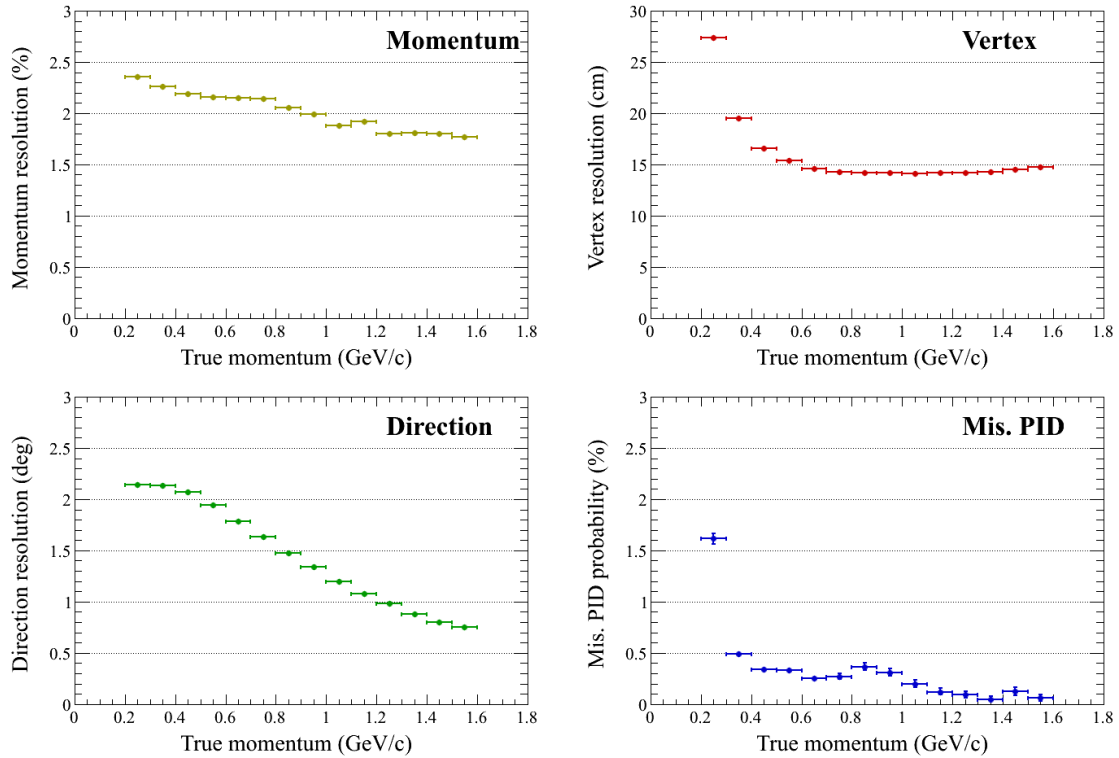
Figure 5.6: Performance of the fiTQun single-ring fit. Top left, top right, bottom left, and bottom right figures show momentum resolution, vertex resolution, direction resolution, and misidentification probability as a function of true momentum. The definitions of these values are described in text.

5.4 Data reduction summary

This section summarizes the T2K data used in this thesis.

T2K started physics data taking in January 2010 and has finished the nine data taking periods: Run 1-9. The Run 9 period ended on May 2018. Although the Run 10 period has started on November 2019, it has not been finished yet. Therefore, the primary analysis in this thesis uses all the data collected until 2018 which correspond to 14.938×10^{20} POT for FHC mode and 16.346×10^{20} POT for RHC mode. Table 5.2 summarize the Run 1-9 accumulated POT.

Table 5.2: Accumulated POT of each Run for the Run 1-9 data taking. FHC and RHC correspond to the ν- and $\bar{\nu}$-modes beam operation, respectively. The numbers are derived from Table 1 in [31].

	FHC POT ($\times 10^{19}$)	RHC POT ($\times 10^{19}$)
Run1	3.26	-
Run2	11.22	-
Run3	15.99	-
Run4	35.96	-
Run5	2.44	5.12
Run6	1.92	35.46
Run7	4.84	34.98
Run8	71.69	-
Run9	2.04	87.88
Total	149.38	163.46

During the data taking periods, the quality of the beam neutrinos was continuously monitored. Figure 5.7 shows the stability of the neutrino beam monitored by the INGRID and MUMON detectors over time. As shown in the figure, the measured beam direction is better than the requirement of 0.4 mrad. In addition to the stable operation in the near detector side, the far detector also operated stably, which resulted in a small constant loss of the beam spills. Figure 5.8 shows the accumulated POT at the far detector as a function of date overlaid with the far detector's inefficiency of the beam spills.
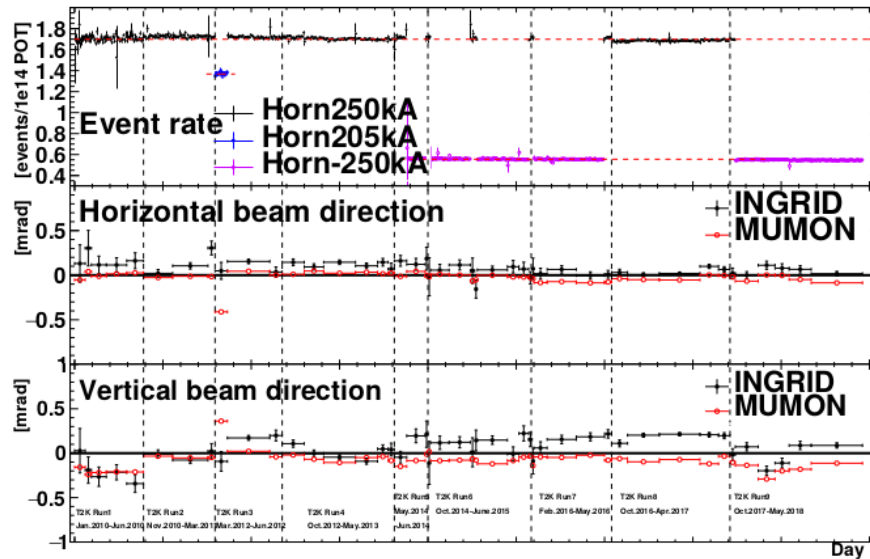
Figure 5.7: Stability of the event rate measured by INGRID (top) and the beam directions measured by the INGRID and MUMON (middle and bottom). Figure taken from [30].
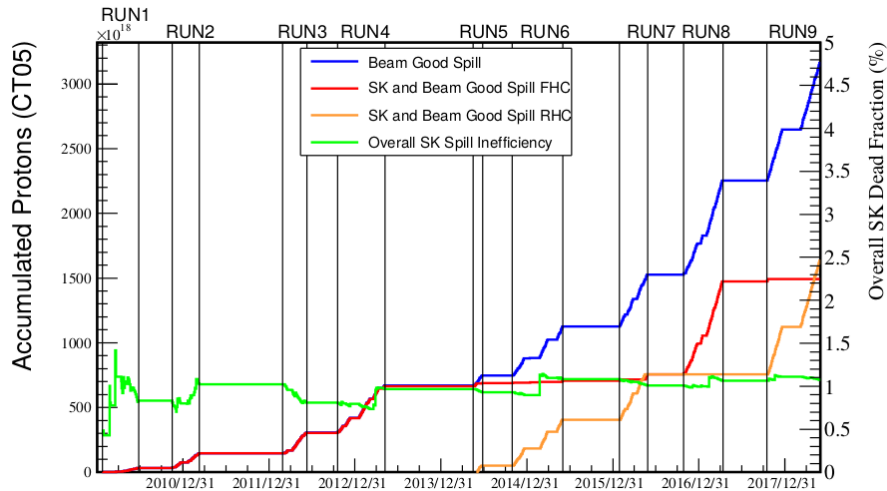
Figure 5.8: Accumulated POT as a function of date. The red and orange lines correspond to the FHC Run 1-9 POT and the RHC Run 5-9 POT, respectively. The green line represents the inefficiency of beam good spill at the far detector and its scale is shown by the right side of this figure. Figure taken from [31].

After the good spill selection and the FC event selection which are described in Section 5.1 and Section 5.2, respectively, there are 1252 (582) FC events for FHC (RHC) mode. Figure 5.9 shows the cumulative number of FC events as function of accumulated POT in comparison to an expectation of constant event rate which is derived from the observed FC events and the accumulated POT. As shown in the figure, the cumulative FC events increases linearly as the accumulated POT increases. Contamination of FC events induced by atmospheric neutrinos is also evaluated by using the atmospheric neutrino data collected at the far detector. For the Run 1-9 data taking periods, the number of FC events induced by the atmospheric neutrinos is expected to be 0.512 [31].

Since the event extraction at the far detector is performed based on the expected beam arrival time, the FC events should hold the timing structure of beam spill which has eight bunches with an interval of $581\,\mathrm{ns}$ between bunches. Therefore, the time difference from the expected beam arrival timing, ΔT_0, is studied. To calculate ΔT_0, two factors, which affect ΔT_0 on an event-by-event basis, are taken into account, one of which is difference in neutrino flight length from the beam target at J-PARC to ν interaction vertex position among the FC events. Due to the large detector volume of the far detector, difference in the flight length results in a time difference of $\mathcal{O}(10\mathrm{ns})$ depending on ν interaction vertex position in the detector. In order to consider this effect, a plane which passes through the detector center and is perpendicular to the beam direction is adopted as a virtual target of the far detector, and then the time-of-flight of incoming neutrino from this plane to reconstructed ν vertex is considered. Also, time delay due to light propagation in water depends on emission position in the detector. Therefore, difference in light propagation in water is also taken into account. In addition to these two effects, the constant time delay

due to the DAQ system described in Section 3.3.2 is considered. Figure 5.10 shows the ΔT_0 distribution of the Run 1-9 FC events with the above timing corrections. As shown in the figure, the eight bunches structure can be clearly seen.
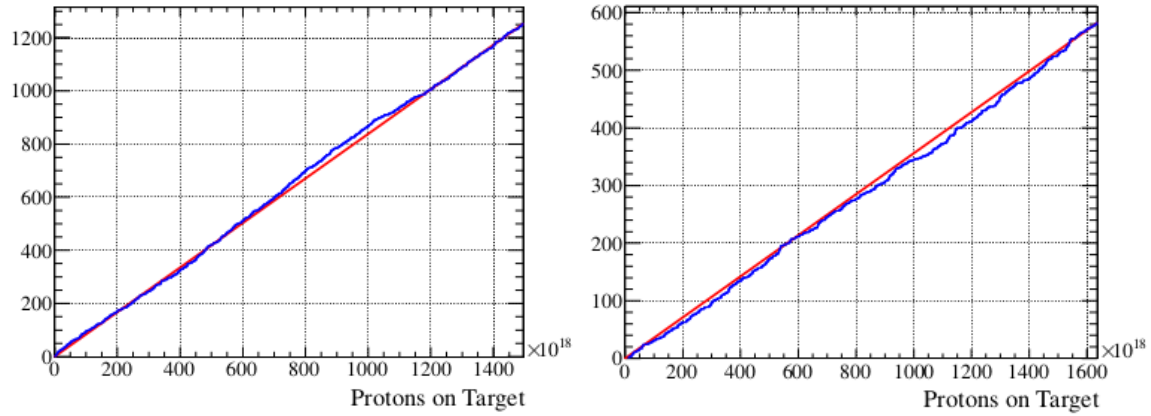
Figure 5.9: Cumulative number of FC events as a function of accumulated POT at the far detector for FHC mode (left) and RHC mode (right). The blue lines correspond to the Run 1-9 data. The red lines represent expectation of constant FC event rates which are obtained from the observed FC events and the accumulated POT. Figure taken from [31].
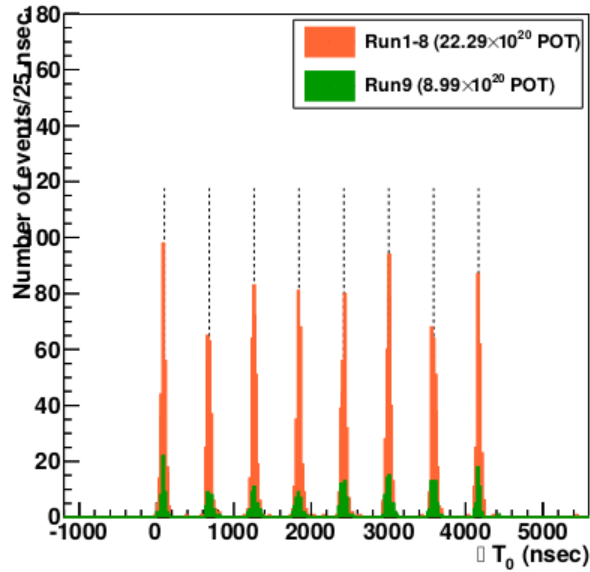
Figure 5.10: Distribution of the time difference from the expected arrival time at the far detector, ΔT_0, for the Run 1-9 FC events. The vertical dashed lines represent fitted bunch center positions. Figure taken from [31].

Chapter 6

Neutron tagging

Since the primary analysis of this thesis aims to measure neutrons, the algorithm used for tagging neutrons needs to be independent on the modeling of neutron production as much as possible. To achieve this, a neutron tagging algorithm was developed for the primary analysis, which consists of two selection stages: the primary neutron candidate selection and the neutral network (NN) classification. In the following, first the definitions of neutron tagging efficiency and accidental background event rate which characterize the performance of the algorithm are given in Section 6.1. Then, Section 6.2 and Section 6.3 detail the primary selection and the NN classification, respectively. A validation of the developed algorithm using a low-energy neutron calibration data is described in Section 6.4. Section 6.5 ontlines the correction to the algorithm due to the SK detector time variation effects.

In a water target, neutrons associated with neutrino interactions are quickly thermalized after they are produced, and are eventually captured by a hydrogen nucleus or an oxygen nucleus. The cross sections of thermal neutron captures for hydrogen and oxygen nuclei are 0.33 barns [206] and 0.17×10^{-3} barns [207], respectively. Thus, almost all of the thermal neutrons are captured by hydrogen nucleus.

A neutron capture on hydrogen nucleus results in the production of a single 2.2 MeV γ ray which is equal to the binding energy of a deuteron as follows:

$$n + \mathrm{H} \rightarrow d + \gamma \ (2.2 \, \mathrm{MeV}). \tag{6.0.1}$$

In SK, the 2.2 MeV γ rays produce Compton scattered electrons which emit Cherenkov photons. By detecting these phtons as PMT hits, neutrons can be tagged. The neutron tagging is therefore equivalent to identify the γ rays.

6.1 Definitions of tagging efficiency and background event rate

The neutron tagging algorithm is applied to ν events on an event-by-event basis. For a ν event, the algorithm searches for neutrons from $+18 \, \mu$s to $+513 \, \mu$s after ν inter-

action. Since the neutron caputre time constant is $\sim 200\,\mu$s, about 92% of neutrons are therefore contained in the search region.

The algorithm finds neutron candidates which consist of true neutron events and accidental background events. The true neutron events are produced by the Cherenkov photons originating from the 2.2 MeV γ rays, whereas the background events are caused by accidental coincidences of noise PMT hits. Since the noise hits stem from random background sources such as PMT's dark noise and radioactive decay products, the background events do not depend on detail of primary neutrino interaction.

The performance of the algorithm are characterized by "neutron tagging efficiency" and "background event rate" defined as follows:

$$\text{tagging efficiency} = \frac{\text{Selected Candidates which are true neutrons}}{\text{All neutron captures}} \qquad (6.1.1)$$

$$\text{background rate} = \frac{\text{Selected Candidates which are backgrounds}}{\text{Total neutrino events}} \qquad (6.1.2)$$

For the tagging efficiency, the denominator includes the neutron captures which happen outside the SK ID as well as the neutron capture occurred inside ID. Therefore neutrons escaping from ID need to be considered and will be discussed in Section 7.2. In addition, neutron captures occurred outside the search window are included into the denominator. The background event rate does not depend on the detail of ν interactions such as the kinematics of the outgoing lepton. Once the rate is estimated, we can subtract the background events of the neutron tagging in the real data by using the number of observed ν events. Such subtraction will be done to measure neutrons in Chapter 8.4.

6.2 Initial selection

In the first stage of the algorithm (hereafter called "primary selection"), neutron candidates are searched. The primary selection is a very simple selection based on number of PMT hits.
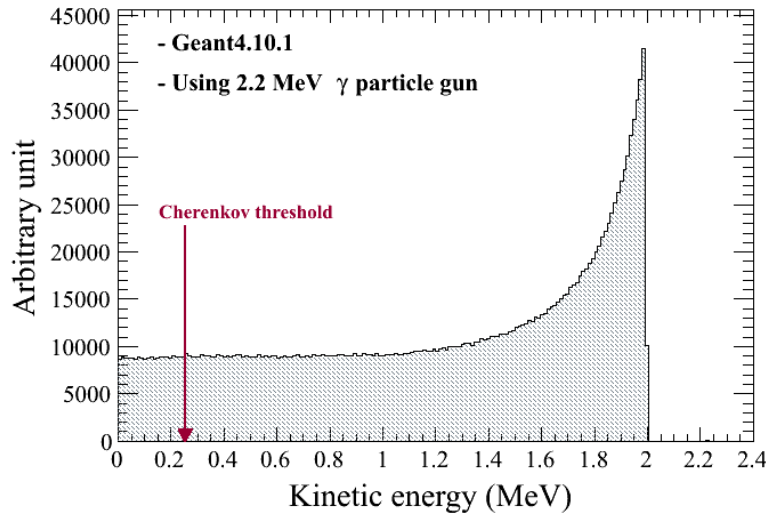
Figure 6.1: Distribution of kinetic energies for electrons which are produced by the Compton scattering of 2.2 MeV γ rays

Once a neutron capture on hydrogen nucleus happens, a single 2.2 MeV γ ray is emitted by the reaction 6.0.1. Then, the γ ray produces one or more recoil electrons via Compton scattering. However, number of PMT hits produced by these Compton scattered electrons is extremely small since their kinetic energies are very low as shown in Figure 6.1. A typical MC ν event display for the PMT hits, which are used in this neutron tagging algorithm, is shown by Figure 6.2. From this figure, it can be seen that indeed true 2.2 MeV γ rays produces extremely small PMT hits (red colored dots).
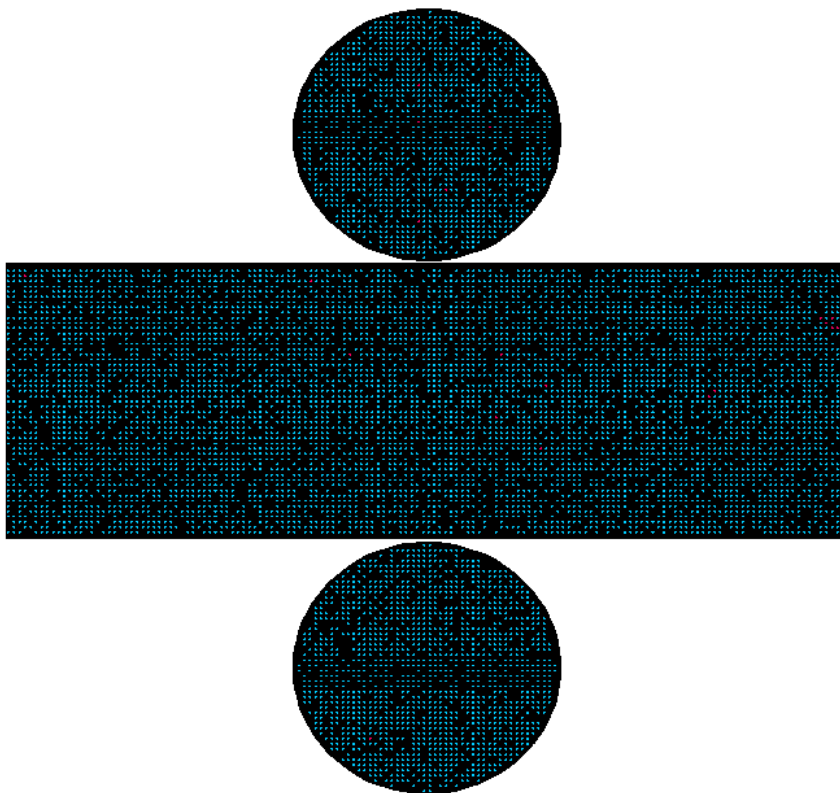
Figure 6.2: Example of event display of a ν event (MC) which have two true neutron captures on hydrogen. The PMT hits after $18\,\mu$s from the primary event trigger are shown. The red and blue dots correspond to PMT being hit by true 2.2 MeV γ ray and noise.

In order to extract the signal of 2.2 MeV γ ray, the primary selection performs a very simple selection based on number of PMT hits by clustering PMT hits in time. Figure 6.3 shows a typical distribution of PMT hit timing of a ν event. As shown in the figure, the PMT hits related to these γ rays tend to be buried under noise PMT hits. Thus, the primary selection begins with a reduction of the noise hits, which utilizes a characteristic of the noise hits. From a recent study of the PMT hits in the dummy spill data, the noise hits have a large time correlated component as shown in Figure 6.4. This component has successive hits probably due to scintillation light emitted from the ID PMT's glass. The correlated component can be removed by imposing a cut on time difference between hits. The cut is applied to each individual PMT as follows:

- Sort hits in increasing order by its recorded time,

- Compute time interval between two successive hits sequentially from the first hit,
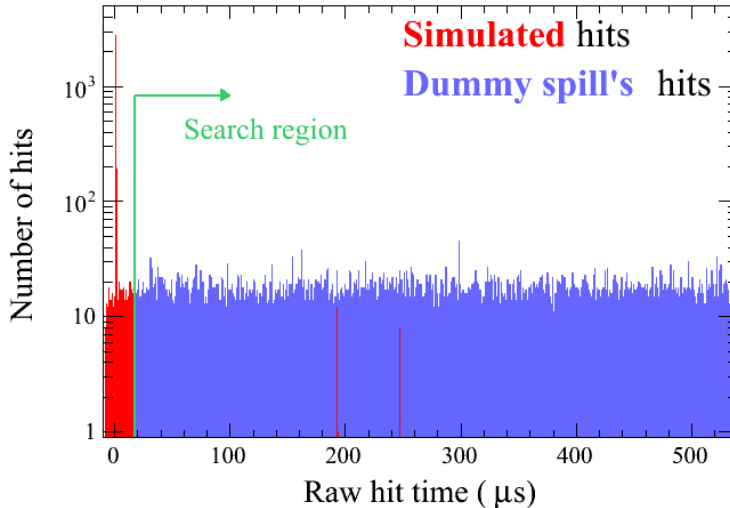
Figure 6.3: Example of raw PMT hit time distribution of a ν event (MC) which has two true neutron captures on hydrogen nucleus. The red and blue correspond the PMT hits simulated in MC and extracted from dummy spill data, respectively. In the red histogram, spikes around $+190\,\mu$s and $+250\,\mu$s are due the two neutron captures.

- If time difference is shorter than $3\,\mu$s, then the two hits used for the calculation of the time difference are identified as the time correlated hits, and thus both hits are removed.

The width of $3\,\mu$s was determined empirically, because this cut removes the hits originating from $2.2\,$MeV γ rays as well as noise hits. In the primary selection, this cut results in about 60% reduction of background events while keeping $\sim$90% of $2.2\,$MeV γ events compared to the case of the absence of this cut. After this noise hits reduction, the primary selection moves to the next step, in which clusters of PMT hits in time are searched for.

As a Compton scattered electron produced by $2.2\,$MeV γ ray can be treated as a point source of Cherenkov photons, PMT hits associated with the γ ray are ideally well clustered in time. However this is not the case in practice, because distance of light traveled from the emission point to hit PMT position is different among these hits. In order to make these hits clustered in time, subtraction of time-of-flight (TOF) need to be done for each individual hit. Although the TOF calculation from neutron capture position is an ideal way for this purpose, in reality this is impossible, because the capture position is unknown. The TOF is computed from ν interaction vertex reconstructed by fiTQun which was mentioned in Section 5.3. As shown in Figure 6.5, most of the neutrons are captured within $2\,$m away from the ν interaction vertex. In addition, the vertex resolution of fiTQun is good enough in comparison to the $2\,$m scale as was shown in Figure 5.6. The use of the fiTQun vertex as an alternative of neutron capture vertex is therefore a good approximation.

94
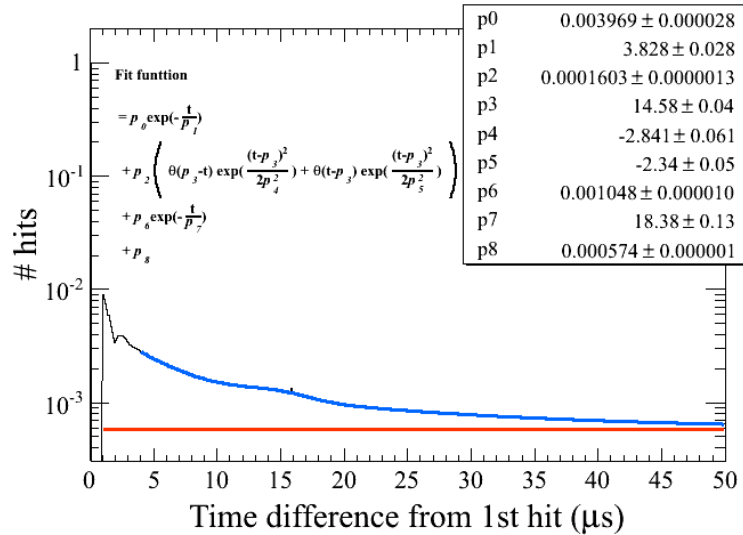
Figure 6.4: Distribution of time difference from the first hit (μs) for dummy spill data which were taken in the beam off period between the Run 6 and Run 7. For each individual PMT, the time differences are computed, but are filled into this histogram. The cyan solid curve is the best result of a χ^2 fit of the distribution to a function consisting of two exponential + an asymmetric gaussian + a constant functions. The orange dashed line shows the fitted constant function.
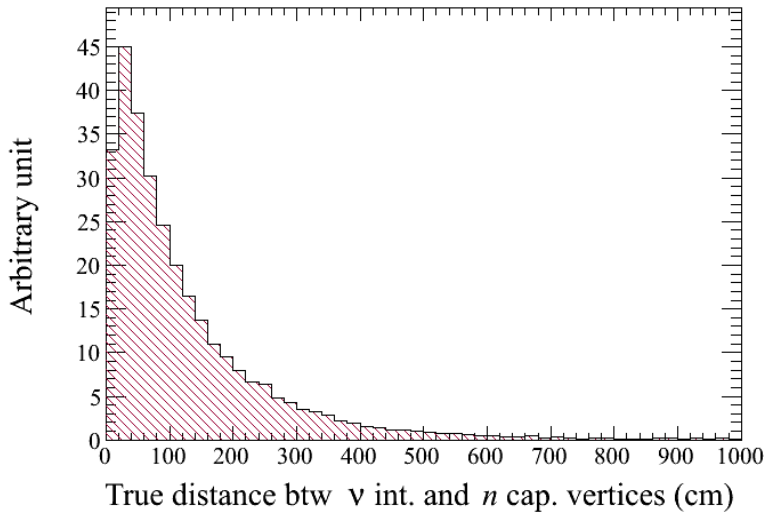
Figure 6.5: Distribution of true distance from ν interaction vertex to neutron capture vertex.

After subtracting TOF from all PMT hits by using reconstructed ν interaction vertex, the TOF subtracted hits are sorted in increasing order by the residual time. Then, number of PMT hits in a 10 ns sliding timing window (hereafter called "$N10_{\mathrm{pvx}}$") is computed as schematically shown in Figure 6.6. Also, the capture time t_0 of the cluster is calculated as the time of the first hit in the $N10_{\mathrm{pvx}}$ hits. A

95
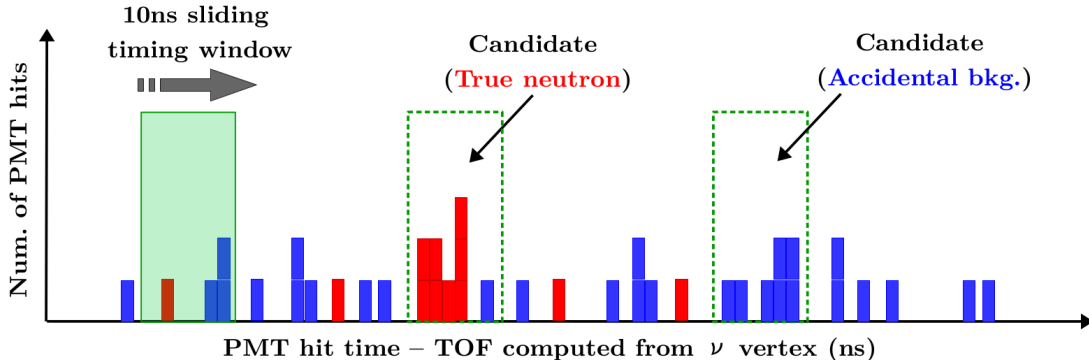
Figure 6.6: A schematic drawing of the calculation of PMT hit clusters using a 10 ns sliding timing window.

$N10_{\mathrm{pvx}}$ cluster is selected as a neutron candidate if it passes the following criteria:

- $N10_{pvx} \leq 50$,

- $N200 \leq 200$,

- Time difference from previous candidate's $t0 \geq 20$ ns,

- $N10_{pvx} \geq 7$,

where $N200$ is the number of PMT hits in the 200 ns surrounding t_0. The first two cuts intend to remove high energy activities such as decay electrons from cosmic ray muons. The third one is used in order to avoid double counting of a 2.2 MeV γ ray (*i.e.* true neutron). The performance of the primary selection is dominantly determined by the last cut.

To evaluate the performance of the primary selection, for MC events, each neutron candidate is judged whether it is a true neutron or not based on MC truth information about true neuron capture time t_{true} [203]. If $|t_0 - t_{true}| < 100$ ns, then the candidate is regarded as a true neutron. Otherwise, it is identified as a background event.

Figure 6.7 shows neutron tagging efficiency and background event rate as a function of lower threshold on $N10_{\mathrm{pvx}}$. Lowering the threshold makes the efficiency higher linearly, whereas the background rate increases exponentially at the same time as shown in Figure 6.8. Although almost all the background events selected in the primary selection will be rejected in the NN classification, too many background events in the primary selection result in a large amount of contamination in true 2.2 MeV γ events, which causes a large contamination of the background events in the observed neutrons. In addition, neutron candidates with small $N10_{\mathrm{pvx}}$ hits do not have strong enough discrimination power between 2.2 MeV γ and background events in the NN classification. The lower threshold of the last cut was therefore chosen to be 7 by considering the above two factors. With this threshold, a ν event has ∼3 background

events after the primary selection, which can be seen in the left panel of Figure 6.8.
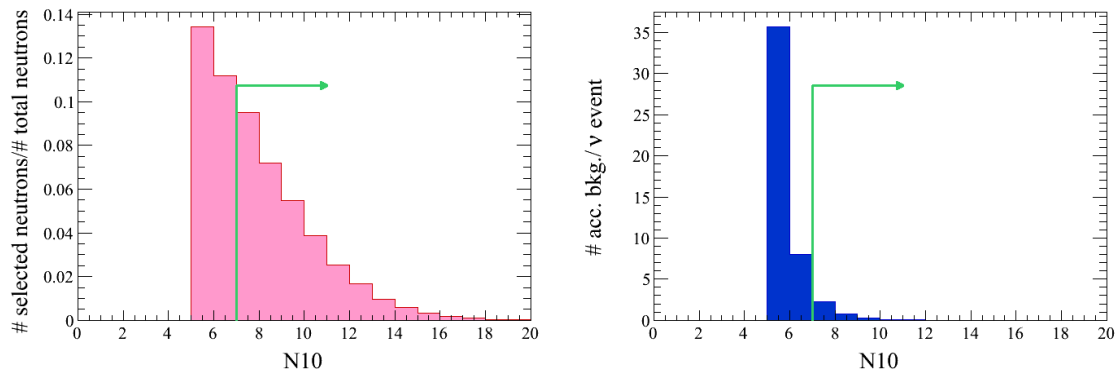
Figure 6.7: Distribution of $N10_{\text{pvx}}$ for the true neutron events (left) and backgrounds events (right), respectively. The green arrows show the lower cut position of $N10_{\text{pvx}}$.
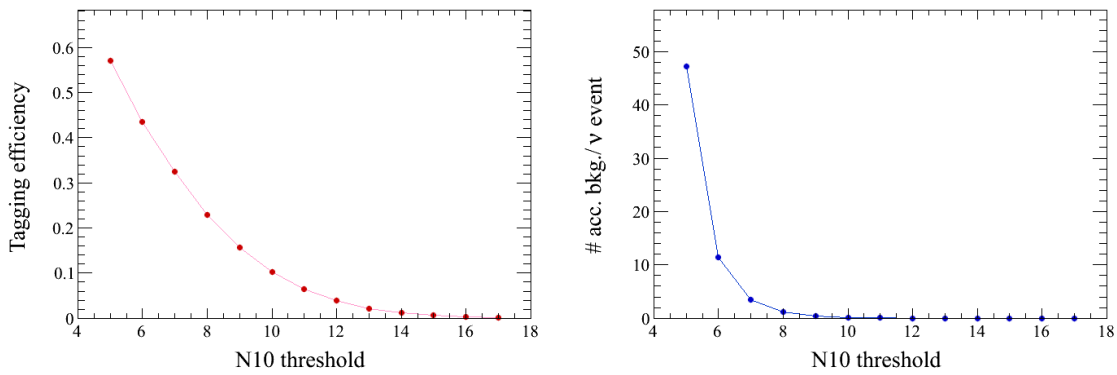
Figure 6.8: Neutron tagging efficiency as a function of $N10_{\text{pvx}}$ threshold (left) and number of accidental background events per ν event as a function of $N10_{\text{pvx}}$ threshold (right). Note that the threshold used for this analysis is $N10_{\text{pvx}} = 7$.

6.3 Neural network classification
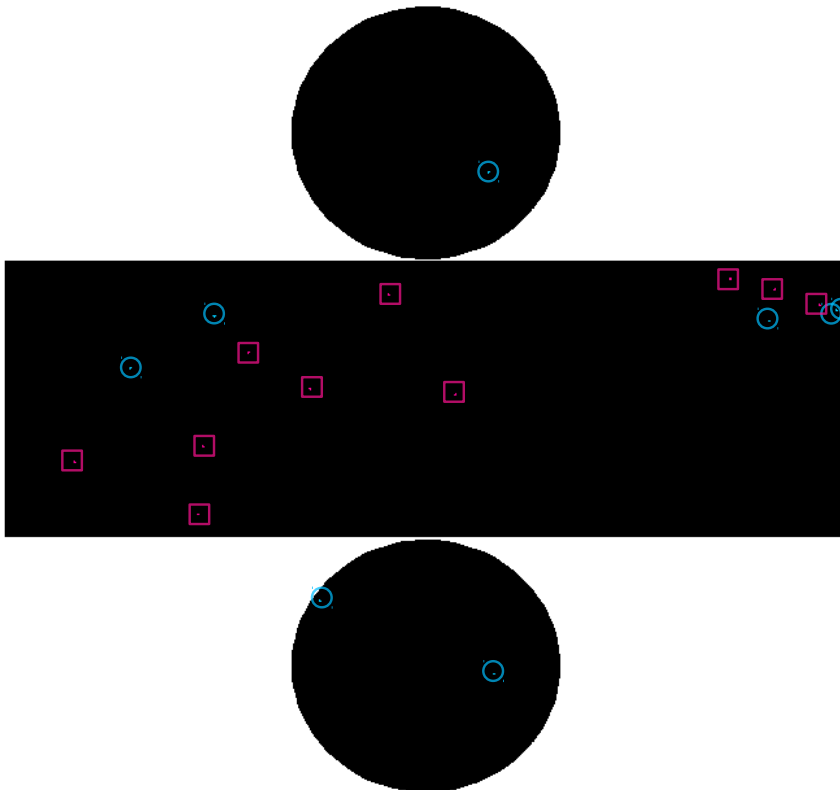
Figure 6.9: Example of typical PMT hits of a signal MC event and a background MC event. The signal (background) event has 10 (8) PMT hits and a NN output value of 0.9906 (0.0007). The hits of signal event (background event are enclosed by pink hollow squares (cyan hollow circles).

After the primary selection, there is still a large contamination of background events in true neutron events. Thus, these background events need to be efficiently removed while keeping true neutron events as much as possible. Since there is no visible difference between signal events and background events as shown in Figure 6.9, such efficient reduction of background events is achieved by employing an artificial neural network (NN) technique. The second selection of the neutron tagging algorithm is therefore the classification of the candidates selected in the primary selection by a NN.

In this classification, a set of 14 feature variables are fed into the NN to produce the output of the NN which reflects how likely that particular set of variables is to belong to the candidate labeled as "signal/background". By using the output, the final selection is done on a candidate-by-candidate basis.

In order to compute the 14 variables, first, neutron capture vertex is reconstructed for each candidate selected in the primary selection. The reconstruction is performed by using $N10_{\mathrm{pvx}}$ hits. As was explained in the previous section, 2.2 MeV γ ray can be treated as point-like source of Cherenkov photons, which leads us to expect that the

spread of the residual time computed from true neutron capture position is minimum. Thus, the capture vertex $\boldsymbol{r}_{ncap}$ is defined as follows:

$$\boldsymbol{r}_{ncap} = \underset{\boldsymbol{r}}{argmin} \left(\sqrt{\frac{1}{N10_{pvx}} \sum_{i=1}^{N10_{pvx}} (\tau_i(\boldsymbol{r}) - \bar{\tau}(\boldsymbol{r}))^2} \right), \qquad (6.3.1)$$

where

$$\tau_i = t_i - TOF_i(\boldsymbol{r}),$$

$\boldsymbol{r}$ is trial vertex, t_i is hit time of i-th hit, $TOF_i(\boldsymbol{r})$ is TOF of i-th hit computed from $\boldsymbol{r}$, and $\bar{\tau}(\boldsymbol{r})$ is the average of the residual time. The left panel of Figure 6.10 shows the distribution of the distance between the true and reconstructed vertices, and the resolution is estimated to be about 134 cm from the distribution. Since 2.2 MeV γ rays travel $\sim$20 cm on average before they undergo the first Compton scattering as shown in the right panel of the figure, the distance between the true and reconstructed vertices is broadened.
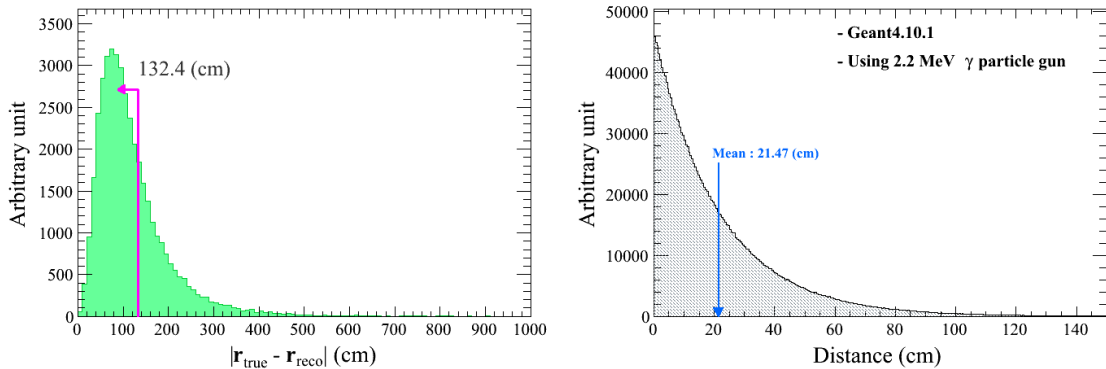
Figure 6.10: Distribution of the distance between the true and reconstructed vertices (left). The arrow shows the 68 percentile of the distribution. Distribution of true distance from the generation point of 2.2 MeV γ ray to the vertex of the first Compton scattering (right).

After the vertex reconstruction, a new set of PMT hits within a 10 ns window using the reconstructed capture vertex is computed. Then, the 14 variables are calculated by using only the newly computed PMT hits and the capture vertex, which means that all the variables do not explicitly include any information regarding primary ν event such as reconstructed distance between ν interaction and neutron capture vertices. Such information is highly dependent on the modeling of neutron production (or particular MC simulations), and thus is likely to introduce a dependence of the modeling of the neutron production into the NN. The neutron tagging

algorithm used in the primary analysis of this thesis has been purposely designed to avoid such model dependence and therefore differs from algorithms used in other SK analyses. As this primary analysis aims to measure neutron itself, a maximum effort needs to be made in order to minimize such model dependence as much as possible. The 14 variables therefore characterize differences in geometrical and time spreads of the hits, and position of reconstructed capture vertex in ID between true neutron and background events. The robustness of the neutron tagging algorithm, which describes how strongly the algorithm depends on a particular MC simulation, will be mentioned in the context of the systematic uncertainty on the neutron tagging efficiency in Section 8.3.13.

6.3.1 The 14 feature variables

In the following, the 14 feature variables used for the NN classification are described. All the 14 feature variables are shown in Figure 6.13. Figure 6.14 shows the linear correlations between the variables for signal and background events.

1. Number of hits in 10 ns: $\boldsymbol{N10_{nvx}}$

    This is the same number of PMT hits which are calculated by using the reconstructed neutron capture vertex as mentioned above. The remaining 13 feature variables are computed using the reconstructed capture vertex and the $N10_{nvx}$ PMT hits except for $N300S$.

2. Number of hits in 300 ns: $\boldsymbol{N300S}$

    The PMT hits of signal events are tightly clustered in the residual timing computed from the reconstructed capture vertex, whereas those of background events tend to be broadly distributed. For instance, Cherenkov photons emitted by β particles produced in decay chain processes of radon may not be tightly distributed in the residual timing since the TOF subtraction is done from reconstructed neutron capture vertex rather than the production vertex. This difference is taken into account by considering $N300$ which is the number of PMT hits in the ± 150 ns surrounding the capture time t_0 of the candidate event. $N300S$ is defined as $N300$ - $N10_{nvx}$.

3. Number of clustered hits: $\boldsymbol{NcS}$

    It is known from studies on background events that the PMT hits of background events tend to be geometrically clustered compared to those of signal events. This tendency is parametrized by the number of clustered PMT hits Nc. To calculate this variable, first hit vector which is defined as the unit vector from the reconstructed n capture vertex to hit PMT position is computed for each PMT hit of the candidate event. Then, for each hit angles between its hit vector and the other's hit vectors are calculated. If a hit has an angle less than $14.1°$, then the hit is regarded

as a clustered hit. This calculation is conducted for all the PMT hits of the candidate event. If the cumulative number of clustered hits is more than 3 hits, then the cumulative number is assigned to be Nc. Otherwise, Nc is set to 0. **NcS** is defined as $N10_{\mathrm{nvx}}$- Nc.

4. Standard deviation of hit timings: **tSD**

   Although the GMT hits of candidate events are clustered in a $10\,\mathrm{NSF}$ window, spread of hit timings in the window still differs between signal and background events. **Tod** is calculated as the standard deviation of the residual time of $N10_{\mathrm{nvx}}$ PMT hits.

5. Minimum standard deviation of hit timings: **tSDMin6**

   Ideally PMT hits of signal events consist of PMT hits related to $2.2\,\mathrm{MeV}$ γ rays from neutron captures on hydrogen nucleus only. However noise hits can contaminate signal events. In order to consider the effect by such contamination, another standard deviation is calculated by using all the possible combinations of 6 hits in the PMT hits of a candidate event. Then, the minimum value is defined as **tSDMin6**.

6. Nearest distance to the ID wall: **nDwall**

   Reconstructed vertex of background events tends to be distributed near the ID wall. This tendency is considered by **nDwall** which is the closest distance from the reconstructed vertex of a candidate event to the ID wall.

7. Closest distance to the ID wall along particle direction: **nTwall**

   The PMT hits of signal events are produced by Compton scattered electron originating from $2.2\,\mathrm{MeV}$ γ rays, which means that these hits have a directionality because of the nature of Cherenkov radiation. On the other hand, background events do not have such directionality since they are caused by accidental coincidences of noise hits. This difference distinguishes between signal and background events even if they have identical value of **nDwall** and is parametrized by **nTwall** which is the closest distance from the reconstructed capture vertex to the nearest ID wall along the candidate's direction. The direction is reconstructed as the average of hit vectors of the candidate.

8. Geometrical acceptance of PMT: **lnAccp**

   The ID PMTs have an angular dependence on detecting photons. In addition, photons emitted by charged particles are attenuated by the light absorption and scattering of the water. Therefore, probability to hit i-th ID PMT by a photon emitted at an ID position $\boldsymbol{r}$ depends on the geometrical relation between the emitted position and the hit PMT position, and can be expressed as:

$$P_i(\boldsymbol{r}) = \frac{a_i(\boldsymbol{r})}{\sum_i^{\text{all ID PMTs}} a_i(\boldsymbol{r})}, \tag{6.3.2}$$

where

$$a_i(\boldsymbol{r}) \equiv \frac{F(\theta_i)}{|\boldsymbol{r} - \boldsymbol{R}_i|^2} \exp\left(-\frac{|\boldsymbol{r} - \boldsymbol{R}_i|}{L_{\mathrm{Att}}}\right),$$

θ_i is the PMT zenith angle of the photon, $F(\theta_i)$ is the angular dependence of the PMT detection efficiency, $\boldsymbol{R}_i$ is the position of i-th PMT, and L_{Att} is the light attenuation length of the water. The angular acceptane, which is obtained from a simulation of optical photons by the detector simulation, is given as:

$$F(\theta) = 0.21 + 0.52 \cos\theta + 0.39 \cos^2\theta - 0.13 \cos^3\theta \qquad (6.3.3)$$

The PMT hits of signal events are produced by photons emitted around reconstructed capture vertex, whereas it may not be the case for background events. This difference is taken into account by **ln*Accep*** which is a likelihood calculated by using the above hit probability.

$$\mathrm{ln}Accep = \frac{1}{N10_{\mathrm{nvx}}} \sum_i^{N10_{\mathrm{nvx}}} -\log_{10} P_i(\boldsymbol{r}_{\mathrm{ncap}}). \qquad (6.3.4)$$

In the above equation, the factor $1/N10_{\mathrm{nvx}}$ is adopted in order to take into account different $N10_{\mathrm{nvx}}$ value among candidate events.

9. Hypothesis testing of Cherenkov angle: **llr*CAng***

For a candidate event, the Cherenkov opening angle can be defined using arbitrary 3 hits as schematically shown in Figure 6.11. Since the PMT hits of signal events are produced by Compton scattered electrons originating from $2.2\,\mathrm{MeV}$ γ rays, the opening angles of signal events tend to be $\sim 42^\circ$ which corresponds to the opening angle of the Compton scattered electrons. On the one hand, those of background events are expected not to have such angular dependence.
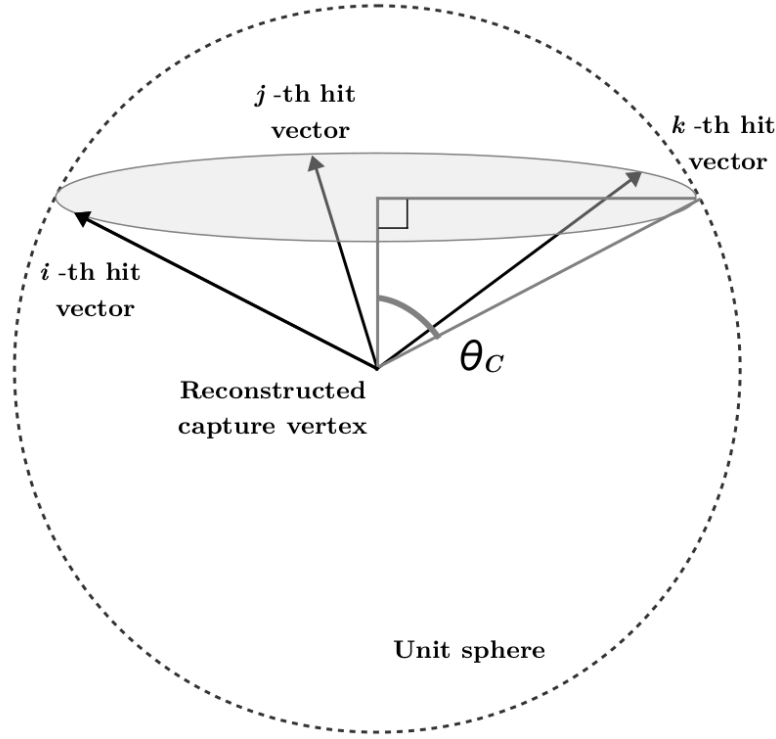
Figure 6.11: A schematic drawing of opening angle defined by 3 hits.

To make use of this difference, a log likelihood ratio, **llr$CAng$**, is constructed as:

$$\text{llr}CAng = \sum_{i}^{N} \ln \mathcal{L}_{\text{Bkg.}}(\theta_{Ci}) - \ln \mathcal{L}_{\text{Sig.}}(\theta_{Ci}), \qquad (6.3.5)$$

where N is all the possible combinations of 3 hits using the candidate's $N10_{\text{nvx}}$ PMT hits, θ_{Ci} is the opening angle of i-th 3 hits combination, and $\mathcal{L}_{\text{Bkg.}}$ and $\mathcal{L}_{\text{Sig.}}$ are the $N10_{\text{nvx}}$ dependent probability density functions (PDFs) of the opening angle for background and signal events, respectively. Figure 6.12 shows the pre-calculated PDFs. As shown in the figure, the signal PDF has the clear peak around at $\sim 42°$.

10. Geometrical anistropy of hits: $\boldsymbol{\beta_{\ell}}$

    The difference in the geometrical spreads of the PMT hits between signal and background events are further utilized. Since this difference originates from different angular distribution of PMT hits, the angular distribution can be used to separate the signal and background events. Although the true angular distribution is not known, it can be approximately obtained as a linear combination of orthogonal spherical harmonics. Therefore, the coefficients of the linear combination are used as the feature variables.
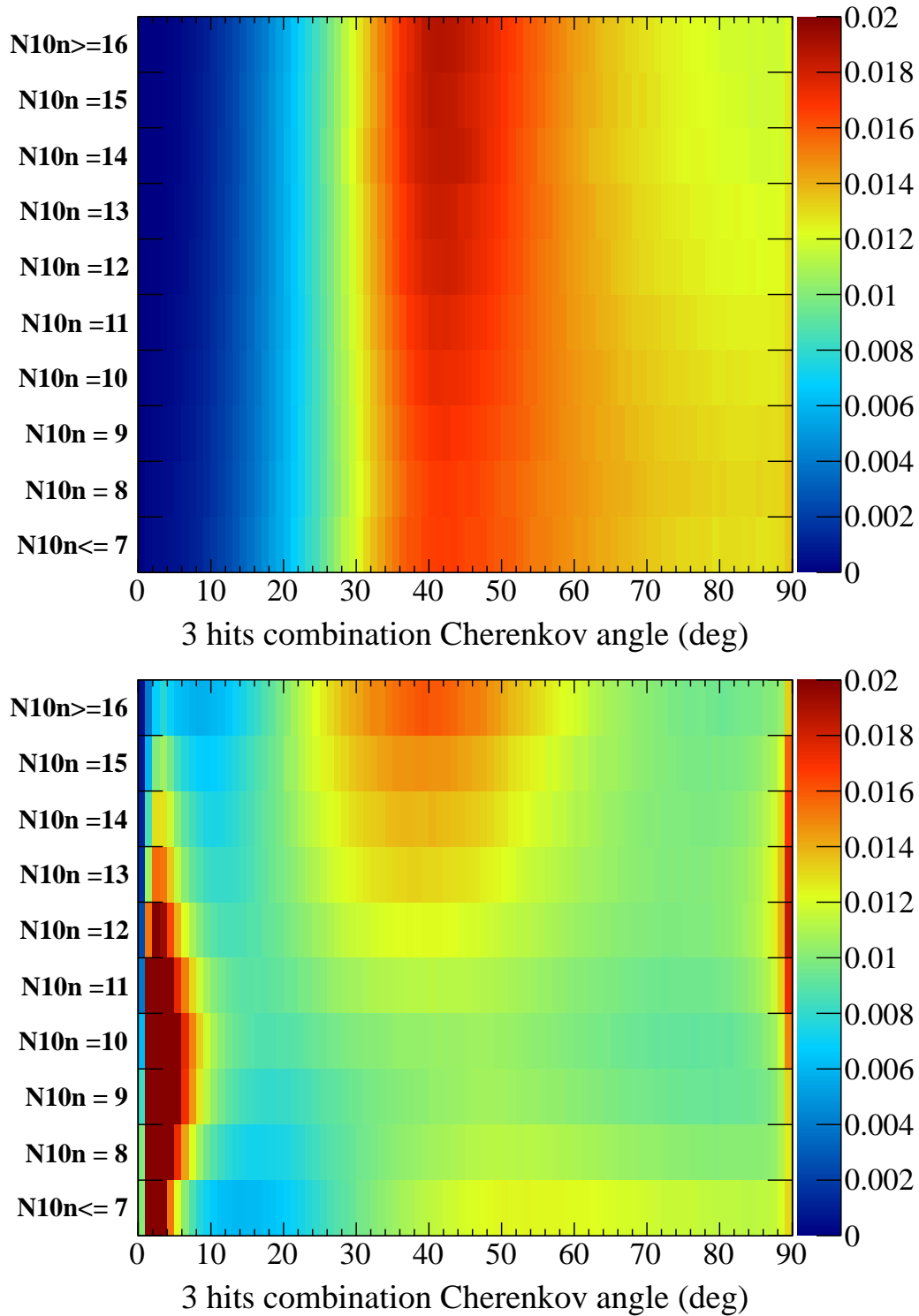
Figure 6.12: Array of one-dimensional PDF of 3 hits Cherenkov angle distribution for the signal (left) and background (right) events. For a given $N10_{\mathrm{nvx}}$, the corresponding horizontal slice is used to calculate **llr$CAng$**. In the left and right plots, $N10n$ denotes $N10_{\mathrm{nvx}}$.

The coefficients are given as:

$$\beta_\ell = \frac{2}{N10_{\mathrm{nvx}}(N10_{\mathrm{nvx}} - 1)} \sum_{i=1}^{N10_{\mathrm{nvx}}} \sum_{j=i+1}^{N10_{\mathrm{nvx}}} \mathcal{P}_\ell(\cos\theta_{ij}), \qquad (6.3.6)$$

where θ_{ij} is the angle between the i-th and j-th hit vectors and $\mathcal{P}_\ell$ are Legendre polynomials. This parametrization had been used in the SNO experiment [208] in the context of separation of CC-NC interactions for the SNO's solar neutrino analysis. β_1, β_2, β_3, β_4 and β_5 are adopted as a part of the feature variables, because the correlations among them are different between signal and background events. The difference in the correlation is shown in Figure 6.14.
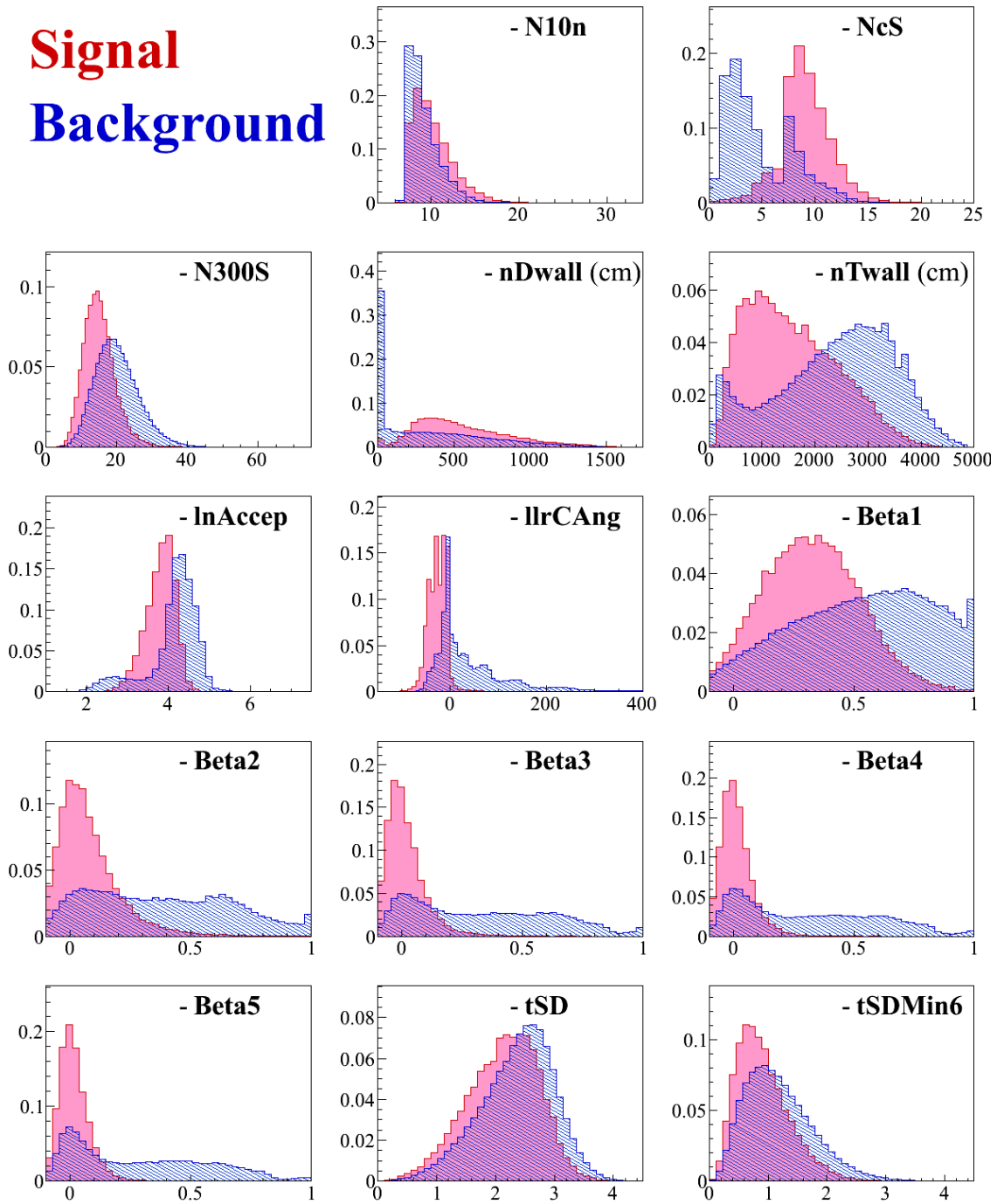
Figure 6.13: Distributions of the 14 feature variables, which are fed into the NN. Red and blue distributions correspond to true neutron events and accidental background events, respectively. All the distributions are area normalized.
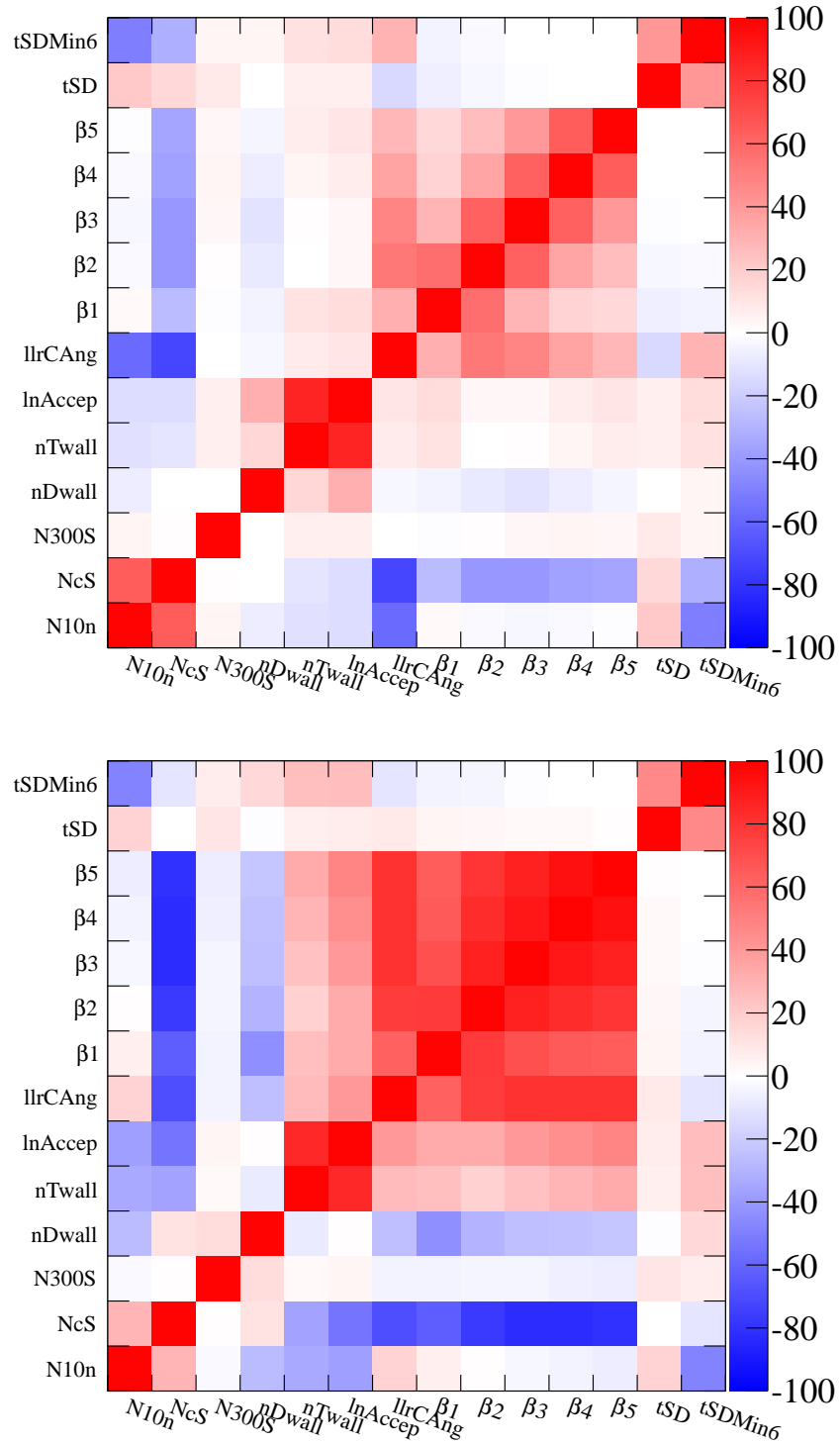
Figure 6.14: Linear correlation matrices for true neutron events (top) and accidental background events (bottom).

6.3.2   Network training

The MLP neural network implemented in the TMVA package [209] which is a feed-forward multilayer perceptron is used. In general, this kind of NN have a few hyper parameters that have to be set by user such as layer architecture. In addition, choice of such parameters is arbitrary, so that these parameters need to be determined empirically. The setting of the NN used in this algorithm was determined after trying a variety of parameter settings. The layer architecture and activation function of the NN were chosen to be 14:11:8:4:1 and hyperbolic tangent, respectively. The NN training and testing processes were done by back propagation algorithm with 650 training cycles and a training rate of 0.001.

Although the NN is applied to the $1R\nu_\mu$ samples which are used in the primary analysis of this thesis, the samples used for the training and testing were made from FCFV (Fully Contained Fiducial Volume) ν events in order to make the NN robust. In order to prepare the samples, the same FCFV cut described in Section 7.2 was applied to half of the second hybrid neutron MC ν events, after which 800,000 true 2.2 MeV γ events and 2,200,000 background events were randomly extracted from the FCFV events. These extracted events were used for the training and testing processes with a one to three ratio for the signal events and the background events. No behaviour of overtraining was found during the training process.

Figure 6.15 shows the NN output distributions for true neutron and background events. As shown in the figure, true neutron and background events peak around at the NN output $= 1$ and $= 0$, respectively. In order to select a final event which is referred to as "tagged neutron" hereafter, a threshold on the NN output needs to be determined. In this determination, one can not utilize any model dependent metric such as $S/\sqrt{S+B}$, because number of neutrons (here it is S) strongly depend on a particular simulation that is used for this determination. As the background events depend only on number of ν events used for the neutron tagging, the cut threshold was determined by setting the background event rate, which is number of tagged background events per ν event, to 0.02 as shown in Figure 6.16. consequently, the value of the determined threshold on NN output is 0.886, and neutron tagging efficiency is $\sim 20\%$.
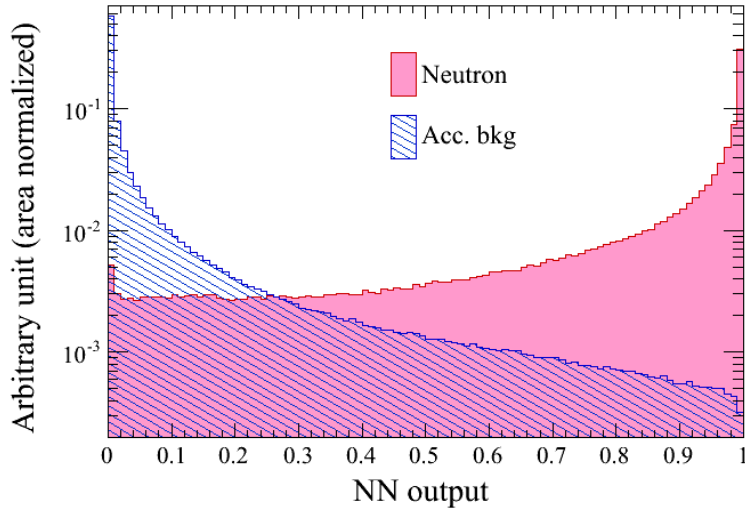
Figure 6.15: Area normalized distribution of the neural network output.

Although there is no strong reason for the value of 0.02 chosen, this low background event rate enables us to have high purity tagged neutron samples for the neutron measurement in Chapter 8. As it will be described in Section 7.3, the fraction of the background events in the detected neutrons is estimated to be less than 10% for both the FHC and RHC 1R ν_μ samples, which are summarized in Table 7.2 and Table 7.3. It should be noted that this determination of the threshold enables us to subtract the backgrounds contained in the real data by using only the number of observed ν events, which means that any systematics varying ν event rate do not affect the background subtraction.
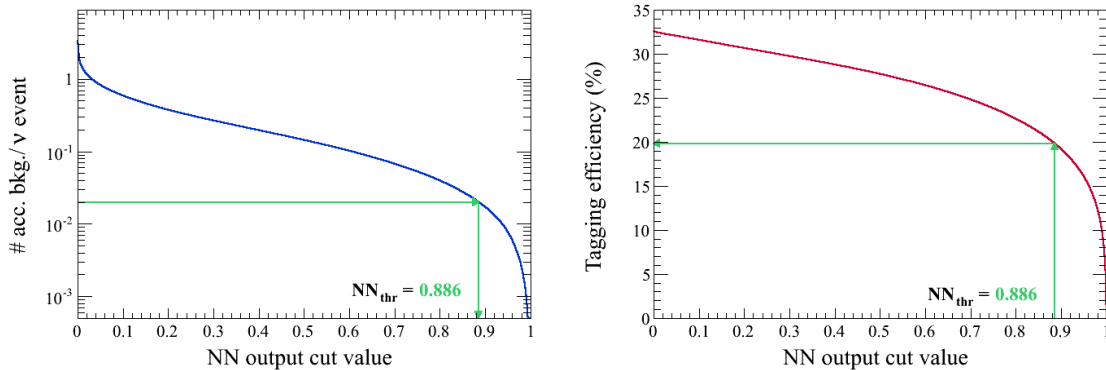
Figure 6.16: The left and right figures shows background event rate (number of background events per ν event) and tagging efficiency as a function of the neural network output threshold, respectively. The vertical green arrow shows the position of the threshold which is determined to be 0.886 by setting background event rate to 0.02.

The performance of the neutron tagging algorithm before and after the NN classification is summarized in Table 6.1. Figure 6.17 shows the neutron tagging efficiency

and background event rate in bins of reconstructed ν interaction vertex.

Table 6.1: Neutron tagging efficiency and background event rate, which is number of tagged background events per ν event, after the primary selection and after the NN classification, respectively. These numbers are obtained by using the FHC and RHC $1R\nu_\mu$ samples which are used for the primary analysis of this thesis. Note that the SK time variation effects are not included here. The effects will be considered in Section 6.5, and the corrected numbers can be found in Table 6.2. Errors represent MC statistical uncertainties.

		Tagging efficiency (%)	Acc. Bkg. rate
After primary selection	FHC	33.29±0.30	3.55±0.02
	RHC	33.71±0.17	3.51±0.02
After NN classification	FHC	19.89±0.23	$(2.10\pm0.67)\times10^{-2}$
	RHC	20.04±0.13	$(1.98\pm0.44)\times10^{-2}$
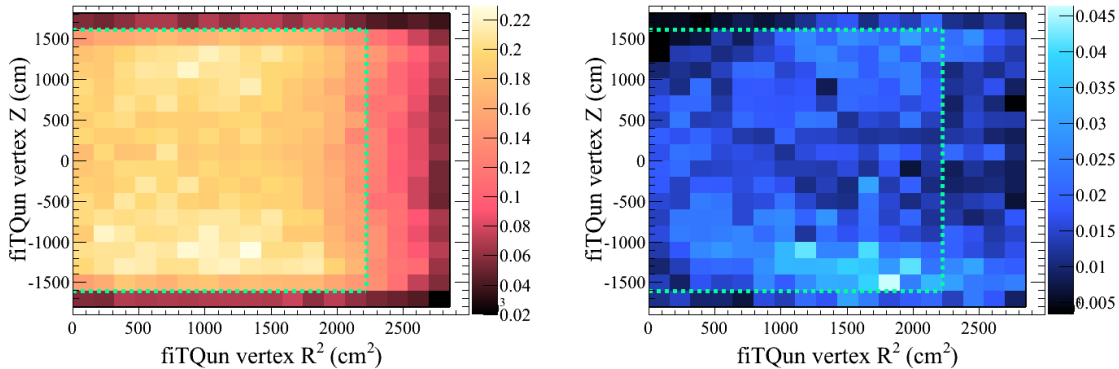
Figure 6.17: Neutron tagging efficiency as a function of reconstructed ν interaction vertex position inside the SK tank (left). Background event rate as a function of reconstructed ν interaction vertex position inside the SK tank (right). R^2 is defined as $X^2 + Y^2$, where X and Y are x and y positions of reconstructed ν interaction, respectively. Green dashed lines represent the fiducial volume used in the primary analysis of this thesis.

6.4 Application to Americium-Beryllium calibration data

The neutron tagging algorithm described in the previous section can be validated by a calibration which exploits an Americium-Beryllium (Am/Be) radioactive source. The

first study using the source [210] was done during the SK-III phase to demonstrate feasibility of neutron tagging in a water Cherenkov detector.

^{241}Am of the Am/Be source emits α particles, and these particles interact with ^{9}Be. One of reaction channels produces a prompt signal of 4.4 MeV γ ray and a delayed neutron as follows:

$$\alpha +^9 Be \to ^{*12}C + n$$
$$^{*12}C \to C + \gamma \,(4.43\,\text{MeV}) \tag{6.4.1}$$

The calibration uses the reaction channel as the signal process to search for neutrons.

The Am/Be source has an intensity of 97 μCi of ^{241}Am. Since this signal reaction occurs as the dominant reaction channel with a probability of $\sim$62%, the source provides the signal prompt 4.4 MeV γ rays with a frequency of 87 Hz.

6.4.1 Experimental setup and data taking

In this calibration, the Am/Be source is embedded into BGO crystal scintillators, which enables detecting the 4.4 MeV gamma rays as the prompt events and thus the delayed neutrons can be searched for by using the detected 4.4 MeV γ events. Figure 6.18 shows the Am/Be source with the BGO scintillators.

Figure 6.18: The Americium-Beryllium source and BGO crystal scintillator.

In the analysis of this section, the calibration data set taken in Dec. 2016 is used. The Am/Be source was put at three different ID positions:

- Center : Am/Be source position (35.3, -70.7, 0) [cm]

- Z+15 m : Am/Be source position (35.3, -70.7, 1500.0) [cm]

- Y-12 m : Am/Be source position (35.3, -1201.9, 0.0) [cm].

The data were taken at each position with SHE (Super High Energy) trigger which can be issued by the scintillation light of BGO scintillators produced by prompt 4.4 MeV γ rays. Following a SHE trigger in which case PMT hit information until the first 35 μs is stored, another trigger (called "AFT" trigger) is issued, by which the information about the PMT hits after the 35 μs is stored until +835 μs. The 835 μs record length of PMT hit information allows us to study the time spectrum of the tagged neutrons in detail.

Since the composition of the noise hits in the calibration is different from that of ν events which is modeled by the T2K dummy spill data, due to the presence of the BGO scintillators, a dedicated accidental background data was taken at the center position with the Am/Be source by a random trigger. The PMT hits of the background data are used for the corresponding simulated events of this calibration.

6.4.2 Data reduction

The calibration data are processed to extract the events related to the prompt 4.4 MeV γ rays by requiring the following conditions:

1. An event issued by SHE trigger has a AFT trigger.

2. Time difference from the previous SHE + AFT triggered event is longer than 1.5 μs.

3. Total charge of PMT hits (*potot*) is in the accepted region.

The first cut ensures that the delayed neutrons can be searched for until +835 μs and the second one avoids contamination of the delayed neutron from the previous prompt event. The third cut intends to select the prompt events which are produced by the scintillation light of 4.4 MeV γ rays. Figure 6.19 shows the distributions of *potot* for the three data taking positions with an indication of the accepted regions.
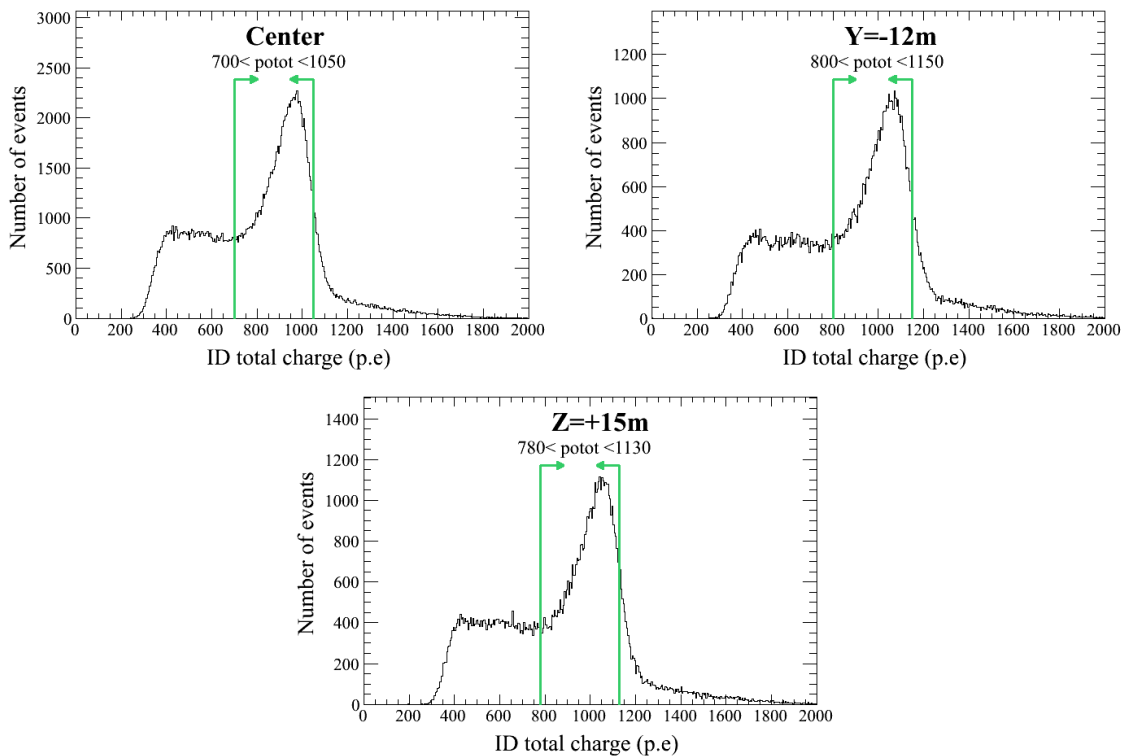
Figure 6.19: Distributions of *potot* for the center (top left), Z+15 m (top right), and Y-12 m (bottom). The events inside the regions surrounded by arrows are selected as the prompt events related to 4.4 MeV γ rays.

6.4.3 MC simulation

Corresponding MC events are simulated by generating neutrons at the same data taking positions. Ideally a precise MC which can simulate both all the γ rays emitted from the Am/Be source and the scintillation light of BGO scintillator is needed to perform a full event simulation. However, such MC is not available at the present moment and is quite challenging to make. Therefore, only the delayed neutrons of the signal reaction are simulated by considering their kinetic energy spectrum. Figure 6.20 shows the kinetic energy spectrum of the delayed neutrons used in this analysis.
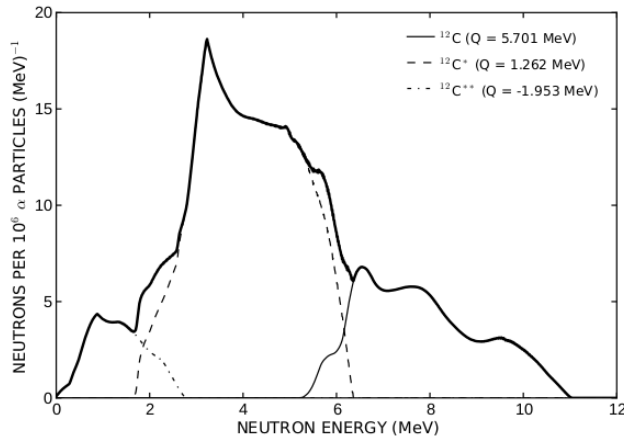
Figure 6.20: Kinetic energy spectra of neutrons produced by $^9\text{Be}(\alpha, n)^{12}\text{C}$ reactions. The broken line peaked around 3 MeV corresponds to the delayed neutrons of the signal reaction: $\alpha + ^9 Be \rightarrow ^{*12} C + n$. Figure taken from [32].

After simulating these neutrons including subsequent 2.2 MeV γ rays produced by neutron capture on hydrogen nucleus, the PMT hit information of the background data taken with a random trigger is injected into these simulated events.

6.4.4 Data-MC comparison

For the data, the neutron tagging algorithm is applied to the prompt events which passes through all the three cuts described in Subsection 6.4.2. On the other hand, in the case of the MC the algorithm is applied to all the simulated events, and thus the number of prompt events is equal to the number of simulated events for the MC.

The algorithm is applied to both the data and the MC from $+18\,\mu\text{s}$ to $+835\,\mu\text{s}$ after the initial trigger. Since the production position of the delayed neutrons is the same as the Am/Be source location which is known, for each data taking position the location of the source is used to seach for neutron candidates. In the analysis of this calibration, an additional variable, N_{200}^{Max}, is calculated when applying the algorithm to both the data and MC. N_{200}^{Max} is the maximum number of PMT hits in a 200 ns sliding timing window from $+18\,\mu\text{s}$ to $+835\,\mu\text{s}$ in a prompt event. This variable is used to avoid a second scintillation light event following the primary scintillation light which is produced by γ rays emitted from the Am/Be source [211, 203]. The cut condition for N_{200}^{Max} is given as:

- $N_{200}^{Max} < 50$

If a prompt event does not satisfy the above condition, the event is rejected, and is not used in the following comparison between the data and the MC.

Figure 6.21 and 6.22 show the distributions of the NN's 14 input variables before and after the NN classification, respectively. As shown in the figures, almost all the background events are removed by the NN classification. In addition, the data shows a good agreement with the MC.
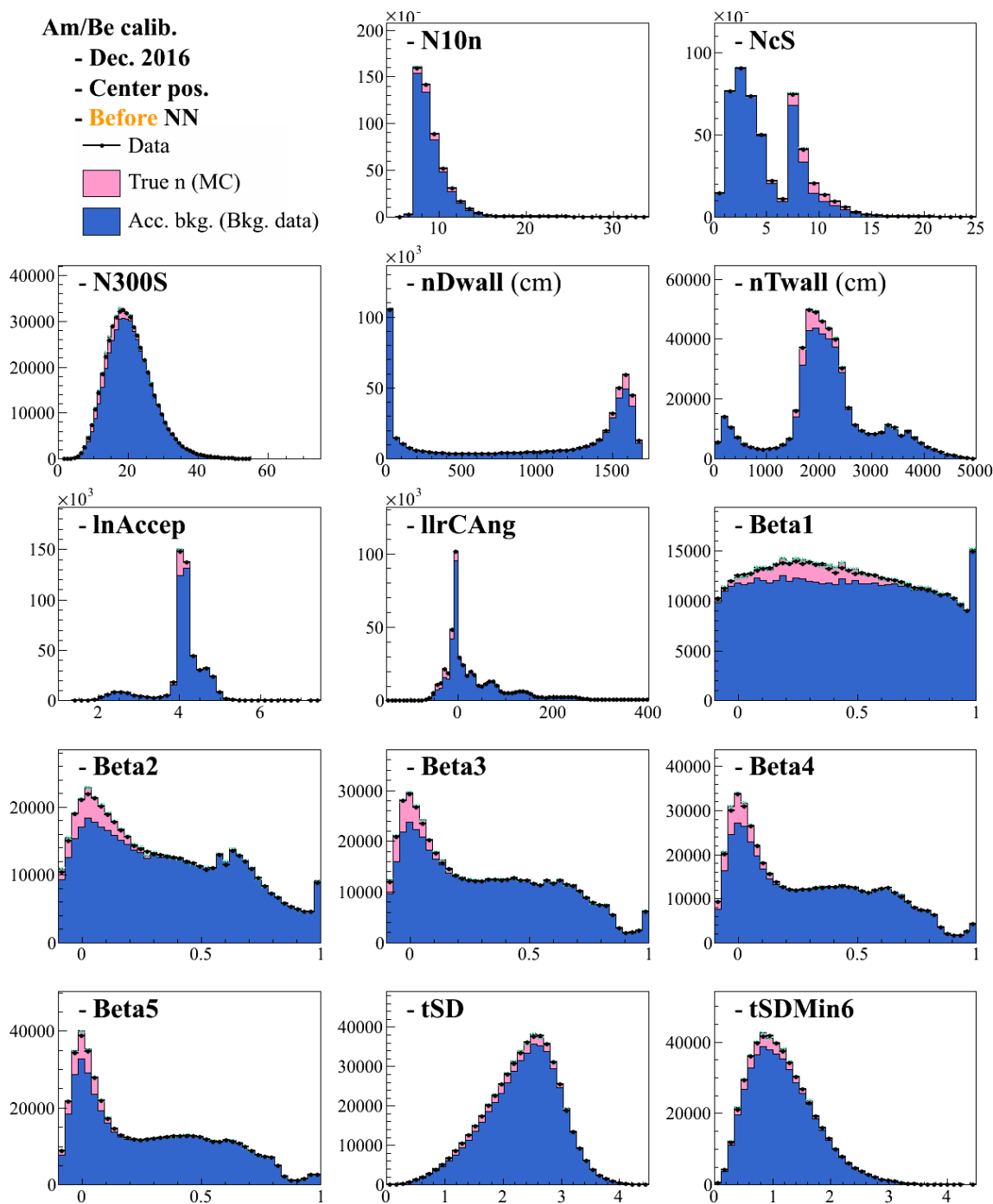
Figure 6.21: Distributions of the 14 input variables before the NN classification. The MC distribtions are shown by stacked histograms consisting of the true signal events (blue) and the true background events (pink). The dots corresponds to the data. Green bands represent the statistical errors of the MC. All the distributions are normalized by the number of the selected prompt events.
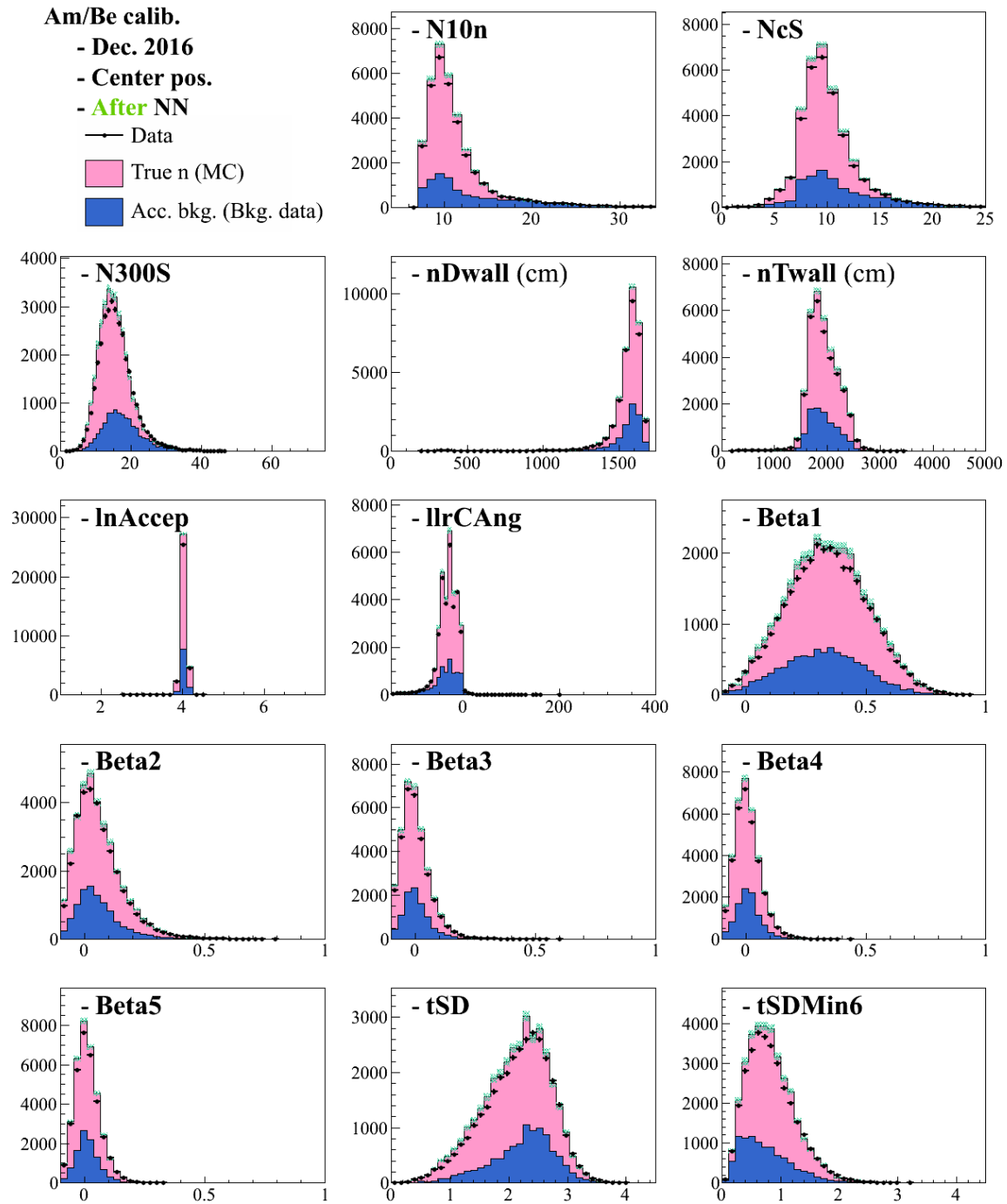
Figure 6.22: Distributions of the 14 input variables after the NN classification. The MC distribtions are shown by stacked histograms consisting of the true signal events (blue) and the true background events (pink). The dots corresponds to the data. Green bands represent the statistical errors of the MC. All the distributions are normalized by the number of the selected prompt events.

The capture time distribution can be used to study the capture time constant and the neutron tagging efficiency by a fit. The fit function is obtained by considering the

following factors. In principle, this calibration can address neutron tagging efficiency by using the number of selected prompt events and the number of tagged neutrons as follows:

$$\text{tagging efficiency} = \frac{n^{delay}}{N^{prom}}, \tag{6.4.2}$$

where n^{delay} is the number of tagged true delayed neutrons and N^{prom} is the number of selected prompt 4.4 MeV γ events. Since there are remaining accidental background events even after the NN classification, the contribution from the remaining background events to the tagged neutrons needs to be taken into account. The background events are caused by accidental coincidences of noise PMT hits. Therefore, the time dependence of the background events is reasonably assumed to be a constant over time. Thus, the fit function at each data taking position consists of an exponential function and a constant function as follows:

$$f(t; \tau, \varepsilon, b) = N \times \left[\varepsilon \frac{1}{\tau} e^{-t/\tau} + b \frac{1}{820 - 20} \right], \tag{6.4.3}$$

where τ is capture time, N is number of selected prompt events, ε is tagging efficiency, and b is background event rate. Since the capture time should be the same among the three data taking positions, τ need to be treated as a common parameter among the three positions. Then, the fit parameters τ, ε, and b are obtained by minimizing a χ^2 given as:

$$\chi^2 = \sum_i \sum_j \frac{\left(\mathcal{E}_{i,j} - \mathcal{O}_{i,j}(\tau, \varepsilon_i, b_i) \right)^2}{\mathcal{E}_{i,j}}, \tag{6.4.4}$$

where i runs over the three different data taking positions, j represents bin number of capture time distribution, $\mathcal{E}$ is number of observed events, and $\mathcal{O}$ is number of expected events.

The minimization is done by the MINUIT algorithm. The resultant τ is 207.7±3.2 μs for the data and 202.3±3.5 μs for the MC, and is consistent between the data and the MC. Also, both of the two fitted τs are consistent with an external measurement result of 204.8±0.4 μs [37]. Figure 6.23 shows the capture time distributions of the data with the fit results in comparison with the corresponding MC.
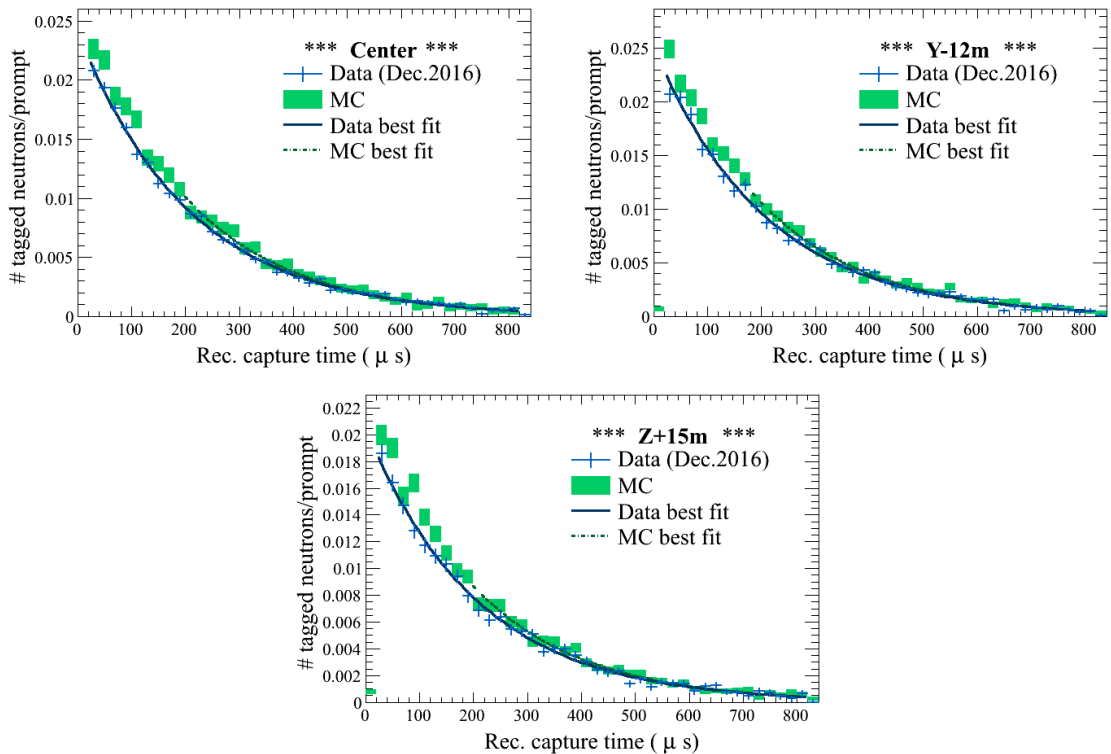
Figure 6.23: Distribution of capture time after the primary selection for the three data taking positions. The top left, top righ, bottom correspond to the center, the Z+15 m, and the Y-12 m data taking positions, respectively. The fitted background component is subtracted. All the distributions are normalized by the number of the selected prompt events.

Since the fit extracts the neutron tagging efficiency as well as the capture time constant, the efficiency is also compared between the data and the MC. In Figure 6.24, the left and right plots show the fitted neutron tagging efficiency and the relative difference from the MC's ones, respectively. As shown in the figure, the efficiency of the data is systematically lower than that of the MC for all the three positions. Possible reason for this systematic disagreement is discussed in the remaining part of this section.

119
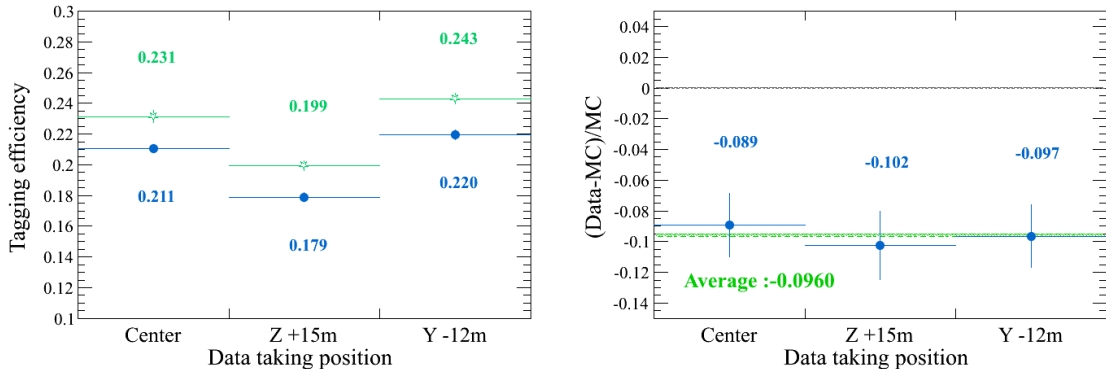
Figure 6.24: The fitted neutron tagging efficiency (left) and the fractional difference with respect to the MC's ones. In the left plot, green and blue points correspond to the MC and the data, respectively. In the right plot, the green dashed line represents the average of the fractional differences. The horizontal axes represent the three data taking positions.

6.4.5 Discussion

As was shown in the above, the data showed the systematically lower neutron tagging efficiency compared to the MC although the extracted capture time constant was consistent with each other. To understand the discrepancy, it is worth noting the difference in the selection of the prompt events between the data and the MC. The prompt events of the data are selected by assuming that the events around the peak in the *potot* distribution shown in Figure 6.19 are produced by signal prompt 4.43 MeV γ rays, whereas that of the MC is equal to all the simulated events, each of which has a delayed neutron. If the assumption made only for the data is not correct, then there may be fake prompt events, in which there are no signal delayed neutrons. Existence of such fake prompt events can lower the data's efficiency as follows:

$$\text{tagging efficiency} = \frac{n^{delay}}{N^{prom} + B}, \tag{6.4.5}$$

where B is the number of fake prompt events.

In order to confirm whether or not such fake prompt events exist only in the data, the data's neutron tagging efficiency was evaluated by varying the cut values of the *potot*. If the assumption that the events around the peak in the *potot* distribution are due to prompt 4.4 MeV γ rays is true, then the efficiency may not change as the cut values on *potot* are varied.

Figure 6.25 shows the fitted neutron tagging efficiency of the data as a function of the lower cut value (ql) and the upper cut value (qh). As shown in the figure, both lowering ql and raising qh resulted in decrease of the fitted tagging efficiency, which strongly indicates that a non-negligible amount of fake prompt event is likely to contaminate the selected true prompt 4.4 MeV γ rays only for the data.
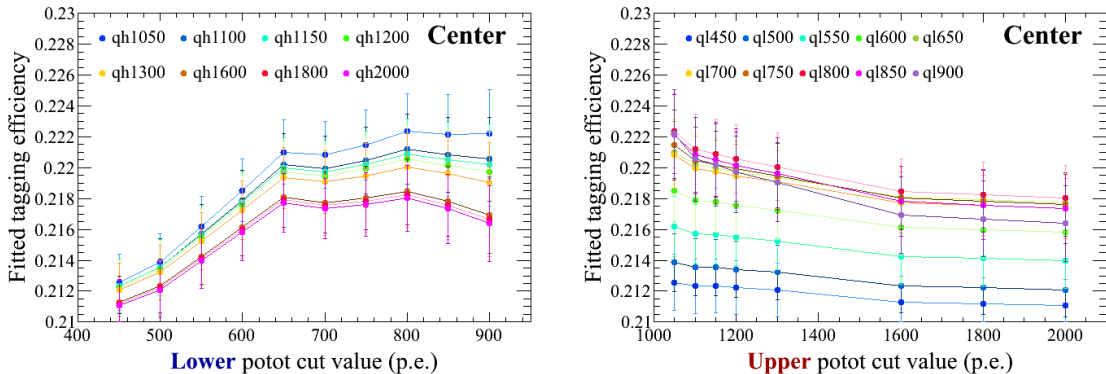
Figure 6.25: Fitted neutron tagging efficiency of the data at the center position for various *potot* cut values. In the left plot, lower cut value is varied while keeping upper cut value. On the other hand, in the right plot, upper cut value is varied while keeping lower cut value. In the left (right) plot, each color represents the corresponding fixed upper (lower) cut value.

In addition to the fake prompt events, there is likely to be another systematic source which can also lower the data's neutron tagging efficiency. The delayed neutrons in Equation 6.4.1 are produced inside the Am/Be source surrounded by the BGO scintillator crystals. It is known that neutrons can be captured on the nuclei contained in the sealing metal of the Am/Be source and the BGO crystals. If such absorption happens, then the prompt 4.4 MeV gamma rays are not accompanied by the delayed neutrons. Therefore, these two effects only for the data might be the primary cause that can explain the systematically lower tagging efficiency of the data compared to that of the MC.

6.5   Correction for detector time variation effects

The primary analysis in this thesis uses the FHC and RHC data taken until 2018 to measure neutrons. This data taking (hereafter called "Run 1-9" data taking) periods spanned the nine years; The Run 1 data taking started in Jan. 2010 and the Run 9 data taking ended in May 2019. Although the operation of the SK was stable enough in terms of ν event reconstruction during the data taking periods, there were known time variations, which may have non-negligible impacts on low energy analyses such as the neutron tagging, and this has never been quantitatively studied. As these variations are likely to affect the nominal neutron tagging efficiencies and background rates estimated around Dec. 2015, which are summarized in Table 6.1, the nominal values need to be corrected for this data taking period properly. Note that the effects are negligibly small, so that no significant impact on primary neutrino events have been seen during the Run 1-9 data taking periods [31].

In this section, first, a short introduction to the SK time variations considered is given. Following this, the procedure for the correction and the results are detailed. Note that the systematic uncertainty related to the following correction will be described in Section 8.3.11.

6.5.1   SK time variations

As described in Section 6.2, the neutron tagging algorithm uses only $\sim$10 PMT hits, which means that either increase or decrease of just one PMT hit due to any time variations of SK may give a visible impact on the performance of this algorithm. During the Run 1-9 data taking periods, such time variations had been observed: the gain of the ID PMTs, the light attenuation length, the hit probability of top-bottom asymmetry (TBA) inside the ID.
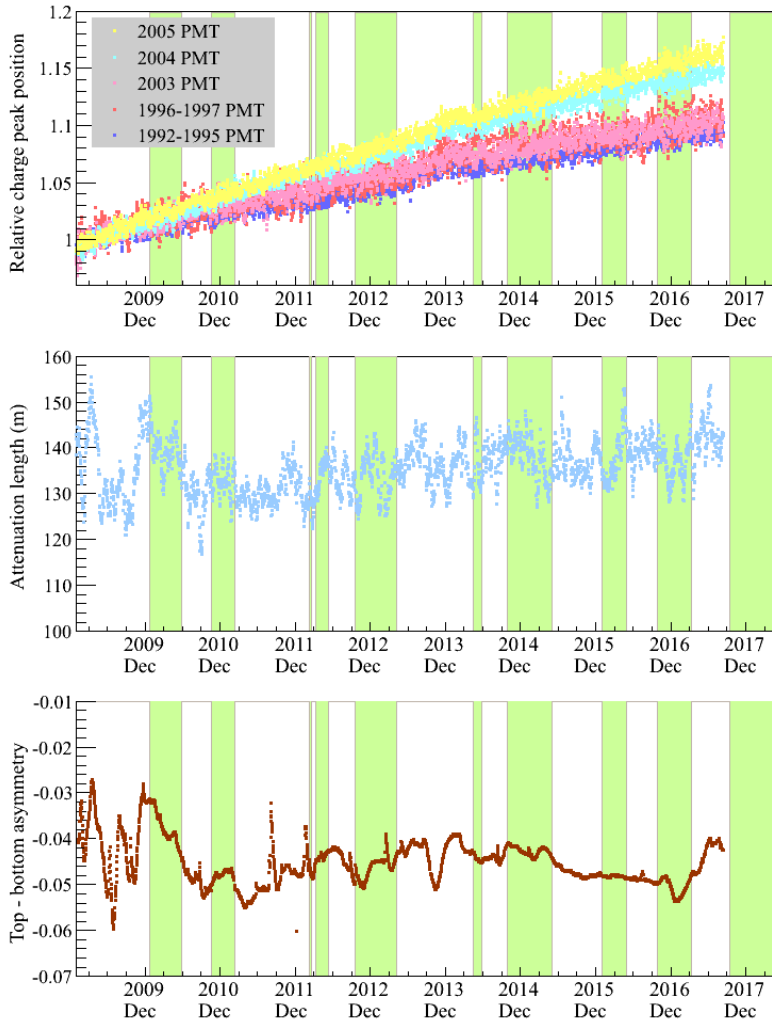
Figure 6.26: The time variations of the ID PMT gain (top), the attenuation length of the water measured by using decay electrons (middle), the TBA measured by the auto Xe light (bottom). For the PMT gain, the vertical axis represents the relative PMT gain with respect to the average value in Apr. 2009. The green bands show the Run 1-9 data taking periods.

Figure 6.26 shows these time variations. As shown in the top panel, the gain of the ID PMT has been continuously increasing over time, depending on the ID PMT production years. The middle and bottom panels show the time variations in the

attenuation length and the TBA of the water, which were described in Section 3.4. Their time evolution is different from that of the PMT gain as shown in these panels, but has still a visible variation from the beginning of the T2K data taking in Jan. 2010.

As was mentioned in Section 4.4, the background events of the neutron tagging algorithm, which are caused by random noise PMT hits, are modeled by using the T2K dummy spill data. Therefore, the time dependence of the dummy spill data also needs to be taken into account. Figure 6.27 shows the time evolution of the average number of PMT hits for the data taken during the beam-off periods. From the figure, a large variation mainly due to the PMT gain's increase can be seen.
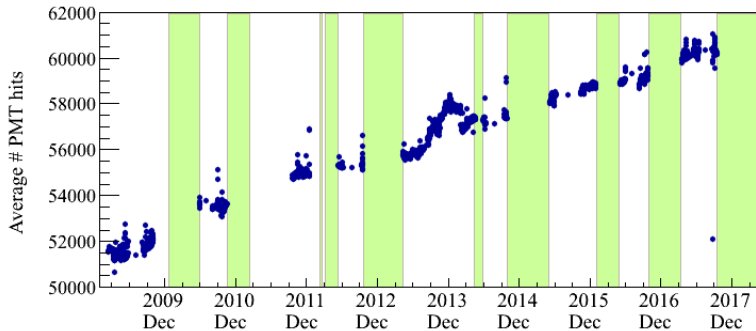
Figure 6.27: The average number of PMT hits of the dummy spill data. The green bands show the Run 1-9 data taking periods.

Since the above time variations affect the probability for making PMT hit, there may be non-negligible impact of these variations on the performance of the neutron tagging. In the following parts of this section, Subsection 6.5.2 describes the stability of the performance over the Run 1-9 data taking periods, and the effect of these time variations in the neutron tagging is taken into account as a correction in Section 6.5.3. Note that the corrected numbers summarized in Table 6.2 will be used for the primary analysis of this thesis to measure neutrons.

6.5.2   Regeneration of MC with time variations

In order to incorporate the effect of the time variations into the nominal tagging efficiency and background event rate, the time evolution of PMT hits produced by both true neutron and background sources need to be traced. This can be done, but the way to trace the evolution is different between true neutron events and background events. As the background events are modeled by the dummy spill data, its time evolution can be evaluated by utilizing the pre-existing dummy spill data. On the one hand, the case of $2.2\,\mathrm{MeV}$ γ ray is conducted by the detector simulation. The procedure of tracing the time evolution is therefore equivalent to regenerate the hybrid neutron MC at various time points.

For each regeneration point, SKDETSIM is rerun on the output of the NEUT used for the production of the nominal hybrid neutron MC with appropriate dummy

spill data, PMT gain, water attenuation length, and TBA. The regeneration points are determined by considering the statistics of both the MC and the dummy spill data. In order to maximize available number of regeneration points, only MC events which pass the $1R\nu_\mu$ analysis cuts described in Section 7.2 are used. After the cuts, there are about 240,000 MC events. As one event of the dummy spill data is used for two MC events due to different record length of PMT hits, 120,000 dummy spill events are needed at each regeneration point. To obtain available number of regeneration points, the events of the pre-existing dummy spill data are sorted in increasing order by time and then, are binned by every 120,000 events. Each bin is treated as one regeneration point and the representative time of a regeneration point is defined as the time when the 60,000-th event (i.e. 50 percentile) is recorded in the bin. The resultant number of regeneration points are 128 in total. The first and last points are in Sep. 2009 and Oct. 2017, respectively.

For each regenerated MC, the neutron tagging efficiency and background event rate are evaluated by using the identical neural network described in Section 6.3 and the results of the ν event reconstruction (i.e. fiTQun) of the nominal MC. Note that retraining NN and ν event reconstruction are very CPU intensive work and are not feasible to be done for each regenerated MC in a realistic time scale.

Figure 6.28 and 6.29 show the time evolution of the tagging efficiency and background event rate after the primary selection, respectively. As shown in the figures, after the primary selection, both the tagging efficiency and background rate are clearly and monotonically increasing over time, which indicates that the dominant effect comes from the increase of the PMT gain. Since the neutron candidates are selected by $N10_{\mathrm{pvx}}$ in the primary selection, it may be interesting to check the time dependence of the $N10_{\mathrm{pvx}}$ distribution. Figure 6.30 shows the comparison of the $N10_{\mathrm{pvx}}$ distributions between the first, nominal, and last regeneration points. As shown in the figure, the distribution of the true neutron events are clearly shifted to higher value, whereas that of the background events is relatively flat over $N10_{\mathrm{pvx}}$ compared to the true neutrons.
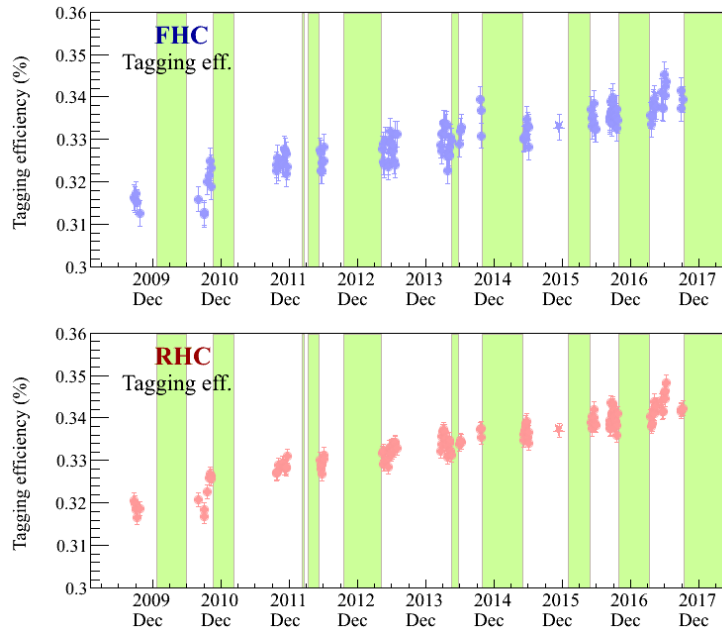
Figure 6.28: Neutron tagging efficiency after the primary selection as a function of time. The top panel and bottom panel correspond to the FHC and RHC $1R\nu_\mu$ MC samples, respectively. The error bars represent the MC statistical errors. The green bands show the Runs 1-9 data taking periods.
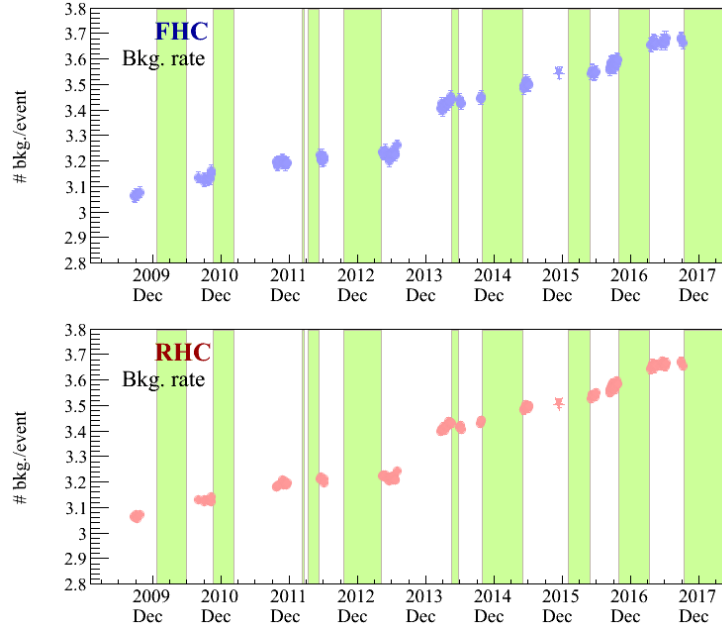
Figure 6.29: Background event rate after the primary selection as a function of time. The top panel and bottom panel correspond to the FHC and RHC $1R\nu_\mu$ MC samples, respectively. The error bars represent the MC statistical errors. The green bands show the Runs 1-9 data taking periods.

125
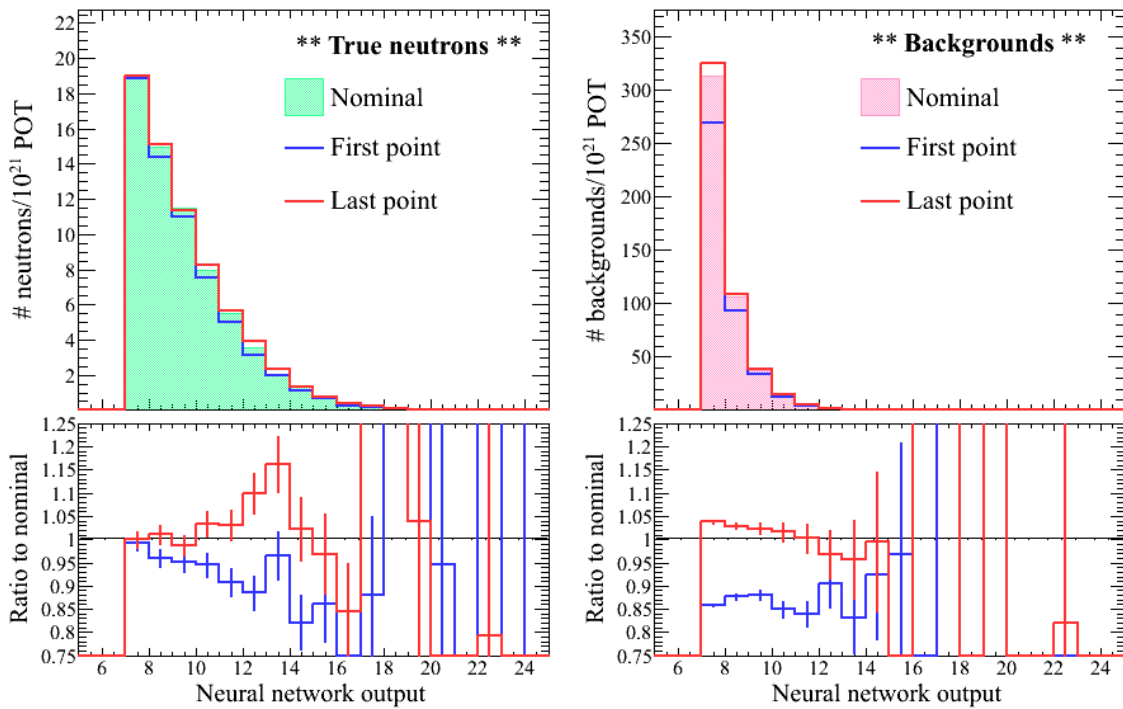
Figure 6.30: Comparison of the $N10_{\mathrm{pvx}}$ distributions between the different MC regeneration points. The left and right plots represent the true neutron and background events, respectively. The green bands show the Runs 1-9 data taking periods.

The tagging efficiency and background rate after the NN classification are shown in Figure 6.31 and 6.32, respectively. It is interesting to notice that the time evolution is very different between the primary selection and NN classification for both the true neutrons and background events.
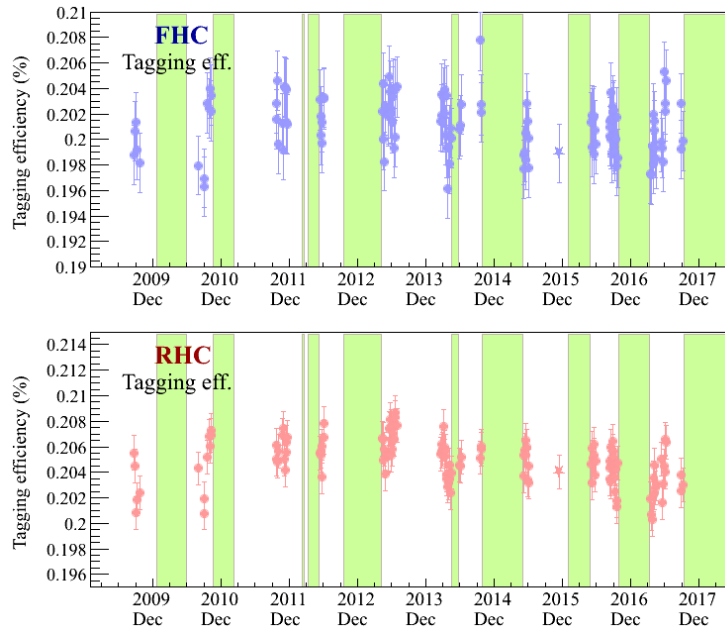
Figure 6.31: Neutron tagging efficiency after the NN classification as a function of time. The top panel and bottom panel correspond to the FHC and RHC $1R\nu_\mu$ MC samples, respectively. The error bars represent the MC statistical errors. The green bands show the Runs 1-9 data taking periods.

After the NN classification, the time variation of the tagging efficiency become smaller compared to the primary selection as shown in the figure. Although the size of the variation is small, the time variation seems to have a weak quadratic structure which is likely to have a peak around Aug. 2013. A possible explanation for this structure may be due to a result of competition by two effects: an increased PMT hits of the true neutron events and a larger contamination of the noise PMT hits. The first effect increase the absolute number of true neutron events selected in the primary selection and enhances the discrimination power of the NN between the true neutron and background events, which results in higher tagging efficiency after the NN classification. On the contrary, the second one may degrades the discrimination power, because some input variables of the NN utilize the difference in the geometrical spreads of the PMT hits, which causes lower tagging efficiency. The probability that the noise hits contaminate a true neutron event increases as the number of noise PMT hits increase due to the increase of the ID PMT gain. The effect of the degradation is therefore expected to become larger as time proceeds.

In case of the background event rate after the NN classification, on the one hand, the value is linearly decreasing over time as opposed to that of after the primary selection. In this case, contamination of PMT hits originating from 2.2 MeV γ rays is negligible, so that the backgrounds tend to be more "background-like" over time.

Comparison of the NN output distributions between the three different points are shown in Figure 6.33. As shown in the figure, the distributions of the true and background events are shifted to "neutron-like" and "background-like", respectively.
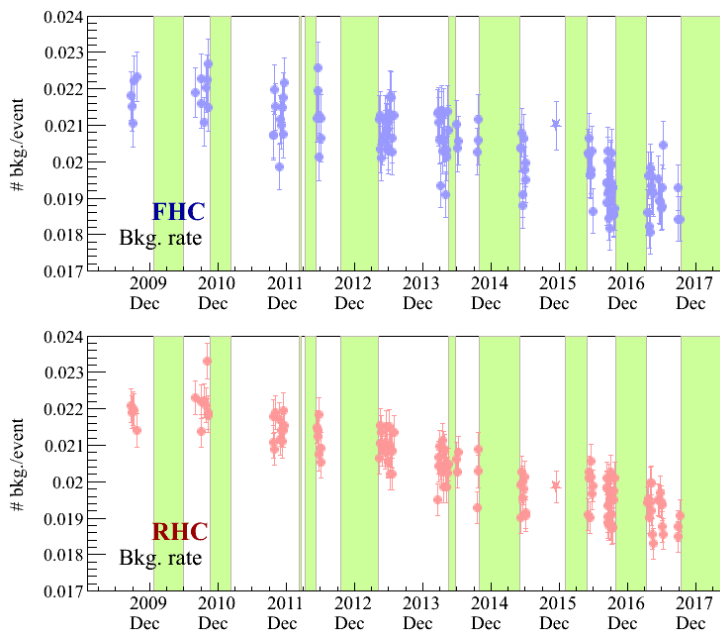
Figure 6.32: Background event rate after the NN classification as a function of time. The top panel and bottom panel correspond to the FHC and RHC $1\mathrm{R}\nu_\mu$ MC samples, respectively. The error bars represent the MC statistical errors. The green bands show the Runs 1-9 data taking periods.
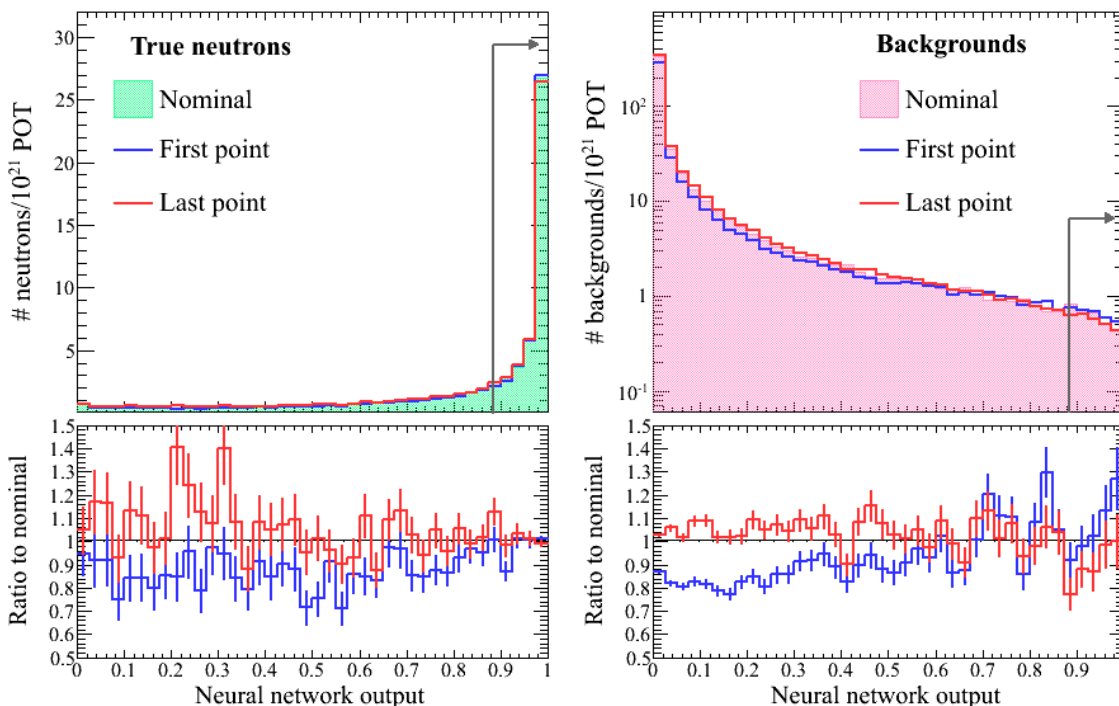
Figure 6.33: Comparison of the NN output distributions between the different regeneration points. Left and right correspond to the true neutron and accidental background events, respectively. The arrow shows the cut position of the NN output.

6.5.3 Correction of the time variation effects

The time evolution of both the tagging efficiency and background event rate is likely to be smooth on average as it can be seen in Figure 6.31 and Figure 6.32. The time evolution during the Run 1-9 data taking periods is therefore extrapolated by a fit to the regenerated MCs and then, the fit result is used to correct the nominal tagging efficiency and background event rate.

The effect of the time variations is probably common among the FHC and RHC $1R\nu_\mu$ samples, because there is no reason which differentiates the two samples in terms of the detector time variations. Thus, it is assumed that the effect is common between the two samples, so that there are common parameters which characterize the time evolution of the two samples. The tagging efficiency and background event rate as a function of time are parameterized as follows:

$$\varepsilon(t) = \varepsilon_0 \left[1 + a_1 \times (t - t_0) + a_2 \times (t - t_0)^2 \right], \tag{6.5.1}$$

$$B(t) = B_0 \left[1 + b_1 \times (t - t_0) \right], \tag{6.5.2}$$

where t_0 is the time where the nominal MC is generated, a_1, a_2 and b_1 account for the time evolution and are common parameters between the two samples, and ε_0 and B_0 are the tagging efficiency and background event rate at t_0, respectively.

The tagging efficiencies and background event rates of the regenerated MCs as well as that of the nominal MC are fitted by Equation 6.5.1 and 6.5.2, respectively. The χ^2 used for this fit is given as:

$$\chi^2(\boldsymbol{\theta}) = \sum_i^{\text{FHC/RHC}} \sum_j^{N_{rege}} \left(\frac{X_{i,j}^{rege} - X_i^{Exp}(t_j; \boldsymbol{\theta})}{\delta X_{i,j}^{rege}} \right)^2, \tag{6.5.3}$$

where

$$\boldsymbol{\theta} \text{ (for tagging efficiency)} = \begin{pmatrix} \varepsilon_0^{FHC} \\ \varepsilon_0^{RHC} \\ a_1 \\ a_2 \end{pmatrix}$$

$$\boldsymbol{\theta} \text{ (for background rate)} = \begin{pmatrix} B_0^{FHC} \\ B_0^{RHC} \\ b_1 \end{pmatrix},$$

X denotes tagging efficiency or background event rate, X^{Exp} is expected value, X^{rege} is value evaluated by regenerated MC, δX is statistical error of X^{rege}, i runs over the FHC and RHC samples, j runs over the regeneration points including the nominal generation point, and t_j is the representative time of j-th regeneration point. It should be noted that the FHC and RHC samples are fitted simultaneously. The minimization of the χ^2 fits are done by the MINUIT algorithm [212] implemented in the ROOT Minuit2 libraries.

After this fit, the best fit results are used to correct the nominal tagging efficiency and background event rate. The correction is performed by considering the different accumulated POT among the MR runs of Run 1-9 as a T2K Run consists of several MR (Main Ring) runs. The corrected numbers are the POT weighted average given as:

$$X^{\text{Run1}-9} = \frac{\sum_i^{\text{MR runs}} \text{POT}_i \times X^{\text{Best}}(t_i^M)}{\sum_i^{\text{MR runs}} \text{POT}_i}, \tag{6.5.4}$$

where i runs over the MR runs of the Run 1-9, POT_i is the total accumulated POT of i-th MR run, X^{Best} is either tagging efficiency or background event rate evaluated by the best fit parameters, and t_i^M is the time when the accumulated POT of i-th MR run reaches 50 percentile. Figure 6.34 and 6.35 show the best fit results and
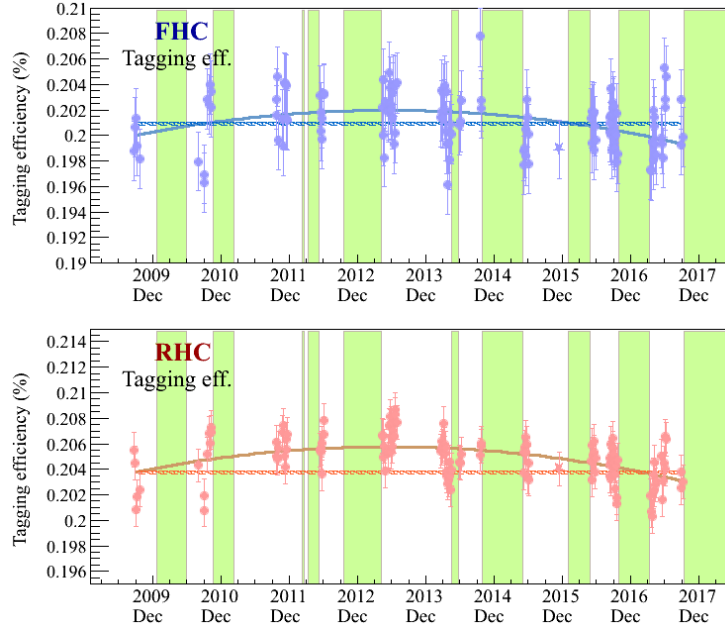
Figure 6.34: The fitted tagging efficiency (left) and the POT weighted averages. The top panel and bottom panel correspond to the FHC and RHC 1Rν_μ samples. The solid curves and broken lines correspond to the best fit results and POT weighted average, respectively. The green bands show the Run 1-9 data taking periods.

Figure 6.35: The fitted background event rate (left) and the POT weighted averages. The top panel and bottom panel correspond to the FHC and RHC $1R\nu_\mu$ samples. The solid curves and broken lines correspond to the best fit results and POT weighted average, respectively. The green bands show the Run 1-9 data taking periods.

the POT weighted averages of the tagging efficiency and background event rate. The $\chi^2/n.d.f$ for the best fit was obtained to be $258.3/254$ and $263.7/255$ for the tagging efficiency and background event rate, respectively. These reasonable value of the reduced χ^2 are consistent with the assumption that the time variation effects are common between the FHC and RHC samples.

Table 6.2 summarizes the tagging efficiencies and background rates before and after the correction. Although the same time evolution is assumed between the FHC and RHC 1R ν_μ samples, the size of the time variation effect is different. This difference arises from the different data taking periods between the FHC and RHC modes. Figure 6.36 shows the POT weights used for the calculation of the averages. For the FHC sample all the Run 1-9 data taking periods contribute the calculation, whereas only the data taking periods after 2014 contribute to the calculation of the RHC sample. Note that the corrected numbers will be used to derive the central values for the neutron measurement described in Chapter 8.

Table 6.2: Tagging efficiencies and background event rates with and without the correction of the time variation effect. The numbers for the nominal are same as summarized in Table 6.1.

		Nominal	Corrected	(Cor. - Nom.)/Nom. (%)
Tagging Efficiency (%)	FHC	19.89	20.09	+0.98
	RHC	20.40	20.37	-0.16
Background rate	FHC	2.10×10^{-2}	2.02×10^{-2}	-3.83
	RHC	1.98×10^{-2}	1.94×10^{-2}	-2.44
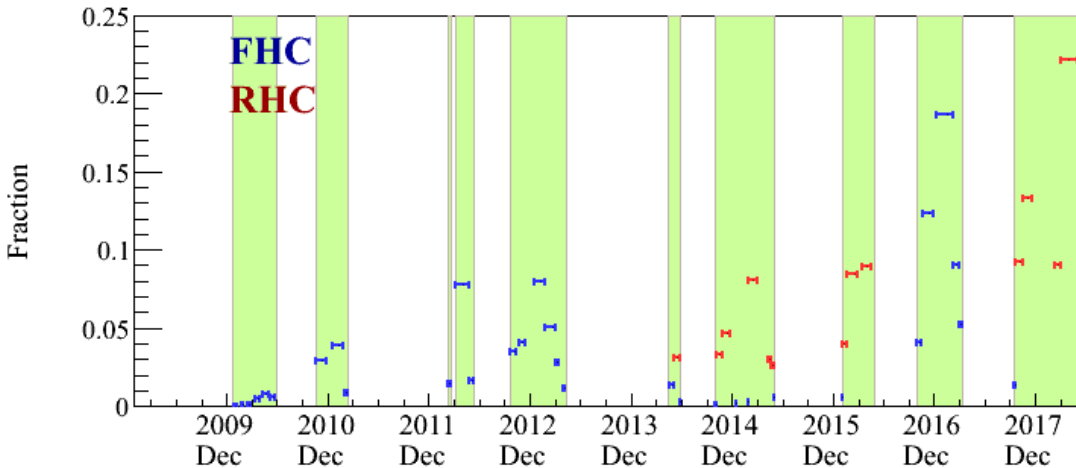
Figure 6.36: Fraction of POT which is computed by dividing the total accumulated POT of each individual MR run by the total Runs $1-9$ POT. The green bands show the Run 1-9 data taking periods.

6.5.4 Statistical uncertainties

The statistical errors on the POT weighted averages need to be considered. As the FHC and RHC $1R\nu_\mu$ samples are simultaneously fitted, there are correlations among the fit parameters. The left and right panels of Figure 6.37 show the correlation matrices for the fit parameters of the tagging efficiency and background rate, respectively. As shown in the figure, the FHC and RHC parameters are correlated, which means that the POT weighted averages are also correlated.

In order to estimate the statistical errors on the averages with the correlations, random throws of the fit parameters are performed using the fit results. The throws are done assuming that the fit parameters are treated as a multivariate Gaussian whose covariance matrix is the one calculated by MINUIT. For each random throw, POT weighted average is computed for the fit parameters which are sampled from the Gaussian using the Cholesky decomposition and then, fractional difference from the POT weighted average for the best fit parameters is calculated.

The random throws were repeated by 200,000 times separately for the tagging

efficiency and background event rate, respectively. The resultant distributions of the fractional differences are made and are shown in Figure 6.38. The resulting 1σ error is computed from the 68% area surrounding the peak of the distribution as in the figure and is estimated to be less than 0.05% and 0.3% for the efficiency and background rate, respectively. Note that the statistical error of each regenerate MC is about $\sim1\%$ and $\sim3\%$ for the tagging efficiency and background rate, respectively, which means that the correction of the time variations by the fit effectively increases MC statistics.
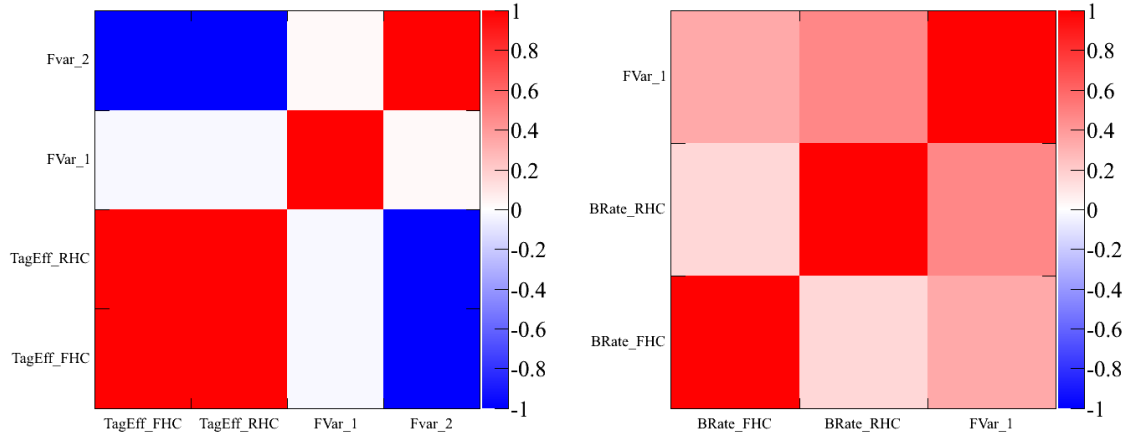
Figure 6.37: Correlation matrices for the parameters of the tagging efficiencies (left) and the background rates (right). In the left side, "TagEff_FHC", "TagEff_RHC", "FVar_1", and "FVar_2" correspond to ε_0^{FHC}, ε_0^{RHC}, a_1, a_2, respectively. In the right side, "BRate_FHC", "BRate_RHC", "FVar_1" correspond to B_0^{FHC}, B_0^{RHC}, b_1, respectively. These paramters are defined in Equation 6.5.3. The matrices are derived from the corresponding covariance matrices calculated by MINUIT.
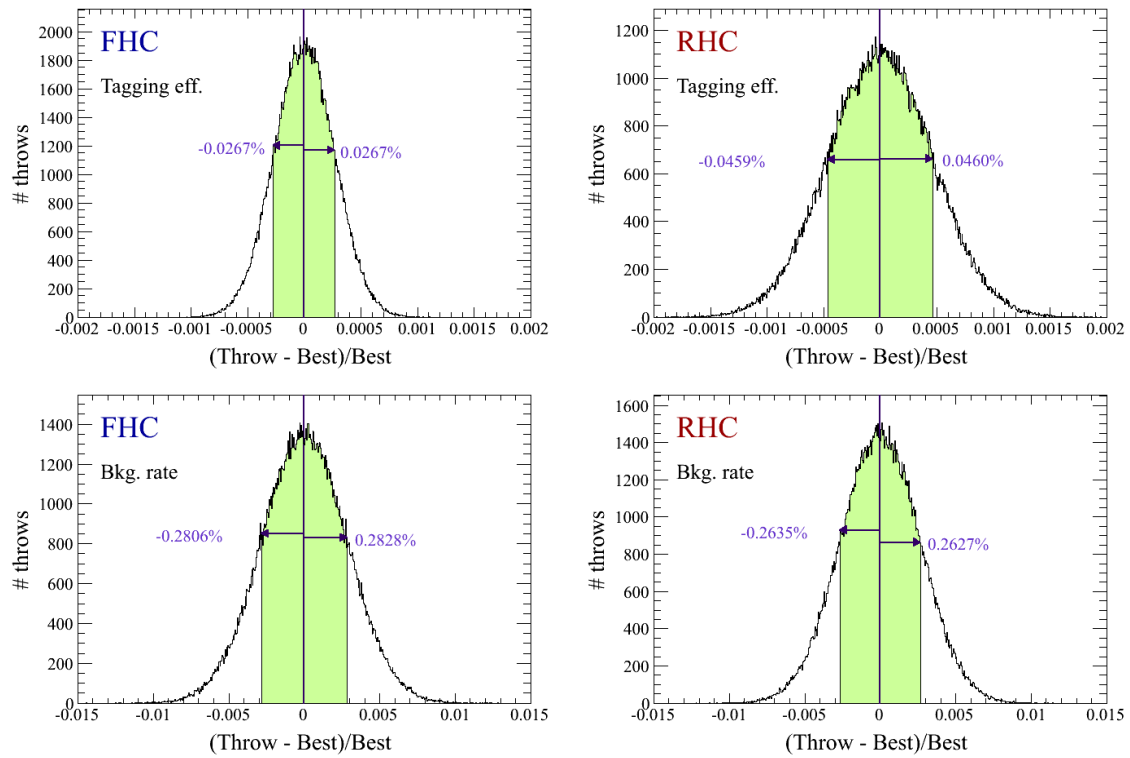
Figure 6.38: Distribution of the fractional errors obtained by throwing the parameters.

Chapter 7

First application of neutron tagging to T2K data

Since the beginning of the first data taking in January 2010, T2K has finished the data taking until Run 9 which ended in May 2018. The collected data has been used for both the neutrino oscillation analyses and the studies on neutrino-nucleus scattering. However, neutrons associated with neutrino and antineutrino interactions in water had never been studied until the primary analysis of this thesis was performed.

In this chapter, the first application of neutron tagging to the T2K data is presented. Prediction of event rate at the far detector is overviewd in Section 7.1, and the selection criteria of the $1R\nu_\mu$ sample used in the primary analysis is described in Section 7.2. Following this, the results of the event selection for the T2K data collected until 2018 is summarized in Section 7.3. Section 7.4 describes the data quality checks in terms of neutron tagging. A set of comparisons between the data and the MC predictions for the detected neutrons is given in Section 7.5.

7.1   Prediction of event rate

The observed neutrino events and the tagged neutrons accompanying the primary neutrino events are compared with the corresponding predictions. For a neutrino flavor which is created as ν_α at J-PARC and is detected as ν_β at the far detector due to neutrino oscillation, the expected number of neutrino events in bins of some observables Θ such as reconstructed neutrino energy, $N_\nu(\Theta)$, is given as:

$$N_\nu(\Theta) = \mathcal{C} \int \Phi(E_\nu)\sigma(E_\nu)P_{\nu_\alpha \to \nu_\beta}(E_\nu)\epsilon(E_\nu)U(E_\nu,\Theta)dE_\nu, \qquad (7.1.1)$$

where $\mathcal{C}$ takes into account the target volume, E_ν is the true energy of the incoming neutrino, $\Phi(E_\nu)$ is the incoming neutrino flux, $\sigma(E_\nu)$ is the neutrino interaction cross section, $P_{\nu_\alpha \to \nu_\beta}(E_\nu)$ is the neutrino oscillation probability, $\epsilon(E_\nu)$ is the detection efficiency by the far detector, $U(E_\nu,\Theta)$ describes how a neutrino with an energy of E_ν is reconstructed in Θ.

Similarly, the expected number of tagged neutrinos accompanying the expected

neutrino events $N_\nu(\Theta)$ is as follows:

$$N_{ntag}(\Theta) = \mathcal{C} \int \Phi(E_\nu)\sigma(E_\nu)P_{\nu_\alpha \to \nu_\beta}(E_\nu)\epsilon(E_\nu)U(E_\nu, \Theta) \times Y(E_\nu)\varepsilon_{ntag}(E_\nu)dE_\nu,$$

$$(7.1.2)$$

where $\varepsilon_{ntag}(E_\nu)$ is the neutron tagging efficiency and $Y(E_\nu)$ is the inclusive neutron yield which includes all the contributions from primary ν-nucleon interactions, hadronic FSI inside oxygen nucleus, and hadronic SI in water.

These calculations are performed based on MC simulations described in Chapter 4. In practice, MC simulations are performed without the effect of neutrino oscillation by using "nominal" beam fluxes and neutrino interaction cross sections. Then, later the oscillation effect and other effects such beam flux tunings and corrections of neutrino interaction cross sections are taken into account by assigning a proper weight on an event-by-event basis. This scheme enables saving computational time.

In order to compute the oscillation probability, the neutrino oscillation parameters in Table 7.1 are used throughout in the remaining part of this thesis except in Section 8.3.9, where systematic uncertainty on neutron tagging efficiency due to uncertainties on oscillation parameters is described. Prob3++ [213] is used to calculate the oscillation probability by considering the Earth's matter effect based on [80]. Since the current T2K oscillation analyses do not use information about neutron tagging, the results of the analyses are applicable for the primary analysis of this thesis.

Table 7.1: Parameters used for calculation of oscillation probabilities. The values of Δm_{21}^2 and $\sin^2 \theta_{12}$ are from [35]. The value of $\sin^2 \theta_{13}$ is from [34]. The values of the other parameters are based on the results of a T2K neutrino oscillation analysis using the data taken until 2018 [36].

Parameter	value
Δm_{21}^2	7.53×10^{-5} eV^2
Δm_{32}^2	2.452×10^{-3} eV^2
$\sin^2 \theta_{12}$	0.304
$\sin^2 \theta_{23}$	0.532
$\sin^2 \theta_{13}$	0.0212
δ_{CP}	-1.885
Mass hierarchy	NH

7.2   Definition of analysis sample

The primary analysis in this thesis aims to study and measure neutrons associated with neutrino interactions on water target. It is therefore important to use ν event

sample which is well known, studied, and established in terms of neutrino interaction cross sections and neutrino fluxes.

The FHC and RHC 1R ν_μ samples used for the T2K neutrino oscillation analyses [140] are suitable for this purpose. The samples mainly consist of CCQE interaction described in Equation 1.2.2 and contain a high purity of ν_μ and $\bar{\nu}_\mu$ events for the FHC and RHC modes, respectively. Since the selection criteria of these samples were optimized by considering uncertainties on cross sections and fluxes [214, 215], the same selection criteria are adopted for this thesis except for the definition of the fiducial volume (FV).

The same criteria are used for both the FHC sample and the RHC sample and are given as:

1. Fully-contained in the SK ID and reconstructed inside the fiducial volume which is defined by $Dwall > 2\,\mathrm{m}$,

2. Number of rings found is one,

3. The ring is identified as a muon-like,

4. Reconstructed momentum $> 200\,\mathrm{MeV/c}$,

5. Number of tagged decay electrons is ≤ 1,

6. Not charged pions like,

where $Dwall$ is the closest distance between the ν vertex and the ID wall. It should be noted that the FV used for the oscillation analyses is defined as $Dwall > 50\,\mathrm{cm}$ and $Towall > 250\,\mathrm{cm}$, where $Towall$ is the nearest distance from the ν vertex to the ID wall along the particle direction.

The current FV used for the T2K oscillation analyses has been optimized to their sensitivity. However, this analysis aims to measure neutrons associated with neutrino interactions on water target rather than oscillation parameters. Thus, the FV of this analysis needs to be determined in terms of neutron tagging.

Neutrons escape from the ID volume depending on their energies and their production points inside ID, and the fraction of these neutrons is dependent on MC simulations. Figure 7.1 shows this fraction as a function of $Dwall$ reconstructed by the fiTQun vertex (i.e. reconstructed ν interaction vertex position) for three different MC neutrino event generators: NEUT, NuWro, and GENIE. It becomes rapidly low when $Dwall < 1\,\mathrm{m}$ and the difference between the generators also becomes large for all the three event generators. As this analysis uses the whole FV to measure neutrons (i.e. neutron tagging efficiency is averaged over FV), the fraction of escaping neutrons as a function of fiducial volume also needs to be considered, and this is shown in Figure 7.2. As shown in the figure, the fraction of the escaping neutrons over the whole FV is less than 0.5% when setting the $Dwall$ cut value to $2\,\mathrm{m}$.
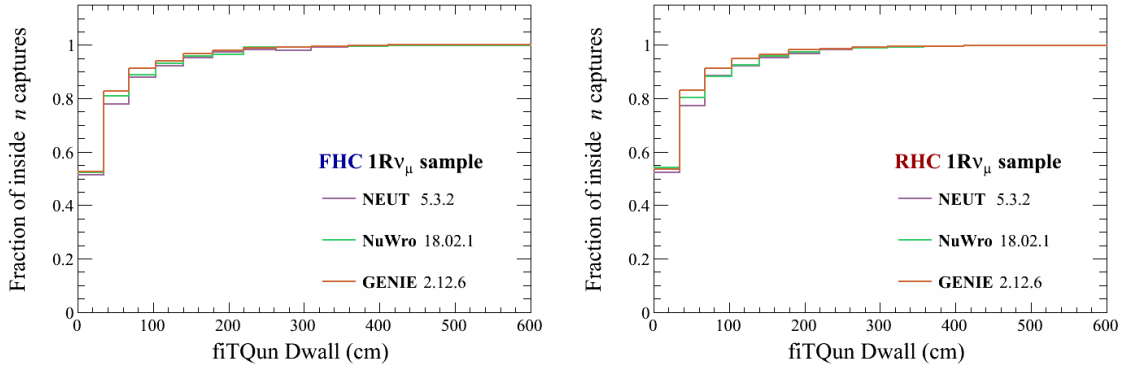
Figure 7.1: Fraction of the neutron captures which happened inside ID as a function of *Dwall* for the three different ν event generators. The left and right correspond to the FHC and RHC 1Rν_μ samples, respectively. *Dwall* is the nearest distance between the ν vertex and ID wall. The analysis cuts (better selection) described in this section are applied except for the FV cut.
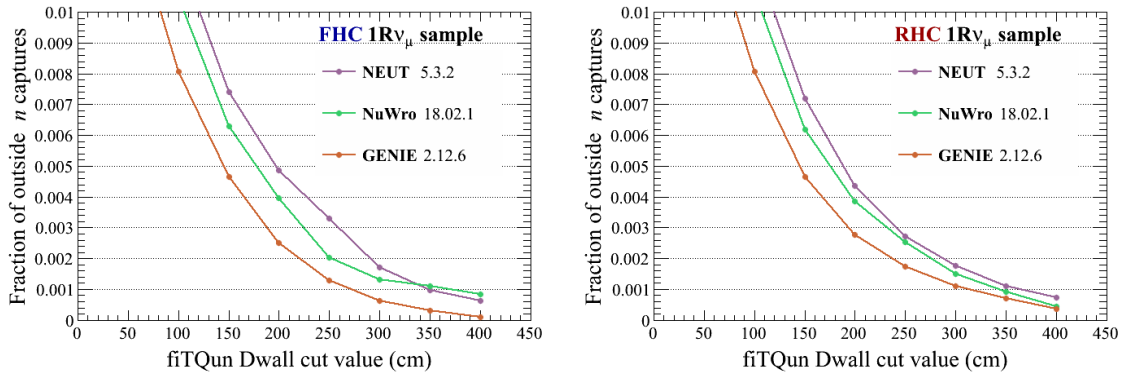
Figure 7.2: Fraction of the neutron captures which happened outside the ID as a function of *Dwall* cut value (i.e. fiducial volume) for the three different ν event generators. The left and right correspond to the FHC and RHC 1Rν_μ samples, respectively. *Dwall* is the nearest distance between the ν vertex and ID wall. The analysis cuts (better selection) described in this section are applied except for the FV cut.

In addition, the neutron tagging efficiency and the background rate need to be taken into account, because these are position dependent in ID. As shown in Figure 7.3, the tagging efficiency becomes very low below at *Dwall* < 2 m region, whereas the background event rate does not. Based on the escaping neutrons from ID and the position dependence of the performance of the neutron tagging, the fiducial volume used for this analysis was defined as *Dwall* > 2 m only.
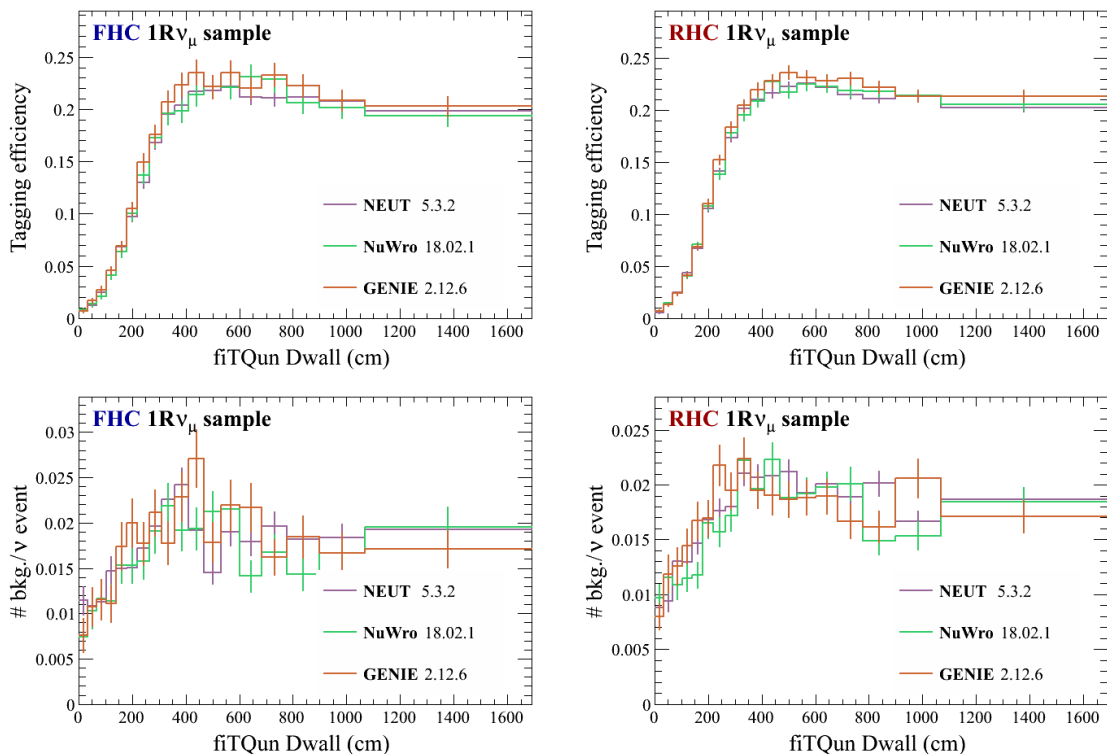
Figure 7.3: Neutron tagging efficiency (top) and background event rate (bottom) as a function of *Dwall* for the three different ν event generators. *Dwall* is the nearest distance between the ν vertex and ID wall. The right and left side plots are for the FHC and RHC $1R\nu_\mu$ samples, respectively. The analysis cuts (better selection) described in this section are applied except for the FV cut.

7.3 Event selection for data collected until 2018

This section summarizes the results of the event selection for the Run 1-9 data. In the remaining part of this section, for all the MC expectations related to neutron tagging, the correction to the time variation effects described in Section 6.5 is considered.

The $1R\nu_\mu$ cuts described in Section 7.2 are applied to the FC samples of the FHC and RHC Run 1-9 data. Figure 7.4 and 7.4 show the distributions of the variables used in the $1R\nu_\mu$ selection for FHC and RHC, respectively. As shown in the figures, the data show a good agreement with the corresponding MC expectations at each selection stage. This can be clearly seen in Figure 7.6, which summarizes the number of ν events at each selection stage and the resultant selection efficiency from the first selection, the FCFV cut. From this figure, it can be found that the MC expectations well reproduce the observations for the neutrino events. On the one hand, however, the MC expectation has overpredicted the tagged neutrons for all the selection stages as shown in Figure 7.7.
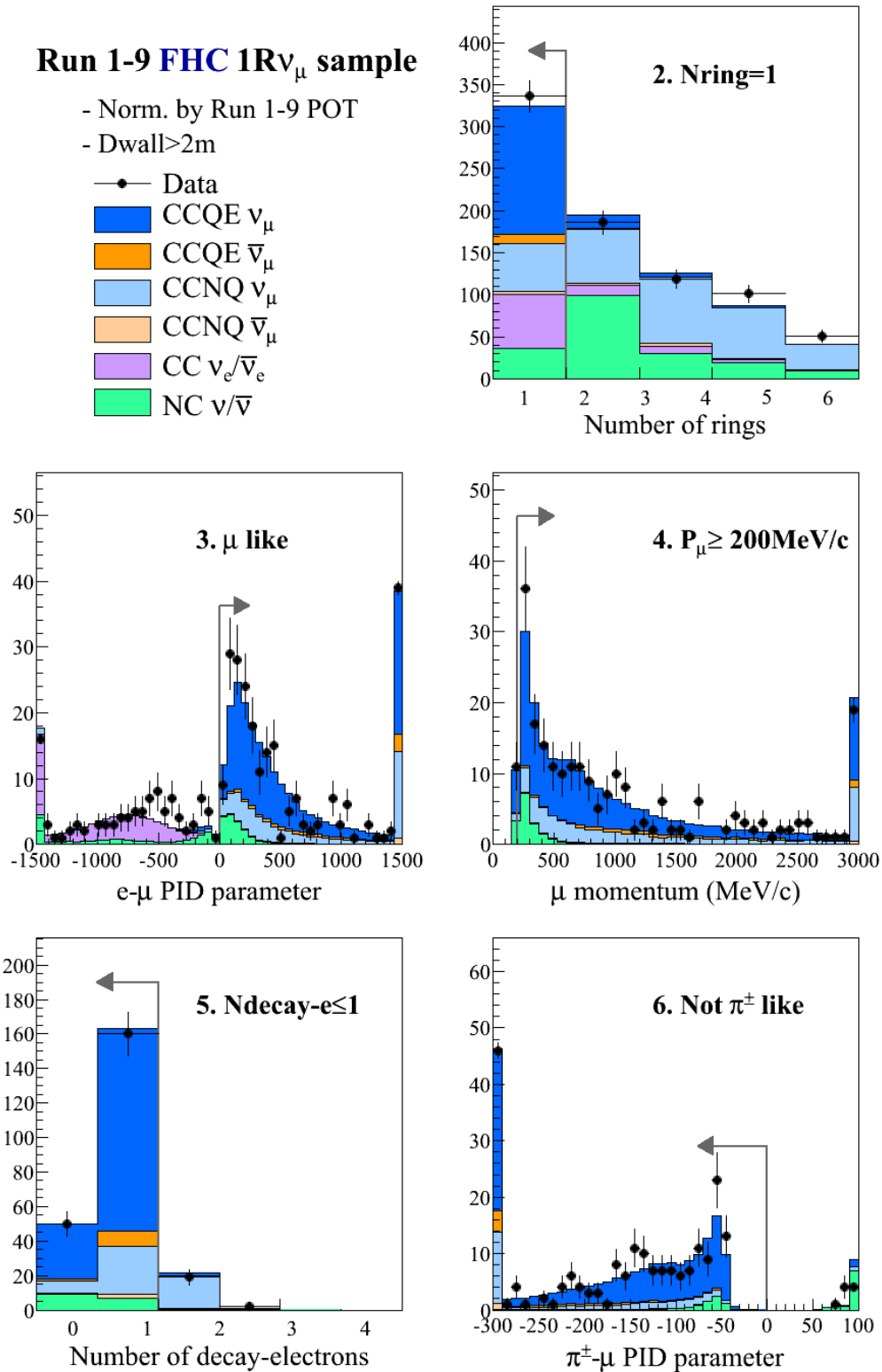
Figure 7.4: Distributions of the variables used in the $1R\nu_\mu$ selection for the FHC mode. The vertical axes represent the number of observed neutrino events. The selection criteria and their order are described in Section 7.2. The arrows indicate the cut positions. All the MC distributions are normalized by the Run 1-9 POT.
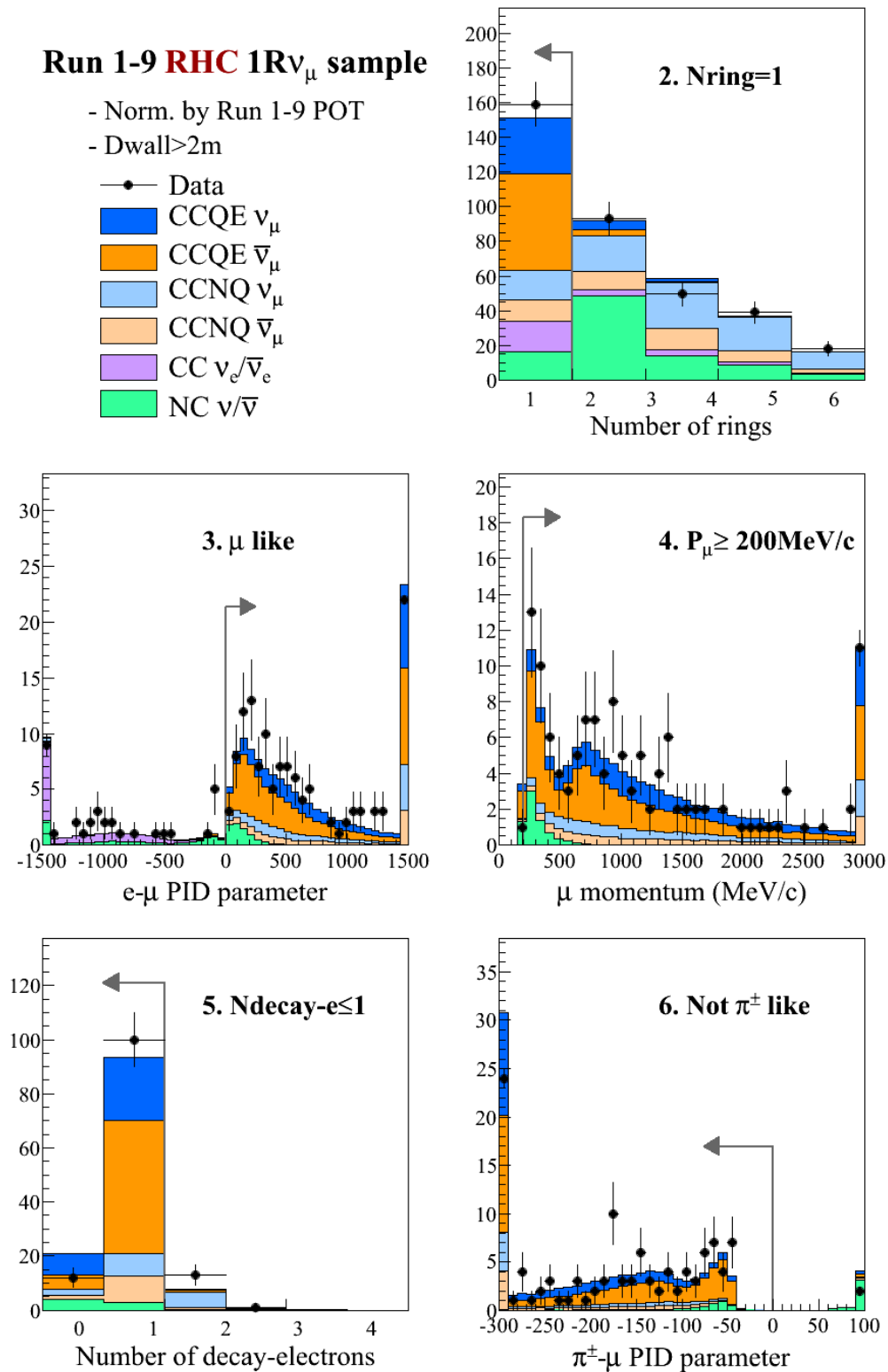
Figure 7.5: Distributions of the variables used in the 1Rν_μ selection for the RHC mode. The vertical axes represent the number of observed neutrino events. The selection criteria and their order are described in Section 7.2. The arrows indicate the cut positions. All the MC distributions are normalized by the Run 1-9 POT.

141
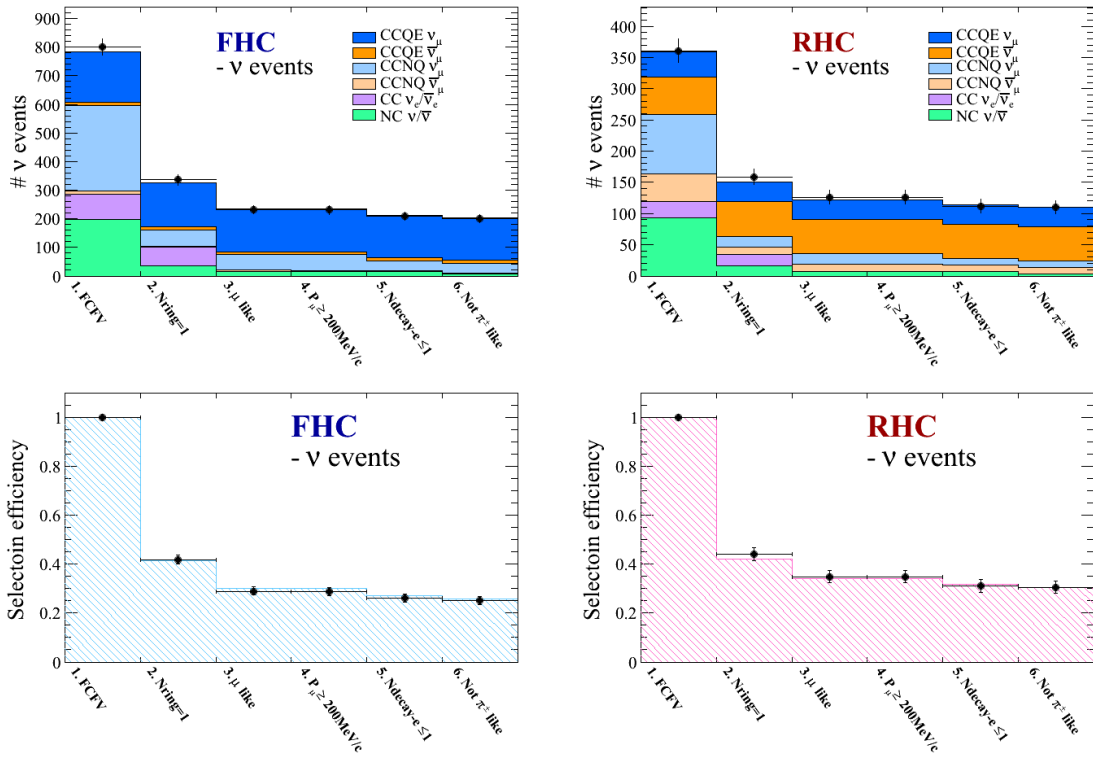
Figure 7.6: Number of ν events (top) and the corresponding selection efficiencies from the FCFV cut (bottom) for each selection stage. The left and right side plots correspond to the FHC and RHC $1R\nu_\mu$ samples, respectively. The MC expectations are normalized by the Run 1-9 POT.
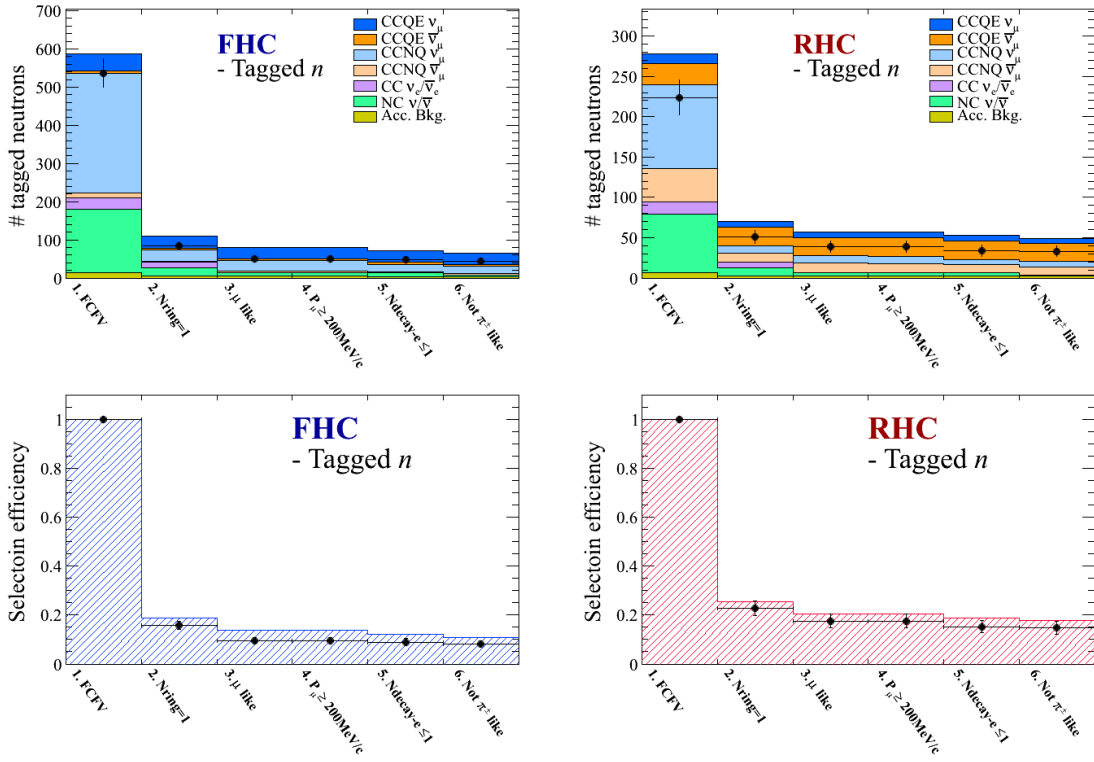
Figure 7.7: Number of tagged neutrons (top) and the corresponding selection efficiencies from the FCFV cut (bottom) for each selection stage. The left and right side plots correspond to the FHC and RHC $1R\nu_\mu$ samples, respectively. The MC expectations are normalized by the Run 1-9 POT.

Table 7.2 and Table 7.3 summarize the observed numbers in comparison to the corresponding Run 1-9 MC expectations for the FHC and RHC $1R\nu_\mu$ samples, respectively. The efficiencies from the FCFV cut for both ν events and tagged neutrons are also summarized in Table 7.4 and Table 7.5, respectively. As described in the tables, the difference in the selection efficiency of the tagged neutrons between the data and the MC prediction is yielded at the single-ring cut for both the FHC and RHC samples. Since most of the NC and CC non-QE events are removed by this cut, the difference could indicate that the fraction of tagged neutrons regarding NC and CC non-QE interactions is different between the data and MC expectations.

Table 7.2: Expected numbers of tagged neutrons N_{tag} and ν events $N_{1\mu}$ passing each selection stage in comparison to the FHC data taken in Run 1-9. The expected numbers are normalized by the Run 1-9 POT.

		CCQE ν_μ	CCQE $\bar{\nu}_\mu$	CCNQ ν_μ	CCNQ $\bar{\nu}_\mu$	CC $\nu_e/\bar{\nu}_e$	NC $\nu/\bar{\nu}$	Total	Acc. bkg.	Data
FCFV	$N_{1\mu}$	175.90	11.41	297.98	12.33	87.96	197.36	782.95	N/A	801
	N_{tag}	44.72	5.71	314.35	12.22	29.31	166.29	572.59	14.26	537
$N_{ring}=1$	$N_{1\mu}$	152.80	10.24	57.90	3.20	63.88	36.53	324.55	N/A	336
	N_{tag}	30.80	4.95	29.86	3.10	14.13	20.62	103.46	6.05	85
μ-like	$N_{1\mu}$	150.75	10.17	55.04	3.14	0.04	16.78	235.93	N/A	232
	N_{tag}	30.48	4.93	27.76	3.05	0.01	10.29	76.52	4.42	51
$P_\mu \geq 0.2 \text{GeV/c}$	$N_{1\mu}$	150.64	10.17	55.01	3.14	0.04	16.59	235.59	N/A	231
	N_{tag}	30.47	4.93	27.74	3.05	0.01	10.23	76.43	4.41	51
$N_{\text{decay}-e} \leq 1$	$N_{1\mu}$	149.07	10.05	34.71	2.88	0.04	16.12	212.87	N/A	210
	N_{tag}	29.43	4.85	19.86	2.77	0.01	9.57	66.49	4.02	48
Not $\pi^\pm$-like	$N_{1\mu}$	147.68	10.00	33.81	2.85	0.04	7.74	202.12	N/A	201
	N_{tag}	29.05	4.83	19.45	2.75	0.01	4.11	60.20	3.88	44

Table 7.3: Expected numbers of tagged neutrons N_{tag} and ν events $N_{1\mu}$ passing each selection stage in comparison to the RHC data taken in the Run 5-9. The expected numbers are normalized by the Run 5-9 POT.

		CCQE ν_μ	CCQE $\bar{\nu}_\mu$	CCNQ ν_μ	CCNQ $\bar{\nu}_\mu$	CC $\nu_e/\bar{\nu}_e$	NC $\nu/\bar{\nu}$	Total	Acc. bkg.	Data
FCFV	$N_{1\mu}$	39.84	59.91	95.49	44.30	26.69	92.82	359.05	N/A	361
	N_{tag}	12.30	25.79	103.62	42.14	14.77	72.44	271.06	6.78	224
$N_{ring}=1$	$N_{1\mu}$	32.01	55.60	17.04	12.29	17.60	16.54	151.07	N/A	159
	N_{tag}	7.35	22.94	9.59	11.32	7.06	9.34	67.61	2.83	51
μ-like	$N_{1\mu}$	31.81	54.99	16.38	12.02	0.01	7.26	122.46	N/A	126
	N_{tag}	7.31	22.74	9.09	11.14	0.00	4.76	55.05	2.27	39
$P_\mu \geq 0.2 \text{GeV/c}$	$N_{1\mu}$	31.81	54.96	16.37	12.02	0.01	7.19	122.35	N/A	126
	N_{tag}	7.31	22.73	9.09	11.14	0.00	4.72	54.99	2.27	39
$N_{\text{decay}-e} \leq 1$	$N_{1\mu}$	31.40	54.33	10.57	11.06	0.01	6.97	114.33	N/A	112
	N_{tag}	7.09	22.35	6.36	10.20	0.00	4.48	50.48	2.12	34
Not $\pi^\pm$-like	$N_{1\mu}$	31.17	53.91	10.37	10.89	0.01	3.25	109.61	N/A	110
	N_{tag}	7.01	22.20	6.23	10.07	0.00	1.87	47.39	2.03	33

Table 7.4: Summary of selection efficiencies from the FCFV cut for the FHC $1R\nu_\mu$ sample. Expected numbers are compared to the data taken in the Run 1-9 data. The errors on the data are binomial statistical errors and are calculated by Bayesian approach with a flat prior.

	Expected		Data	
	$N_{1\mu}$	N_{tag}	$N_{1\mu}$	N_{tag}
FCFV	1.000	1.000	1.000	1.000
$N_{ring} = 1$	0.415	0.187	0.419 $\left(^{+0.018}_{-0.018}\right)$	0.158 $\left(^{+0.017}_{-0.016}\right)$
μ-like	0.301	0.138	0.290 $\left(^{+0.017}_{-0.016}\right)$	0.095 $\left(^{+0.014}_{-0.013}\right)$
$P_\mu \geq 0.2\mathrm{GeV/c}$	0.301	0.138	0.288 $\left(^{+0.017}_{-0.016}\right)$	0.095 $\left(^{+0.014}_{-0.013}\right)$
$N_{\mathrm{decay-e}} \leq 1$	0.272	0.120	0.262 $\left(^{+0.016}_{-0.016}\right)$	0.089 $\left(^{+0.014}_{-0.012}\right)$
Not $\pi^\pm$-like	0.258	0.109	0.251 $\left(^{+0.016}_{-0.016}\right)$	0.082 $\left(^{+0.014}_{-0.012}\right)$

Table 7.5: Summary of selection efficiencies from the FCFV cut for the RHC $1R\nu_\mu$ sample. Expected numbers are compared to the data taken in the Run 5-9 data. The errors on the data are binomial statistical errors and are calculated by Bayesian approach with a flat prior.

	Expected		Data	
	$N_{1\mu}$	N_{tag}	$N_{1\mu}$	N_{tag}
FCFV	1.000	1.000	1.000	1.000
$N_{ring} = 1$	0.421	0.254	0.440 $\left(^{+0.028}_{-0.027}\right)$	0.228 $\left(^{+0.032}_{-0.029}\right)$
μ-like	0.341	0.206	0.349 $\left(^{+0.027}_{-0.026}\right)$	0.174 $\left(^{+0.029}_{-0.026}\right)$
$P_\mu \geq 0.2\mathrm{GeV/c}$	0.341	0.206	0.349 $\left(^{+0.027}_{-0.026}\right)$	0.174 $\left(^{+0.029}_{-0.026}\right)$
$N_{\mathrm{decay-e}} \leq 1$	0.318	0.189	0.310 $\left(^{+0.026}_{-0.025}\right)$	0.152 $\left(^{+0.028}_{-0.024}\right)$
Not $\pi^\pm$-like	0.305	0.178	0.305 $\left(^{+0.026}_{-0.025}\right)$	0.147 $\left(^{+0.028}_{-0.024}\right)$

As a summary of the event selection for the Run 1-9 data, after all the selection stages, there are 201±14 (110±10) neutrino events in the FHC (RHC) $1R\nu_\mu$ data sample when 202.12 (109.61) events are expected. On the other hand, for the tagged neutrons 44±6.6 (33±5.7) tagged neutrons are observed in the FHC (RHC) $1R\nu_\mu$ data sample, whereas the expected number of tagged neutrons is 64.08 (49.42). It should be noted that in order to obtain these expected numbers, the values of "Total" needs to be added to the value of "Acc. bkg." in Table 7.2 and Table 7.3 since the former and the latter correspond to tagged true neutron events and accidental background events, respectively. These errors on the observation represent the Poisson statistical errors.

7.4   Quality checks for tagged neutrons

In the previous section, the first application of neutron tagging to the T2K data was presented, and for the tagged neutrons there is a relatively large discrepancy between the data and the MC expectations. However, such discrepancy could be caused by different behaviour of the neutron tagging algorithm between the data and the simulated events if such difference exists. Therefore, several studies were performed to check whether or not the neutron tagging algorithm does work properly for the data. In the following, the first part mentions the observed response for the NN classification and the stability of neutron tagging over the Run 1-9 data taking periods. The subsequent parts describe the studies on the distributions associated with the reconstructed neutron capture vertex and the neutron capture time distribution.

NN output distribution and tagged neutron rate

Figure 7.8 shows the observed distribution of NN output in comparison to the equivalent MC distribution. As shown in the figure clear peaks can be found around 0 and 1, which supports that the neural network does work and does distinguish between true neutron events and accidental backgrounds events. The distributions of the NN input variables before and after the NN classification can be found in Appendix B.
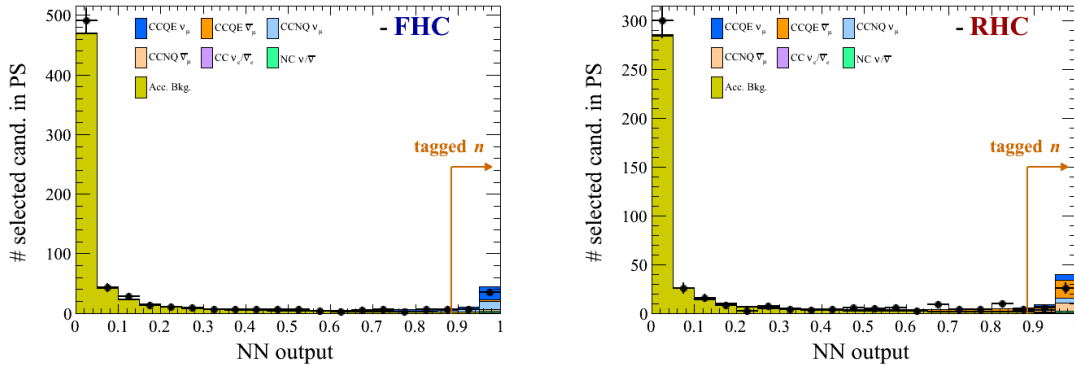
Figure 7.8: Distribution of the NN output for the Run 1-9 data overlaid with the corresponding MC distribution. The left and right side plots correspond to the FHC and RHC $1R\nu_\mu$ samples, respectively. The MC expectations are normalized by number of observed tagged neutrons.

Figure 7.9 shows the cumulative number of tagged neutrons as a function of accumulated POT. Since the cumulative numbers are assumed to be proportional to accumulated POT, the assumption needs to be validated. If the assumption was not reasonable enough, there would be a non-negligible time variation in neutron tagging. To validate this assumption, a Kolmogorov-Smirnov (KS) test is performed. In order to perform the test, an estimate of tagged neutron rate (i.e. number of tagged neutrons/POT) is needed to construct the null hypothesis. This is done based on the observed tagged neutrons, and thus the resulting rate is $0.295/10^{19}$ POT ($0.202/10^{19}$ POT) for the FHC (RHC) sample. The observed KS distance, which is the maximum

distance of the cumulative distribution function between the data and the data driven expectation, is 0.115 and 0.044 for the FHC and RHC samples, respectively. Using the KS distances, the KS p-value which is the probability obtaining the KS distance under the constant tagged neutron rate is estimated to be 63.4% and 75.1% for the FHC and RHC samples, respectively. It is concluded from the result that the observed cumulative distribution function is consistent with the assumption of the constant tagged neutron rate.
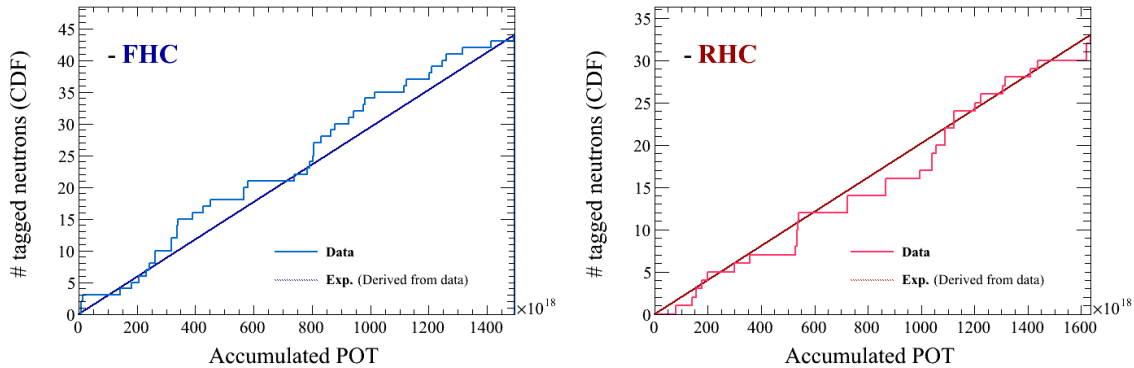
Figure 7.9: Cumulative number of tagged neutrons as a function of accumulated POT. The left and right side plots are for the FHC and RHC $1R\nu_\mu$ samples, respectively. The solid lines correspond to expectation which is derived from the number of observed tagged neutrons and Run 1-9 POT.

Neutron capture vertex distributions

As the neutron tagging algorithm reconstructs neutron capture vertex for each tagged neutron, vertex for the observed tagged neutrons can be studied. Figure 7.10 shows the two-dimensional distributions of the reconstructed neutron capture vertex for R^2-Z and X-Y. As shown in the figure, the observed distributions are likely to be distributed uniformly or are likely not to be clustered at a particular region.
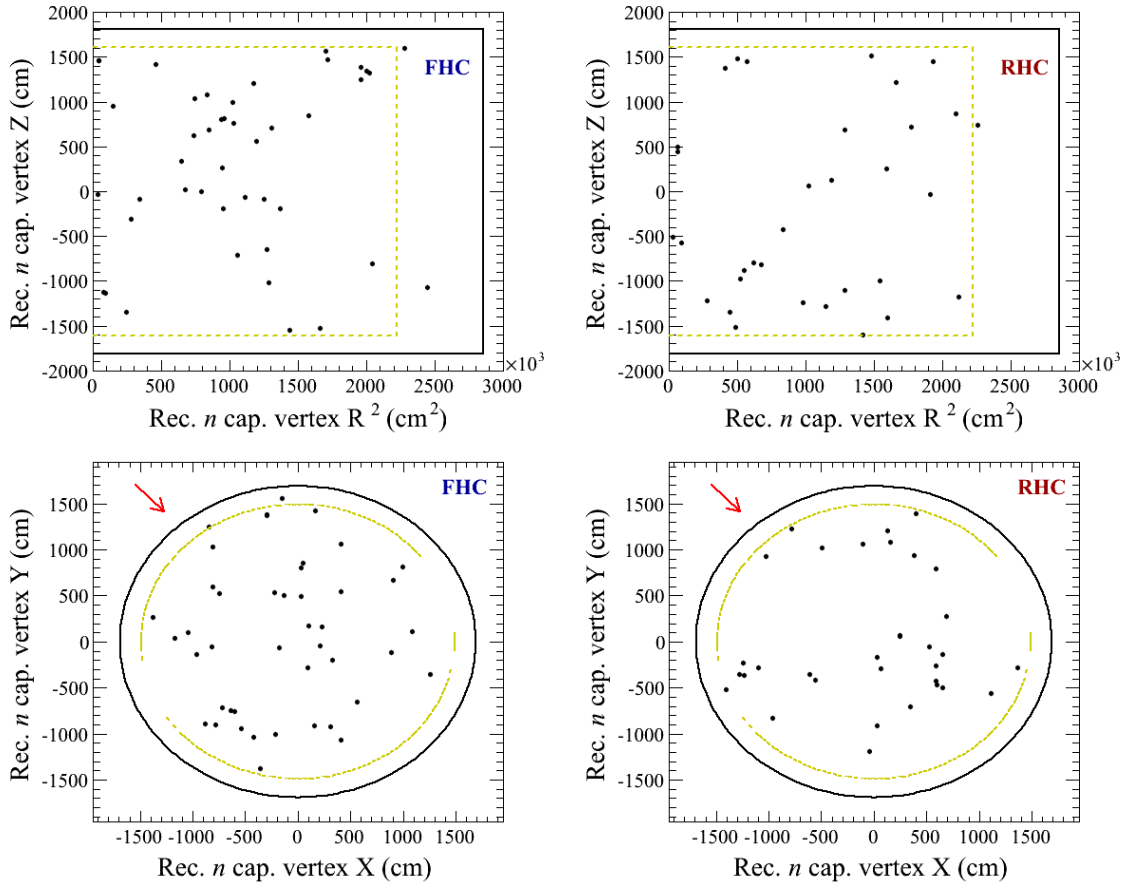
Figure 7.10: Two dimensional distribution of reconstructed neutron capture vertex distributions of the Run 1-9 data. The top and bottom figures show the distribution of the vertical vertex position versus the square of the radial distance and the vertex distribution projected onto the horizontal plane of the inner detector, respectively. The left and right side plots are for the FHC and RHC $1R\nu_\mu$ samples, respectively. The black solid lines represent the inner detector wall. The yellow broken lines represent the fiducial volume used in this analysis. The red arrows represent the beam direction in the SK coordinate.

Since the neutron tagging algorithm has a position dependence in the detector as shown Figure 7.3, shape of distribution associated with the reconstructed capture vertex is therefore determined by the dependence. In other words, difference in such shape between the data and the MC may indicates a bias in the neutron tagging algorithm if it exists. Therefore, there different statistical tests for shape comparison between two histograms was performed to quantify the level of agreement between the data and the MC.

For this test, one-dimensional distributions of the capture vertex, $Dwall$, R^2, and Z, are used. The $Dwall$ distribution may be useful to check if there is a bias for the discrimination of accidental backgrounds events, because most of these background events are populated on the inner detector wall. The R^2 and Z distributions can be utilized to validate the position dependence of the neutron tagging algorithm.

Figure 7.11 shows the *Dwall*, R^2, and Z distributions for the Run 1-9 data.
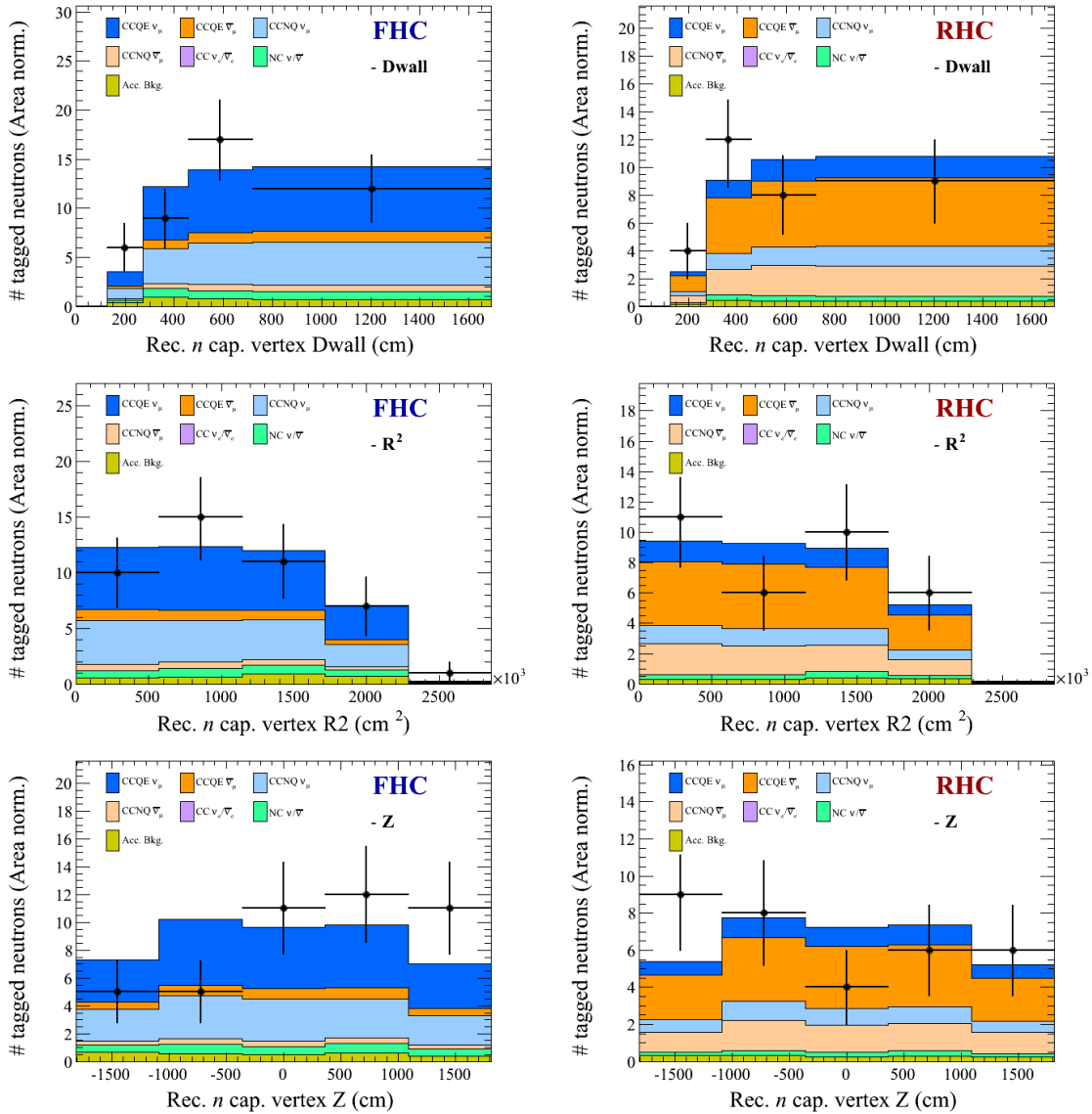
Figure 7.11: Distributions of the reconstructed neutron capture vertex for the Run 1-9 data. The left and right side figures correspond to the FHC and RHC $1R\nu_{\mu}$ samples, respectively. The top figures show the distribution of the distance from the reconstructed vertex to the closest ID wall. The middle figures show the distribution of the square of the radial distance in the SK ID. The bottom figures show the distribution of the vertical position in the SK ID. All the MC distributions are normalized by the number of observed tagged neutrons of the Run 1-9 data.

As shown in the figure, statistics of each bin content for all the distributions is not large enough to make a normal approximation, which means that in general there is no unique way to quantify the agreement between two histograms (i.e. the data and the MC). The agreement is therefore evaluated by three different non-parametric

methods:

- Kolmogorov-Smirnov (KS) test

- Cramer-von-Mises (CVM) test

- Anderson-Darling (AD) test

The test statistic for each test is derived from Ref. [216], and is given as:

$$
T_{\mathrm{KS}} = \max_i |E_i^{obs} - E_i^{exp}|
$$

$$
T_{\mathrm{CVM}} = \frac{1}{4} \sum_{i=1}^{k} (n_i^{obs} + n_i^{exp}) \left[E_i^{obs} - E_i^{exp} \right]^2 \qquad (7.4.1)
$$

$$
T_{\mathrm{AD}} = \sum_{i=k_{min}}^{k_{max}-1} \frac{(n_i^{obs} + n_i^{exp})}{(E_i^{obs} + E_i^{exp})(2 - E_i^{obs} - E_i^{exp})} \left[E_i^{obs} - E_i^{exp} \right]^2 ,
$$

where n_i is number of tagged neutrons of i-th bin, k_{min} and k_{max} are the first bin and the last bin where either histogram has non-zero counts, E_i is empirical cumulative distribution function and is defined as follows

$$
E_i = \frac{\sum_{j=1}^{i} n_j}{\sum_{j=1}^{\mathrm{All\ bins}} n_j}.
$$

In order to derive the above test statistics, all the MC distributions are normalized to the number of observed tagged neutrons, since the effect of statistical fluctuations on the shape comparison is taken into account by random throws in the following procedure.

The CVM and AD tests use the sum of the squared difference between the two cumulative distribution functions, whereas the KS test uses the maximum difference. The AD test is similar to the CVM test, but it is designed to be sensitive to the tails of a cumulative distribution function. It is therefore more sensitive to the *Dwall* and R^2 distributions compared to the other tests, because these distributions have tail structure.

Figure 7.12 shows the cumulative distribution functions of *Dwall*, R^2, Z for the Run 1-9 data.
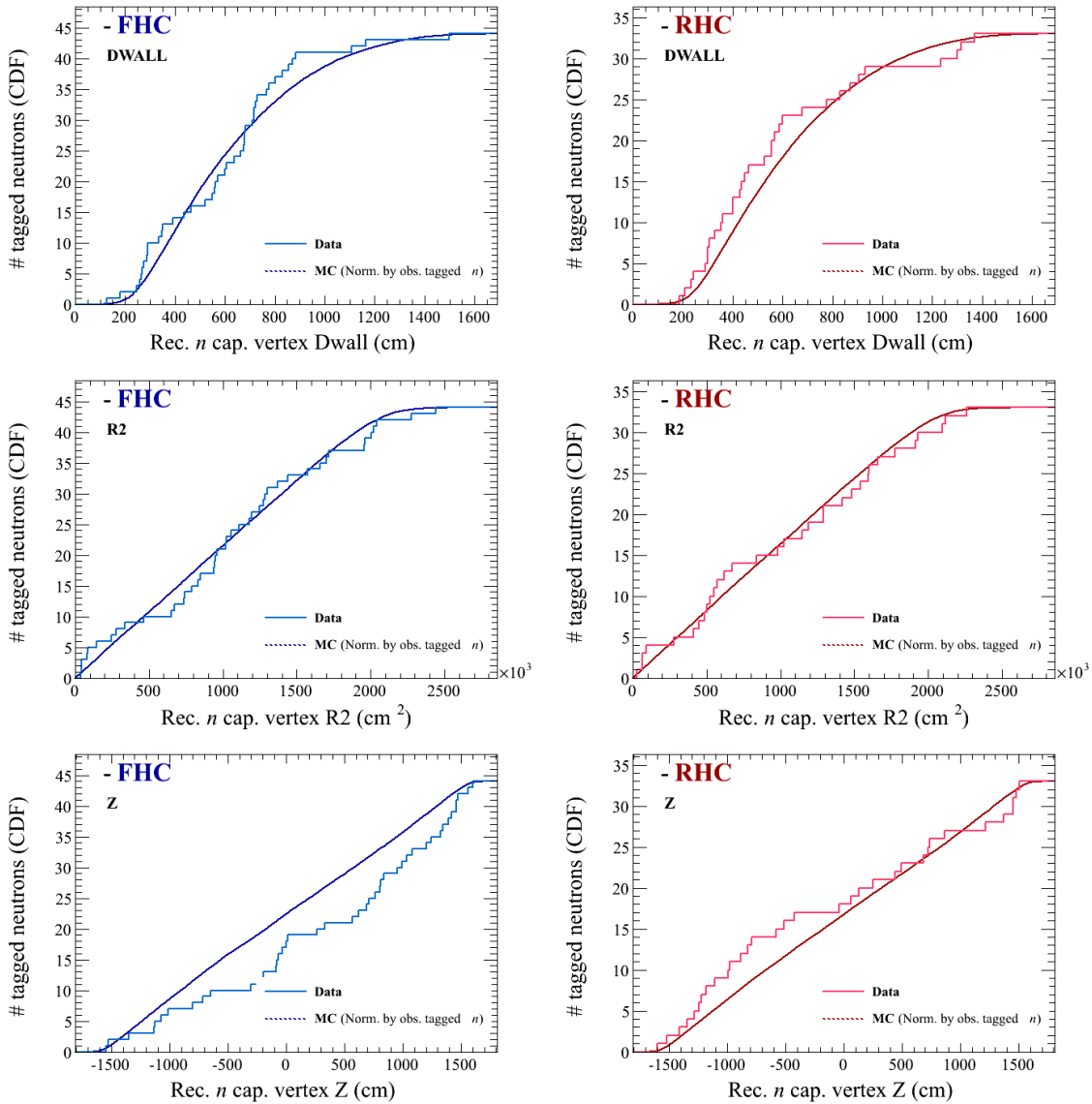
Figure 7.12: Cumulative distribution functions of the reconstructed neutron capture vertex distributions for the Run 1-9 data. The left and right side plots correspond to the FHC and RHC $1R\nu_\mu$ samples, respectively. The top figures show the distribution of the distance from the reconstructed vertex to the closest inner detector wall. The middle figures show the distribution of the square of the radial distance in the SK ID. The bottom figures show the distribution of the vertical position in the inner detector. The broken lines are the corresponding cumulative distributions function of the MC distributions.

For each test and each vertex distribution, p-value, which is probability observing the test statistic under the null hypothesis by statistical fluctuation, is calculated as an upper tail probability of the test statistic distribution. The p-value is calculated from toys which are generated by random throws. The procedure to generate the toys is as follows:

- Sample N_{tag}^{obs} tagged neutrons from the nominal MC distribution of interest, where N_{tag}^{obs} is number of observed tagged neutrons (i.e. 44 and 33 for the FHC and RHC $1R\nu_\mu$ samples, respectively).

- Make a finely binned histogram using the sampled tagged neutrons.

- Make a cumulative distribution function from the histogram made just above.

- Compute test statistic of interest by using the cumulative distribution functions of the nominal MC and toy MC.

- Repeat 10,000 times.

Using generated toys, distribution of test statistic is made. Figure 7.13 shows example of the test statistic distribution made from the toys for *Dwall* distribution of the FHC $1R\nu_\mu$ sample.
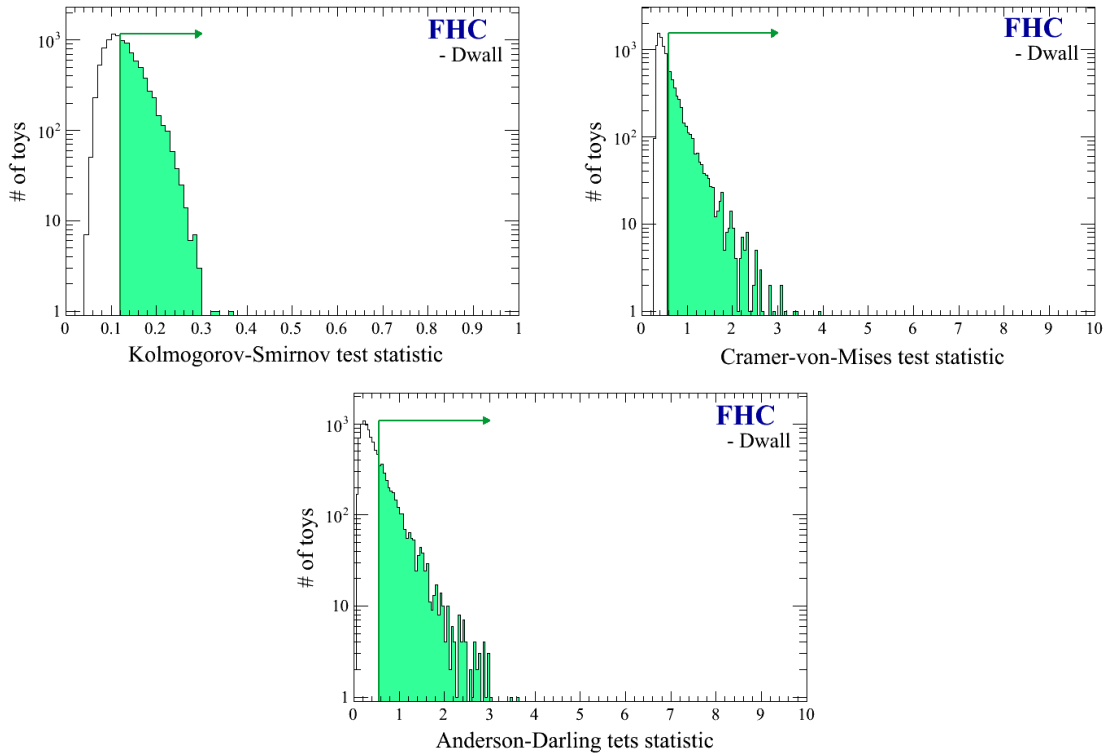
Figure 7.13: Distributions of test statistics produced by random throws for the *Dwall* of the tagged neutrons of the FHC $1R\nu_\mu$ sample. The top left, top right, and bottom figures correspond to distributions of KS, CVM, and AD test statistics, respectively. The green arrows show the values of the test statistics obtained by the Run 1-9 FHC $1R\nu_\mu$ data sample.

The p-value is then estimated by Equation 7.4.2.

$$p - \text{value} = \int_{T_{Data}}^{+\infty} F(T)\, dT, \qquad (7.4.2)$$

where T_{Data} is the test statistic obtained by the data, $F(T)$ is the probability density function made from the generated toys. In addition to the p-values for $Dwall$, R^2, and Z, a combined p-value of $R^2 + Z$ is also considered. This may address the validity of the neutron tagging algorithm across the volume of the inner detector.

As the p-values for R^2 and Z are treated as independent, the Fisher's method can be employed to evaluate the combined p-value. In this case the method uses a χ^2 which follows a chi-square distribution with four degrees of freedom and is defined as follows.

$$\chi^2_{\text{Fisher}} = -2\ln P_{R^2} - 2\ln P_Z, \qquad (7.4.3)$$

where P_{R^2} and P_Z are the p-value of the R^2 and Z distributions, respectively. The combined p-value is therefore calculated as the upper tail probability of the chi-square distribution.

Table 7.6 summarizes the p-values for the $Dwall$, R^2, Z, and combined $R^2 + Z$ distributions for all the tests performed. As shown in the table, there have been no significantly small p-values.

Table 7.6: p-values of $Dwall$, R^2, Z, and combined $R^2 + Z$ obtained by the KS, CVM, AD tests using toy MC for the tagged neutrons of the Run 1-9 FHC and RHC $1R\nu_\mu$ samples.

Beam mode	Sample	KS	CVM	AD
FHC	$Dwall$	49.6%	33.3%	27.9%
	R^2	82.6%	75.0%	69.0%
	Z	5.1%	3.0%	2.9%
	$R^2 + Z$	53.1%	41.8%	43.0%
RHC	$Dwall$	37.1%	18.4%	19.8%
	R^2	94.3%	89.8%	86.1%
	Z	32.9%	28.8%	29.0%
	$R^2 + Z$	88.3%	84.6%	85.3%

Neutron capture time distributions

The neutron tagging algorithm tags the accidental backgrounds as well as the true neutrons. The correlation of the time difference from the neutrino interaction is dif-

ferent between the true neutrons and backgrounds, because the true neutrons have an exponential time structure with the capture time of about $200\,\mu$s, whereas the backgrounds have a flat time structure. The capture time distribution is therefore useful to validate the neutron tagging. In addition, in principle the expected number of backgrounds described in Table 7.2 and 7.3 can be checked by the observed distributions. In order to extract these quantities, the observed distributions are fitted by a function consisting of an exponential and a constant components defined by Equation 7.4.4.

$$f(t; \tau, \mu_S, \mu_B) = \mu_S \frac{\exp(-t/\tau)}{[\exp(-18/\tau) - \exp(-513/\tau)]} + \mu_B \frac{1}{513 - 18}, \tag{7.4.4}$$

where τ is capture time, μ_S is number of tagged true neutrons, and μ_B is number of tagged backgrounds. As the number of observed tagged neutrons are 44 and 33 for the FHC and RHC $1R\nu_\mu$ sample, respectively, a Gaussian χ^2 fit is not relevant to extract τ, μ_S, and μ_B. A binned Poisson negative log likelihood is therefore used for the fit and is defined in Equation 7.4.5.

$$\mathcal{L} = -\ln L(\tau, \mu_S, \mu_B)$$
$$= \sum_{i=1}^{5} \mathcal{E}_i - \mathcal{O}_i + \mathcal{O}_i \ln(\mathcal{O}_i/\mathcal{E}_i), \tag{7.4.5}$$

where

$$\mathcal{E}_i = \int_{t_i-45}^{t_i+45} f(t; \tau, \mu_S, \mu_B)\ dt,$$

is number of expected tagged neutrons and $\mathcal{O}_i$ is number of observed tagged neutrons in i-th bin. The likelihood is minimized by the MINUIT algorithm.

Figure 7.14 shows the observed capture time distributions with the fitted functions. Table 7.7 summarizes the numbers obtained from the fit, which include the fitted τ, μ_S, and μ_B. The fitted τ and μ_B for the FHC (RHC) $1R\nu_\mu$ sample are 39.4 $\pm$ 22.6 (155.9 $\pm$ 38) and 20.0 $\pm$ 6.1 (2.7$\times 10^{-6}$ $\pm$ 5.4), respectively. As shown in the table, these fitted numbers differ from their expectations, but the difference is obtained probably due to the small statistics.
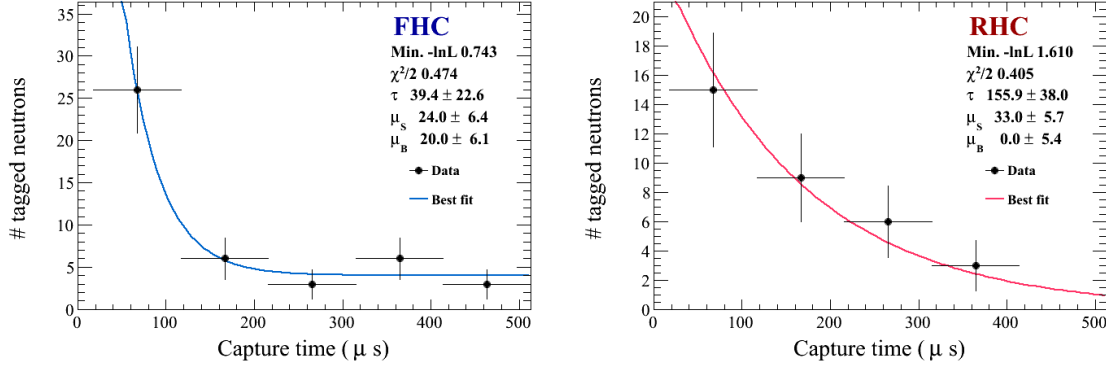
Figure 7.14: Time difference between ν event and neutron capture. Left and right are for the FHC and RHC $1R\nu_\mu$ samples, respectively. The solid lines correspond to the best fit results of the binned log likelihood fit.

Table 7.7: Summary of the results of the bin log likelihood fit to the capture time distribution. The expected τ, μ_S, and μ_B are obtained from an experimental result [37], Table 7.2, and Table 7.3, respectively. It should be noted that the fitted μ_S can differ from the expectation, because this analysis does aim to measure μ_S itself.

Beam mode	Parameter	Fit results	Expected
	τ	39.4 ± 22.6	204.8 ± 0.4 μs
	μ_S	24.0 ± 6.4	60.2 (Can be different)
FHC	μ_B	20.0 ± 6.1	3.9
	$-\ln L$	0.743	N/A
	χ^2/ndf	$0.948/(5\text{-}3)$	N/A
	τ	155.9 ± 38	204.8 ± 0.4 μs
	μ_S	33.0 ± 5.7	47.4 (Can be different)
RHC	μ_B	$2.7 \times 10^{-6} \pm 5.4$	2.0
	$-\ln L$	1.610	N/A
	χ^2/ndf	$0.809/(5\text{-}3)$	N/A

A study using toy MC fits is done in order to confirm whether or not the data fit results can be described by the small statistic. The procedure is as follows:

- Set true τ, μ_S, and μ_B of toy MC :

  - τ : $204.8\,\mu$s
  - μ_S : 44-3.9 (33-2.0) for the FHC (RHC) $1R\nu_\mu$ sample
  - μ_B : 3.9 (2.0) for the FHC (RHC) $1R\nu_\mu$ sample

- Generate tagged true neutrons and background events by Poisson distributions with mean value of the true μ_S and μ_B above, respectively. For each generated

neutron (background event), its capture time is sampled from an exponential function with the true τ (a flat function).

- Make capture time distribution from the generated tagged true neutrons and background events.

- Fit the capture time distribution made above to extract τ, μ_S, and μ_B in the same way as the data fit.

- Repeat 30,000 times.

Using the fitted parameters of the toy MCs, distributions for these parameters are constructed, and can be used to know how precisely these parameter are fitted for this small statistics. Figure 7.15 shows the distributions for the fitted parameters in comparison to the data fit results. As shown in the figure, the binned log likelihood fit does not extract the parameters well for this small statistics, and thus the fitted parameters are not distributed as Gaussian.

From this results, the results of the data fit are reasonably explained due to the small statistics of the Run 1-9 data. In order to quantify the results of the data fit, goodness-of-fit (GoF) is evaluated using the minimum $\mathcal{L}$ distribution. Distribution of the minimum $\mathcal{L}$ can be also made using the toy MC fit results as shown in Figure 7.16. Then, the GoF is obtained as an upper tail probability of the distribution and is estimated to be be 59.2% and 31.9% for the FHC and RHC samples, respectively.
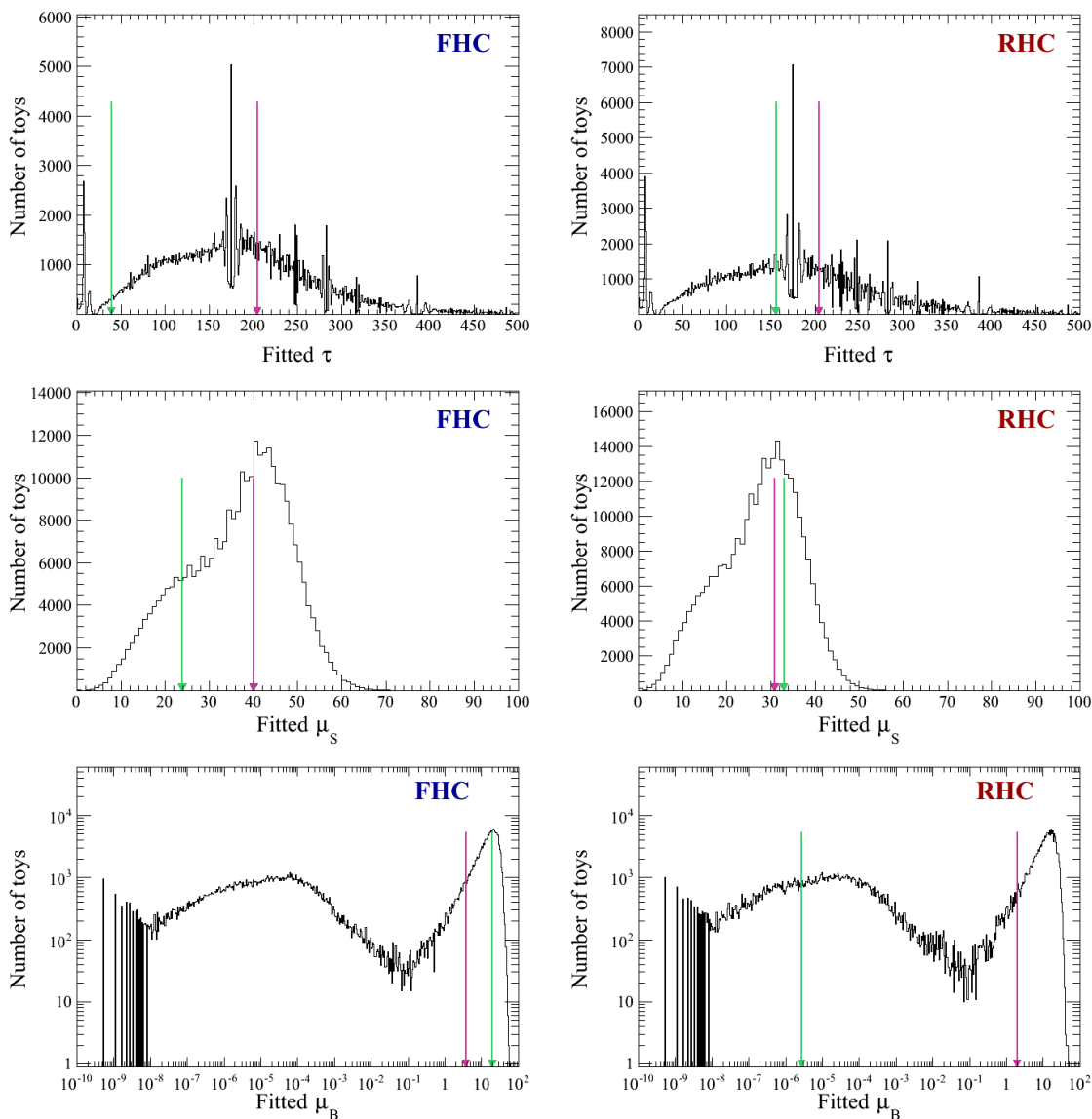
Figure 7.15: Distributions of the fitted τ, μ_S, μ_B of the toy MCs. The left and right panels correspond to the FHC and RHC $1R\nu_\mu$ samples, respectively. The top, middle, and bottom figures represent the fitted τ, μ_S, and μ_B. The magenta arrows show the true values used for the generation of the toy MC. The green arrows represent the data fit results.
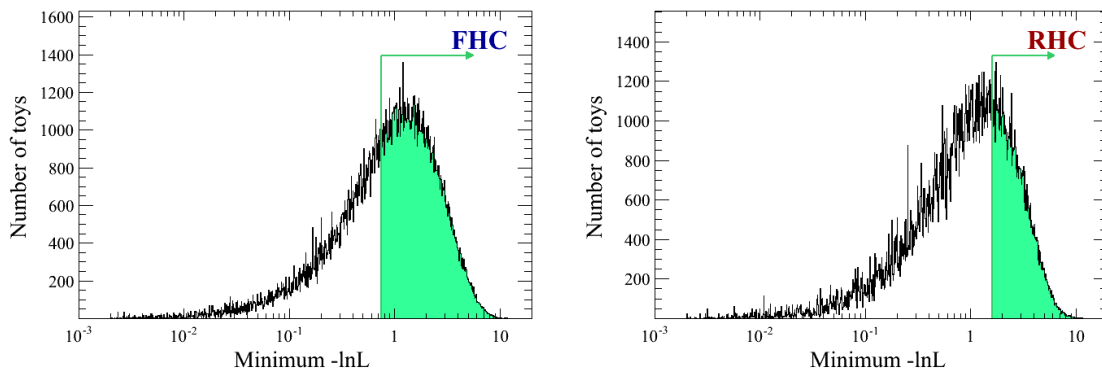
Figure 7.16: Distribution of minimum $\mathcal{L}$ obtained by the toy MC fits. Left and right are for the FHC and RHC $1R\nu_\mu$ samples, respectively. The green arrows show the minimum $\mathcal{L}$ obtained by the data fit.

7.5 Distributions related to tagged neutrons

Although this analysis aims to measure mean multiplicities, it may be interesting to know the agreement regarding tagged neutrons between the data and the MC expectations. A variety of distributions related to tagged neutrons for the Run 1-9 data are therefore overlaid with the corresponding MC expectations.

The MC expectations are made with flux tuning, correction of cross sections, and oscillation probabilities calculated from the oscillation parameters which are summarized in Section 7.1, and then are normalized by the Run 1-9 POT (14.938×10^{21} POT and 16.346×10^{21} for the FHC and RHC expectations, respectively).

Figure 7.17 shows the tagged neutron multiplicities. The number of ν events with tagged neutrons $= 0, = 1, \geq 2$, and their fractions are summarized in Table 7.8. It may be interesting to notice the fact that in both of the FHC and RHC data, the maximum tagged neutrons is 2 while the MC expectation has lager tagged neutrons.

Figure 7.17: Distribution of tagged neutron multiplicity for the Run 1-9 FHC (left) and the Run 5-9 RHC data (right). Note that the accidental backgrounds are included in the tagged neutrons. The MC expectations are normalized by the Run 1-9 POT.
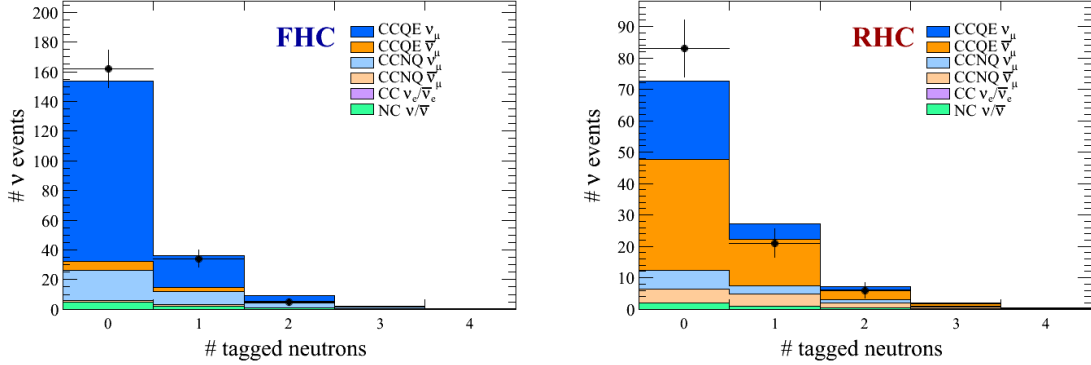
		Expected			Data		
		ntag= 0	ntag= 1	ntag≥ 2	ntag= 0	ntag= 1	ntag≥ 2
FHC	events	153.70	36.16	12.26	162.00	34.00	5.00
	fraction	0.76	0.18	0.06	0.81 (0.06)	0.17 (0.03)	0.02 (0.01)
RHC	events	72.64	27.29	9.68	83.00	21.00	6.00
	fraction	0.66	0.25	0.09	0.75 (0.08)	0.19 (0.04)	0.05 (0.02)

Table 7.8: Expected and observed numbers of ν events with tagged neutrons $= 0, = 1, \geq 2$ and their fractions compared to the Run 1-9 FHC and RHC data. For the expectation, the backgrounds are included. The expectations are normalized by the Run 1-9 POT.

7.5.1 Muon kinematics dependence

As neutron productions in FSI and SI depend on the energy transfer from incoming neutrino to hadronic system at neutrino interactions, it may be interesting to check mean tagged neutron multiplicity as a function of kinematic variables which are correlated with the energy transfer.

Figure 7.18 shows the mean tagged neutron multiplicity as function of the reconstructed muon momentum.
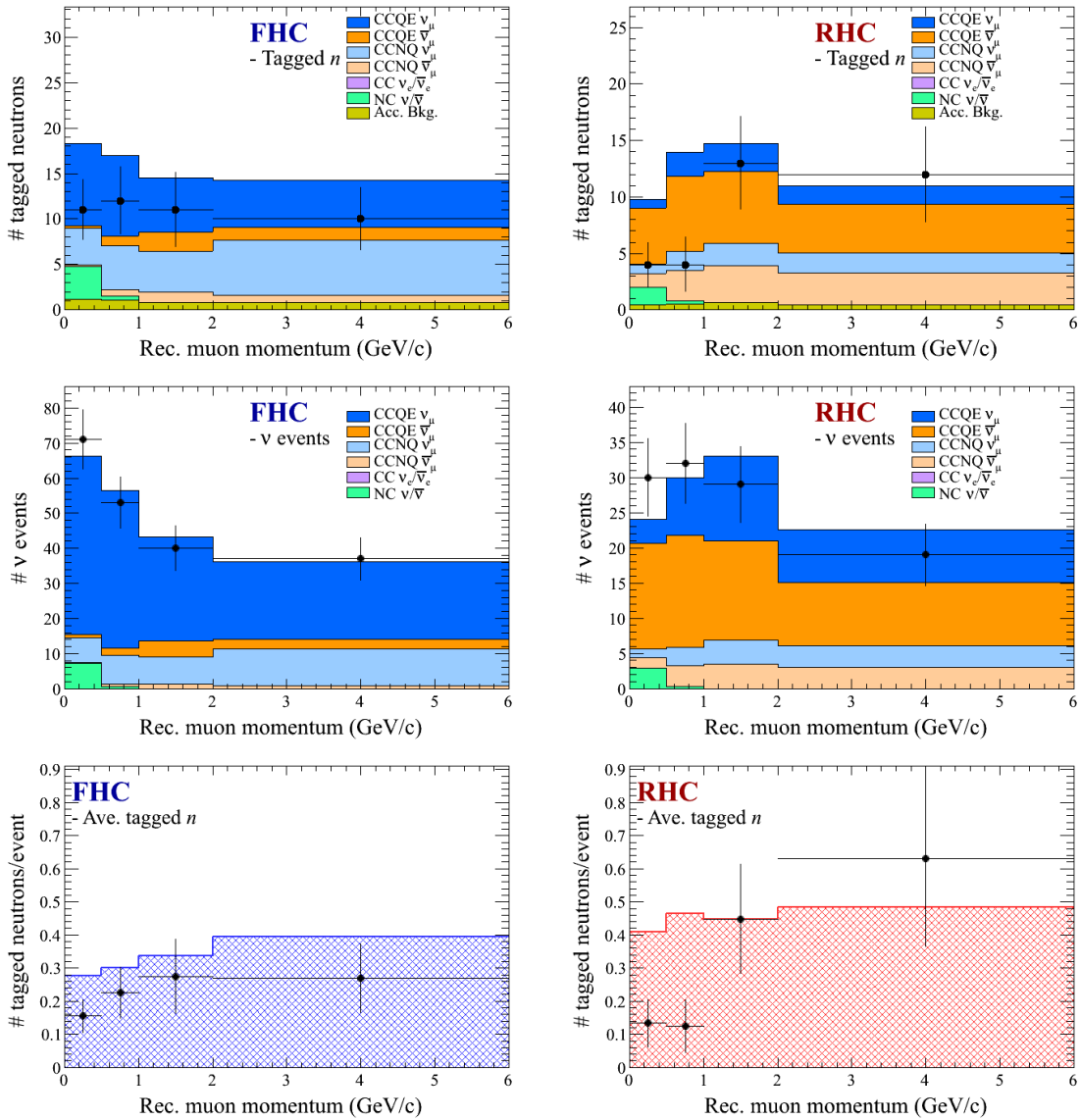
Figure 7.18: Number of tagged neutrons (top), number of ν events (middle), and average number of tagged neutrons (bottom) as a function of reconstructed muon momentum. The left and right side plots are for the FHC and RHC $1R\nu_{\mu}$ samples, respectively. The expected numbers are normalized by the Run 1-9 POT.

Figure 7.19 shows the mean tagged neutron multiplicity as function of the reconstructed muon transverse momentum.
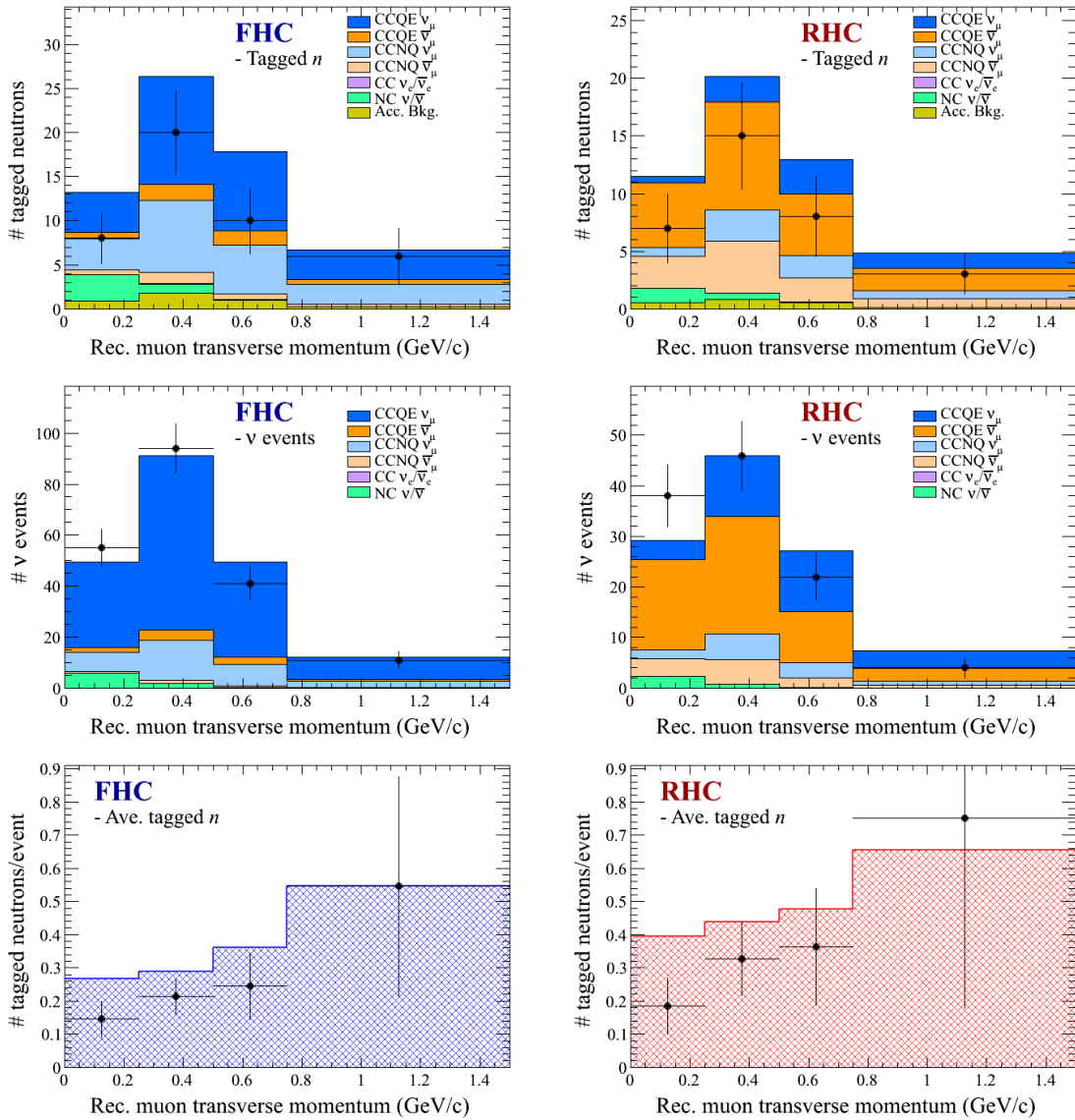
Figure 7.19: Number of tagged neutrons (top), number of ν events (middle), and average number of tagged neutrons (bottom) as a function of reconstructed muon transverse momentum. The left and right side plots are for the FHC and RHC $1R\nu_\mu$ samples, respectively. The expected numbers are normalized by the Run 1-9 POT.

Since the $1R\nu_\mu$ samples have a high purity of CCQE interaction events, the reconstructed neutrino energy calculated by assuming CCQE interaction is a good approximation to its true energy. Thus, the neutrino energy dependence of the tagged neutrons are also studied. The reconstructed energy is calculated by Equation 7.5.1.

$$E_{\nu\ CCQE}^{Rec} = \frac{(M_n - V_{\mathrm{nuc}})E_\mu - m_\mu^2/2 + M_n V_{\mathrm{nuc}} - V_{\mathrm{nuc}}^2/2 + (M_p^2 - M_n^2)/2}{M_n - V_{\mathrm{nuc}} - E_\mu + P_\mu \cos\theta_{\mathrm{beam}}}, \quad (7.5.1)$$

where M_n (M_p) is the neutron (proton) mass, V_{nuc} is the binding energy of the neu-

tron in oxygen (taken to be 27 MeV), m_μ is the mass of muon, P_μ is the reconstructed momentum under muon hypothesis, E_μ is its total energy, and θ_{beam} is the angle between the neutrino beam direction and the reconstructed lepton direction.

Figure 7.20 shows the mean tagged neutron multiplicity as function of the reconstructed neutrino energy.
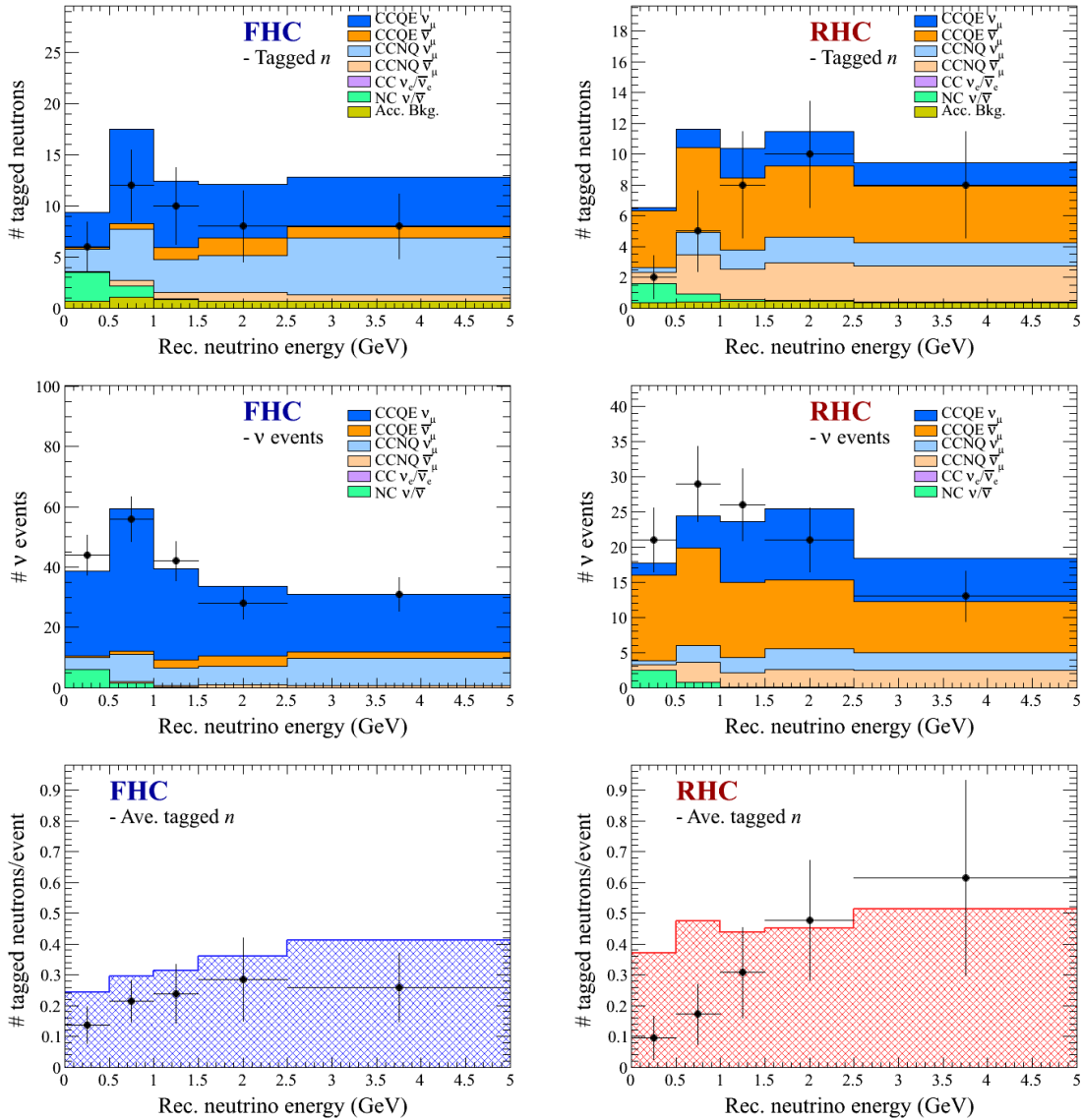
Figure 7.20: Number of tagged neutrons (top), number of ν events (middle), and average number of tagged neutrons (bottom) as a function of reconstructed neutrino energy. The left and right side plots are for the FHC and RHC $1R\nu_\mu$ samples, respectively. The distributions are normalized by the Run 1-9 POT.

Once the reconstructed neutrino energy is obtained, it is also possible to compute the reconstructed four momentum transfer squared by Equation 7.5.2.

$$Q^{2\,Rec}_{CCQE} = 2E^{Rec}_{\nu\,CCQE}\left(E_\mu - p_\mu \cos\theta_{\text{beam}}\right) - m^2_\mu. \qquad (7.5.2)$$

Figure 7.21 shows the mean tagged neutron multiplicity as function of the reconstructed four momentum transfer squared.
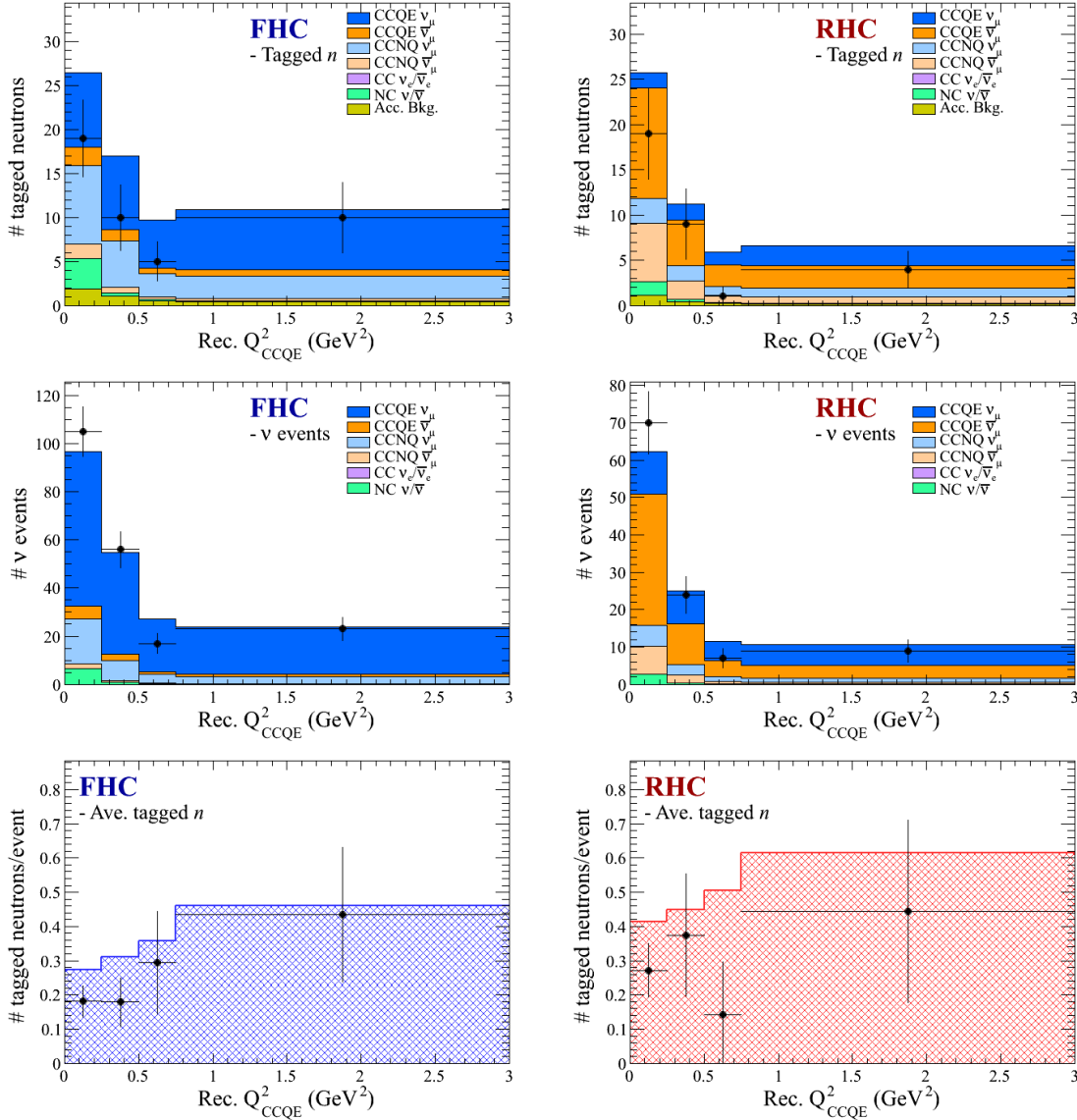
Figure 7.21: Number of tagged neutrons (top), number of ν events (middle), and average number of tagged neutrons (bottom) as a function of the reconstructed negative four momentum transfer squared. The left and right side plots are for the FHC and RHC $1R\nu_\mu$ samples, respectively. The distributions are normalized by the Run 1-9 POT.

Figure 7.22 shows the mean tagged neutron multiplicity as function of the cosine of the angle between the reconstructed muon and beam directions.
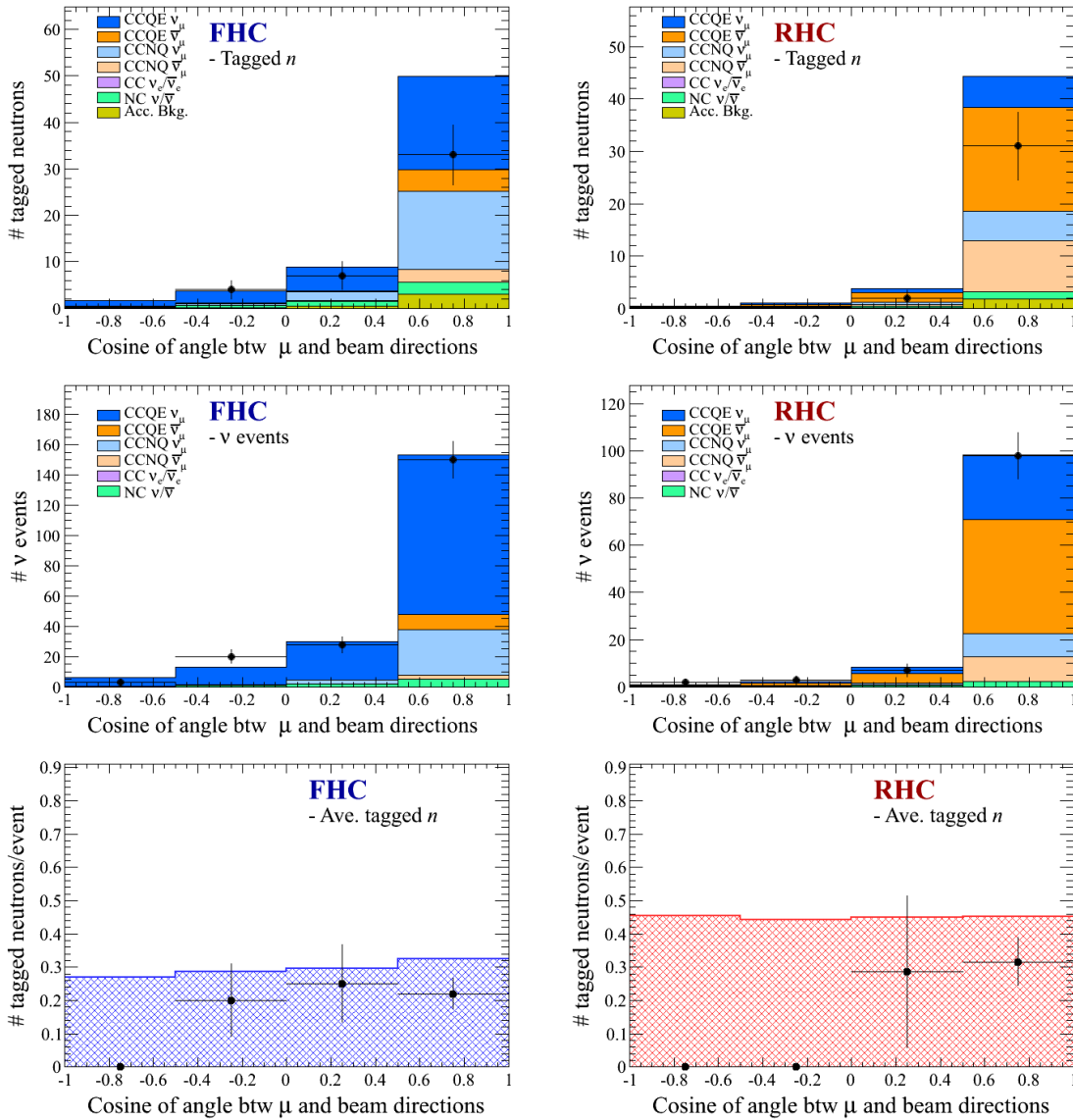
Figure 7.22: Number of tagged neutrons (top), number of ν events (middle), and average number of tagged neutrons (bottom) as a function of the cosine of the angle between the reconstructed muon and beam directions. The left and right side plots are for the FHC and RHC $1R\nu_\mu$ samples, respectively. The distributions are normalized by the Run 1-9 POT.

7.5.2 Kinematics of tagged neutrons

In principle, as will be mentioned in Section 8.1, travel distance, which is the distribution of distance between ν interaction and neutron capture vertices, contains information regarding number of post-FSI hadrons (i.e. hadron multiplicities) and their energy distributions. Distributions of reconstructed distances are therefore checked.

Figure 7.23 shows the distribution of reconstructed travel distance. In addition
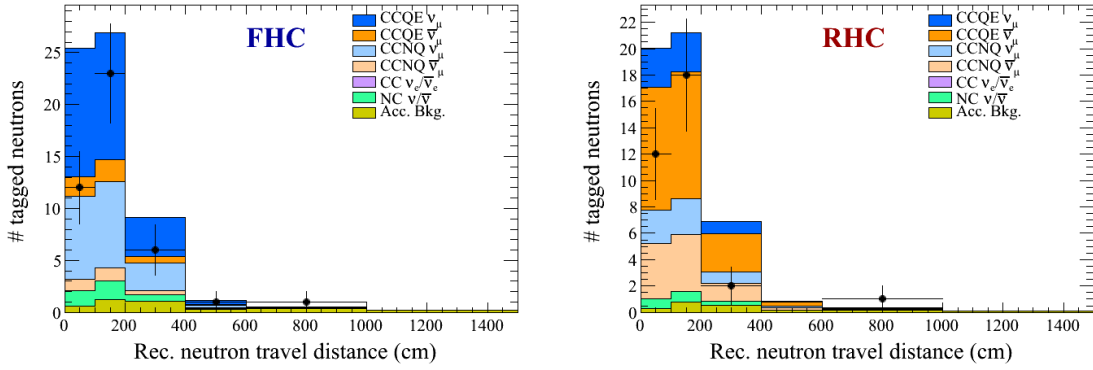
Figure 7.23: Distribution of the reconstructed neutron travel distance which is defined as the distance between the ν intraction and neutron capture vertices. The left and right correspond to the FHC and RHC $1R\nu_\mu$ samples, respectively. The distributions are normalized by the Run 1-9 POT.

to the reconstructed travel distance above, it may be interesting to check both longitudinal distance and transverse distance, which are the distance projected onto the beam direction and the distance perpendicular to the beam direction, respectively. Figures 7.24 and 7.25 show the distributions of the longitudinal and transverse distances, respectively.
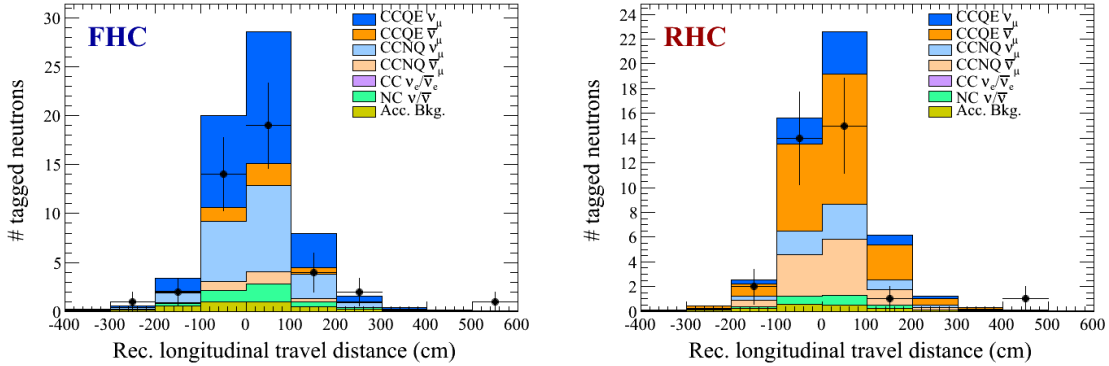
Figure 7.24: Distribution of the reconstructed longitudinal travel distance, which is the travle distance projected onto the beam direction. The left and right correspond to the FHC and RHC $1R\nu_\mu$ samples, respectively. The distributions are normalized by the Run 1-9 POT.

If the direction from ν vertex to neutron capture vertex is interpreted as the momentum direction of a tagged neutron, the momentum direction of neutron can be reconstructed:

$$\hat{d}_{rec} = \frac{\boldsymbol{r}_{ncap} - \boldsymbol{r}_{\nu\ int}}{|\boldsymbol{r}_{ncap} - \boldsymbol{r}_{\nu\ int}|},$$

where $\boldsymbol{r}_{ncap}$ and $\boldsymbol{r}_{\nu\ int.}$ are the reconstructed ν vertex and neutron capture vertex,

165
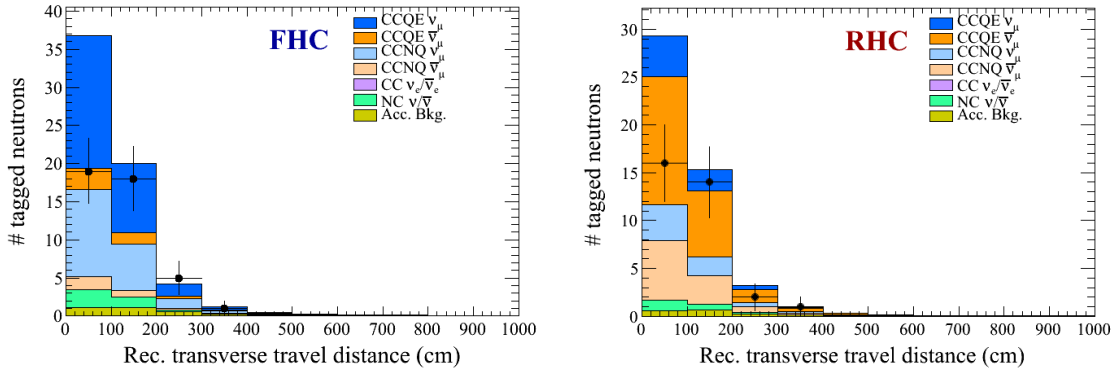
Figure 7.25: Distribution of the reconstructed transverse travel distance, which is the travel distance perpendicular to the beam direction. The left and right correspond to the FHC and RHC $1R\nu_\mu$ samples, respectively. The distributions are normalized by the Run 1-9 POT.

respectively.

Using the reconstructed momentum direction of tagged neutron, two angular variables can be studied. The first one is cosine of the actual angle which is the angle between the beam and reconstructed momentum directions, which may address the momentum directions of the hadrons leaving the target nucleus with respect to the beam direction. Figure 7.26 shows the distribution of cosine of the actual angle.
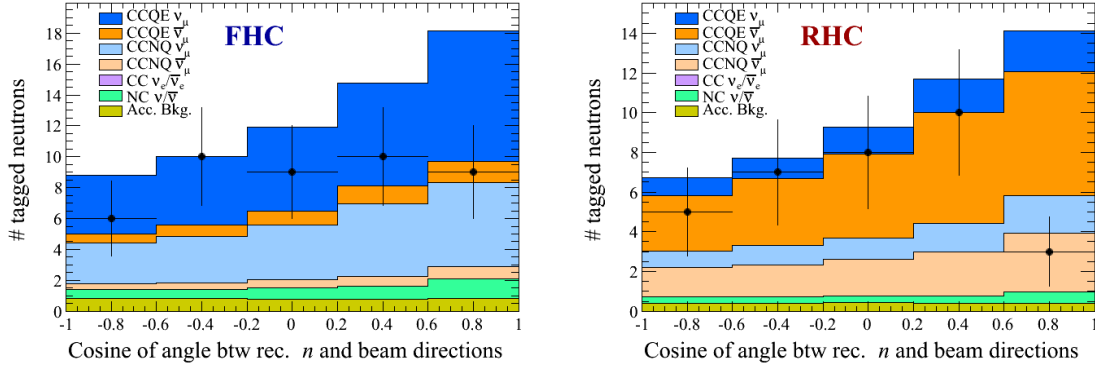
Figure 7.26: Distribution of cosine of the actual angle which is the angle between the beam direction and reconstructed momentum direction. The left and right plots are for the FHC and RHC $1R\nu_\mu$ samples, respectively. The distributions are normalized by the Run 1-9 POT.

The other angule is cosine of the inferred angle which is the angle between the inferred and reconstructed momentum directions. The inferred direction can be calculated by assuming that all the ν events observed are due to true CCQE interaction and the tagged neutron is associated with the outgoing nucleon of CCQE interaction, and is given as:

166

$$\hat{d}_{inf} = \frac{E_{\nu}^{Rec}{}_{CCQE}\boldsymbol{b} - \boldsymbol{P}_{1\mu}}{|E_{\nu}^{Rec}{}_{CCQE}\boldsymbol{b} - \boldsymbol{P}_{1\mu}|},$$

where $E_{\nu}^{Rec}{}_{CCQE}$ is reconstructed neutrino energy defined in Equation 7.5.1, $\boldsymbol{b}$ is the beam direction, and $\boldsymbol{P}_{1\mu}$ is the reconstructed μ momentum.

Figure 7.27 shows the distribution of $\cos(\hat{d}_{rec} \cdot \hat{d}_{inf})$.
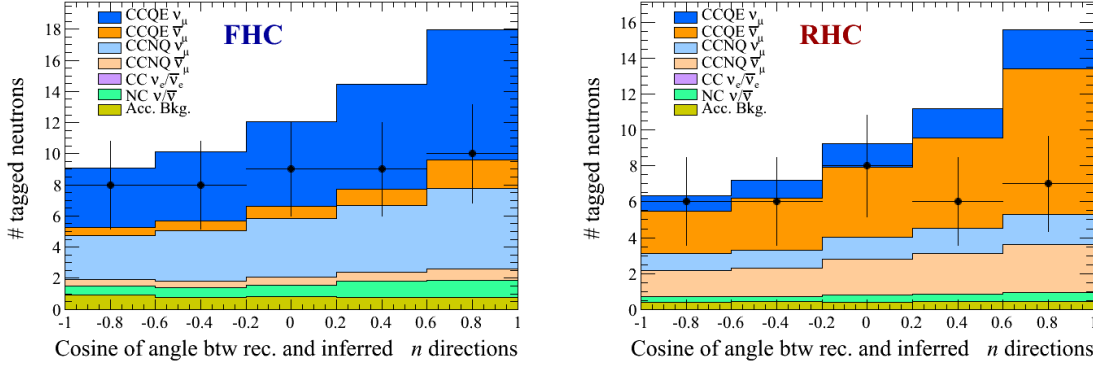
Figure 7.27: Distribution of cosine of the inferred angle which is the angle between the inferred direction and reconstructed momentum direction. The left and right plots are for the FHC and RHC $1R\nu_{\mu}$ samples, respectively. The distributions are normalized by the Run 1-9 POT.

As was shown by the distributions regarding the reconstructed distances and angular variables above, the shapes of the observed distributions do not agree well with those of the corresponding MC distributions. In case of the angular variables shown in Figure 7.26 and Figure 7.27, relatively large deficits in the forward region can be seen, although the statistical uncertainties are still large. This may indicate that there might be non-negligible difference in either or both of the kinematics of hadrons after FSI and their secondary interactions in water between the data and the simulations.

As a conclusion, in general the distributions related to the neutrino events show good agreement between the data and the MC predictions. On the other hand, the observed distributions associated with tagged neutrons show that the MC prediction tends to produce more tagged neutrons than that of the data. It is worth noting that the neutron tagging algorithm does work properly for both the data and the MC predictions as described in Section 7.4.

Chapter 8

Measurement of mean neutron multiplicity

The primay aim of this thesis is to measure neutrons associated with neutrino interactions on water target with a proper systmatic uncertainty, and make a quantitative comparison between experimental data and simulations. Both the neutron tagging algorithm described in Chapter 6 and the result of its application to the T2K data accumulated until 2018 presented in Chapter 7 are the ingredients to this aim.

In this Chapter, first the production of those neutrons are described using MC simulations in Section 8.1. Following this, Section 8.2 describes the strategy of this analysis, and a series of extensive studies on systematic uncertainties on this neutron mesurement is summarized in Section 8.3. Finally Section 8.4 presents the measureent result, and a discussion on the result is given in Section 8.5.

8.1 Simulation studies

As was introduced in Section 1.2.1, neutrons related to neutrino interactions in water, which are measured in this thesis, are produced via three sequential processes: primary ν-nucleon interaction in nuclear medium, hadronic FSI inside the target nucleus, and hadronic SI in water. In practice, current scheme to simulate the three processes uses two separate MC simulations, which has been adopted in neutrino oscillation experiments for both atmospheric and accelerator neutrinos.
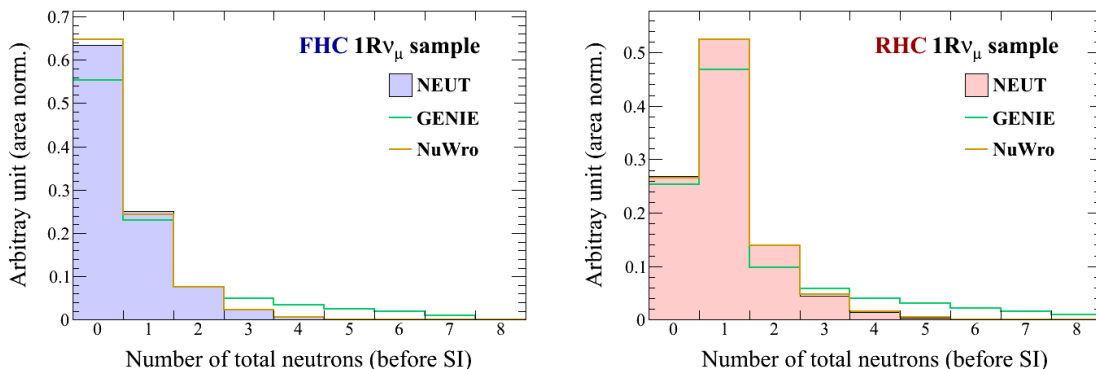
Figure 8.1: Distribution of true neutron multiplicity before SI for three different Monte Carlo ν event generators. The left and right correspond to the FHC and RHC 1Rν_μ samples, respectively.

For the first two processes, MC simulation called "ν event generator" is used. Modern neutrino oscillation experiments and ν-nucleus interaction experiments have used several generators such as GENIE [11], NEUT [135], and NuWro [136]. These generators consider almost same primary interaction channels, but differences in adopted interaction model, treatment of nuclear effect, and implementation method by itself make different simulation results. Figure 8.1 shows neutron multiplicities after primary interactions and FSI for the FHC and RHC 1Rν samples, which are used for this analysis. As shown in the figure, a large difference is seen between GENIE and the others, which mainly originates from different way of simulating FSI. Both NEUT and NuWro perform their FSI simulation within framework of cascade model by tracking hadrons inside the target nucleus on basis of microscopic interaction cross-section, whereas GENIE uses a cascade-like model, "hA", in which particle tracking is not conducted and the simulation of FSI is performed by single MC calculation (*i.e.* single throwing of random number) in accordance with a look-up table.
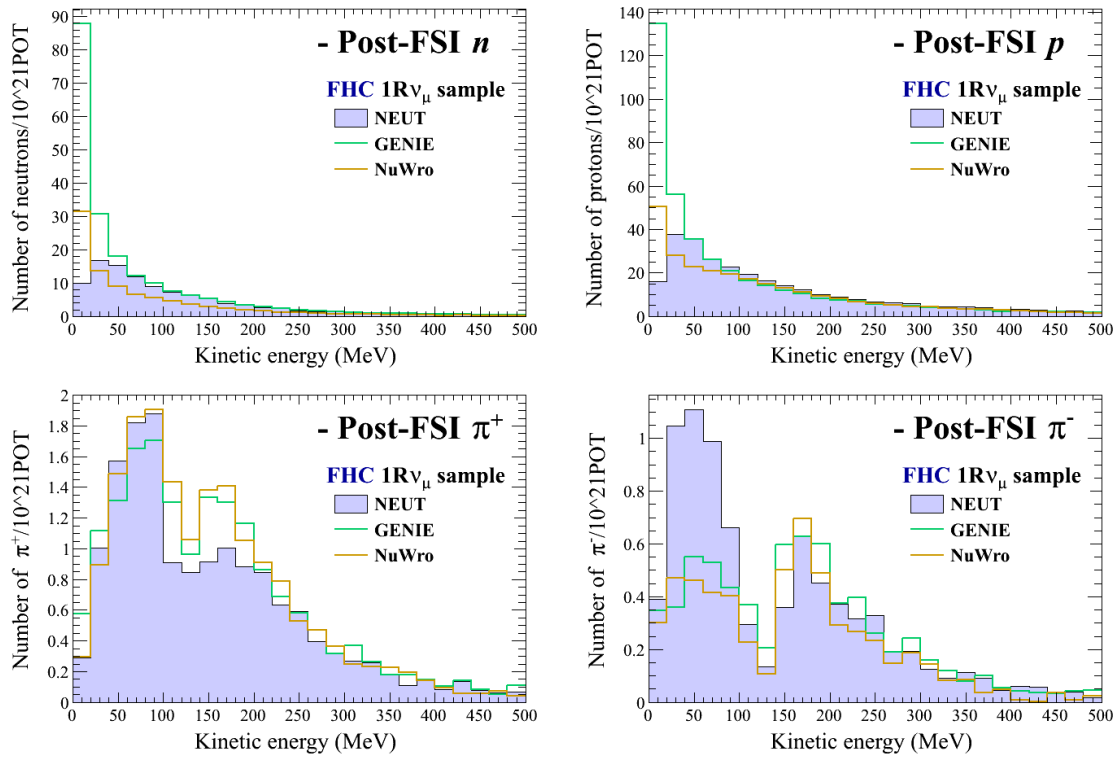
Figure 8.2: Distribution of kinetic energy for neutrons (top left), protons (top right), π^+ (bottom left), and π^- (bottom right) which have left the target nucleus, but have not undergone their secondary interactions in detector. The FHC $1R\nu_\mu$ samples are used for these hadrons. All the distributions are normalized by 10^{21} POT.
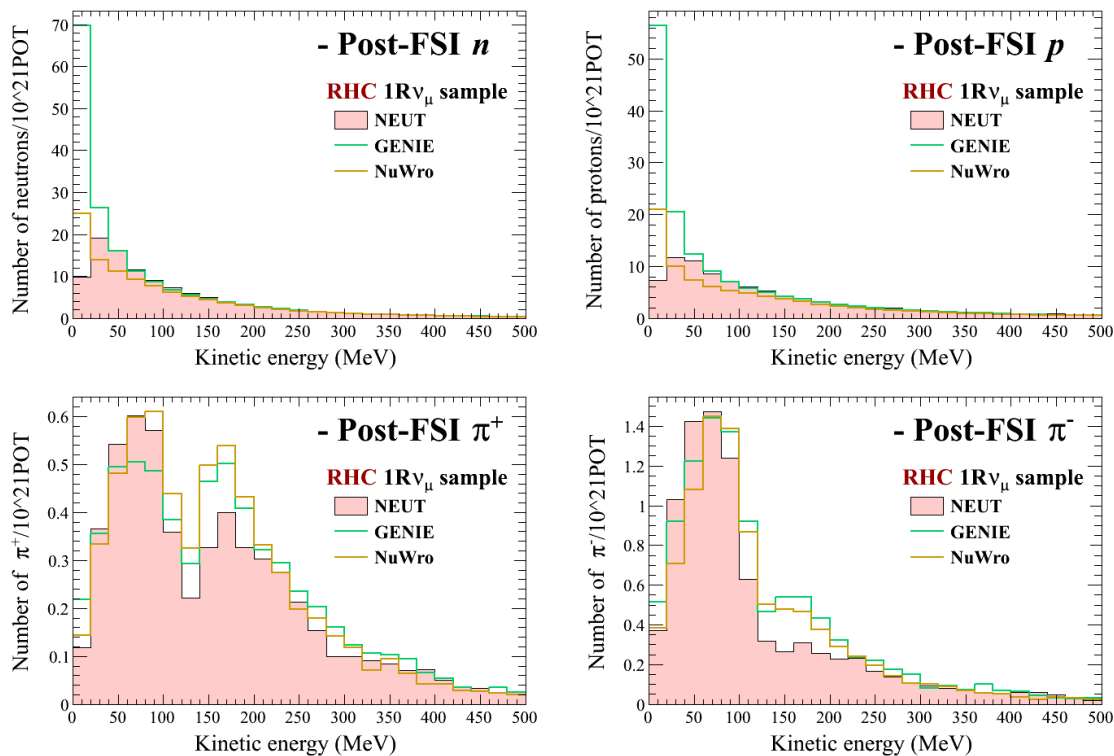
Figure 8.3: Distribution of kinetic energy for neutrons (top left), protons (top right), π^+ (bottom left), and π^- (bottom right) which have left the target nucleus, but have not undergone their secondary interactions in detector. The RHC $1R\nu_\mu$ samples are used for these hadrons. All the distributions are normalized by 10^{21} POT.

The difference in the neutron multiplicity between NEUT and NuWro is marginal between them. However, they have a visible difference in distribution of kinetic energy of neutron. Figure 8.2 and 8.3 show distributions of kinetic energy for post-FSI hadrons including neutrons, which just escaped from the target nucleus and do not undergo their SI in water, for the FHC and RHC $1R\nu_\mu$ samples. As shown in the figures, NuWro predicts post-FSI nucleons with lower energies compared to NEUT. In a water Cherenkov detector, neutrons after all the three processes are detected and they are indistinguishable in terms of production process. Since neutron production by SI strongly depends on energies of post-FSI hadrons, prediction of resultant neutron multiplicity after all the processes is also affected by difference in kinetic energies as shown in Figure 8.4.

The figure also shows difference between SKDETSIM and Geat4.10.1 with an option of `FTFP_BERT_HP`. Although both simulations adopt same SI's simulation scheme based on the Bertini's cascade model, the results are different since the details in the treatment and implementation methods of the model differs between them. Alongside the energy and simulation dependencies on the neutron production in SI, in order to understand the dominant contribution to the neutron production by SI, it is helpful to notice that the number of post-FSI $\pi^\pm$ is much less than that of post-FSI nucleons in the $1R\nu_\mu$ samples. Therefore, according to the MC expectations,

neutrons and protons mainly contribute to the neutron production by SI in this analysis.
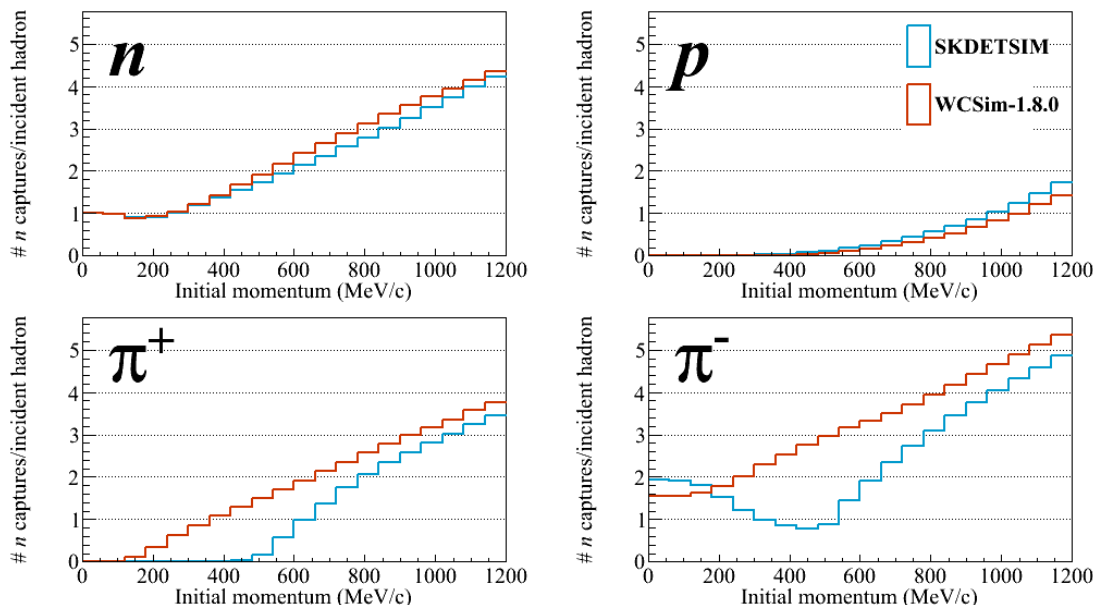
Figure 8.4: Mean neutron captures as a function of incident kinetic energy for neutrons, protons, and $\pi^{\pm}$. Orange and cyan lines correspond to expectation of SKDETSIM and Geat4.10.1 with an option of `FTFP_BERT_HP`, respectively. In SKDETSIM, GCALOR is used to simulate hadrons except only for pions with momenta below $500\,\mathrm{MeV/c}$, and NEUT simulates pions for the momentum region. These hadrons are generated by the particle guns of the two simulations.

In a region of neutrino energies ranging from Sub-GeV up to several GeV, many neutrons are produced in SI. Figure 8.5, for instance, shows the neutron multiplicities before and after SI of the 1Rν samples and more than half of the total neutrons are produced in SI, on average. The difference in the neutron multiplicity after the SI among the three event generators is also shown in Figure 8.6. Even after SI, NuWro still predicts similar neutron multiplicity to NEUT, whereas GENIE predicts more neutrons than the other generator. Nevertheless, there is still remaining experimentally visible difference between the three generators. In a water Cherenkov detector, energy of neutron can not be measured, because neutrons can only be detected by using gamma rays emitted from neutron capture on nuclei. However, thanks to neutron capture, any energies of neutrons can be detected, and the distance from primary ν interaction vertex to neutron capture vertex can be reconstructed for each neutron capture. Since the distance is correlated with energies of post-FSI hadrons as shown in Figure 8.7, the distance, therefore, has information about the difference in primary ν interactions and FSI among three generators as shown in Figure 8.8. Moreover, the distance would be an important input to the modeling of the two processes if SI could be simulated precisely or constrained experimentally very well.
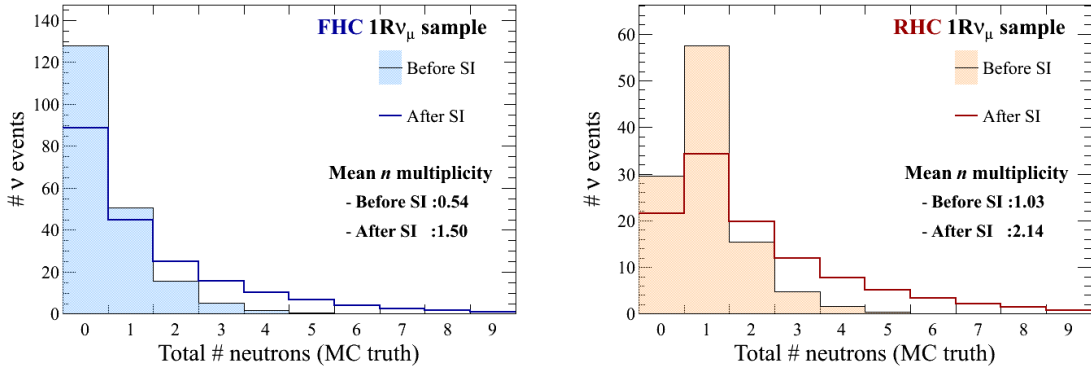
Figure 8.5: Distribution of true neutron multiplicity for the FHC 1Rν_μ sample (left) and the RHC 1Rν_μ sample (right). Filled histograms and solid lines correspond to true neutron multiplicity before SI and after SI, respectively. All the distributions are normalized by the Run 1-9 POT.
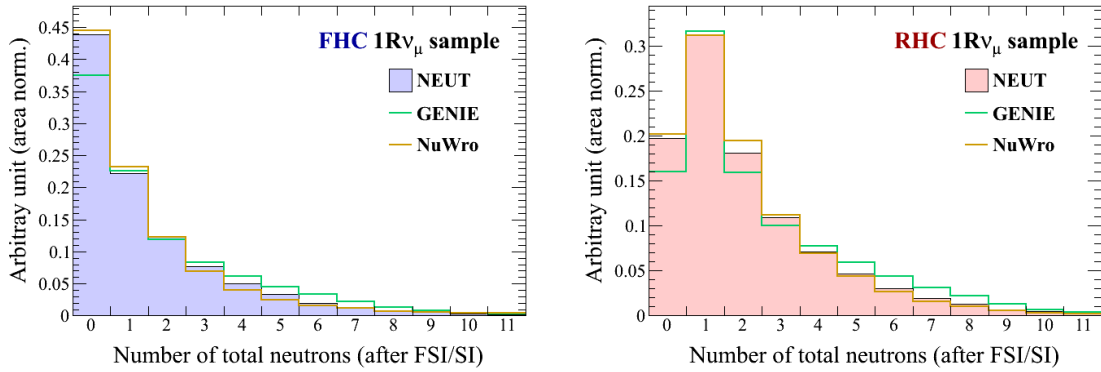
Figure 8.6: Distribution of true neutron multiplicity for the three popular ν event generators, NEUT, NuWro, and GENIE. All the contributions from neutrino interactions, hadronic FSI and SI are included in the multiplicities. The left and right plots correspond to the FHC and RHC 1Rν_μ samples, respectively. The secondary interactions of the hadrons produced by the generators are common among the three generators. (i.e. the identical detector simulation is used). All the distributions are area normalized.
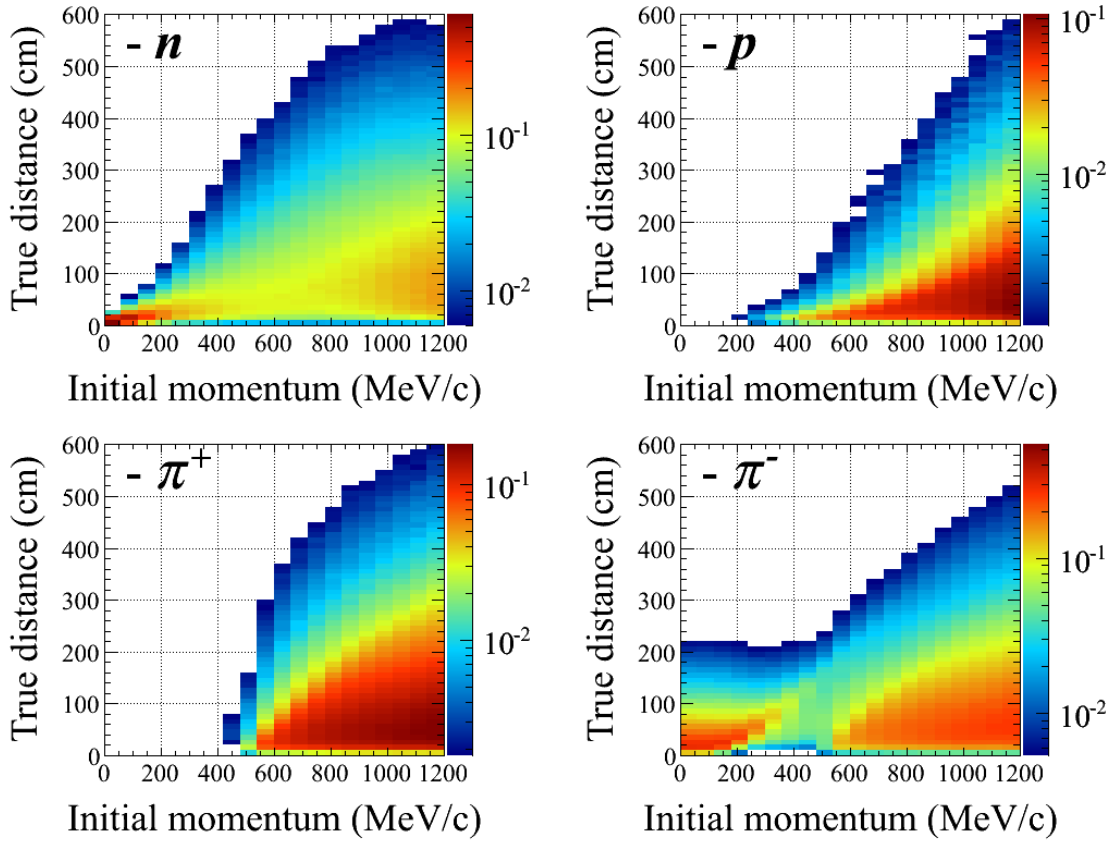
Figure 8.7: True travel distance of neutron captures per incident hadron as a function of initial momentum for n, p, π^+, π^-. The Z-axes show the number of neutron captures.
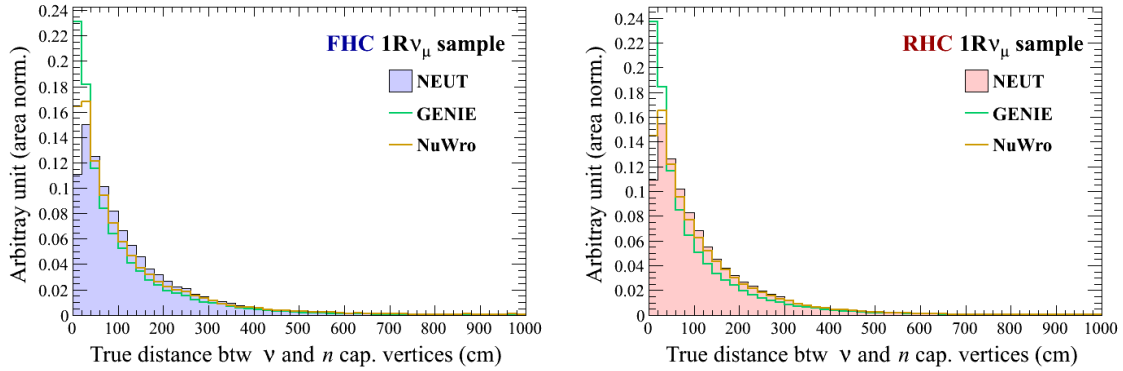
Figure 8.8: Distribution of true distance between ν interaction and neutron capture vertices for the NEUT, NuWro, and GENIE. The left and right plots correspond to the FHC and RHC $1R\nu_\mu$ samples, respectively. The secondary interactions for the hadrons produced by the generators are common among the three generators. All the distributions are normalized by 10^{21} POT.

8.2 Analysis strategy

In this analysis, a set of mean neutron multiplicities are measured rather than multiplicity distributions. As was described in Section 6.3, typical neutron tagging efficiency of the neutron tagging algorithm is ~20%. In addition, all the neutrons produced in hadronic FSI (Final State Interactions) and hadronic SI (Secondary Interactions) as well as primary ν interactions are included in the observed neutrons at SK.

When a neutrino interaction happens inside a nucleus, hadrons are produced by the interaction within the nucleus. These hadrons interact with nucleons in the nucleus before they leave it. These interactions are referred to as hadronic FSI. Once those hadrons exit the nucleus in which they are produced, they propagate through detector mediums (*i.e.* water for the SK far detector) and interact with these mediums, which is referred to as hadronic SI.

The predictions for FSI and SI strongly depend on the hadron multiplicities and the energy distributions of the hadrons produced in primary ν interaction, which means that one can not extract the neutrons produced at a particular process of interest without any assumption (i.e. introducing model dependence). Thus, the measured neutrons in this analysis includes all the contributions from three processes and is performed in a minimal model dependent way.
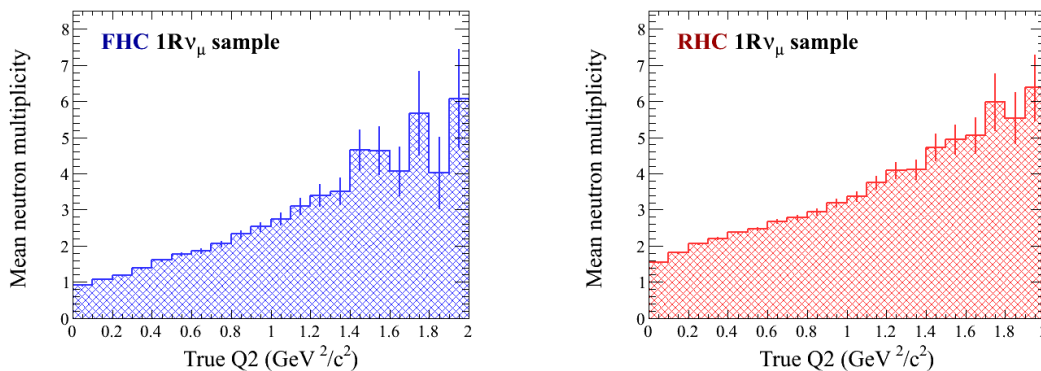
Figure 8.9: Mean neutron multiplicity as a function of true Q^2. The left and right correspond to the FHC and RHC $1R\nu_\mu$ samples, respectively. The error bars represent the MC statistical uncertainties.

Neutron multiplicity is expected to become large as the four momentum transfer squared Q^2 to the hadronic system at the primary ν-nucleus interaction increases, as shown in Figure 8.9. Since the direction of beam ν is known, reconstructed muon transverse momentum P_t, which is a good indicator of Q^2, can be calculated. Figure 8.10 shows the relation between true Q^2 and reconstructed P_t. As shown in this figure, a clear positive relation can be seen. This analysis therefore measures the mean neutron multiplicity as a function of P_t using the FHC and RHC $1R\nu_\mu$ samples as follows:

$$\bar{M}_i = \frac{1}{\varepsilon_i} \times \frac{\left(N_{tag,i} - b \times N_{1\mu,i}\right)}{N_{1\mu,i}}, \qquad (8.2.1)$$

where i represents i-th P_t bin, $N_{tag,i} = \sum_{j=1}^{N_{1\mu,i}} m_{ij}$, $N_{1\mu,i}$ is number of observed $1R\nu_\mu$ events, m_{ij} is number of tagged neutrons of j-th $1R\nu_\mu$ event, b is accidental background event rate of the neutron tagging, and ε_i is neutron tagging efficiency. Neutron tagging efficiency and accidental background event rate are defined in Equation 6.1.1 and Equation 6.1.2, respectively.

The relation between the transverse momenta and the true neutrino energies can be found in Appendix C.
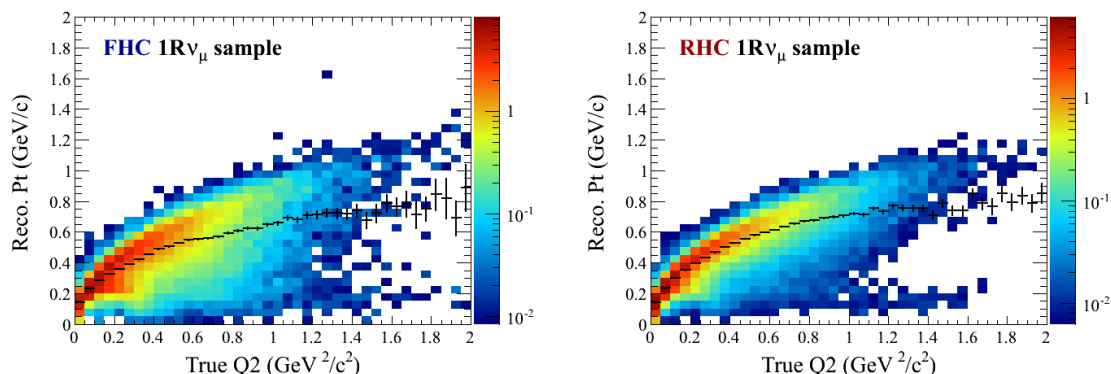
Figure 8.10: Relation between true Q^2 and reconstructed P_t. The left and right correspond to the FHC and RHC $1R\nu_\mu$ samples, respectively. The Z-axes show the number of neutrino events normalized by 10^{21} POT The black lines represent the mean reconstructed P_t at each true Q^2 bin.

8.3 Systematic uncertainties on tagging efficiency

This analysis aims to measure neutrons in the less model dependent way by following Equation 8.2.1. Estimates of systematic uncertainties on the neutron tagging efficiency and the background event rate is therefore important. However, the estimates need to be done only for the tagging efficiency.

As the background event rate of the neutron tagging algorithm is estimated by T2K dummy spill data, there is no systematics regarding simulations, and only the time variation effect needs to be considered, which has been taken into account in Section 6.5. Thus, this section describes the estimates of systematic uncertainties on the neutron tagging efficiency.

8.3.1 Overview

In the following, the sources of systematics considered are mainly categorized by simulations associated with neutrons and others. As was described in Section 6.2, the tagging algorithm uses ν interaction vertex to search for neutron candidates, which introduces dependence on distance between ν interaction and neutron capture vertices into the neutron tagging efficiency. This dependence is shown in Figure 8.11, and the efficiency goes down as the distance increases. As it can be found from the figure shown, systematics, which effect the shape of the true distance, causes a variation in the efficiency. Therefore, the uncertainties on neutrino interaction cross sections, neutrino fluxes, nucleon and pion FSI/SI, μ^- and π^- captures on oxygen nucleus, and oscillation parameters, which are associated with the simulations of neutrons, are taken into account. The uncertainty on the $1R\nu_\mu$ event selection described in Section 7.2 is also considered, because it can affect the shape of the distance distribution.
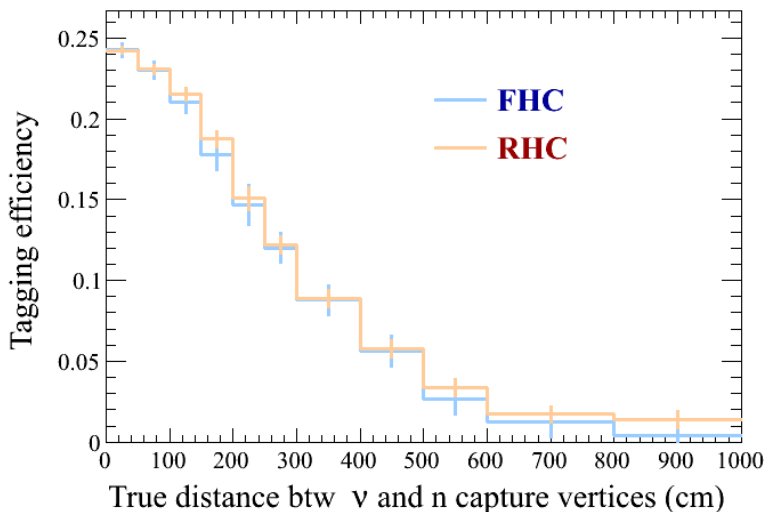
Figure 8.11: Neutron tagging efficiency as a function of true distance from ν interaction and neutron capture vertices for the FHC (left) and RHC (right) $1R\nu_\mu$ samples.

Other systematic sources which are reconstruction error of ν vertex, simulation of the PMT gain increase over time, and detector response for $2.2\,\mathrm{MeV}$ γ rays. In addition, the statistical errors of the MC events are taken into account on top of the SK time variations described in Section 6.5.4.

In the following parts, the systematic uncertainties regarding these sources are estimated for the tagging efficiency as a function of the reconstructed muon transverse momentum and the tagging efficiency averaged over the transverse momentum.

8.3.2 Neutrino cross sections

The systematic variations on the tagging efficiency due to uncertainties regarding the neutrino interaction cross sections are studied. The inputs to the uncertainties associated with the neutrino interactions are the same as used in the cross section analyses at the T2K near detectors. The following uncertainties are considered based on the works done by the T2K neutrino interaction working group [217]. The parameters which account for the uncertainties on neutrino interactions are categorized by true interaction modes. Table 8.1 summarizes the parameters considered. In the table, "shape" parameter have kinematic dependence and "norm" parameter is normalization parameter.

Table 8.1: List of parameters which describe uncertainties on neutrino cross sections

Parameter	Interaction catergories applied	Type	Nominal value and 1σ error
p_F^O	CCQE	shape	225 ± 31 MeV/c
E_B^O	CCQE	shape	27 ± 9 MeV
M_A^{CCQE}	CCQE	shape	1.2 ± 0.41 GeV/c^2
$2p2h$	2p2h	norm	1.0 ± 1.0
C_{A5}^{RES}	CC/NC1π	shape	1.01 ± 0.12
M_A^{RES}	CC/NC1π	shape	0.95 ± 0.15 GeV/c^2
BG_A^{RES}	CC/NC1π	shape	1.3 ± 0.2
CC other	CC other	shape	0.0 ± 0.4
CC coherent	CC coherent	norm	1.0 ± 0.3
NC coherent	NC coherent	norm	1.0 ± 0.3
NC other	NC other	norm	1.0 ± 0.3
Radiative corrections	CC ν_e	norm	1 ± 0.03

For CCQE interaction, its uncertainty is described by the axial mass M_A^{CCQE}, Fermi momentum of oxygen nucleus p_F^O, and binding energy of oxygen nucleus E_B^O.

The uncertainty on $2p - 2h$ interaction is taken into account by an overall normalization parameter.

For single pion interactions, their uncertainties are described by the parameters which vary the axial mass M_A^{RES}, $I = 1/2$ continuum background (i.e. isospin BG), and axial form factor C_{A5}^{RES}.

There are normalization parameter and energy dependent parameter to account for the uncertainties on CC coherent and CC other interactions, respectively. The uncertainties regarding NC coherent and NC other interactions are separately treated by two independent normalization parameters.

The effect of Bremsstrahlung from electron as the final state lepton is also considered and is treated by a normalization parameter.

The uncertainty on each individual parameter is propagated to the tagging efficiency by reweighting the nominal MC on an event-by-event basis. The weights applied are generated by a T2K software package (T2KReWeight v1r23). Figure 8.12 shows the resultant fractional variations in the tagging efficiency. As shown in the figure, all the parameters considered have very small impacts. Since the uncertainties

regarding these parameters are commonly applied to both the denominator and the numerator in Equation 6.1.1, these are largely cancelled out for the tagging efficiency.
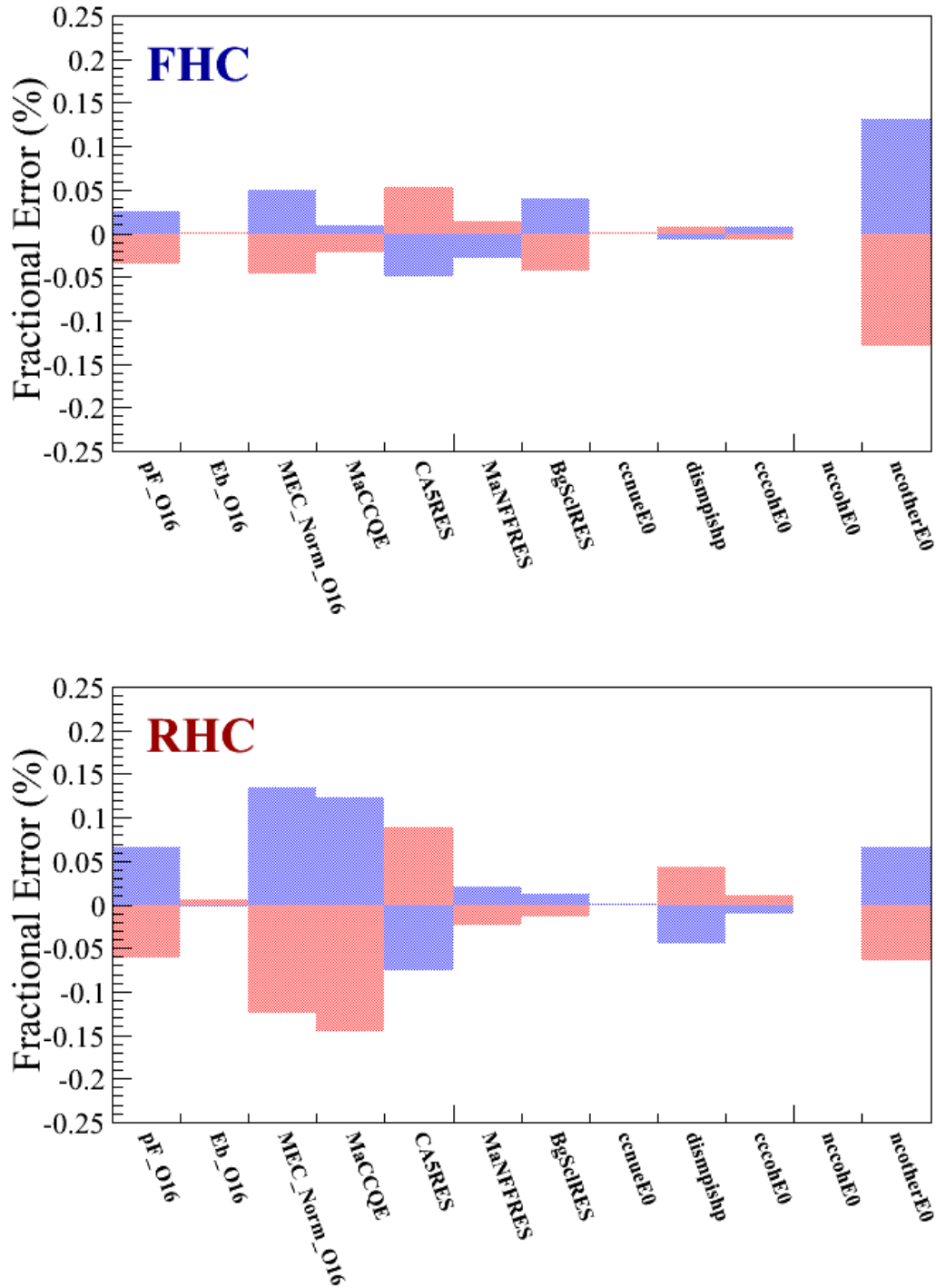
Figure 8.12: Fractional change in the average tagging efficiency due to $\pm 1\,\sigma$ variations of each individual parameter for the FHC (top) and RHC (bottom) $1R\nu_{\mu}$ samples. The blue and red bars correspond to $\pm 1\,\sigma$ variations, respectively.

The total systematic uncertainty due to the cross section parameters are computed by adding each fractional variation in quadrature as follows:

$$\delta\varepsilon_{\text{XSec}} = \sqrt{\sum_i \max\{|\delta\varepsilon_i(+1\sigma)|, |\delta\varepsilon_i(-1\sigma)|\}^2} \qquad (8.3.1)$$

The resultant systematic variation in the average neutron tagging efficiency is estimated to be $\sim 0.2\%$ as shown in Table 8.11.

8.3.3 Neutrino beam fluxes

The ν beam fluxes are binned by true ν energy and the fractional uncertainty of each individual bin is treated as a systematic parameter. The binning is summarized in Table 8.2. Figure 8.13 shows the fractional uncertainties on the beam fluxes. The dominant contribution to the $1R\nu_\mu$ samples comes from the energy region ranging from sub-GeV to a few GeV where the corresponding uncertainties are about less than 8%. In order to estimate the systematic uncertainties regarding these parameters,

Table 8.2: True ν energy binning of the beam fluxes for their systematic parameters.

Beam mode	Flux type	True ν energy bin edges (GeV)	Number of bins
FHC	ν_μ	0.0, 0.4, 0.5, 0.6, 0.7, 1.0, 1.5, 2.5, 3.5, 5.0, 7.0, 30.0	11
	$\bar{\nu}_\mu$	0.0, 0.7, 1.0, 1.5, 2.5, 30.0	5
	ν_e	0.0, 0.5, 0.7, 0.8, 1.5, 2.5, 4.0, 30.0	7
	$\bar{\nu}_e$	0.0, 2.5, 30.0	2
RHC	ν_μ	0.0, 0.7, 1.0, 1.5, 2.5, 30.0	5
	$\bar{\nu}_\mu$	0.0, 0.4, 0.5, 0.6, 0.7, 1.0, 1.5, 2.5, 3.5, 5.0, 7.0, 30.0	11
	ν_e	0.0, 2.5, 30.0	2
	$\bar{\nu}_e$	0.0, 0.5, 0.7, 0.8, 1.5, 2.5, 4.0, 30.0	7

fractional change in the tagging efficiency is computed for $\pm 1\sigma$ variations of each individual parameter. The computation is done by reweighting the nominal MC on an event-by-event basis. Figure 8.14 shows the resulting fractional changes in the total average efficiencies. As shown in the figure, the size of all the variations are less than 0.8%.
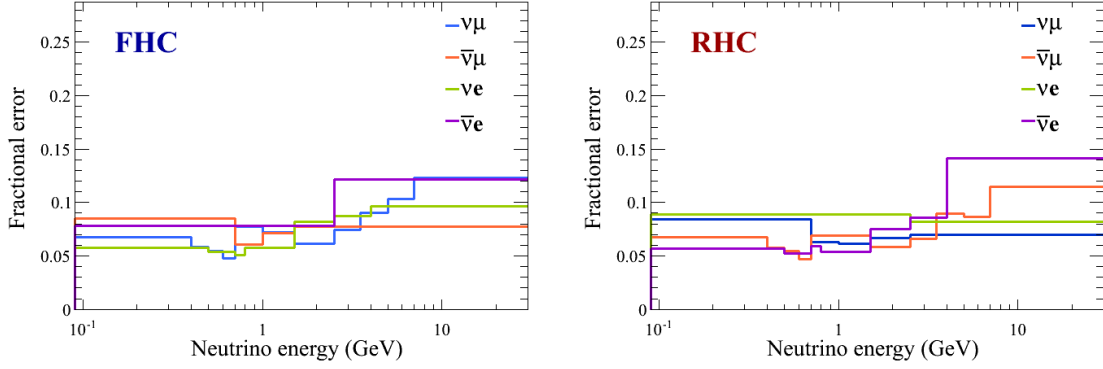
Figure 8.13: Fractional uncertainties on the ν beam fluxes. The uncertainties are taken from TN-354 [33]
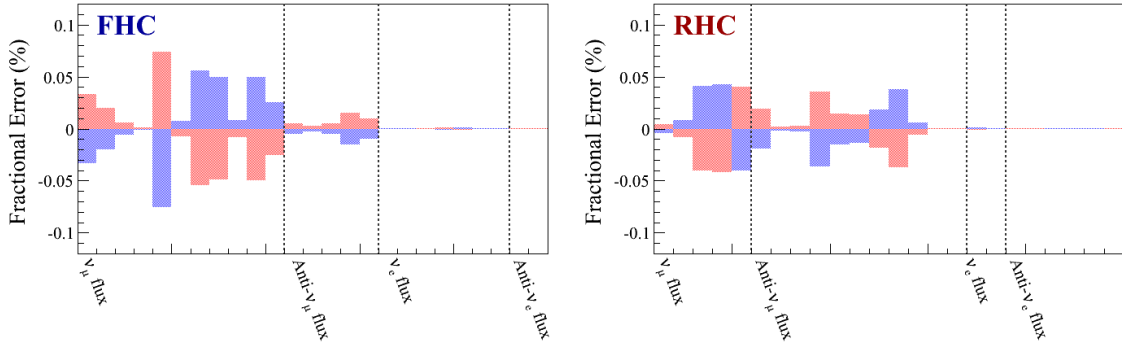
Figure 8.14: Fractional change in the total average tagging efficiency. Right and left are for the FHC and RHC $1R\nu_\mu$ samples, respectively. As the $1R\nu_\mu$ samples are dominantly composed by the ν_μ and $\bar{\nu}_\mu$ fluxes, only the systematic parameters of these fluxes have therefore visible variations. The blue and red bars correspond to $\pm 1\sigma$ variations, respectively.

Although the correlations among the flux parameters are studied well, these are ignored, because the impacts of all the parameters on the tagging efficiency are marginal. The total fractional uncertainties on the efficiency are estimated by adding each parameter variation linearly as follows. In the case of the average tagging efficiency, it is estimated to be less than 0.38%, which is summarized in Table 8.11, and is very small.

$$\delta\varepsilon_{\text{Flux}} = \sum_i \max\{|\delta\varepsilon_i(+1\sigma)|, |\delta\varepsilon_i(-1\sigma)|\}. \tag{8.3.2}$$

8.3.4   Pion FSI/SI

Uncertainties on pion FSI/SI affect final states (i.e. visible topology) in SK, because the processes of QE scattering, absorption, and charge exchange (CX) can alter energy deposition, number of visible particles, etc. These uncertainties can vary the

composition of the $1R\nu_\mu$ samples, which results in variations in neutron tagging efficiency. Since both pion FSI and SI are handled by the same cascade model in NEUT described in Section 4.2.1, the FSI and SI uncertainties are propagated by varying a set of systematic parameters of the model.

The NEUT's cascade model is divided into two pion energy regions. In each region, the microscopic cascade interaction probabilities are scaled via the following systematic parameters. In the low energy region (pion momentum $p_\pi < 500 \,\mathrm{Med/c}$), `FSIABS`, `FSIQE`, and `FSICX` consider uncertainties on the interaction probabilities for the absorption, QE scattering including CX, and the branching fraction of CX, respectively. In the above $p_\pi > 500 \,\mathrm{MeV/c}$ region, pions have enough energy to produce hadrons and the pion absorption becomes smaller. Thus, uncertainties on the QC scattering, the inelastic processes, CX in the high energy region are treated by `FSIQEH`, `FSIQEH`, and `FSICX`, respectively.

These parameters are constrained by various experimental pion scattering data and a 1-σ surface in the parameter space is constructed from the constraint. From the surface, 16 sets of the parameters are chosen, and used to evaluate the systematic uncertainties on neutron tagging efficiency. Table 8.3 summarizes the 16 sets. The detail of the procedure to derive the 16 sets can be found in [218]. For each

Table 8.3: π FSI/SI 1 σ parameter sets.

Comment	Par. set number	FSIQE	FSIQEH	FSIINEL	FSIABS	FSICX	FSICXH
Nominal	0	1.0	1.8	1	1.1	1.0	1.8
	15	0.6	1.1	1.5	0.7	0.5	2.3
	16	0.6	1.1	1.5	0.7	1.6	2.3
	17	0.7	1.1	1.5	1.6	0.4	2.3
	18	0.7	1.1	1.5	1.6	1.6	2.3
Had. Prod. Up	19	1.4	1.1	1.5	0.6	0.6	2.3
	20	1.3	1.1	1.5	0.7	1.6	2.3
	21	1.5	1.1	1.5	1.5	0.4	2.3
	22	1.6	1.1	1.5	1.6	1.6	2.3
	23	0.6	2.3	0.5	1.1	0.5	1.3
	24	0.6	2.3	0.5	1.1	1.6	1.3
	25	0.7	2.3	0.5	1.1	0.4	1.3
	26	0.7	2.3	0.5	1.1	1.6	1.3
Had. Prod. Down	27	1.4	2.3	0.5	1.1	0.6	1.3
	28	1.3	2.3	0.5	1.1	1.6	1.3
	29	1.5	2.3	0.5	1.1	0.4	1.3
	30	1.6	2.3	0.5	1.1	1.6	1.3

parameter set, event-by-event weights are generated, and are used to reweight the nominal MC events. Fractional errors for neutron tagging efficiency are computed for each parameter set by the reweighting. Figure 8.15 shows the fractional errors for the average tagging efficiency.

All the 16 sets represent the $1\,\sigma$ uncertainty of the model. The systematic uncertainties due to pion FSI/SI are therefore computed as the RMS of the fractional errors, and are estimated to be less than 0.2% for the average tagging efficiency as

shown in Table 8.11.
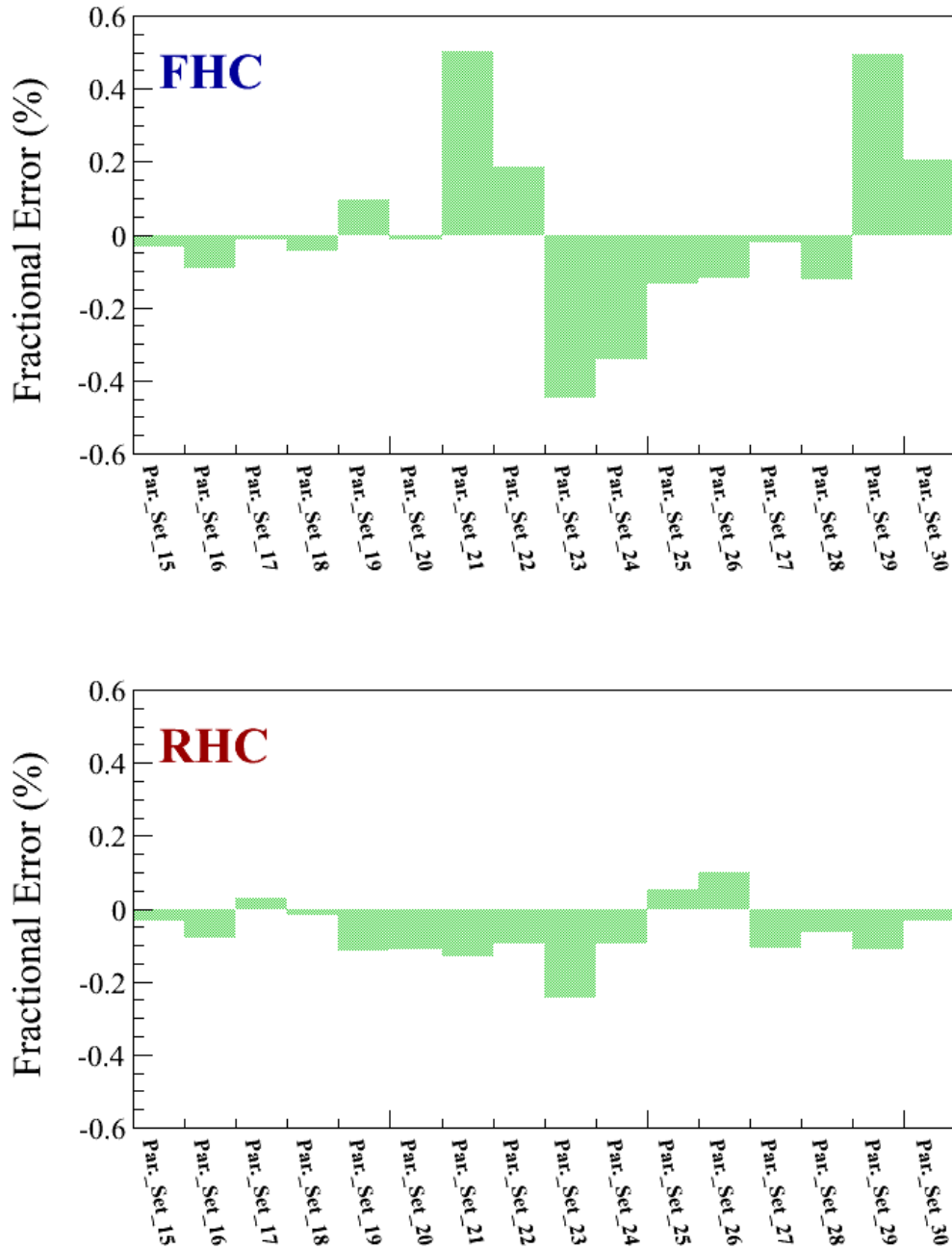
Figure 8.15: Fractional changes in the average neutron tagging efficiency due to pion FSI/SI uncertainty. Top and bottom figures are for the FHC and RHC $1R\nu_\mu$ samples, respectively. The horizontal axes represent the parameter sets described in Table 8.3.

8.3.5   Nucleon FSI

Uncertainties associated with nucleon FSI are estimated by using a GENIE MC. In the case of GENIE, nucleon FSI is simulated by a data-driven model called hA. It simulates the charge exchange, elastic scattering, inelastic scattering, and absorption.

Table 8.4: List of parameters which describe the nucleon final state interactions in GENIE. Numbers taken from [38].

Parameter name	Description	Fractional error
x_{mfp}^{N}	Total rescattering probability	$\pm 20\%$
x_{cex}^{N}	Charge exchange probability	$\pm 50\%$
x_{el}^{N}	Elastic reaction probability	$\pm 30\%$
x_{inel}^{N}	Inelastic reaction probability	$\pm 40\%$
x_{abs}^{N}	Absorption probability	$\pm 20\%$
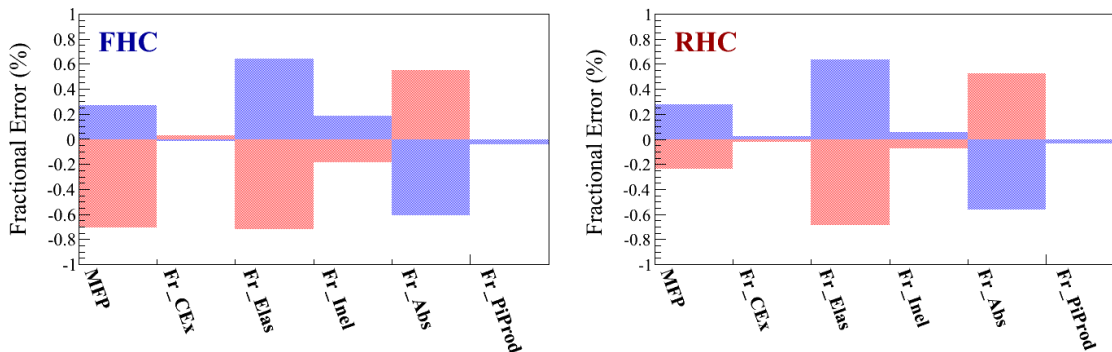
Figure 8.16: Fractional change in the average tagging efficiency for the FHC (left) and RHC (right) $1R\nu_\mu$ samples. The blue and red bars correspond to $\pm 1\,\sigma$ variations, respectively.

The uncertainties on these processes are parameterized by x_{mfp}^{N}, x_{cex}^{N}, x_{el}^{N}, x_{inel}^{N}, and x_{abs}^{N}, respectively. The first parameter alter the total interaction probability, whereas the others vary the fraction of the corresponding interaction process. Table 8.4 shows the $1\,\sigma$ errors of the parameters.

These errors are propagated by reweighting the nominal GENIE MC on an event-by-event basis. Figure 8.16 shows the resulting fractional change in the average tagging efficiency for $\pm 1\,\sigma$ variations of a parameter of interest. Total systematic uncertainties on the tagging efficiencies are estimated by adding the fractional changes in quadrature. As described in Table 8.11, the estimated uncertainties are $\sim 1\%$.

8.3.6   Nucleon SI

Uncertainties regarding nucleon SI affect the distance from ν interaction and neutron capture vertices directly. As was mentioned in Section 6.2, in the primary selection

184

neutron candidates are searched using ν interaction vertex. In the first step of the selection, the vertex is alternatively used as the true neutron capture's one, which introduce a weak correlation between the two vertices. Thus, uncertainties regarding nucleon SI can vary the neutron tagging efficiencies through the correlation.

The simulation of nucleon SI is handled by GCALOR [134] in SKDETSIM as described in Section 4.3. For the energies of the T2K beam neutrinos, nucleons are simulated by HETC [195][196] and MICAP [197] codes in GCALOR. Protons are simulated by HETC only. In the case of neutrons, HETC and MICAP are called for above and below 20 MeV kinetic energy regions, respectively.

In the following parts, uncertainties regarding HETC and MICAP are described separately. As the results of the MICAP simulation should be fully correlated with that of HETC, the total systematic uncertainties regarding nucleon SI are calculated by adding the resulting fractional variations due to HETC and MICP linearly, and etimated to be $\sim 7\%$ as shown in Table 8.11.

Nucleon SI in high energy region

In HETC, the interaction probability as well as interaction channel is calculated based on the Bertini's free nucleon-nucleon cross sections [185]. Thus, uncertainties on the cross sections can directly vary the distance between ν interaction and neutron capture vertices, and result in variations in the neutron tagging efficiency. Figure 4.6 show the total free nucleon-nucleon cross sections used in HETC.

An experimental constraint on the cross sections by nucleon-oxygen scattering in the T2K energy region may be an ideal input to be propagated to the neutron tagging efficiency. However, there is no such experimental data. A conservative error assignment on the cross sections is therefore made based on an analysis of world experimental data of proton-carbon scattering [219]. In that analysis, the theoretical cross sections of carbon were calculated by NEUT which uses the same Bertini's cross sections [135] as used in HETC. The calculated cross sections were compared to several theoretical calculations as well as the data. The comparison showed that the total Bertini's cross sections need to be varied by $\pm 30\%$ in order to cover both the other calculations and the data. Based on the comparison, we determined to assign a 30% error on the total Bertini's cross section as the input of the systematic uncertainty regarding HETC.

In order to propagate the cross section error to the neutron tagging efficiencies of the $1R\nu_\mu$ samples, the nominal hybrid neutron MC described in Section 4.5 was regenerated varying the total cross section by $\pm 30\%$.

The left panel of Figure 8.17 shows distribution of true distance from ν interaction vertex and neutron capture vertex for total neutrons. As shown in the figure, the ± 30 % errors have large impacts on the normalization of the distribution (i.e. number of total neutrons), and vary the total number of neutrons by $+6/-9\%$ and $+10/-15\%$ for the FHC and RHC $1R\nu_\mu$ samples, respectively. In addition, the shape of the distribution is also largely varied. Similar variations are seen for the tagged neutrons as shown in the middle panel of the figure. Since the effects of the uncertainty on the cross sections are similar between the total and tagged neutrons, most of the

variations in the total and tagged neutrons are therefore largely cancelled out when calculating the neutron tagging efficiency. The resultant neutron tagging efficiency is shown in the right panel of Figure 8.17. The systematic uncertainty due to the Bertini's cross sections are estimated to be less than 6.7% for the average neutron tagging efficiency.
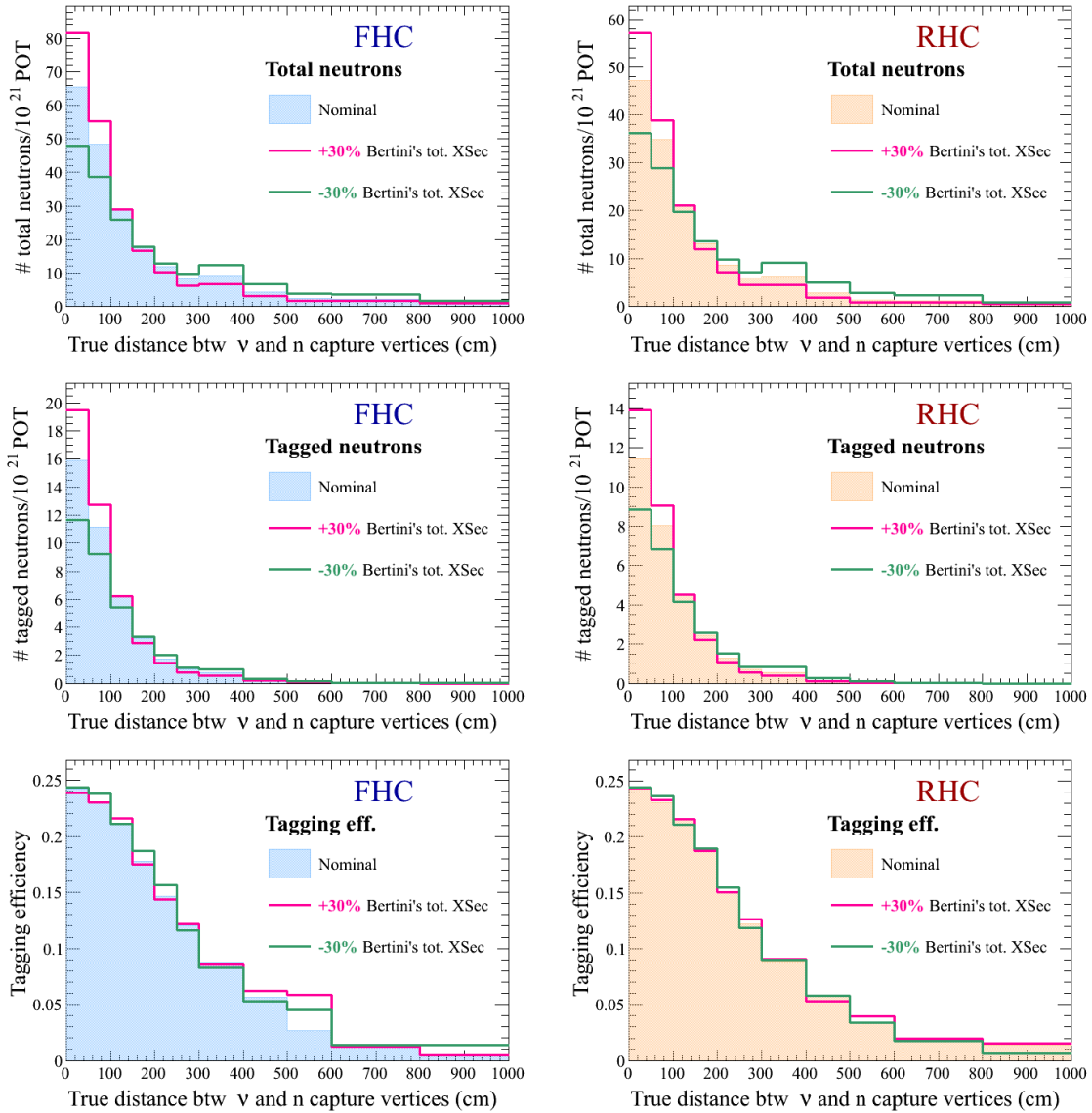
Figure 8.17: Distribution of the true distance from ν interaction and neutron capture vertices for the total neutrons (top) and the tagged neutrons (middle). Neutron tagging efficiency as a function of the true distance (bottom) (i.e. middle/top). The right and left side plots correspond to the FHC sample and RHC $1R\nu_\mu$ samples, respectively. All the distributions are normalized by 10^{21} POT. The histograms filled by the colors are made from the nominal MC, whereas the pink and green solid lines are made from the regenerated MC with the $\pm 30\%$ variation of the Bertini's total free N-N cross sections, respectively.

Neutron SI in below 20 MeV region

The remaining part describes the systematic uncertainties regarding the cross section for the neutrons whose kinetic energy is below 20 MeV.

Neutrons in this energy region are simulated by MICAP which utilizes the ENDF/B (Evaluated Neutron Data Files version B) cross section data to calculate the interaction probabilities and resulting interaction channel. The MICAP program uses a thinned ENDF/B version V in which version the number of data points are reduced from its original version. The original version was released more than 20 years ago, whereas there have been several version updates with visible changes from the version V. The version VIII0 is the latest one as of this moment. Figure 8.18 shows comparison of the microscopic total cross sections. As shown in the figure, the microscopic total cross sections of hydrogen nucleus has changed slightly from the thinned version V used for MICAP and the relative changes from MICAP are less than 2.5%. On the one hand, there are clear differences between the two versions, which mainly comes from the absorption cross sections.
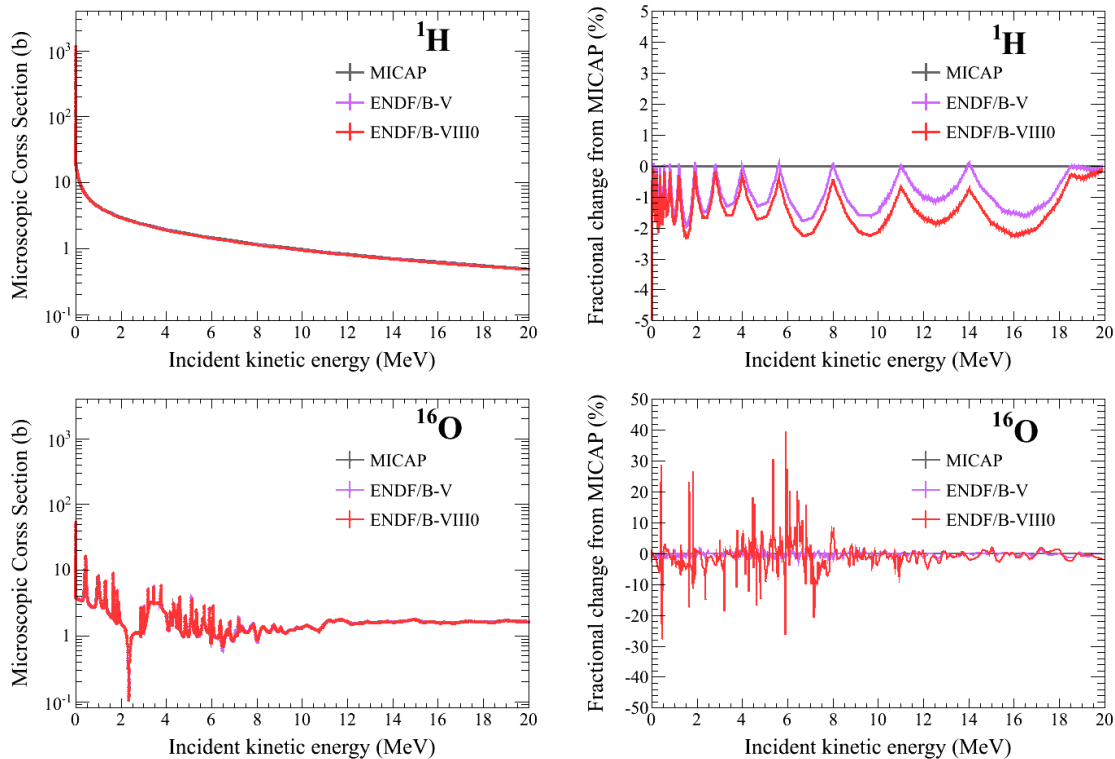
Figure 8.18: Comparison of ENDF/B microscopic total cross section between different versions. MICAP use a thinned version V and thus, there are difference between the MICAP's one and version V (formatted in ENDF-6).

There are relatively large differences between two versions especially for oxygen nucleus in the figure shown. The uncertainties on the cross section used for MICAP are therefore assigned as the differences between the two versions. In order to estimate the impacts of the cross section differences, the ENDF/B-VIII0 cross sections

needed to be implemented to SKDETSIM. The original MICAP code was modified
and a new code was developed in order to replace the MICAP's cross sections with
the ENDF/B-VIII0's ones.

After the modifications, the nominal hybrid neutron MC was regenerated with
the ENDF/B-VIII0's ones. Figure 8.19 shows the distribution of the true distance
between the ν interaction and neutron capture vertices for the nominal and regener-
ated MCs.

Figure 8.19: Distribution of the true distance between the true distance between the
ν interaction and neutron capture vertices. The histograms filled by the colors and
solid lines are made from the nominal MC and regenerated MC with the ENDF/B-
VIII0, respectively. The left and right plots are for the FHC sample and RHC $1R\nu_\mu$
samples, respectively.

As shown in the figure, the shapes of the distributions are relatively similar, but
the normalization (i.e. number of total neutrons) differs between the two MCs. The
reason for the variation (i.e. similar shape and different normalization) is explained
as follows. The origin of the similar shapes come from the fact that in this energy
region the mean distance from the generation point to the capture position is very
short and is less than 35 cm as shown in Figure 8.20. Thus, the cross section dif-
ferences do not result in a large variation in the distance and alter the shape of the
distributions of the $1R\nu_\mu$ samples slightly. For the difference in the normalization,
the fraction of the disappearance interaction of oxygen nucleus in which there is no
out-going neutron is largely different between the two versions and the version VIII0
has clearly higher fraction as shown in Figure 8.21. In the regenerated MC with
the version VIII0, number of neutrons which disappear before thermalization and

neutron capture by hydrogen nucleus therefore increased compared to the nominal MC.

The systematic uncertainties due to the cross sections used for MICAP are assigned as the differences between the nominal and regenerated MCs and are estimated to be less than 0.2% for the average tagging efficiency.

Figure 8.20: Mean true distance between generation and neutron capture positions for the MICAP's thinned ENDF/B-V and ENDF/B-VIII0 versions. These are made from results of neutron particle gun MC of the detector simulation.
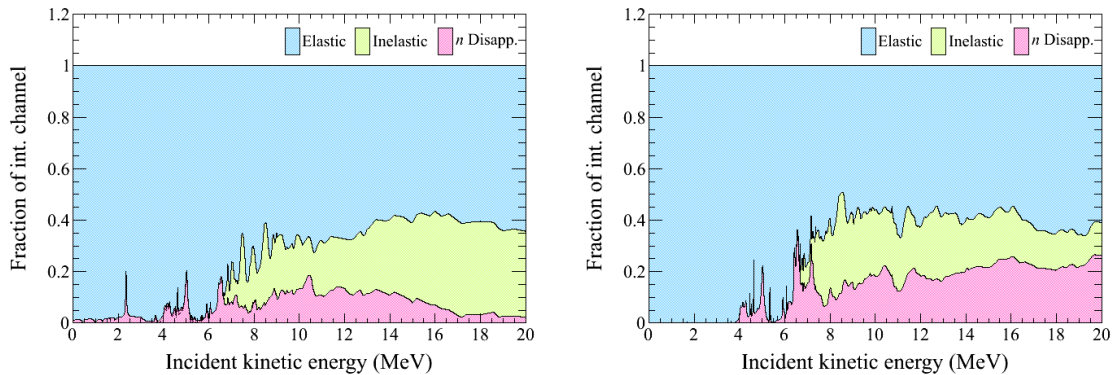
Figure 8.21: Fraction of interaction channel of oxygen nucleus for the MICAP's thinned version V (left) and ENDF/B-VIII0 (right).

8.3.7 μ^- and π^- captures on oxygen

The uncertainties on neutron productions by the μ^- and π^- captures on oxygen nucleus are considered. As was described in Section 4.4, in the nominal hybrid neutron MC G4MuonMinusCaptureAtRest and G4PiMinusAbsorptionAtRest simulate these productions, respectively. Although these simulation codes are the default models

in Geant4.9.6, Geant4.9.6 also provides alternative models. The uncertainties on these production are therefore taken into account by taking the differences between models.

In the case of the μ^- capture, the alternative model is CHIPS (Chiral Invariant Phase Space) which is derived from a non-perturtative theory of QCD. The nominal hybrid neutron MC was regenerated by replacing `G4MuonMinusCaptureAtRest` with `G4QCaptureAtRest` which is the class in CHIPS codes. Figure 8.22 shows the distribution of the true distance between ν interaction and neutron capture vertices for `G4MuonMinusCaptureAtRest` and `G4QCaptureAtRest`. As shown in the Figure, the difference is marginal and thus, the resulting fractional variations in the tagging efficiency are also small and is estimated to be less than 1.5% for the average tagging efficiency.
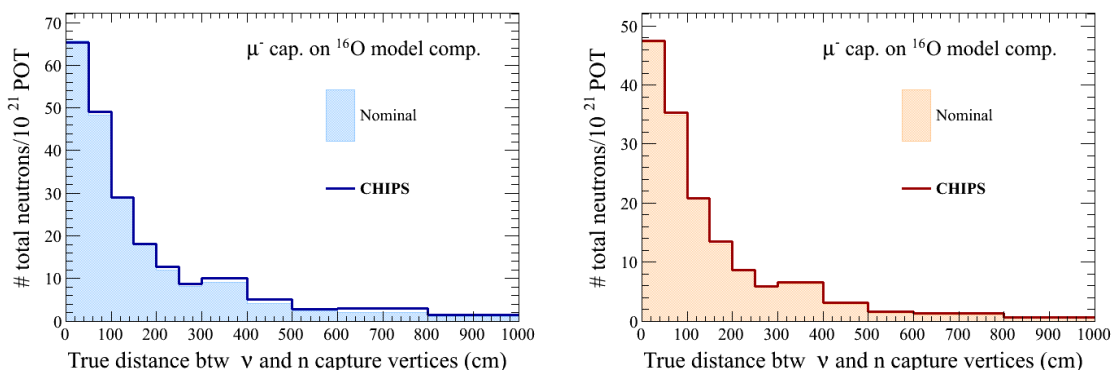
Figure 8.22: Comparison of the different simulation of neutron productions by the distribution of true distance between the ν interaction and neutron capture vertices. The left and rights plot are for the FHC and RHC $1R\nu_\mu$ samples, respectively. In the plots, "Nominal "corresponds to the nominal MC generated with `G4MuonMinusCaptureAtRest`, whereas "CHIPS "corresponds to the regenerated MC with `G4QCaptureAtRest` instead. All the distributions are normalized by 10^{21} POT.

For the π^- capture, in addition to CHIPS, there is another alternative model which is a similar cascade model to HETC. The uncertainty regarding the π capture is therefore assigned from the differences between `G4PiMinusAbsorptionAtRest`, `G4QCaptureAtRest`, and `G4PiMinusAbsorptionBertini`. These differences are obtained by regenerating the nominal MC in the same way as the case of μ^- capture. Figure 8.23 shows the resulting distribution of the true distance between the ν interaction and neutron capture vertices for the three MCs. The average tagging efficiency varied by $\sim$1% due to the differences as shown in Table 8.11.
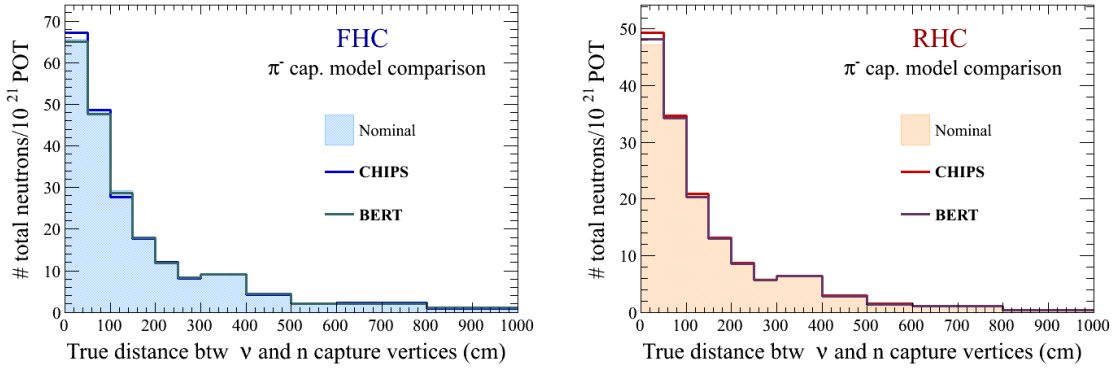
Figure 8.23: The distributions of true distance between the ν interaction and neutron capture vertices for the three different models of the neutron productions by π^- capture. The left and right plots are for the FHC and RHC $1R\nu_\mu$ samples, respectively. In the plots, "Nominal "corresponds to the nominal MC generated with `G4PiMinusAbsorptionAtRest`, whereas "CHIPS "and "BERT "correspond to the regenerated MC with `G4QCaptureAtRest` and `G4PiMinusAbsorptionBertini`, respectively.

8.3.8   Detector response for ν events

Uncertainty on the detector response which affects the selection efficiency of the $1R\nu_\mu$ events may vary the shape of the true neutron travel distance, which cases systematic variation on the tagging efficiencies. As such uncertainty has been estimated in the from of the covariance matrix described in [220], the covariance matrix is therefore used. In the covariance matrix, the $1R\nu\mu$ events are categorized based on the interaction modes, neutrino flavor, and reconstructed neutrino energy as summarized in Table 8.5. Figure 8.24 shows the uncertainty regarding the selection efficiency of the $1R\nu_\mu$ events for each event category.   Fractional changes in the tagging efficien-

Table 8.5: Categorization of the $1R\nu_\mu$ events for the systematic uncertainty on the detector response. The reconstructed energy is computed as in Equation 7.5.2

Beam mode	True event category	Reco. ν energy bin edges (GeV)	Number of bins
FHC	$\nu_\mu/\bar{\nu}_\mu$ CCQE	0.0, 0.4, 1.1, 30.0	4
	$\nu_\mu/\bar{\nu}_\mu$ CCNQ	0.0, 30.0	1
	$\nu_e/\bar{\nu}_e$ CC	0.0, 30.0	1
	NC	0.0, 30.0	1
RHC	$\nu_\mu/\bar{\nu}_\mu$ CCQE	0.0, 0.4, 1.1, 30.0	4
	$\nu_\mu/\bar{\nu}_\mu$ CCNQ	0.0, 30.0	1
	$\nu_e/\bar{\nu}_e$ CC	0.0, 30.0	1
	NC	0.0, 30.0	1

cies are computed for 1σ variation of each individual event category by reweighting
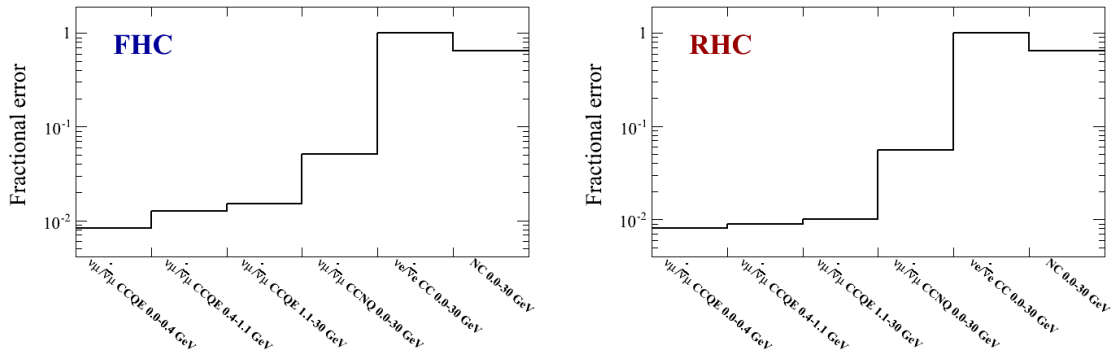
Figure 8.24: Fractional uncertainties on each event category which are derived from the uncertainty on the detector response. The left and right plots are for the FHC and RHC $1R\nu_\mu$ samples, respectively.

the nominal MC on event-by-event basis. Figure 8.25 shows the resulting fractional changes. The systematic uncertainties due to the detector systematics are evaluated in the same manner as the flux uncertainties and are estimated to be less than 0.4% for the average tagging efficiency, which are described in Table 8.11.
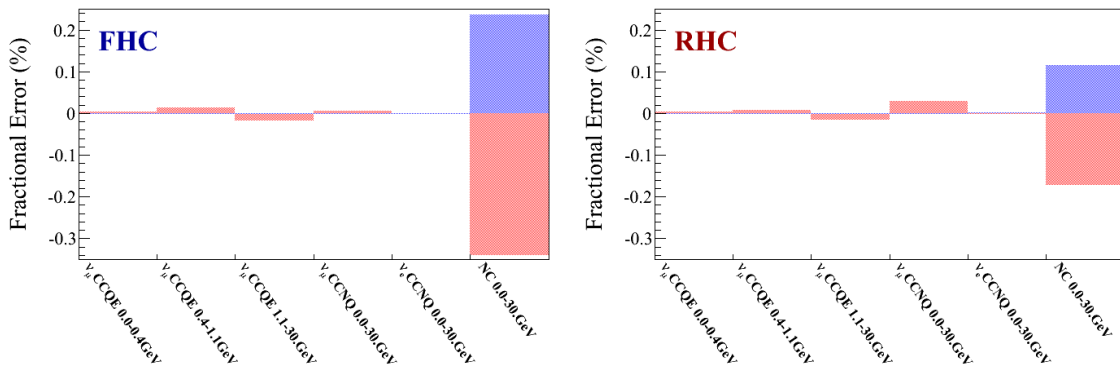
Figure 8.25: Fractional change in the average tagging efficiency for the FHC (left) and RHC (right) $1R\nu_\mu$ samples.

8.3.9   Oscillation parameters

The uncertainties on the oscillation probabilities are considered. As the neutrons are not used in the oscillation analyses for the Run 1-9 data, the measured oscillation parameters using the data can be used as the input of the systematics regarding the oscillation probabilities. Table 8.6 summarizes the 1σ uncertainties on the oscillation parameters used for the oscillation probability calculation. In order to estimate the impacts on the tagging efficiency, oscillation probability is re-calculated for the nominal MC on an event-by-event basis by varying $\pm 1\sigma$ for each individual parameter and then, fractional variations in the efficiency are computed. As shown in Table 8.7, the systematic variations due to the oscillation parameters are very small.

Table 8.6: List of nominal values and 1σ intervals of the parameters used for the oscillation probability calculation. Taken from Table 7 in [36].

Parameter	Nominal value	1σ interval
$\sin^2\theta_{13}$	0.0212	[0.0225,0.0323]
$\sin^2\theta_{23}$	0.532	[0.495,0.562]
$\Delta m^2_{23}\ 10^{-3}\ \text{eV}^2$	2.452	[2.382,2.523]
δ_{CP}	-1.885	[-2.460,-1.187]

The total systematic uncertainty due to the oscillation parameters is calculated by the same way as the flux uncertainties using Equation 8.3.2 since the know correlation between the parameters are ignored. As shwon in Table 8.11, the estimated uncertainties on the average tagging efficiency are ∼0.2%.

Table 8.7: Fractional change in the total average tagging efficiencies for $\pm 1\sigma$ variations of each oscillation parameter.

	$\sin^2\theta_{13}$ $+1\sigma/-1\sigma$	$\sin^2\theta_{23}$ $+1\sigma/-1\sigma$	Δm^2_{23} $+1\sigma/-1\sigma$	δ_{CP} $+1\sigma/-1\sigma$
FHC	-0.00%/+0.00%	+0.12%/-0.01%	-0.01%/+0.05%	-0.00%/+0.00%
RHC	-0.00%/+0.00%	+0.08%/-0.01%	+0.05%/-0.03%	+0.00%/-0.00%

8.3.10 ν vertex

The neutron tagging uses ν vertex to select the neutron candidates, which was mentioned in Section 6.2. The uncertainties on the resolution and shift for the ν reconstructed vertex may affect the performance of the selection. These uncertainties have been studied using cosmic ray muons and these studies are summarized in [221] and in [220]. The estimated resolution and shift errors are 2.5 cm and 5 cm, respectively.

In order to propagate these errors to the neutron tagging efficiency, three artificial vertex shifts are added to the nominal MC on an event-by-event basis as follows:

- Isotropic shift : add isotropic 2.5 cm vertex shift.

- Forward shift : add 5 cm vertex shift along the particle momentum direction.

- Backward shift : add 5 cm vertex shift along the opposite direction to the particle momentum direction.

The vertex resolution error is taken into account by the first shift, whereas the vertex shift error is considered by the last two shifts. The tagging efficiency is computed for each individual shift and then, the fractional change in the efficiency is evaluated. Table 8.8 summarizes the resulting fractional change in the average tagging efficiency. The total systematic uncertainties regarding these vertex errors are computed by

Table 8.8: Fractional changes in the average neutron tagging efficiency due to the artificial vertex shifts

| | Resolution error | Shift error | |
	Isotropic shift	Forward shift	Backward shift
FHC	-0.07%	0.26%	-0.11%
RHC	-0.06%	0.22%	-0.22%

adding the variations by the resolution and shift errors in quadrature. The estimated uncertainties are ∼0.3%, which are described in Table 8.11.

8.3.11 Simulation of PMT gain increase

The SK time variations described in Section 6.5 affect both the neutron tagging efficiency and the background event rate. The effects of the time variations are estimated and have been corrected to the nominal values by utilizing the simulation for 2.2 MeV γ rays and T2K dummy spill data for the background events, respectively. However, there is a non-negligible systematic uncertainty associated with the simulation of the PMT gain increase. It should be noted that this is related only to the simulation of 2.2 MeV γ rays and thus, there is no such uncertainty on the accidental background events which are modeled by T2K dummy spill data.

As shown in Figure 6.26, the PMT gain has continuously increased, which makes the hit probability higher as time proceeds. In SKDETSIM, the increase of the gain is simulated by scaling charge of the hit PMT Q while keeping the threshold on the charge. The scaling is performed as follows:

$$Q \times \left(1 + \frac{G(t) - G_0}{G_0}\right), \qquad (8.3.3)$$

where $G(t)$ is the PMT gain at time t and G_0 is the average of the PMT gain measured in Oct. 2008.

Thus, this way to simulate charge of PMT hit naturally increase number of PMT hits for a given fixed energy deposition as the gain increases as shown in the left side panel of Figure 8.26.
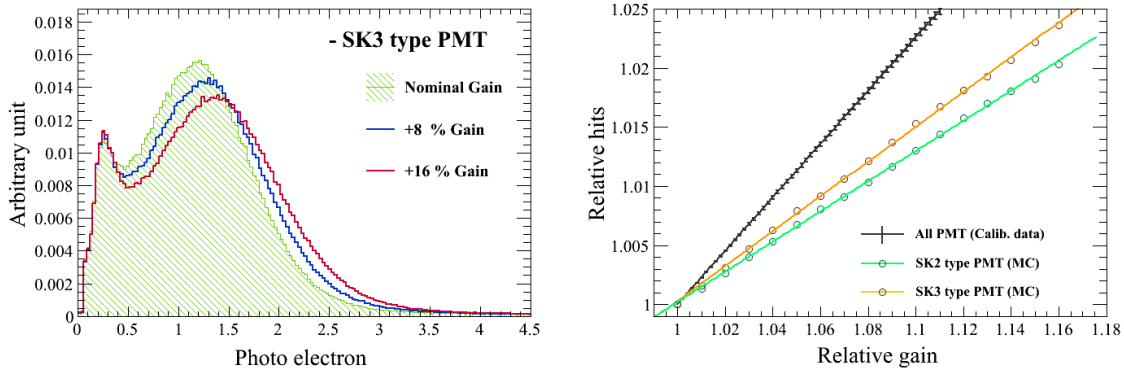
Figure 8.26: Distribution of the single photo-electron of the SK-III type PMTs used in SKDETSIM (left) and Relation between relative number of PMT hits and relative PMT gain for the data derived from various calibrations and MC (right). In left side plot, the green filled histogram corresponds to the nominal gain and the blue and red lines correspond to +8% and +16% gain from the nominal value, respectively.

In the neutron tagging, what is the most important in the detector simulation is to reproduce the time evolution of the number of PMT hits rather than PMT gain itself. If the number of PMT hits as a function of PMT gain differs between the data and the MC, then it causes a systematic variation in the neutron tagging efficiency. It can be assumed from the studies on the various calibration data performed in SK that the relative number of PMT hits are proportional to the relative PMT gain. The proportional constant has been estimated to be 0.226 based on the calibration data [222]. For the detector simulation, on the other hand, the proportional constant evaluated from the gain simulation is $\sim$1.6 times smaller compared to the data. The right panel of Figure 8.26 shows the linear relation obtained by the calibration data in comparison with that of MC. The disagreement of the proportional constant is therefore interpreted as the systematic uncertainty regarding the gain simulation.

In order to account for the disagreement, an extra scaling factor α is introduced into the gain simulation as follows:

$$Q \times \left(1 + \alpha \times \frac{G(t) - G_0}{G_0}\right). \tag{8.3.4}$$

Then, additional MC regeneration with $\alpha = 1.6$ was performed in the same way as described in Section 6.5.2. It should be noted that the case of $\alpha = 1.0$ is the same as what was done in Section 6.5.

Figure 8.27 shows the comparison of the neutron tagging efficiency and the background event rate between the $\alpha = 1.0$ and $\alpha = 1.6$ cases. As shown in the figure, the efficiency clearly differs between the two cases, whereas there is no visible variation for the background event rate. This is as expected, because the extra scaling is

195

applied only to the simulation of $2.2\,\mathrm{MeV}$ γ rays and the contamination of the PMT
hits produced by the γ rays in the background events is marginal.
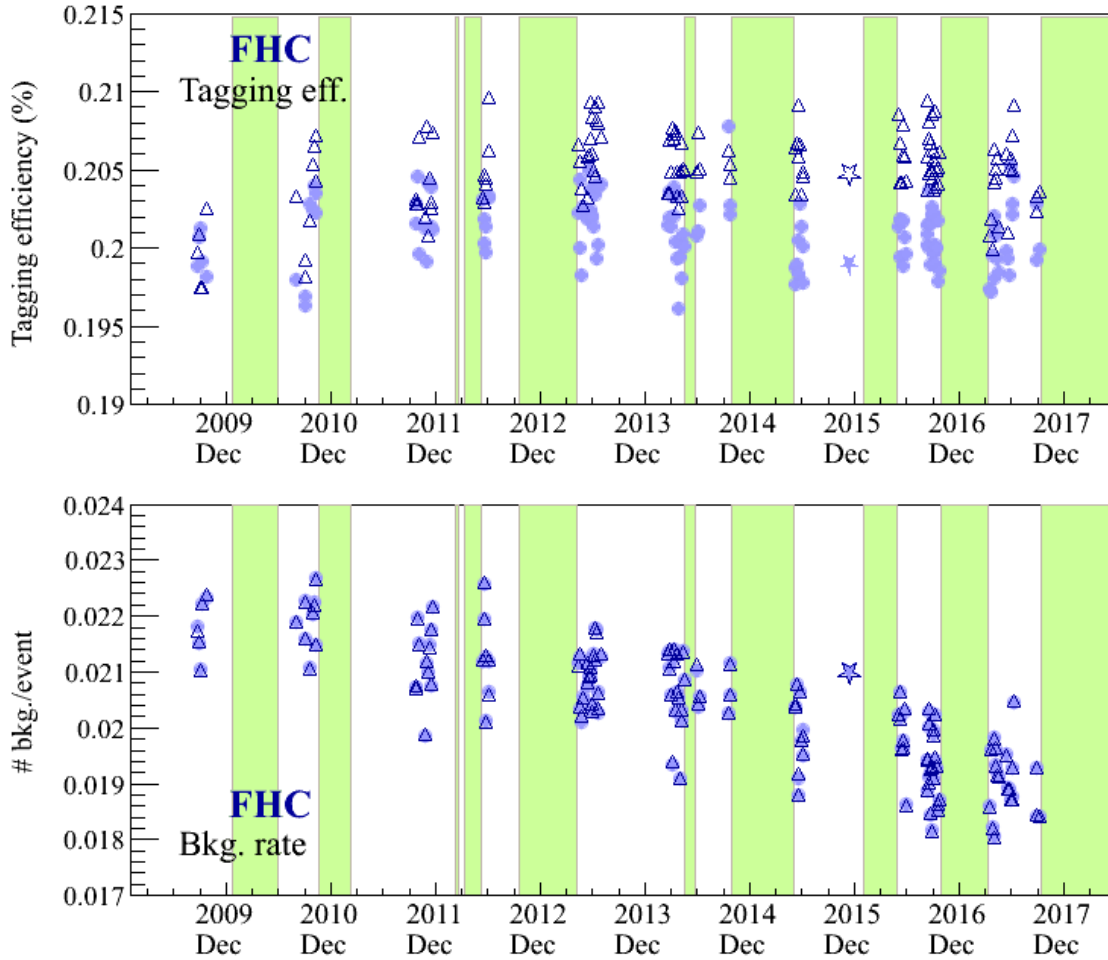
Figure 8.27: Comparison of the $\alpha = 1.0$ and $\alpha = 1.6$ cases for the tagging efficiency
(top) and background rate (bottom) after the NN classification. The filled circles and
open triangles are for the regenerated MCs with $\alpha = 1.0$ and $\alpha = 1.6$, respectively.
These plots are for the FHC $1\mathrm{R}\nu_\mu$ sample, but same tendency is also found for the
RHC $1\mathrm{R}\nu_\mu$ sample.

Following the procedure detailed in Section 6.5.3, the tagging efficiencies of the
regenerated MCs with $\alpha = 1.6$ are fitted and then the POT weighted average of the
tagging efficiency is computed. Figure 8.28 shows the fit result and the resultant
average. Even for the case of $\alpha = 1.6$, the fit function defined in Equation 6.5.1 was
applicable, which produced an acceptable $\chi^2/\mathrm{n.d.f} = 275.7/254$.

Table 8.9 summarizes the POT weighted averages for both of the two cases. The
difference between the two cases is then assigned as the systematic uncertainty due
to the simulation of the PMT gain increase. The resultant systematic unertainty on
the average tagging efficiency is $\sim 2\%$ as shown in Table 8.11.
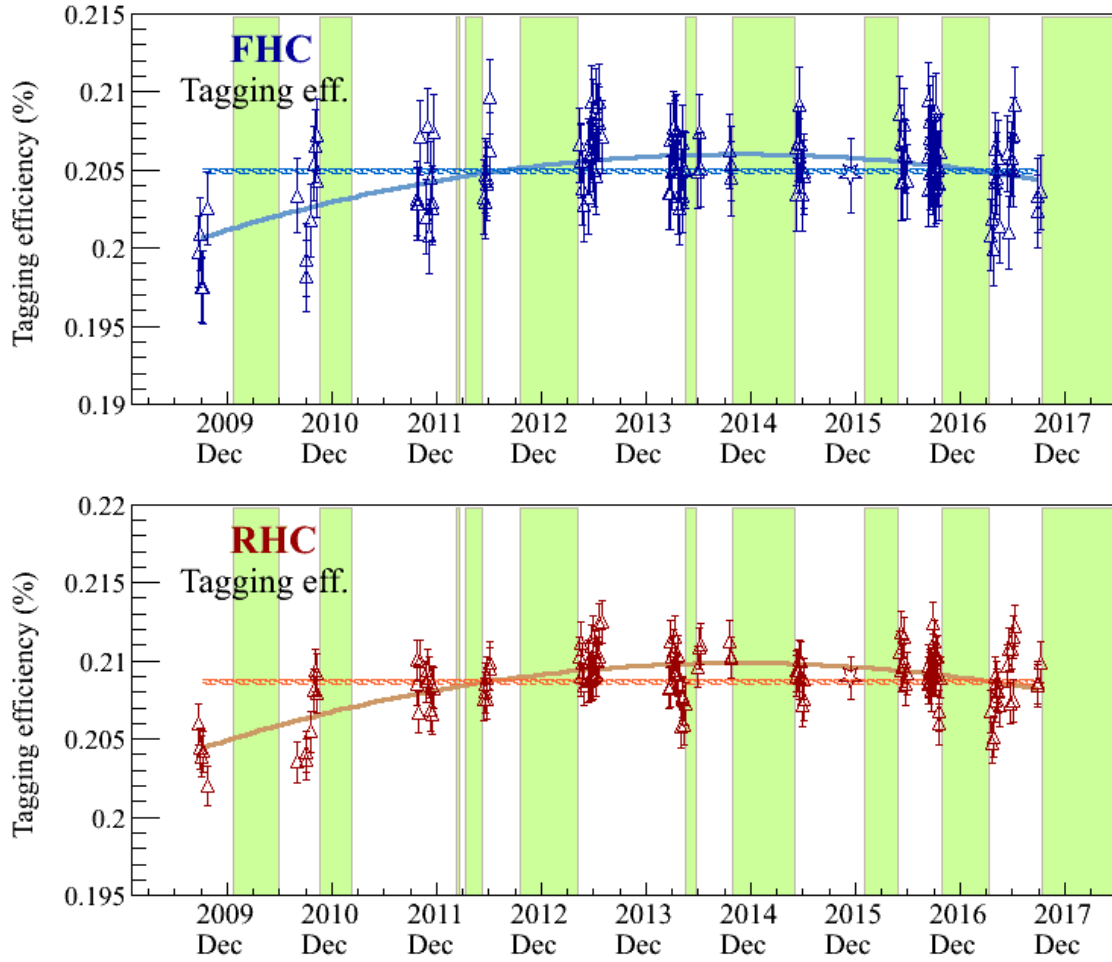
Figure 8.28: Tagging efficiency after the NN classification as a function of time for $\alpha = 1.6$. The solid curves and broken lines correspond to the best fit results and POT weighted averages, respectively. The top and bottom plots correspond to the FHC and RHC $1R\nu_\mu$ samples, respectively.

Table 8.9: POT weighted total average tagging efficiency and background rate for the $\alpha = 1.0$ and $\alpha = 1.6$ cases. X represents either tagging efficiency or background event rate. Note that the numbers for $\alpha = 1.0$ are the same as listed in Table 6.38.

		$\alpha = 1.0$	$\alpha = 1.6$	$(X_{\alpha=1.6} - X_{\alpha=1.0})/X_{\alpha=1.0}$
Tagging Efficiency (%)	FHC	20.09	20.48	+1.98%
	RHC	20.37	20.86	+2.40%
# acc. bkg./ν event	FHC	2.02×10^{-2}	2.02×10^{-2}	0.00%
	RHC	1.94×10^{-2}	1.94×10^{-2}	0.00%

8.3.12 Detector response to 2.2 MeV γ rays

Uncertainty regarding the detector response for 2.2 MeV γ rays is estimated using the Am/Be low energy neutron calibration data described in Section 6.4. Since in principle the calibration enables estimating neutron tagging efficiency, ideally, direct comparison of tagging efficiency between data and MC is desirable to address systematics regarding detector response for 2.2 MeV γ rays.

As was discussed in Subsection 6.4.5, however, such direct comparison needs estimations of both the contamination of fake prompt events in which there is no signal delayed neutrons and neutron absorption by the geometry of the calibration, because these effects cause a systematic decrease of neutron tagging efficiency only for the data. In order to estimate these effects, a precise MC which can simulate both γ rays from the Am/Be source and scintillation light of the BGO scintillator is needed, but is not available at the present moment and is quit challenging to be made. Therefore, a novel method which can avoid those effects was newly developed for this analysis. In this method, systematic uncertainties on the primary selection and NN classification of the neutron tagging algorithm are separately estimated.

$N10_{\mathrm{pvx}}$ primary selection

As was described in Section 6.2, the primary neutron candidate selection is a simple selection based on $N10_{\mathrm{pvx}}$ which is number of PMT hits in a 10 ns timing window. The performance of the primary selection strongly depends on PMT hit yield, and thus difference in PMT hit yield between the data and MC can be systematics regarding the primary selection. The PMT hit yield difference was estimated by comparing the shape of $N10_{\mathrm{pvx}}$ distribution between the data and the MC, because the shape should not be affected by the effects of the fake prompt events and the neutron absorption.

In order to compare the shape and quantify the resulting shape difference, PMT hit yield needs to be parametrized for MC. In SKDETSIM, parametrization of PMT hit yield is not trivial, but quantum efficiency QE (so called `COREPMT`) which is not true quantum efficiency of PMT and is an overall scaling factor of PMT hit probability is employed as an effective parameter. Figure 8.29 demonstrates that

the QE parameter can vary shape of $N10_{\mathrm{pvx}}$ distribution. Figure 8.30 shows the
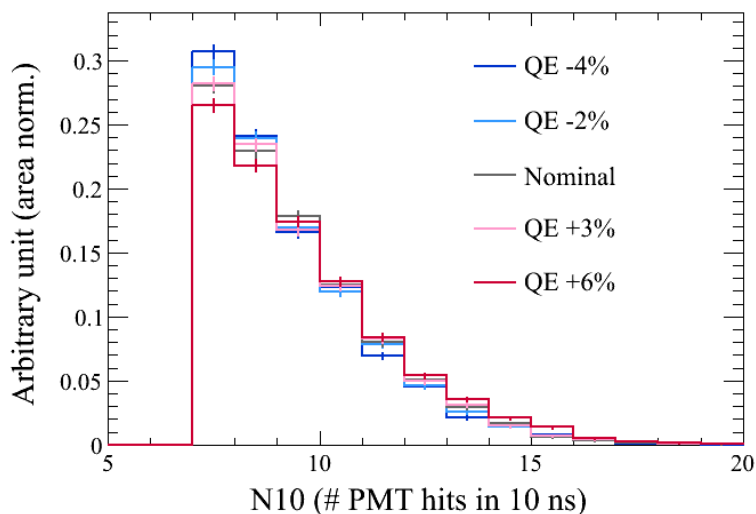
Figure 8.29: QE dependence of $N10_{\mathrm{pvx}}$ shape. The distributions are made from neutron particle gun MC events which are generated by varying QE.

$N10_{\mathrm{pvx}}$ distribution of the data taken at the detector center position. As shown in the plot, the distribution is dominated by the accidental background events selected in the primary selection, and the accidental background component needs to be subtracted for the shape comparison.

As the background data of the calibration was taken with the Am/Be source and a periodic trigger, the $N10_{\mathrm{pvx}}$ distribution of the background data should be same as the accidental background component of the signal calibration data. The background subtraction can be done by scaling the $N10_{\mathrm{pvx}}$ distribution of the background data by the number of prompt events, because the accidental background events do not depend on whether or not prompt event is true $4.4\,\mathrm{MeV}$ γ ray event. Figure 8.31 shows the shape of the accidental background subtracted $N10_{\mathrm{pvx}}$ distribution of the data for the center position.
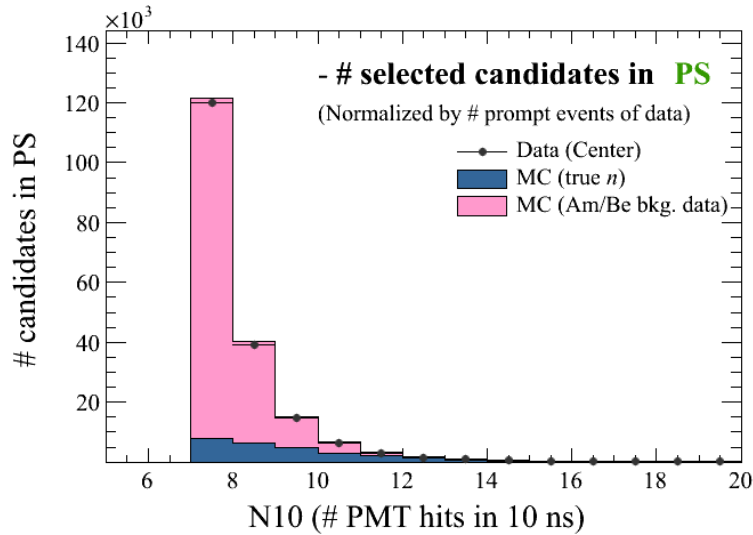
Figure 8.30: $N10_{pvx}$ distribution of the data taken at the center position of the Am/Be calibration. Both the data and MC distributions are normalized by number of prompt events.
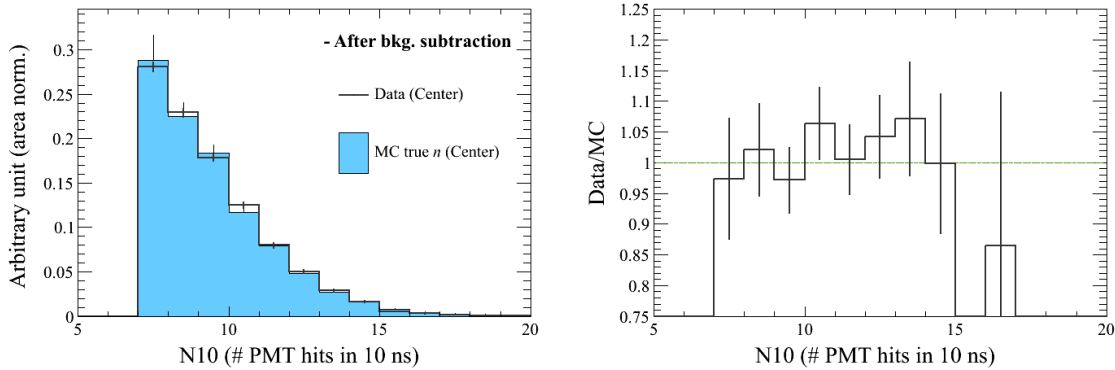
Figure 8.31: $N10_{pvx}$ shape of the data taken at the detector center position of the Am/Be calibration (left) and its ratio to the corresponding MC (right). The shape of the data shown in left panel was obtained by subtracting scaled accidental background of the background data from the $N10_{pvx}$ distribution shown in Figure 8.30.

A χ^2 fit for the shape of $N10_{pvx}$ distribution is performed to address the PMT hit yield of the data. For this fit, a set of MC was generated by varying the QE parameter and then χ^2 is calculated by comparing the shape of $N10_{pvx}$ distributions of the data and MCs. The best fit point of the QE value was estimated by a least square fit of a quadratic function to the calculated χ^2 as shown in the left panel of Figure 8.32. As shown in the plot, the calculated χ^2 values seem not to be smooth. This is due to the statistical fluctuation of the MC, because the available statistics of the MC is limited by the background data statistics. Since the fitted χ^2 curve may change slightly due to the MC statistical fluctuation, the 1σ fractional uncertainty on the PMT hit yield σ_{QE} is conservatively assigned as:

$$\sigma_{QE} = \frac{QE_{+1\sigma} - QE_{Nom}}{QE_{Nom}}, \qquad (8.3.5)$$

where $QE_{+1\sigma}$ is the $+1\sigma$ QE value estimated by the fitted χ^2 curve and QE_{Nom} is the nominal QE value.

The assigned σ_{QE} is 1.9% and is propagated to neutron tagging efficiency of the primary selection. There is a linear relation between relative tagging efficiency and relative QE with respect to the nominal value as shown in the right panel of Figure 8.32. Using the relation, propagation of the uncertainty on the PMT hit yield is done and the resulting variation in the tagging efficiency is estimated to be 2.8%.
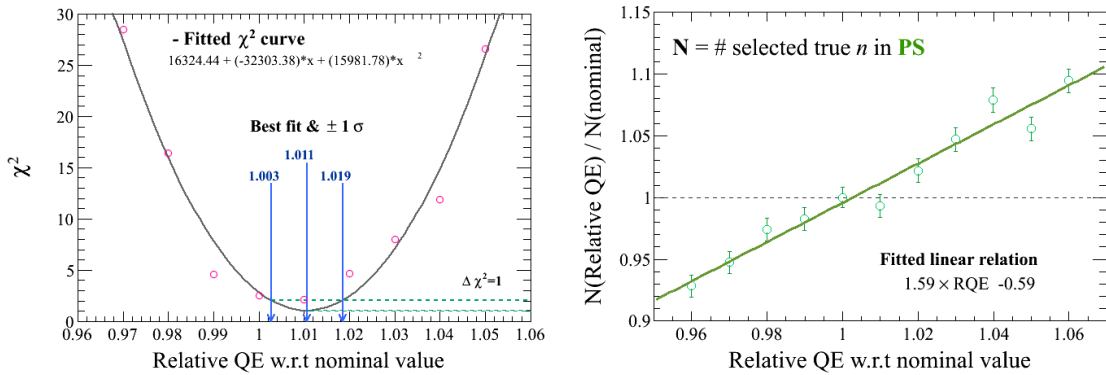
Figure 8.32: $N10_{\text{pvx}}$Calculated χ^2 by comparing $N10_{\text{pvx}}$shape between data ad MC (left). The solid curve is fitted χ^2 obtained by a least square fit with a quadratic function. Relative number of selected true 2.2 MeV γ candidates in the primary selection as a function of relative QE with respect to the default value (right). The error bars are the MC statistical errors. The solid line is obtained by fitting a linear function to the points and is used in order to propagate the QE difference estimated by the shape fit to the neutron tagging efficiency.

Neural network classification

The uncertainty on the NN classification is estimated from the difference in relative efficiency between the data and MC. The relative efficiency is the efficiency from the primary selection and is given as:

$$\text{relative efficiency} = \frac{\text{Selected true neutrons in NN classification}}{\text{Selected true neutrons in primary selection}} \qquad (8.3.6)$$

The relative efficiency does not depend on number of selected prompt events, which means that possible contamination of the fake prompt events can be avoided. In addition, the effect of neutron absorption by the geometry of this calibration should be same between the denominator and numerator. Thus, the relative efficiency is

not affected by those effects.

Both the numerator and the denominator in Equation 8.3.6 can be statistically obtained from the capture time distributions after the primary selection and NN classification, respectively. In order to obtain the numerator and the denominator, a Gaussian χ^2 fit to the capture time distributions is performed by modifying Equation 6.4.3 as follows:

$$\chi^2 = \sum_i \sum_j \frac{\left(\mathcal{E}_{i,j} - \mathcal{O}_{i,j}(\tau, \varepsilon_i, b_i)\right)^2}{\mathcal{E}_{i,j}} + \left(\frac{204.8 - \tau}{0.4}\right)^2, \qquad (8.3.7)$$

Figure 8.33 and 8.34 show the capture time distributions with the best fit curves for the primary selection and NN classification, respectively. As shown in the plots, fraction of the accidental backgrounds significantly differ between the primary selection and NN classification. In the case of the primary selection the huge background events affect extracting τ due to its statistical fluctuation, whereas τ is well extracted in the NN classification. This can potentially cause difference in fitted τ between the primary selection and NN classification, but τ should be same between them. In addition, such difference may cause a systematic bias in relative efficiency. In order to stably fit τ, the penalty term $(204.8 - \tau/0.4)^2$ is added to the χ^2 in the equation. The constraint $204.8 \pm 0.4\,\mu s$ comes from an external experiment result [37]. The fitted τ is $204.8 \pm 0.4\,\mu s$ and $204.9 \pm 0.4\,\mu s$ for the primary selection and NN classification, respectively.
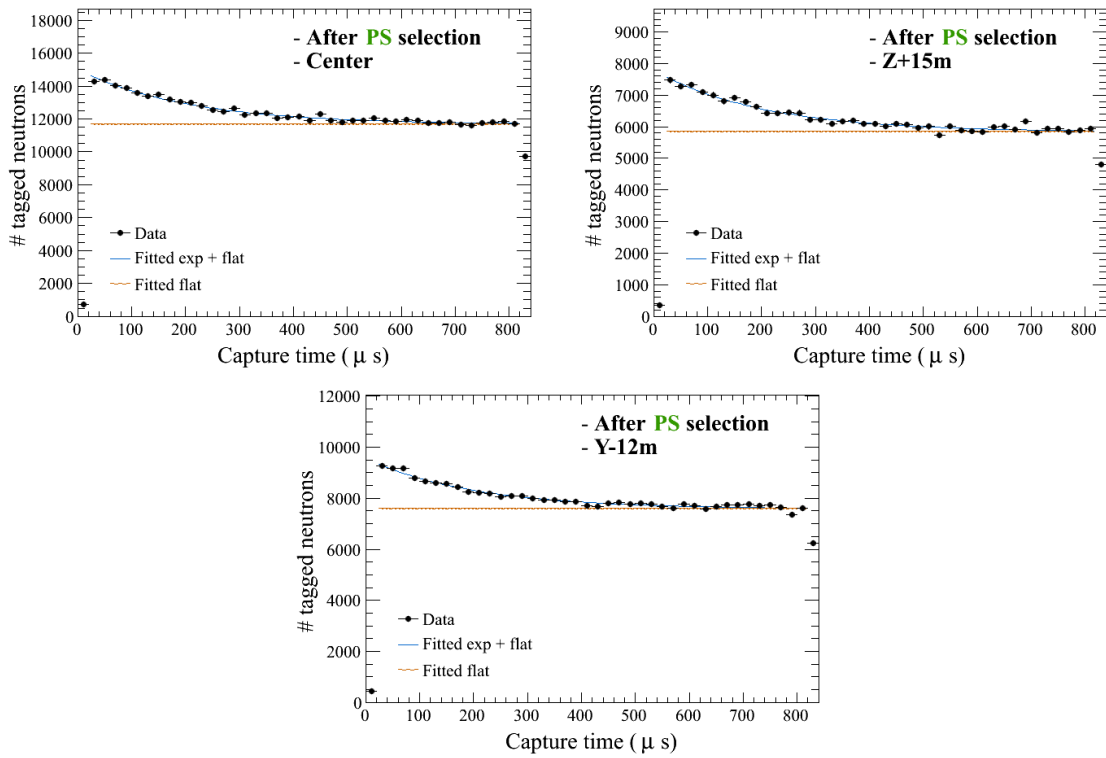
Figure 8.33: Distribution of capture time after the primary selection for the three data taking positions. The top left, top right, bottom correspond to the center, the Z+15 m, and the Y-12 m data taking positions, respectively.
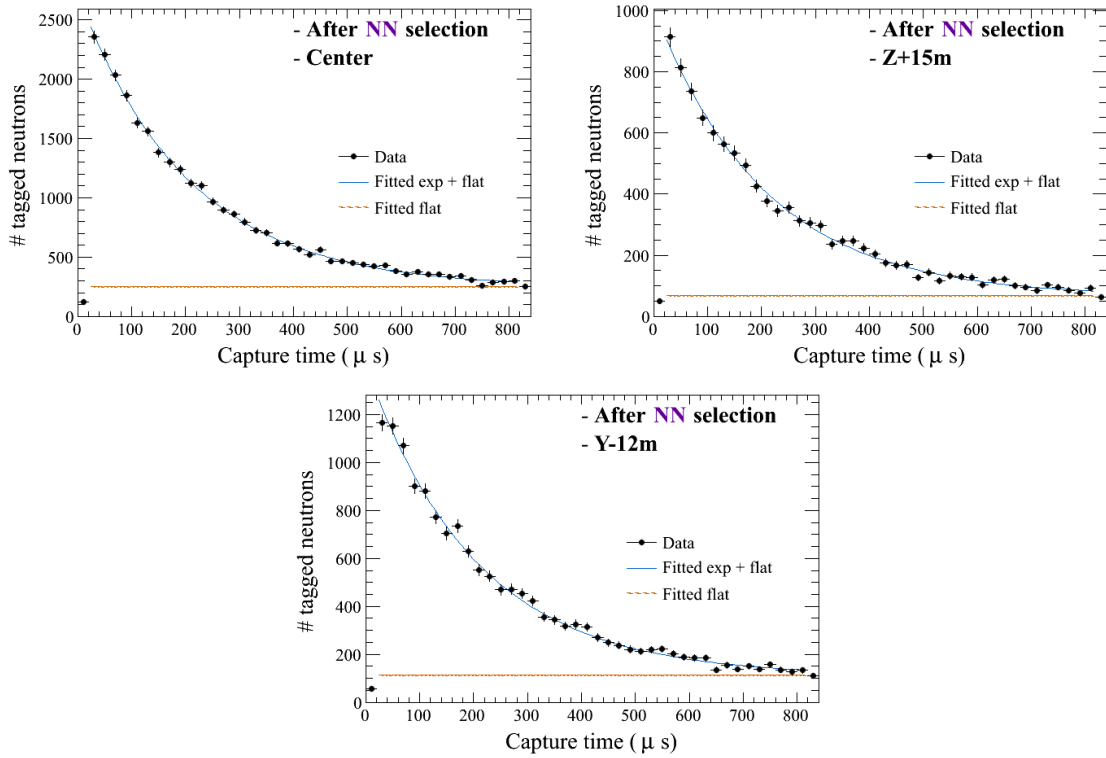
Figure 8.34: Distribution of capture time after the neural network classification for the three data taking positions. The top left, top right, bottom correspond to the center, the Z+15 m, and the Y-12 m data taking positions, respectively.

Once the fit is performed, in practice the relative efficiency can be obtained by dividing fitted ε of the NN classification by the primary selection's one. Table 8.10 summarizes the relative efficiencies obtained by the fit for the data and MC. Using the numbers summarized in the table, the ratio of the relative efficiency between the data and MC is computed and is treated as the systematics regarding the NN classification. Figure 8.35 shows the calculated ratio.

Table 8.10: Relative efficiency of the Am/Be calibration. ε_{PS} and ε_{NN} is the fitted neutron tagging efficiencies of the primary selection and NN classification, respectively.

	Relative efficiency $\varepsilon_{NN}/\varepsilon_{PS}$		
	Center	Z+15m	Y-12m
Data	0.742	0.483	0.658
MC	0.719	0.516	0.646

204
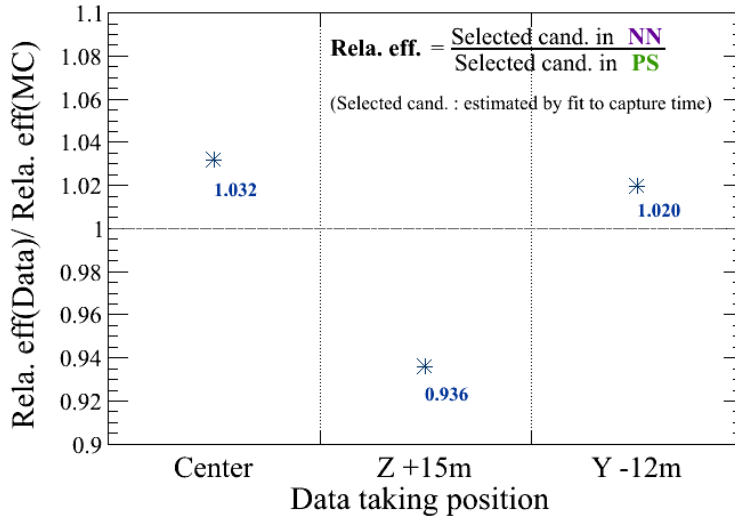
Figure 8.35: Ratio of the fitted relative efficiency between the data and MC.

In order to evaluate the impact of the uncertainty of the NN classification on the neutron tagging efficiency, the uncertainty needs to be propagated properly to the efficiency. As was mentioned in Section 7.2, the neutron tagging efficiency depends on $Dwall$ of the ν vertex (i.e position of the ID), which is shown in Figure 7.3. Since the calibration data was taken at three different positions in the inner detector, a $Dwall$ dependent NN classification error can be adopted by dividing up the ID volume based on the three data taking positions. The inner detector volume is divided into three regions based on the $Dwall$ of the data taking position in such a way that the volume between the neighbor two data taking positions is equally divided. Figure 8.36 shows the $Dwall$ of the three data taking positions and the divided volume with the assigned systematics regarding the NN classification.

The $Dwall$ dependent uncertainty is propagated by reweighting the nominal MC on an event-by-event basis as follows:

$$m_i^{true} \rightarrow m_i^{true} \times (1 + \delta\varepsilon_{NN}(Dwall)), \tag{8.3.8}$$

where m_i^{true} is number of tagged true neutrons of i-th ν event, $\delta\varepsilon_{NN}(Dwall)$ is the $Dwall$ dependent systematics regarding the NN classification. Full correlation among the three regions is assumed for a conservative estimate of the systematics on the tagging efficiency when propagating the source errors. The resulting fractional variation in the averaged neutron tagging efficiency is estimated to be 3.51%.
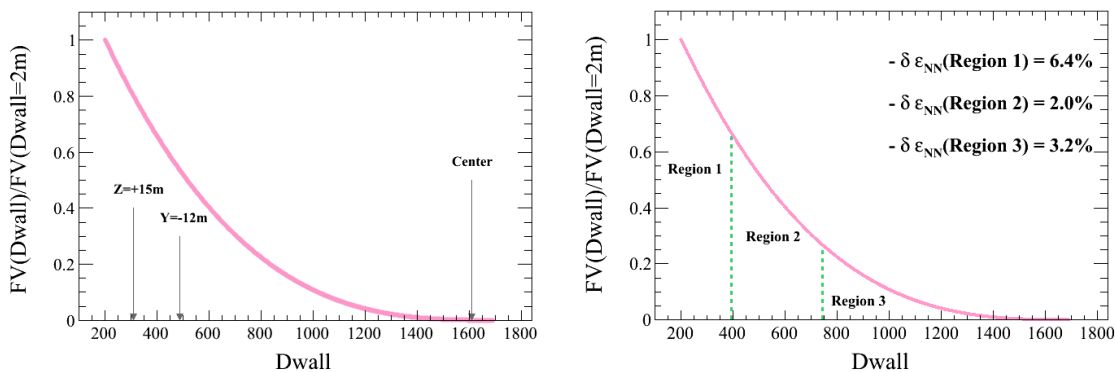
Figure 8.36: *Dwall* of the data taking positions (left) and the assignment of the *Dwall* dependent error on the relative efficiency (right). In the right side plot, $\delta\varepsilon_{NN}$ is the fractional error of the relative efficiency between the data and MC.

Total systematic uncertainty

In the previous parts, the systematic uncertainty on the tagging efficiency due to the primary selection and NN classification was estimated to be 2.8% and 3.5%, respectively. The total systematics regarding the detector response for $2.2\,\mathrm{MeV}$ γ rays is obtained by adding those two uncertainties in quadrature and is estimated to be 4.4%.

8.3.13   Total systematic uncertainties

The total systematic uncertainty on the neutron tagging efficiency is evaluated by adding each fraction variation described in the previous sections in quadrature. The estimated fractional uncertainty on the averaged efficiency is +6.74/-7.70% and +7.22/-8.09% for the FHC ad RHC $1R\nu_\mu$ samples, respectively.

The RHC $1R\nu_\mu$ sample is a $\bar{\nu}$ CCQE interaction enriched sample and thus there are more neutrons produced in the ν interactions and hadron FSI. These neutrons tend to have higher energy than neutrons produced by hadron secondary interactions and are more affected by the variation of the nucleon SI described in Section 8.3.6. The relatively larger uncertainty of the RHC sample compared to the FHC's one therefore comes from this difference.

The fractional uncertainty on the averaged efficiency for each individual error component is summarized in Table 8.11 and is visualized in Figure 8.37. The neutron tagging efficiency with the estimated total systematic uncertainty is also compared with the efficiencies evaluated by using the GENIE- and NuWro-based MCs. Figure 8.38 and 8.39 show the tagging efficiency as a function of P_t and the tagging efficiency averaged over P_t, respectively. As shown in the figures, the estimated total systematics covers the difference in the tagging efficiencies between the three MCs.

Table 8.11: Summary of fractional uncertainty of the average neuron tagging efficiency for each individual systematic source. All the estimations of thses numbers are detailed in Sections 8.3.2- 8.3.12.

Source neame	Fractional uncertainty (%)	
	FHC	RHC
ν cross section	±0.16	±0.23
ν beam flux	±0.37	±0.30
π FSI/SI	±0.25	±0.10
Nucleon FSI	±1.20	±0.94
Nucleon SI(GCALOR)	+4.00 -5.82	+4.96 -6.61
μ^-/π^- captures on ^{16}O	±1.89	±0.71
Oscillation probability	±0.17	±0.14
MC statistics	+0.03 -0.03	+0.05 -0.05
Detector response for ν events	±0.38	±0.23
Detector response for 2.2 MeV γ	+4.47 -4.47	+4.47 -4.47
ν event vertex	±0.27	±0.23
PMT gain simulation	+1.98 -0.00	+2.41 -0.00
Total	+6.74 -7.70	+7.22 -8.09
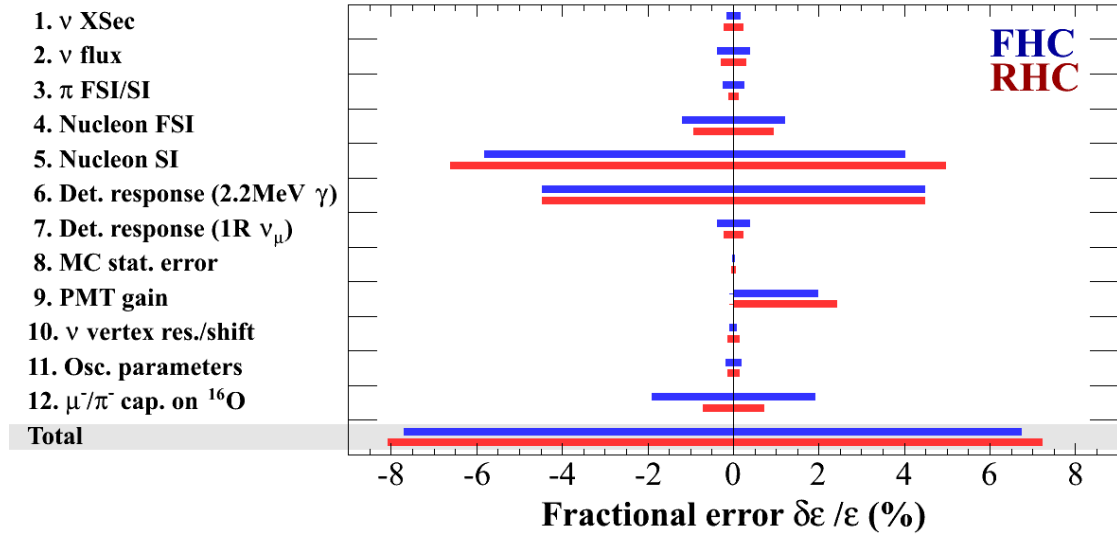
Figure 8.37: Fractional variation in the average tagging efficiency for each individual systematic source. The total variations are calculated by adding each uncertainty in quadrature. The blue and red lines correspond to the uncertainties of the FHC and RHC $1R\nu_\mu$ samples, respectively.
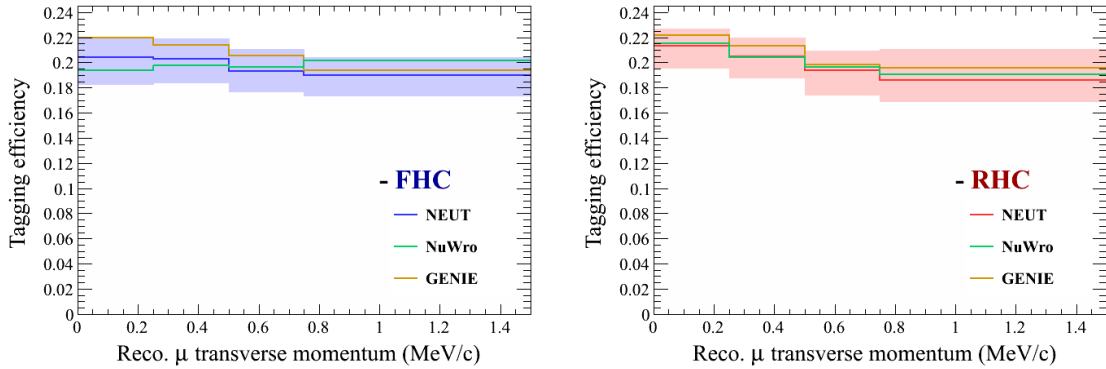
Figure 8.38: Tagging efficiency as a function of reconstructed muon transverse momentum in comparison with equivalent efficiency estimated by GENIE and NuWro MCs. The bands shows the $\pm 1\sigma$ envelope of the total systematic uncertainty. The left and right figures show the FHC and RHC $1R\nu_\mu$ samples, respectively.

208
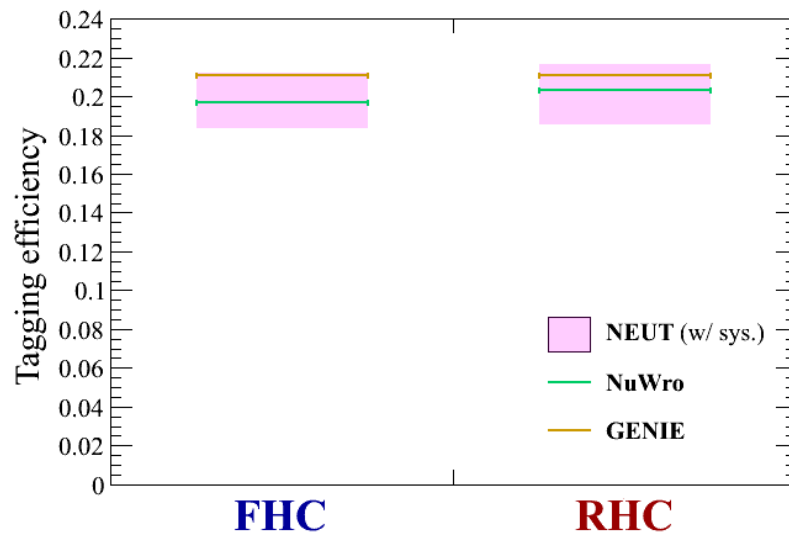
Figure 8.39: Averaged neutron tagging efficiency of the FHC and RHC $1R\nu_\mu$ samples in comparison with equivalent efficiency estimated by GENIE and NuWro MCs.

8.4 Results

This section describes the measurement results. Two types of the mean neutron multiplicities are measured:

- Mean neutron multiplicity as a function of reconstructed muon transverse momentum P_t

- Mean neutron multiplicity averaged over P_t

These mean neutron multiplicities, $\bar{M}_i$, are measured following Equation 8.2.1. The statistical errors are evaluated from the square root of the number of observed tagged neutrons (i.e. $\sqrt{N_{tag}}$) and the systematic uncertainties come from the systematics regarding the neutron tagging efficiency described in Section 8.3. The total uncertainty of the measured mean multiplicity is calculated by adding the statistical and systematic errors in quadrature.

Table 8.12 summarizes the definition of binning of P_t and numbers used for the measurements.

Table 8.12: Summary of the numbers used to calculate the measured mean neutron multiplicities. The numbers for All P_t are used to compute the mean neutron multiplicity averaged over P_t. Note that N_{tag} and $N_{1\mu}$ are the results of the Run 1-9 observation. The background event rate b is the same value as summarized in Table 6.2

Beam mode	$P_t$bin	N_{tag}	$N_{1\mu}$	ε	$b \times N_{1\mu}$	$\bar{M}$	$\delta\bar{M}_{stat.}(\%)$	$\delta\bar{M}_{syst.}(\%)$	$\delta\bar{M}_{tot.}(\%)$
FHC	$0.00 < P_t < 0.25$	8	55	0.204	1.056	0.618	± 40.733	$+7.050 \atop -10.457$	$+41.339 \atop -42.054$
	$0.25 < P_t < 0.50$	20	94	0.203	1.805	0.954	± 24.579	$+8.042 \atop -9.277$	$+25.861 \atop -26.272$
	$0.50 < P_t < 0.75$	10	41	0.193	0.787	1.164	± 34.325	$+9.253 \atop -8.296$	$+35.551 \atop -35.314$
	$P_t \geq 0.75$	6	11	0.190	0.211	2.768	± 42.315	$+7.278 \atop -8.505$	$+42.936 \atop -43.161$
	All P_t	44	201	0.199	3.860	1.004	± 16.525	$+6.737 \atop -7.703$	$+17.846 \atop -18.232$
RHC	$0.00 < P_t < 0.25$	7	38	0.213	0.705	0.777	± 42.028	$+6.496 \atop -8.057$	$+42.527 \atop -42.793$
	$0.25 < P_t < 0.50$	15	46	0.205	0.853	1.500	± 27.377	$+7.284 \atop -8.394$	$+28.329 \atop -28.635$
	$0.50 < P_t < 0.75$	8	22	0.194	0.408	1.783	± 37.255	$+8.199 \atop -9.818$	$+38.147 \atop -38.527$
	$P_t \geq 0.75$	3	4	0.186	0.074	3.926	± 59.199	$+13.103 \atop -9.216$	$+60.632 \atop -59.912$
	All P_t	33	110	0.202	2.040	1.396	± 18.555	$+7.219 \atop -8.088$	$+19.910 \atop -20.241$

Figure 8.40 and 8.41 shows the measurement results of the mean neutron multiplicity as a function of the reconstructed μ transverse momentum P_t and the mean neutron multiplicity averaged over P_t for the Run 1-9 FHC and RHC 1Rν_μ samples.

Table 8.13 summarizes the measured mean neutron multiplicities in comparison to the equivalent expectations which are derived from the NEUT-based MC. As shown in Figure 8.41, the measured mean multiplicity averaged over P_t shows a tendency that the RHC sample has higher mean multiplicity than that of the FHC sample. Since in general CC $\bar{\nu}_\mu$ interactions produce more neutrons compared to CC ν_μ interactions (e.g. CCQE interaction) in the neutrino energies of this analysis, the observed tendency is consistent with the expectation.

The deviation from the NEUT expectation is -2.75 σ (-2.69 σ) for the FHC (RHC) 1Rν_μ sample based on the total error of this measurement.
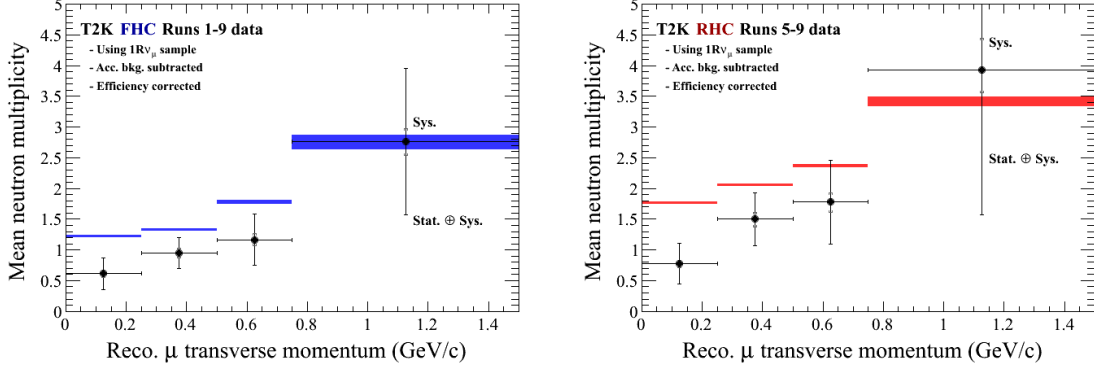
Figure 8.40: Measured mean neutron multiplicity as a function of reconstructed muon transverse momentum for the Run 1-9 FHC and RHC 1Rν_μ samples. The left and right figures correspond to the FHC and RHC samples, respectively. The color bands represent the equivalent expectations which are obtained the NEUT-based MC. The widths of the bands correspond to the size of the MC statistical error of the expectations.

Table 8.13: Summary of the measured mean neutron multiplicities of the Run 1-9 data in comparison to the expected numbers. For the expected numbers which are derived from the NEUT-based MC, the errors are the MC statistical uncertainties. For the data results, the first errors and second errors represent the statistical and systematic uncertainties, respectively.

P_t bin	FHC		RHC	
	Expected	Measured	Expected	Measured
0.0 - 0.25 (GeV/c)	1.22 ± 0.02	$0.62 \pm 0.25\ ^{+0.04}_{-0.06}$	1.76 ± 0.02	$0.78 \pm 0.33\ ^{+0.05}_{-0.06}$
0.25 - 0.5 (GeV/c)	1.33 ± 0.02	$0.95 \pm 0.23\ ^{+0.08}_{-0.09}$	2.05 ± 0.02	$1.50 \pm 0.41\ ^{+0.11}_{-0.13}$
0.5 - 0.75 (GeV/c)	1.77 ± 0.04	$1.16 \pm 0.40\ ^{+0.11}_{-0.10}$	2.36 ± 0.03	$1.78 \pm 0.66\ ^{+0.15}_{-0.18}$
> 0.75 (GeV/c)	2.75 ± 0.12	$2.77 \pm 1.17\ ^{+0.20}_{-0.24}$	3.41 ± 0.08	$3.93 \pm 2.32\ ^{+0.51}_{-0.36}$
Averaged over P_t	1.50 ± 0.02	$1.00 \pm 0.17\ ^{+0.07}_{-0.08}$	2.14 ± 0.02	$1.40 \pm 0.26\ ^{+0.10}_{-0.11}$

The measurement results are also compared with the expectations of the GENIE- and NuWro-based MCs as well as the NEUT's one as shown in Figures 8.42 and
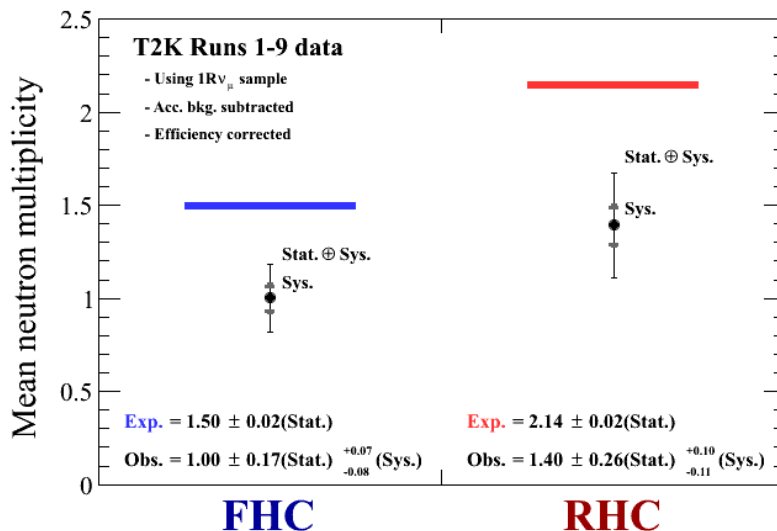
Figure 8.41: Measured mean neutron multiplicity averaged over reconstructed muon transverse momentum for the Run 1-9 FHC and RHC $1R\nu_\mu$ samples. All the observed tagged neutrons and ν events in the $1R\nu_\mu$ samples are integrated over P_t before calculating this multiplicity. The color bands represent the equivalent expectations which are obtained the NEUT-based MC. The widths of the bands correspond to the size of the MC statistical error of the expectations.

8.43. Although the statistical errors of the measurement results are large, it can be understood from the figure that in the region below $P_t < 0.75\,\text{GeV/c}$ the measured mean multiplicities are smaller compared to the expectation. It should be noted that this tendency observed is common to both of the FHC and RHC $1R\nu_\mu$ samples and between the three different MCs. As small P_t corresponds to small four momentum transfer squared Q^2 at the primary ν interaction, the results may indicate that the simulation used for making the expectations overpredict neutrons in the small Q^2 region.
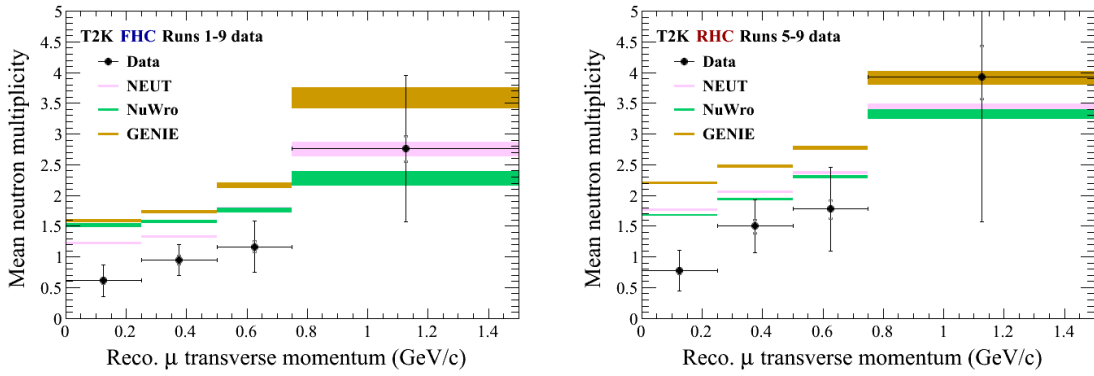
Figure 8.42: Mean neutron multiplicity as a function of reconstructed muon transverse momentum in comparison to the equivalent expectations of the NEUT-, NuWro-, and GENIE-based MCs. The left and right figures show the FHC and RHC 1Rν_μ samples, respectively.
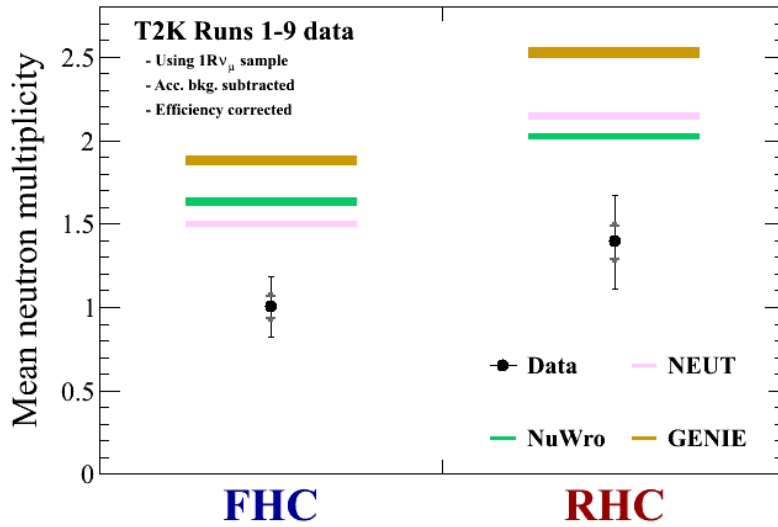
Figure 8.43: Mean neutron multiplicity averaged over P_t for the Run 1-9 data with the three different expectations. All the observed tagged neutrons and ν events in the 1Rν_μ sample are integrated over P_t before calculating the multiplicity.

8.5 Discussion

In the previous section, the measurement result of this analysis showed a relatively large discrepancy between data and simulations although the statistical error of the data is still large. In the following, possible causes of the discrepancy are discussed.

This analysis measure neutrons produced in the three processes: the primary ν-nucleon interaction in nuclear medium, hadronic FSI inside oxygen nucleus, and hadronic SI in the detector medium. Since this analysis can not address a particular neutron production process of interest because of the detection method, it is therefore hard to reveal the origin of the observed discrepancy by this measurement only. However, it is worth noting following points:

- About half of the neutrons are produced in hadronic SI as shown in Figure 8.1, which indicates that systematic uncertainty regarding the SI may affect the MC expectations in a visible way.

- As shown in Figure 8.2, the number of post-FSI charged pions, which have left the target nucleus and have not undergone SI in water, is much smaller than that of post-FSI nucleons. Thus the contribution to the neutron production in SI from the post-FSI charged pins are expected to be also small. By using the energy distributions of the post-FSI hadrons (shown in Figure 8.2) and average of number of neutron captures produced in hadron SI as a function of initial hadron energy (shown in Figure 8.7), the number of neutrons produced in SI for each post-FSI hadron and its energy are obtained and are shown in Figure 8.44. As shown in the figure, in both the FHC and RHC samples the contributions from the post-FSI nucleons are much larger than those of the post-FSI charged pions. Therefore, the post-FSI nucleons dominantly contribute to the neutron production in the hadronic SI.
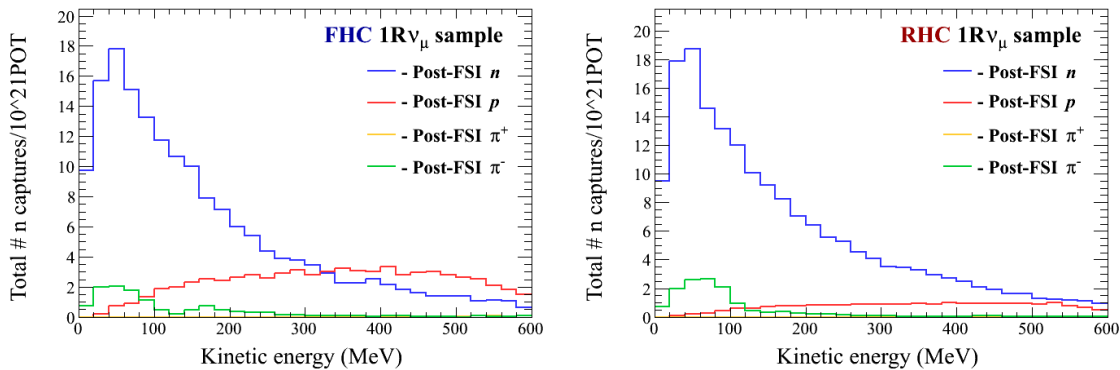
Figure 8.44: Number of neutron captures produced by post-FSI neutrons (blue), protons (red), π^+ (yellow), and π^- (green) of the $1R\nu_\mu$ sample. The left and right corresponds to the FHC and RHC smaples, respectively.

- The neutron production by the nucleon SI is handled by the GCALOR which is based on Bertini's style cascade model. The cross-section of the Bertini's free N-N scattering on ^{16}O may have large uncertainty, and such large uncertainty vary the total number of neutrons, the number of tagged neutrons, and the resultant distance from ν interaction to n capture vertices. Indeed, the ± 30 % uncertainty on the cross-section assigned in Subsection 8.3.6 varies the total number of neutrons by ~ 10 %. Also, it should be noted that there has already been visible difference in the neutron productions by the SI as was shown in Figure 8.4.

- In addition, modeling of ν interactions and hadronic FSI is largely different between the three ν event generators used in this analysis: NEUT, NuWro, and GENIE. This also results in different true distance distribution as well as different total number of neutrons.

If these variations are put together into one prediction, then the nominal MC expectations based on NEUT have a large prediction uncertainty. For instance, Figure 8.45 shows the distribution of the observed reconstructed distance from ν interaction to n capture vertices in comparison with the corresponding MC distribution. In the figure, the green envelopes correspond to the nominal MC expectations with the ± 30 % variations in the Bertini's total free N-N cross sections. A visible variation can be seen in the first two bins in which the data shows a relatively large discrepancy. The differences among NEUT, NuWro, and GENIE are also included into the orange envelopes by combining the variations due to the ± 30 % nucleon cross section error in quadrature. Although the orange envelopes, which reflect the uncertainties on the ν interactions, the hadronic FSI and the nucleon SI, are relatively large, the envelops seem not to cover the data in the first bin. Since short distance corresponds to nucleons in a low energy region as shown in Figure 8.7, the data could indicate that the MC simulations used in this analysis overpredict neutrons in a low energy region. It may be interesting to recall that as mentioned in Subsection 1.2.3, MINERvA's measurement of neutrons associated with antineutrino interactions on a hydrocarbon target has shown a ~ 25 % overprediction in a low apparent velocity region for neutron candidates.
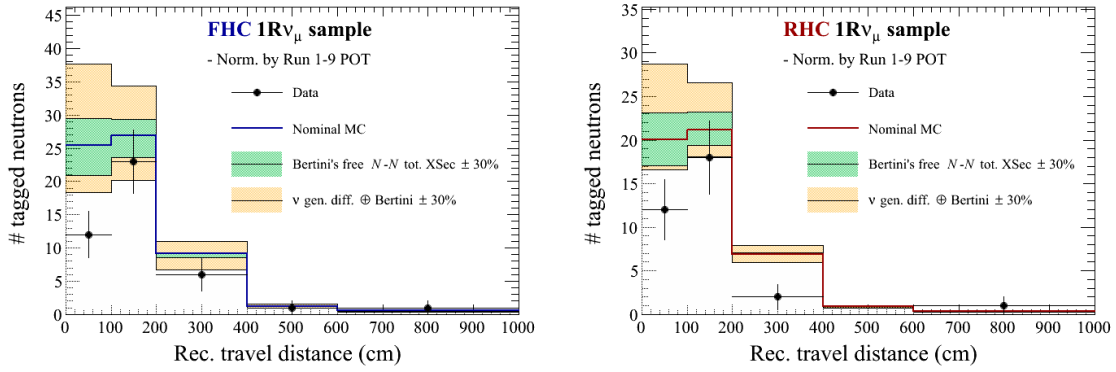
Figure 8.45: Distribution of reconstructed distance for the Run 1-9 FHC 1Rν_μ sample (left) and the Run 1-9 RHC 1Rν_μ sample (right). Solid lines correspond to the nominal MC expectations based on NEUT. Green envelops correspond to a ±30 % variations in the Bertini's total cross sections used for the nucleon SI in GCALOR. Orange envelopes represent the nominal MC expectation with the $\pm30\%$ variations in the total nucleon SI cross sections and the differences among NEUT, NuWro, and GENIE. All the MC distributions are normalized by the Run 1-9 POT. The data are shown with the statistical uncertainties only.

Chapter 9

Summary and outlook

Since the discovery of neutrino oscillation, remarkable efforts have been made in the last two decades to study the nature of neutrinos. However, the value of δ_{CP} and the neutrino mass ordering (the sign of Δm^2_{31}) are still unknown although these are especially important. The value of δ_{CP} would provide information to explain the origin of the matter-antimatter asymmetry in the universe. Also, determination of the neutrino mass hierarchy (MH) may helps to understand the patterns of mixing and masses between the particles of the Standard Model.

To understand the remaining unknowns of nature, building larger detectors with advanced detection technology and further improvements to analysis methods are needed. Indeed, possibility of such improvement on analysis has been studied in future experiments adopting water Cherenkov detectors such as SK-Gd [124] and the Hyper-Kamiokande [125] and the experiments plan to utilize neutrons associated with ν interactions in water for their main physics analyses. In order to utilize such neutrons, predicting the production of these neutrons precisely by a MC simulation is key. Current MC simulations, however, produce different predictions due to large uncertainties on ν-nucleon interactions in nuclear medium, hadronic FSI in nuclei, and hadronic SI in detector medium. In addition, no extensive study has been made for water. Therefore, it is quite worth studying those neutrons and evaluating the validity of the simulations by using well understood neutrino source.

In the T2K experiment, primarily ν_μ and $\bar{\nu}_\mu$ beams with a peak energy of 0.6 GeV are produced, which enables us to study such neutrons with a well understood ν source. In this thesis, neutrons associated with ν interactions on a water target using accelerator neutrinos and antineutrinos were studied for the first time. For this study, a neutron tagging algorithm which does not depend explicitly on the modeling of neutron production was developed, and was applied to the T2K beam neutrino data accumulated at the SK far detector until 2018, which corresponds to 1.4938×10^{21} POT for the FHC mode and 1.6346×10^{21} POT for the RHC mode.

After applying the $1R\nu_\mu$ selection to the T2K FC neutrino events, the observed neutrino events agreed well with the corresponding expectations. On the one hand, for the tagged neutrons, the observation showed less tagged neutrons than expected. Table 9.1 summarizes the number of observed neutrino events and the number of

tagged neutrons with the corresponding expectations. Since the neutron production

Table 9.1: Summary of the number of neutrino events and tagged neutrons for the Runs 1-9 POT with the following oscillation parameter values: Δm_{21}^2=7.53 $\times 10^{-5}$ eV^2, Δm_{32}^2=2.452 $\times 10^{-3}$ eV^2, $\sin^2 \theta_{23}$=0.532, $\sin^2 \theta_{13}$=0.0212, δ_{CP}=-1.885, Mass Hierarchy = normal. All the expectations are normalized to the Run 1-9 POT.

	Number of ν events		Number of tagged n	
	Expected	Observed	Expected	observed
FHC 1Rν_μ	202.12	201	64.08	44
RHC 1Rν_μ	109.61	110	49.42	33

depends on the four momentum transfer squared Q^2 to the hadronic system at the primary ν-nucleus interaction, the mean neutron multiplicity as a function of reconstructed transverse muon momentum P_t, which is a good indicator of Q^2, was measured by using ν events and tagged neutrons with a systematic uncertainty of $\sim$8 %. It should be noted that the transverse momentum can be reconstructed only for beam neutrinos, because their incoming directions are known. The measured mean neutron multiplicity averaged over P_t is:

Runs $1-9$ FHC 1Rν_μ sample : 1.00 ± 0.17 (stat.)$^{+0.07}_{-0.08}$ (syst.) neutrons/ν event

Runs $5-9$ RHC 1Rν_μ sample : 1.40 ± 0.26 (stat.)$^{+0.10}_{-0.11}$ (syst.) neutrons/ν event,

whereas the corresponding expectations of the NEUT-based MC are:

FHC 1Rν_μ sample : 1.50 ± 0.02 (stat.) neutrons/ν event

RHC 1Rν_μ sample : 2.14 ± 0.02 (stat.) neutrons/ν event.

The deviation from the expectation is $2.75\,\sigma$ $(2.69\,\sigma)$ for the FHC (RHC) sample based on the total error of the measured value.

Since this analysis showed a discrepancy of $\sim$40% between the observation and the prediction, it may be helpful to evaluate how much this 40% discrepancy in neutron production affects a particular physics analysis. As an improved analysis method, which utilizes those neutrons aggressively, has been developed [7], such impact is estimated by comparing sensitivity to δ_{CP} between the conventional and improved analysis methods, in context of Hyper-Kamiokande atmospheric ν oscillation analysis. The conventional analysis method is detailed in [85, 223, 224].

Hyper-Kamiokande is a next generation underground experiment employing water Cherenkov detector and will be build on the successful operation of Super-Kamiokande. Although an option of two-tanks is being considered, a 258 kton tank with 40% photocoverage is adopted as the baseline design [125]. In this design, for high-energy neutrinos such as atmospheric neutrinos, the detector performance of Hyper-Kamiokande is expected to be roughly the same as Super-Kamiokande's one [125], which means that the number of expected atmospheric neutrino events at Hyper-Kamiokande can be obtained by scaling the equivalent numbers at Super-Kamiokande by exposure. On the other hand, thanks to the higher detection efficiency of single-photoelectron signal of a photosensor newly developed for Hyper-Kamiokande, neutron tagging efficiency has been evaluated to be $\sim70\%$ even for neutron capture by hydrogen nucleus [125]. In addition, an option of gadolinium loading is also being considered, in which case neutron tagging efficiency is expected to be higher than 70%. Therefore, the following impact study is done by scaling the equivalent sensitivity of Super-Kamiokande by exposure, and assuming a 70% neutron tagging efficiency as was adopted in the previous work [7].

To obtain the equivalent sensitivity, the pre-existing analysis framework developed by the Super-Kamiokande collaboration [85] is used. In this analysis framework, the sensitivity is evaluated by a χ^2 defined as:

$$\chi^2 = 2\sum_n \left(\mathcal{E}_n(1 + \sum_i f_n^i \epsilon_i) - \mathcal{O}_n + \mathcal{O}_n \ln \frac{\mathcal{O}_n}{\mathcal{E}_n(1 + \sum_i f_n^i \epsilon_i)} \right) + \sum_i \left(\frac{\epsilon_i}{\sigma_i} \right)^2,$$

$$(9.0.1)$$

where $\mathcal{E}_n$ and $\mathcal{O}_n$ are the number of expected and observed neutrino events of n-th bin and f_n^i represents the systematic variation in $\mathcal{E}_n$ due to a systematic uncertainty corresponding to ϵ_i. This treatment of systematic errors is based on the pull method [225]. In order to find the best oscillation parameter, the above χ^2 is minimized over the systematic error parameters at each value of δ_{CP}, which is equivalent to solve $\frac{\partial \chi^2}{\partial \epsilon_i} = 0$ for every ϵ_i.

In order to estimate the impact of the observed 40% discrepancy in neutron production, the sensitivity defined in the above equation is computed three times at each oscillation parameter point for the improved analysis method [7], which enables improved estimation of neutrino energy and better sample selection in terms of separations of ν-$\bar{\nu}$ and CC-NC interactions. The first computation is done for the nominal atmospheric MC set, which is used for developing the improved method, without any consideration of systematic uncertainty on neutron production. In the remaining calculations, neutron production error is taken into account by treating the 40% difference as an inclusive error on neutron production. Two fake data sets are therefore generated varying the neutron multiplicity of the nominal MC set by $\pm40\%$ on an event-by-event basis, and sensitivity is calculated for each fake data set. The resultant difference in the sensitivity between the first calculation and the other calculations is interpreted as the systematic variations in the sensitivity due to neutron production uncertainty. Figure 9.1 shows the resultant variations in com-

parison to the sensitivity of the conventional analysis method, which does not use information about tagged neutrons, and demonstrates that the 40% discrepancy can yield non-negligible systematic variations in a particular pysics analysis. It should be noted that this is the first estimation of impact of neutron production uncertainty based on experimental data.
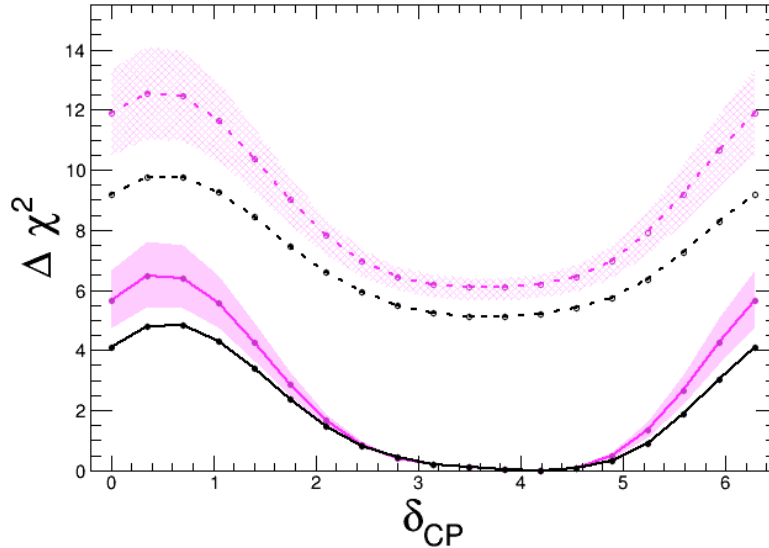
Figure 9.1: Impact of the observed 40% discrepancy in neutron production to the sensitivity to δ_{CP} using the atmospheric neutrinos at Hyper-Kamiokande. The exposure time is assumed to be five years of one tank of 258 kton with a 40% photocoverage. Black lines correspond to the conventional analysis method developed by the SK collaboration based on reconstructed lepton energy. Magenta lines correspond to the improved analysis method in which case an energy correction and a better event selection using tagged neutrons are applied with an assumption of a 70% neutron tagging efficiency. White magenta bands represent the systematic variations in the magenta line due to an overall $\pm 40\%$ error on neutron production. Solid (Dashed) lines correspond to the case where the χ^2 is computed assuming normal (inverted) mass hierarchy. The lower (upper) side corresponds to the overall -40% (+40%) variation in neutron multiplicity. The setting of oscillation parameter values are as follows: $\Delta m_{21}^2 = 7.65 \times 10^{-5}\,\mathrm{eV}^2$, $\Delta m_{32}^2 = 2.5 \times 10^{-3}\,\mathrm{eV}^2$, $\sin^2\theta_{23} = 0.575$, $\sin^2\theta_{12} = 0.309$, $\sin^2\theta_{13} = 0.0219$, $\delta_{CP} = 4.189$ rad, Mass Hierarchy = normal.

As shown in Figure 9.1, a considerable reduction of prediction uncertainty on neutron production needs to be done. To this aim, understanding of the observed discrepancy may be the first step by similar measurement with higher data statistics since the measurement presented in this thesis is statistically limited. Such measurement can be realized in near future by SK-Gd. In the SK-Gd experiment, the same measurement can be performed with improved reconstruction of the neutron capture vertex and with much higher neutron tagging efficiency. Figure 9.2 shows an expected vertex resolution in SK-Gd. As shown in the figure, the vertex resolution of

neutron capture is expected to be almost twice better than that of the current one, which allows us to address more detailed information about the neutron kinematics. In addition, the tagging efficiency of SK-Gd is expected to be higher than 70%. Since T2K has planed to extend its data taking until 2026 [226] and the initial Gd loading to SK will happen in 2020, SK-Gd will be able to conduct the same neutron measurement with significantly improved precision.
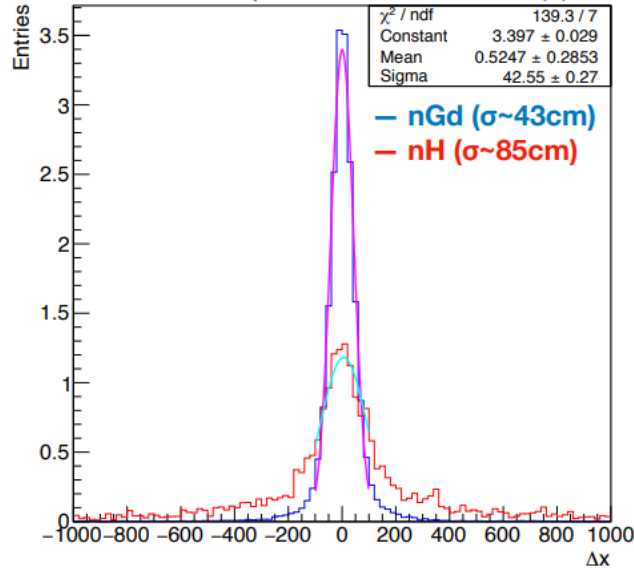
Figure 9.2: Comparison of vertex resolution of n captures between SK and SK-Gd. In SK, only neutron capture by hydrogen nucleus can happen, whereas ~80% of neutrons will be captured by gadolinium in the full configuration of SK-Gd.

ANNIE (Accelerator Neutrino Neutron Interaction Experiment) [227, 138] is an ongoing experiment at Fermilab, in which a Gd-doped water Cherenkov detector is used to measure neutrons related to neutrino interactions from the Booster Neutrino Beam with a peak energy of 0.7 GeV. Future results from ANNIE will be very useful to validate the measurement result of this analysis. As a long-term project, E61 [125, 228] which is an intermediate water Cherenkov detector used for the long-baseline neutrino oscillation program of the HK is also planed to perform similar measurement. The experiment will enable us to study the neutron production by a Gaussian neutrino flux, which has never been realized. Such Gaussian neutrino beam will significantly reduce systematic uncertainties related to primary ν-nucleus interactions, and thus a more accurate measurement would be realized.

Although these experiments will produce crucial inputs to build a precise MC simulation for the utilization of neutrons to various important physics analyses, these experiments cannot disentangle the complicated neutron production processes: the primary ν-nucleon interactions in nucleus, hadronic FSI inside the nucleus, and hadronic SI in water. To understand the neutron production and build MC simulation, disentanglement of these processes is quite important and at least the contribution from SI has to be isolated. One way to achieve this is to measure neutron

productions by hadronic SI in water using hadron beams. Such such idea has been proposed, and possible measurement is being included into the plan of a test water Cherenkov experiment at CERN [229].

By combining efforts from all of these future experiments, we would be able to utilize neutrons associated with ν interactions in water for various important physics analyses including precision measurements of neutrino oscillations and SRN searches. It is my humble wish that this measurement will be useful to accelerate experimental studies and development of simulations for these neutrons.

Bibliography

[1] K. Abe et al. Constraint on the matter-antimatter symmetry-violating phase in neutrino oscillations. *arXiv (submitted for publication)*, 2019.

[2] Sheldon Stone. New physics from flavour. *PoS*, ICHEP2012:033, 2013.

[3] A.Himmel. First Oscillation Results with Neutrino and Antineutrino Beams in NOvA. *Fermilab JETP (Wine & Cheese) Seminar*, June 2019.

[4] G L Fogli, E Lisi, A Mirizzi, and D Montanino. Probing supernova shock waves and neutrino flavour transitions in next-generation water cherenkov detectors. *Journal of Cosmology and Astroparticle Physics*, 2005(04):002–002, apr 2005.

[5] Ken'ichiro Nakazato et al. SPECTRUM OF THE SUPERNOVA RELIC NEU-TRINO BACKGROUND AND METALLICITY EVOLUTION OF GALAX-IES. *The Astrophysical Journal*, 804(1):75, may 2015.

[6] M. Ikeda et al. Evaluation of gadolinium's action on water cherenkov detector systems with egads. *arXiv (submitted for publication)*, 2019.

[7] P.F.Menendez. Neutrino Physics in Present and Future Kamioka Water-Cerenkov Detectors with Neutron Tagging. *Ph.D thesis, University Autonomous of Madrid*, 2017.

[8] S.Ando. Cosmic star formation history and the future observation of supernova relic neutrinos. *The Astrophysical Journal*, 607(1):20–31, may 2004.

[9] S. Ando, K. Sato, and T. Totani. Detectability of the supernova relic neutrinos and neutrino oscillation. *Astroparticle Physics*, 18(4):307 – 318, 2003.

[10] K.Ueno. Study of neutral-current de-excitation gamma-rays with the T2K neutrino beam. *PhD thesis, University of Tokyo*, 2014.

[11] C. Andreopoulos et al. The genie neutrino monte carlo generator. *Nucl. Instrum. Meth. A*, 614(1):87 – 104, 2010.

[12] S. Agostinelli et al. Geant4 a simulation toolkit. *Nucl. Instrum. Meth. A*, 506(3):250 – 303, 2003.

[13] B. Aharmim et al. Measurement of neutron production in atmospheric neutrino interactions at the sudbury neutrino observatory. *Phys. Rev. D*, 99:112007, 2019.

[14] M. Elkins et al. Neutron measurements from antineutrino hydrocarbon reactions. *Phys. Rev. D*, 100:052002, 2019.

[15] K. Abe et al. Characterization of nuclear effects in muon-neutrino scattering on hydrocarbon with a measurement of final-state kinematics and correlations in charged-current pionless interactions at t2k. *Phys. Rev. D*, 98:032003, Aug 2018.

[16] K. Abe et al. The t2k experiment. *Nucl. Instrum. Meth. A*, 659, 2011.

[17] K. Abe et al. T2k neutrino flux prediction. *Phys. Rev. D*, 87:012001, Jan 2013.

[18] S. Fukuda et al. The super-kamiokande detector. *Nucl. Instrum. Meth. A*, 501(2):418 − 462, 2003.

[19] S. Yamada et al. *S. Yamada, et al., in: 16th IEEE-NPSS Real Time Conference Proceedings, 2009, p. 201.*

[20] K. Iyogi et al. T2K data acquisition and FC event selection at Super-Kamiokande. *T2K-TN-27 (internal note)*, 2011.

[21] K. Abe et al. Calibration of the super-kamiokande detector. *Nucl. Instrum. Meth. A*, 737, 2014.

[22] Y.Zhang. Experimental Studies of Supernova Relic Neutrinos at Super-Kamiokande-IV. *PhD thesis, Tsinghua University*, 2015.

[23] K. Abe and other. Solar neutrino measurements in super-kamiokande-iv. *Phys. Rev. D*, 94:052010, Sep 2016.

[24] L.Haegel. Measurement Of Neutrino Oscillation Parameters Using Neutrino And Antineutrino Data Of The T2K Experiment. *Ph.D thesis, University of Geneva*, 2017.

[25] T.Golan. Modeling nuclear effects in NuWro Monte Carlo neutrino event generator. *Ph.D thesis, University of Wroclaw*, 2014.

[26] Patrick de Perio. Neut pion fsi. *AIP Conference Proceedings*, 1405(1):223–228, 2011.

[27] C. Zeitnitz and T.A. Gabriel. *THE GEANT-CALOR INTERFACE USER'S GUIDE*, Oak Ridge National Laboratory, 2001.

[28] S.Tobayama. An Analysis of the Oscillation of Atmospheric Neutrinos. *PhD thesis, Uniertsity of British Columbia*, 2016.

[29] S. Berkman et al. fiTQun: A New Reconstruction Algorithm for Super-K. *T2K-TN-146 (internal note)*, 2013.

[30] K. Nakamura. Measurement of Neutrino Oscillation with a High Intensity Neutrino Beam. *Ph.D thesis, Kyoto University*, 2018.

[31] R. Akutsu et al. Super-Kamiokande data quality for T2K Run 9. *T2K-TN-355 (internal note)*, 2018.

[32] R.J.Edward. High Pressure Xenon Detectors for Rare Physics Searches. *Ph.D thesis, University of California, Berkeley*, 2014.

[33] T. Vladisavljevic et al. Flux Prediction and Uncertainty with NA61/SHINE 2009 Replica-Target Data. *T2K-TN-354 (internal note)*, 2017.

[34] M. Tanabashi et al. Review of particle physics. *Phys. Rev. D*, 98:030001, Aug 2018.

[35] K.A. Olive. Review of particle physics. *Chinese Physics C*, 40(10):100001, oct 2016.

[36] C. Andreopoulos et al. T2K Neutrino and Anti-Neutrino 3-Flavour Joint Analysis of Run 1-9 data sets. *T2K-TN-360 (internal note)*, 2019.

[37] D. Cokinos and E. Melkonian. Measurement of the 2200m/sec neutron-proton capture cross section. *Phys. Rev. C*, 15:1636, 1977.

[38] Andreopoulos et al. The GENIE Neutrino Monte Carlo Generator: Physics and User Manual. 2015.

[39] W. Pauli. Letter of the 4th december 1930. *Pauli Archive at CERN*.

[40] C. L. Cowan, F. Reines, F. B. Harrison, H. W. Kruse, and A. D. McGuire. Detection of the free neutrino: a confirmation. *Science*, 124(3212):103–104, 1956.

[41] Raymond Davis, Jr. and Don S. Harmer. Attempt to observe the $Cl^{37}(\bar{\nu}e^-)Ar^{37}$ reaction induced by reactor antineutrinos. *Bull. Am. Phys. Soc.*, 4:217, 1959.

[42] T. D. Lee and C. N. Yang. Parity nonconservation and a two-component theory of the neutrino. *Phys. Rev.*, 105:1671–1675, Mar 1957.

[43] C. S. Wu, E. Ambler, R. W. Hayward, D. D. Hoppes, and R. P. Hudson. Experimental test of parity conservation in beta decay. *Phys. Rev.*, 105:1413–1415, Feb 1957.

[44] Richard L. Garwin, Leon M. Lederman, and Marcel Weinrich. Observations of the failure of conservation of parity and charge conjugation in meson decays: the magnetic moment of the free muon. *Phys. Rev.*, 105:1415–1417, Feb 1957.

[45] M. Goldhaber, L. Grodzins, and A. W. Sunyar. Helicity of neutrinos. *Phys. Rev.*, 109:1015–1017, Feb 1958.

[46] R. P. Feynman and M. Gell-Mann. Theory of the fermi interaction. *Phys. Rev.*, 109:193–198, Jan 1958.

[47] E. C. G. Sudarshan and R. E. Marshak. Chirality invariance and the universal fermi interaction. *Phys. Rev.*, 109:1860–1862, Mar 1958.

[48] G. Danby, J-M. Gaillard, K. Goulianos, L. M. Lederman, N. Mistry, M. Schwartz, and J. Steinberger. Observation of high-energy neutrino reactions and the existence of two kinds of neutrinos. *Phys. Rev. Lett.*, 9:36–44, Jul 1962.

[49] Sheldon L. Glashow. Partial-symmetries of weak interactions. *Nuclear Physics*, 22(4):579 – 588, 1961.

[50] A. Salam. Weak and Electromagnetic Interactions. *Conf. Proc.*, C680519:367–377, 1968.

[51] S. Weinberg. A model of leptons. *Phys. Rev. Lett.*, 19:1264–1266, Nov 1967.

[52] O. W. Greenberg. Spin and unitary-spin independence in a paraquark model of baryons and mesons. *Phys. Rev. Lett.*, 13:598–602, Nov 1964.

[53] M. Y. Han and Y. Nambu. Three-triplet model with double SU(3) symmetry. *Phys. Rev.*, 139:B1006–B1010, Aug 1965.

[54] M. L. Perl et al. Evidence for anomalous lepton production in $e^+ - e^-$ annihilation. *Phys. Rev. Lett.*, 35:1489–1492, Dec 1975.

[55] G. S. Abrams et al. Initial measurements of z-boson resonance parameters in e^+e^- annihilation. *Phys. Rev. Lett.*, 63:724–727, Aug 1989.

[56] D. DeCamp et al. Determination of the number of light neutrino species. *Physics Letters B*, 231(4):519 – 529, 1989.

[57] P. Aarnio et al. Measurement of the mass and width of the z0-particle from multihadronic final states produced in e+e annihilations. *Physics Letters B*, 231(4):539 – 547, 1989.

[58] B. Adeva et al. A determination of the properties of the neutral intermediate vector boson z0. *Physics Letters B*, 231(4):509 – 518, 1989.

[59] K. Kodama et al.

[60] Raymond Davis, Don S. Harmer, and Kenneth C. Hoffman. Search for neutrinos from the sun. *Phys. Rev. Lett.*, 20:1205–1209, 1968.

[61] John N. Bahcall, Neta A. Bahcall, and Giora Shaviv. Present status of the theoretical predictions for the ^{37}Cl solar-neutrino experiment. *Phys. Rev. Lett.*, 20:1209–1212, 1968.

[62] K. S. Hirata et al. Observation of ^{8}B solar neutrinos in the kamiokande-ii detector. *Phys. Rev. Lett.*, 63:16–19, Jul 1989.

[63] A. I. Abazov et al. Search for neutrinos from the sun using the reaction ^{71}Ga$(\nu_e,e^-)^{71}$ge. *Phys. Rev. Lett.*, 67:3332–3335, 1991.

[64] W. Hampel et al. Gallex solar neutrino observations: results for gallex iv. *Physics Letters B*, 447(1):127 – 133, 1999.

[65] M. Altmann et al. Gno solar neutrino observations: results for gno i. *Physics Letters B*, 490(1):16 – 26, 2000.

[66] S. Fukuda et al. Determination of solar neutrino oscillation parameters using 1496 days of super-kamiokande-i data. *Physics Letters B*, 539(3):179 – 187, 2002.

[67] Q. R. Ahmad et al. Direct evidence for neutrino flavor transformation from neutral-current interactions in the sudbury neutrino observatory. *Phys. Rev. Lett.*, 89:011301, Jun 2002.

[68] K.S. Hirata and othres. Experimental study of the atmospheric neutrino flux. *Physics Letters B*, 205(2):416 – 420, 1988.

[69] Y. Fukuda et al. Atmospheric ν_μ/ν_e ratio in the multi-gev energy range. *Physics Letters B*, 335(2):237 – 245, 1994.

[70] R. Becker-Szendy et al. Electron- and muon-neutrino content of the atmospheric flux. *Phys. Rev. D*, 46:3720–3724, 1992.

[71] W.W.M. Allison et al. Measurement of the atmospheric neutrino flavour composition in soudan 2. *Physics Letters B*, 391(3):491 – 500, 1997.

[72] Y. Fukuda et al. Evidence for oscillation of atmospheric neutrinos. *Phys. Rev. Lett.*, 81:1562–1567, Aug 1998.

[73] M. H. Ahn et al. Measurement of neutrino oscillation by the k2k experiment. *Phys. Rev. D*, 74:072003, Oct 2006.

[74] N. Agafonova et al. Final results of the opera experiment on ν_τ appearance in the cngs neutrino beam. *Phys. Rev. Lett.*, 120:211801, May 2018.

[75] B. Pontecorvo. Mesonium and anti-mesonium. *Sov. Phys. JETP*, 6:429, 1957. [Zh. Eksp. Teor. Fiz.33,549(1957)].

[76] Ziro Maki, Masami Nakagawa, and Shoichi Sakata. Remarks on the Unified Model of Elementary Particles. *Progress of Theoretical Physics*, 28(5):870–880, 11 1962.

[77] K.A. Olive. Review of particle physics. *Chinese Physics C*, 38(9):090001, aug 2014.

[78] L. Wolfenstein. Neutrino oscillations in matter. *Phys. Rev. D*, 17:2369–2374, May 1978.

[79] S. P. Mikheyev and A. Yu. Smirnov. Resonance Amplification of Oscillations in Matter and Spectroscopy of Solar Neutrinos. *Sov. J. Nucl. Phys.*, 42:913–917, 1985. [,305(1986)].

[80] V. Barger, K. Whisnant, S. Pakvasa, and R. J. N. Phillips. Matter effects on three-neutrino oscillations. *Phys. Rev. D*, 22:2718–2726, Dec 1980.

[81] Bruce T. Cleveland et al. Measurement of the solar electron neutrino flux with the homestake chlorine detector. *The Astrophysical Journal*, 496(1):505–526, mar 1998.

[82] G. Bellini et al. Measurement of the solar ^{8}B neutrino rate with a liquid scintillator target and 3 mev energy threshold in the borexino detector. *Phys. Rev. D*, 82:033006, Aug 2010.

[83] J. Hosaka et al. Solar neutrino measurements in super-kamiokande-i. *Phys. Rev. D*, 73:112001, Jun 2006.

[84] T. Araki et al. Measurement of neutrino oscillation with kamland: Evidence of spectral distortion. *Phys. Rev. Lett.*, 94:081801, Mar 2005.

[85] K. Abe et al. Atmospheric neutrino oscillation analysis with external constraints in super-kamiokande i-iv. *Phys. Rev. D*, 97:072001, Apr 2018.

[86] M. G. Aartsen et al. Measurement of atmospheric neutrino oscillations at 6–56 gev with icecube deepcore. *Phys. Rev. Lett.*, 120:071801, Feb 2018.

[87] K. Abe et al. Measurement of neutrino oscillation parameters from muon neutrino disappearance with an off-axis beam. *Phys. Rev. Lett.*, 111:211803, Nov 2013.

[88] K. Abe et al. Precise measurement of the neutrino mixing parameter θ_{23} from muon neutrino disappearance in an off-axis beam. *Phys. Rev. Lett.*, 112:181801, May 2014.

[89] K. Abe et al. Measurements of neutrino oscillation in appearance and disappearance channels by the t2k experiment with 6.6×10^{20} protons on target. *Phys. Rev. D*, 91:072010, Apr 2015.

[90] P. Adamson et al. First measurement of muon-neutrino disappearance in nova. *Phys. Rev. D*, 93:051104, Mar 2016.

[91] P. Adamson et al. Measurement of the neutrino mixing angle θ_{23} in nova. *Phys. Rev. Lett.*, 118:151802, Apr 2017.

[92] M. A. Acero et al. New constraints on oscillation parameters from ν_e appearance and ν_μ disappearance in the nova experiment. *Phys. Rev. D*, 98:032012, Aug 2018.

[93] P. Adamson et al. Measurement of neutrino and antineutrino oscillations using beam and atmospheric data in minos. *Phys. Rev. Lett.*, 110:251801, Jun 2013.

[94] K. Abe et al. Indication of electron neutrino appearance from an accelerator-produced off-axis muon neutrino beam. *Phys. Rev. Lett.*, 107:041801, Jul 2011.

[95] F. P. An et al. Observation of electron-antineutrino disappearance at daya bay. *Phys. Rev. Lett.*, 108:171803, Apr 2012.

[96] J. K. Ahn et al. Observation of reactor electron antineutrinos disappearance in the reno experiment. *Phys. Rev. Lett.*, 108:191802, May 2012.

[97] Y. Abe et al. Indication of reactor $\overline{\nu}_e$ disappearance in the double chooz experiment. *Phys. Rev. Lett.*, 108:131801, Mar 2012.

[98] K. Abe et al. Observation of electron neutrino appearance in a muon neutrino beam. *Phys. Rev. Lett.*, 112, 2014.

[99] A. D. Sakharov. Violation of CP Invariance, C asymmetry, and baryon asymmetry of the universe. *Pisma Zh. Eksp. Teor. Fiz.*, 5:32–35, 1967. [Usp. Fiz. Nauk161,no.5,61(1991)].

[100] Nicola Cabibbo. Unitary symmetry and leptonic decays. *Phys. Rev. Lett.*, 10:531–533, Jun 1963.

[101] Makoto Kobayashi and Toshihide Maskawa. CP-Violation in the Renormalizable Theory of Weak Interaction. *Progress of Theoretical Physics*, 49(2):652–657, 02 1973.

[102] J. H. Christenson, J. W. Cronin, V. L. Fitch, and R. Turlay. Evidence for the 2π decay of the k_2^0 meson. *Phys. Rev. Lett.*, 13:138–140, Jul 1964.

[103] R. Aaij et al. Measurement of matter antimatter differences in beauty baryon decays. *Nature Phys*, 13, 2017.

[104] M. Fukugita and T. Yanagida. Barygenesis without grand unification. *Physics Letters B*, 174(1):45 – 47, 1986.

[105] M. A. Acero et al. First measurement of neutrino oscillation parameters using neutrinos and antineutrinos by nova. *Phys. Rev. Lett.*, 123:151803, Oct 2019.

[106] A Yu Smirnov. Neutrino mass and new physics. *Journal of Physics: Conference Series*, 53:44–82, nov 2006.

[107] Guido Altarelli and Ferruccio Feruglio. Discrete flavor symmetries and models of neutrino mixing. *Rev. Mod. Phys.*, 82:2701–2729, Sep 2010.

[108] Stephen F King and Christoph Luhn. Neutrino mass and mixing with discrete symmetry. *Reports on Progress in Physics*, 76(5):056201, may 2013.

[109] Stephen F King. Models of neutrino mass, mixing and CP violation. *Journal of Physics G: Nuclear and Particle Physics*, 42(12):123001, nov 2015.

[110] R.N. Mohapatra and A.Y. Smirnov. Neutrino mass and new physics. *Annual Review of Nuclear and Particle Science*, 56(1):569–628, 2006.

[111] K. Hirata et al. Observation of a neutrino burst from the supernova sn1987a. *Phys. Rev. Lett.*, 58:1490–1493, Apr 1987.

[112] R. M. Bionta et al. Observation of a neutrino burst in coincidence with supernova 1987a in the large magellanic cloud. *Phys. Rev. Lett.*, 58:1494–1496, Apr 1987.

[113] G. A. Tammann, W. Loeffler, and A. Schroeder. The galactic supernova rate. *apjs*, 92:487, Jun 1994.

[114] Roland Diehl et al. Radioactive 26al from massive stars in the galaxy. *Nature*, 439(7072), 2006.

[115] John F. Beacom. The diffuse supernova neutrino background. *Annual Review of Nuclear and Particle Science*, 60(1):439–462, 2010.

[116] S.Ando and K.Sato. Relic neutrino background from cosmological supernovae. *New Journal of Physics*, 6:170–170, nov 2004.

[117] T. Totani, K. Sato, H. E. Dalhed, and J. R. Wilson. Future detection of supernova neutrino burst and explosion mechanism. *The Astrophysical Journal*, 496(1):216–225, mar 1998.

[118] Keitaro Takahashi, Mariko Watanabe, Katsuhiko Sato, and Tomonori Totani. Effects of neutrino oscillation on the supernova neutrino spectrum. *Phys. Rev. D*, 64:093004, Oct 2001.

[119] B. Aharmim et al. A search for neutrinos from the SolarhepReaction and the diffuse supernova neutrino background with the sudbury neutrino observatory. *The Astrophysical Journal*, 653(2):1545–1551, dec 2006.

[120] G. Bellini et al. Study of solar and other unknown anti-neutrino fluxes with borexino at lngs. *Physics Letters B*, 696(3):191 – 196, 2011.

[121] K. Bays et al. Supernova relic neutrino search at super-kamiokande. *Phys. Rev. D*, 85:052007, Mar 2012.

[122] H. Zhang et al. Supernova relic neutrino search with neutron tagging at super-kamiokande-iv. *Astroparticle Physics*, 60:41 – 46, 2015.

[123] A. Gando et al. SEARCH FOR EXTRATERRESTRIAL ANTINEUTRINO SOURCES WITH THE KamLAND DETECTOR. *The Astrophysical Journal*, 745(2):193, jan 2012.

[124] John F. Beacom and Mark R. Vagins. Antineutrino spectroscopy with large water Čerenkov detectors. *Phys. Rev. Lett.*, 93:171101, Oct 2004.

[125] K. Abe et al. Hyper-Kamiokande Design Report. 2018.

[126] T. Adam et al. Juno conceptual design report. 2015.

[127] John F. Beacom et al. Physics prospects of the jinping neutrino experiment. *Chinese physics C*, 41(2):23002, 2017.

[128] Teppei Katori and Marco Martini. Neutrino–nucleus cross sections for oscillation experiments. *Journal of Physics G: Nuclear and Particle Physics*, 45(1):013001, dec 2017.

[129] K. Abe et al. Measurement of the neutrino-oxygen neutral-current interaction cross section by observing nuclear deexcitation γ rays. *Phys. Rev. D*, 90:072012, Oct 2014.

[130] H. ZHANG (Super-Kamiokande collaboration. Proceedings, 32nd International Cosmic Ray Conference (ICRC 2011). 2011.

[131] L. Aliaga et al. Design, calibration, and performance of the minerva detector. *Nucl. Instrum. Meth. A*, 743:130 – 159, 2014.

[132] A. A. Aguilar-Arevalo et al. Measurement of the neutrino neutral-current elastic differential cross section on mineral oil at $E_\nu \sim 1$ GeV. *Phys. Rev. D*, 82:092005, Nov 2010.

[133] D. Casper. The nuance neutrino physics simulation, and the future. *Nuclear Physics B - Proceedings Supplements*, 112(1):161 – 170, 2002.

[134] C. Zeitnitz and T.A. Gabriel. *Nucl. Instr. Meth. A*, 349, 1994.

[135] Yoshinari Hayato. A neutrino interaction simulation program library NEUT. *Acta Phys. Polon.*, B40:2477–2489, 2009.

[136] Tomasz Golan, Cezary Juszczak, and Jan T. Sobczyk. Effects of final-state interactions in neutrino-nucleus interactions. *Phys. Rev. C*, 86:015505, Jul 2012.

[137] C Anderson et al. The ArgoNeuT detector in the NuMI low-energy beam line at fermilab. 7(10):P10019–P10019, oct 2012.

[138] A. R. Back et al. Accelerator neutrino neutron interaction experiment (annie): Preliminary results and physics phase proposal. 2017.

[139] K. Abe et al. Search for *cp* violation in neutrino and antineutrino oscillations by the t2k experiment with 2.2×10^{21} protons on target. *Phys. Rev. Lett.*, 121, 2018.

[140] K. Abe and others. Combined analysis of neutrino and antineutrino oscillations at t2k. *Phys. Rev. Lett.*, 118, 2017.

[141] Y. Sato. High Power Beam Operation of the J-PARC RCS and MR. pages 2938–2942, 2018.

[142] K. Matsuoka et al. Development and production of the ionization chamber for the t2k muon monitor. *Nucl. Instrum. Meth. A*, 623(1), 2010.

[143] K. Matsuoka et al. Design and performance of the muon monitor for the t2k neutrino oscillation experiment. *Nucl. Instrum. Meth. A*, 624(3), 2010.

[144] D. Beavis et al. techreport bnl-52459. *Brookhaven National Lab, NY*, 1995.

[145] S. Gomi et al. Development and study of the multi pixel photon counter. *Nucl. Instrum. Meth. A*, 581(1), 2007.

[146] M. Yokoyama and other. Development of multi-pixel photon counters. 2006.

[147] S. Aoki et al. The t2k side muon range detector (smrd). *Nucl. Instrum. Meth. A*, 698:135 – 146, 2013.

[148] S. Assylbekov et al. The t2k nd280 off-axis pi   zero detector. *Nucl. Instrum. Meth. A*, 686:48 – 63, 2012.

[149] N. Abgrall et al. Time projection chambers for the t2k near detectors. *Nucl. Instrum. Meth. A*, 637(1):25 – 46, 2011.

[150] I. Giomataris et al. Micromegas in a bulk. *Nucl. Instrum. Meth. A*, 560(2):405 – 408, 2006.

[151] P.-A. Amaudruz and other. The t2k fine-grained detectors. *Nucl. Instrum. Meth. A*, 696:1 – 31, 2012.

[152] D Allan et al. The electromagnetic calorimeter for the t2k near detector ND280. *Journal of Instrumentation*, 8(10):P10019–P10019, 2013.

[153] I. M. Frank and I. E. Tamm. Coherent visible radiation of fast electrons passing through matter. *Compt. Rend. Acad. Sci. URSS*, 14, 1937.

[154] N. Nishino et al. *in: Nuclear Science Symposium Conference Record, 2007, NSS' 07, IEEE, vol. 1, 2008, p. 127.*

[155] A. Suzuki, M. Mori, K. Kaneyuki, T. Tanimori, J. Takeuchi, H. Kyushima, and Y. Ohashi. Improvement of 20 in. diameter photomultiplier tubes. *Nucl. Instrum. Meth. A*, 329(1):299 – 313, 1993.

[156] R. Becker-Szendy et al. Calibration of the imb detector. *Nucl. Instrum. Meth. A*, 352(3):629 – 639, 1995.

[157] H. Nishino et al. High-speed charge-to-time converter asic for the super-kamiokande detector. *Nucl. Instrum. Meth. A*, 610(3):710 – 717, 2009.

[158] A.Renshaw. First Direct Evidence for Matter Enhanced Neutrino Oscillation, Using Super-Kamiokande Solar Neutrino Data. *Ph.D thesis, University of California, Irvine*, 2013.

[159] Y.Nakano. ^{8}B solar neutrino spectrum measurement using Super-Kamiokande IV. *Ph.D thesis, University of Tokyo*, 2016.

[160] G. Battistoni et al. The fluka code: description and benchmarking. *AIP Conference Proceedings*, 896(1):31–49, 2007.

[161] R. Brun et al. GEANT3. 1987.

[162] N. Abgrall et al. Measurements of cross sections and charged pion spectra in proton-carbon interactions at 31 gev/*c*. *Phys. Rev. C*, 84:034604, Sep 2011.

[163] N. Abgrall et al. Measurement of production properties of positively charged kaons in proton-carbon interactions at 31 gev/*c*. *Phys. Rev. C*, 85:035210, Mar 2012.

[164] T. Eichten et al. Particle production in proton interactions in nuclei at 24 gev/c. *Nuclear Physics B*, 44(2):333 – 343, 1972.

[165] I. Chemakin et al. Pion production by protons on a thin beryllium target at 6.4, 12.3, and 17.5 gev/*c* incident proton momenta. *Phys. Rev. C*, 77:015209, Jan 2008.

[166] N. Abgrall et al. *The European Physical Journal C*, 76(11):617, 2016.

[167] C. H. Llewellyn Smith.

[168] R. Gran et al. Measurement of the quasielastic axial vector mass in neutrino interactions on oxygen. *Phys. Rev. D*, 74, 2006.

[169] A. A. Aguilar-Arevalo et al. First Measurement of the Muon Neutrino Charged Current Quasielastic Double Differential Cross Section. *Phys. Rev.*, D81, 2010.

[170] R.A. Smith and E.J. Moniz. Neutrino reactions on nuclear targets. *Nucl. Phys. B*, 101(2):547, 1975.

[171] J. Nieves, I. Ruiz Simo, and M. J. Vicente Vacas. Inclusive charged-current neutrino-nucleus reactions. *Phys. Rev. C*, 83:045501, Apr 2011.

[172] M. Martini, M. Ericson, G. Chanfray, and J. Marteau. Unified approach for nucleon knock-out and coherent and incoherent pion production in neutrino interactions with nuclei. *Phys. Rev. C*, 80:065501, Dec 2009.

[173] A. A. Aguilar-Arevalo et al. First measurement of the muon antineutrino double-differential charged-current quasielastic cross section. *Phys. Rev. D*, 88, 2013.

[174] R. Gran, J. Nieves, F. Sanchez, and M. J. Vicente Vacas. Neutrino-nucleus quasi-elastic and 2p2h interactions up to 10 gev. *Phys. Rev. D*, 88:113007, Dec 2013.

[175] Dieter Rein and Lalit M Sehgal. Neutrino-excitation of baryon resonances and single pion production. *Annals of Physics*, 133(1):79 – 153, 1981.

[176] Dieter Rein and Lalit M. Sehgal. Coherent 0 production in neutrino reactions. *Nuclear Physics B*, 223(1):29 – 44, 1983.

[177] Reya E.& Vogt Gl ü ck, M. *A. Eur. Phys. J. C, 5, 461*, 1998.

[178] A. Bodek and U. K. Yang. Modeling neutrino and electron scattering inelastic cross sections, 2003.

[179] Torbjorn Sjostrand. Pythia 5.7 and jetset 7.4 physics and manual. 1995.

[180] R. Serber. Nuclear reactions at high energies. *Phys. Rev.*, 72:1114–1115, Dec 1947.

[181] M. L. Goldberger. The interaction of high energy neutrons and heavy nuclei. *Phys. Rev.*, 74:1269–1277, Nov 1948.

[182] N Metropolis et al. Monte carlo calculations on intranuclear cascades. i. low-energy studies. *Phys. Rev.*, 110:185–203, Apr 1958.

[183] N. Metropolis, R. Bivins, M. Storm, J. M. Miller, G. Friedlander, and Anthony Turkevich. Monte carlo calculations on intranuclear cascades. ii. high-energy studies and pion processes. *Phys. Rev.*, 110:204–219, Apr 1958.

[184] Hugo W. Bertini. Low-energy intranuclear cascade calculation. *Phys. Rev.*, 131, 1963.

[185] HUGO W. BERTINI. Intranuclear-cascade calculation of the secondary nucleon spectra from nucleon-nucleus interactions in the energy range 340 to 2900 mev and comparisons with experiment. *Phys. Rev.*, 188, 1969.

[186] Roger D. Woods and David S. Saxon. Diffuse surface optical model for nucleon-nuclei scattering. *Phys. Rev.*, 95:577–578, Jul 1954.

[187] L. D. Landau and I. Pomeranchuk. Limits of applicability of the theory of bremsstrahlung electrons and pair production at high-energies. *Dokl. Akad. Nauk Ser. Fiz.*, 92:535–536, 1953.

[188] Leo Stodolsky. Formation Zone Description in Multiproduction. In *Proceedings: International Colloquium on Multiparticle Reactions, 6th, Oxford, Eng., Jul 14-19, 1975*, page 577, 1975.

[189] D. S. Baranov et al. AN ESTIMATE FOR THE FORMATION LENGTH OF HADRONS IN NEUTRINO INTERACTIONS. 1984.

[190] E. S. Pinzon Guerra et al. Using world $\pi^{\pm}$-nucleus scattering data to constrain an intranuclear cascade model. *Phys. Rev. D*, 99:052007, Mar 2019.

[191] L.L. Salcedo, E. Oset, M.J. Vicente-Vacas, and C. Garcia-Recio. Computer simulation of inclusive pion nuclear reactions. *Nuclear Physics A*, 484(3):557 – 592, 1988.

[192] K Nakamura et al. Review of particle physics. *Journal of Physics G: Nuclear and Particle Physics*, 37(7A):075021, jul 2010.

[193] Hugo W. Bertini. Nonelastic interactions of nucleons and π mesons with complex nuclei at energies below 3 gev. *Phys. Rev. C*, 6, 1972.

[194] A. Fass. et al. Fluka 92. *Proceedings of the Workshop on Simulating Accelerator Radiation Environments,*, 1993.

[195] *HETC:MonteCarloHigh-EnergyNucleon-MesonTransportCode*, Oak Ridge National Laboratory RSIC Computer Code Collection CCC-178.

[196] R.G. Alsmiller, F.S. Alsmiller, and O.W. Hermann. The high-energy transport code hetc88 research sponsored by office of high energy and nuclear physics, u.s. department of energy under contract no. de-ac05-84or21400 with martin marietta energy systems, inc. and comparisons with experimental data. *Nucl. Instrum. Meth. A*, 295, 1990.

[197] J.O.Johnson and T.A.Gabriel. *A monte carlo ionization chamber analysis packag*, ORNL/TM-10340, 1988.

[198] W.A. Coleman and T.W. Armstrong. Nucleon–meson transport code nmtc.

[199] M.P. Guthrie. Evap-4: Another modification of a code to calculate particle evaporation from excited compound nuclei.

[200] I. Dostrovsky, Z. Fraenkel, and G. Friedlander. Monte carlo calculations of nuclear evaporation processes. iii. applications to low-energy reactions. *Phys. Rev.*, 116:683–702, Nov 1959.

[201] Robert Hofstadter. Electron scattering and nuclear structure. *Rev. Mod. Phys.*, 28:214–254, Jul 1956.

[202] J. O. Johnson and T. A. Gabriel. Development and evaluation of a Monte Carlo Code System for analysis of ionization chamber responses. 1987.

[203] T.J.Irvine. Development of Neutron-Tagging Techniques and Application to Atmospheric Neutrino Oscillation Analysis in Super-Kamiokande. *PhD thesis, University of Tokyo*, 2014.

[204] R. Akutsu et al. A study of neutrons associated with CC $\nu_\mu/\bar{\nu}_\mu$ interactions on water at the far detecto. *T2K-TN-371 (internal note)*, 2019.

[205] R.B. Patterson, E.M. Laird, Y. Liu, P.D. Meyers, I. Stancu, and H.A. Tanaka. The extended-track event reconstruction for miniboone. *Nucl. Instrum. Meth. A*, 608(1):206 – 224, 2009.

[206] B. Hamermesh, G. R. Ringo, and S. Wexler. The thermal neutron capture cross section of hydrogen. *Phys. Rev.*, 90:603–606, May 1953.

[207] R. B. Firestone and Zs. Revay. Thermal neutron capture cross sections for ^{16,17,18}O and ^{2}H. *Phys. Rev. C*, 93:044311, Apr 2016.

[208] J.A. Dunmore. The Separation of CC and NC Events in the Sudbury Neutrino Observatory. *Ph.D thesis, Oxford University*, 2004.

[209] Andreas Hoecker, Peter Speckmayer, Joerg Stelzer, Jan Therhaag, Eckhard von Toerne, and Helge Voss. TMVA: Toolkit for Multivariate Data Analysis. *PoS*, ACAT:040, 2007.

[210] H. Watanabe et al. First study of neutron tagging with a water cherenkov detector. *Astroparticle Physics*, 31(4):320 – 328, 2009.

[211] H.Zhang. Study of Low Energy Electron Anti-neutrinos at Super-Kamiokande IV. *PhD thesis, Tsinghua University*, 2012.

[212] F. James. MINUIT Reference Manual. *Technical report, CERN*, 2000.

[213] R. Wendell. Prob3++ software for computing three flavor neutrino oscillation probabilities. *http://webhome.phy.duke.edu/ raw22/public/Prob3++/*, 2012.

[214] X.Li. A Joint Analysis of T2K Beam Neutrino and Super-Kamiokande Sub-GeV Atmospheric Neutrino Data. *PhD thesis, Stony Brook University*, 2018.

[215] X. Li and M. Wilking. FiTQun Event Selection Optimization. *T2K-TN-319 (internal note)*, 2017.

[216] Frank C. Porter. Testing Consistency of Two Histograms. 2008.

[217] K. Mahn. For Summer 2016 XSEC analyses and onward. 2018.

[218] P. de Perio et al. NEUT Systematic Studies for 2010a Analysis. *T2K-TN-32 (internal note)*, 2011.

[219] W. Y. Ma, E. S. Pinzon Guerra, M. Yu, A. Fiorentini, and T. Feusels. Current status of final-state interaction models and their impact on neutrino-nucleus interactions. *J. Phys. Conf. Ser.*, 888(1):012171, 2017.

[220] J. Imber et al. T2K-SK Systematic Error Summary for the 2017 Oscillation Analysis. *T2K-TN-326 (internal note)*, 2017.

[221] R. Wendell for the SK-LB J. Kameda and T2K-SK groups. Study on Super-K events and systematic errors relevant for the ν_μ disappearance analysis with T2K 3.23×10 19 POT data. *T2K-TN-214 (internal note)*, 2014.

[222] L.Wan. Experimental Studies on Low Energy Electron Antineutrinos and Related Physics. *PhD thesis, Tsinghua University*, 2018.

[223] R.A.Wendell. Three flavor oscillation analysis of atmospheric neutrinos in Super-Kamiokande. *PhD thesis, University of Tokyo*, 2008.

[224] L.K.Pik. Study of the neutrino mass hierarchy with the atmospheric neutrino data observed in Super-Kamiokande. *PhD thesis, University of Tokyo*, 2012.

[225] G. L. Fogli, E. Lisi, A. Marrone, D. Montanino, and A. Palazzo. Getting the most from the statistical analysis of solar neutrino oscillations. *Phys. Rev. D*, 66, Sep 2002.

[226] K. Abe et al. Proposal for an extended run of t2k to 20×10^{21} pot. *arXiv*, 2016.

[227] I. Anghel et al. Letter of intent: The accelerator neutrino neutron interaction experiment (annie). 2015.

[228] S. Bhadra et al. Letter of Intent to Construct a nuPRISM Detector in the J-PARC Neutrino Beamline. 2014.

[229] M Barbi et al. A Water Cherenkov Test Beam Experiment for Hyper-Kamiokande and Future Large-scale Water-based Detectors. Technical Report CERN-SPSC-2019-042. SPSC-I-254, CERN, Geneva, 2019.

Appendix A

Implementation of neutron productions by μ^-/π^- captures

Neutron productions by μ^- and π^- captures on oxygen nucleus had never been simulated. For the primary analysis of this theis, these captures are implemented to SKDETSIM using Geant4.9.6.

Technically `G4MuonMinusCaptureAtRest` and `G4PiMinusAbsorptionAtRest` which are the classes of Geant4.9.6 and are used as the default models, are directly called from SKDETSIM via an interface which connects SKDETSIM with Geant4.9.6. The neutrons produced by these simulation codes are modeled based on both theory and experimental data. The neutron multiplicity and kinetic energy distribution of the μ^- and π^- captures are shown in Figure A.1. Figure A.2 shows the distribution of the true distance between the ν interaction and neutron capture positions before and after the implementation. As shown in the plots, these captures produce a non-negligible number of neutrons depending on the distance. The total number of neutrons in the samples used for the analysis which also be mentioned in Section 7.2 are increased by 16% and 10% for the FHC and RHC cases, respectively.

Figure A.1: Neutron multiplicity (top) and kinetic energy distribution (bottom). Left and right correspond to μ^- and π^- captures on oxygen nucleus, respectively. All the figures are obtained by by generating $5\,\mathrm{MeV}$ μ^- and π^-. `G4MuonMinusCaptureAtRest` (`G4PiMinusAbsorptionAtRest`) is used for the μ^- (π^-) capture.
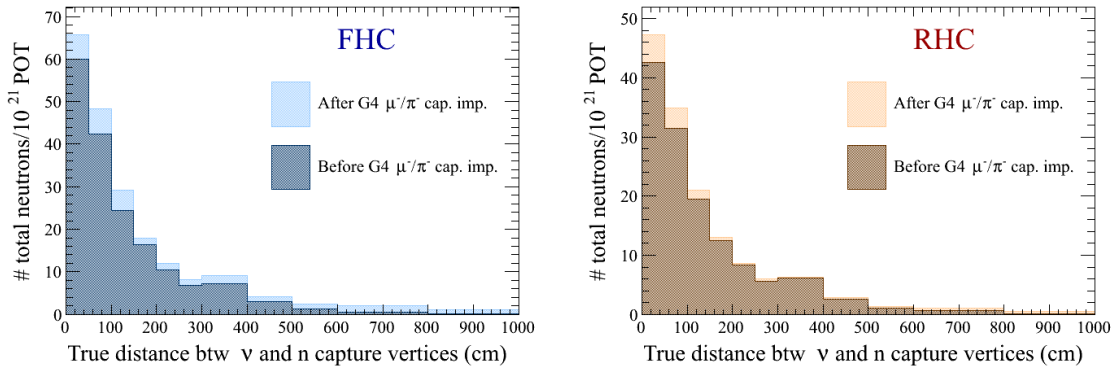
Figure A.2: Distribution of the true distance from ν interaction vertex to neutron capture vertex before and after the implementation of the μ^- and π^- capture on ^{16}O. Left and right figures are for the FHC and RHC $1R\nu_\mu$ samples, respectively. The distributions are normalized to 10^{21}POT.

Appendix B

Distribution of NN input variables

The distributions of the NN input variables before the NN classification (i.e. just after the primary selection) and after the NN classification are cheked as shown in Figure B.1 to B.4. All the distributions of the MC are normalized to the number of observed neutron candidates in order to validate whether or not the shape of the data agree with the equivalent MC's one.
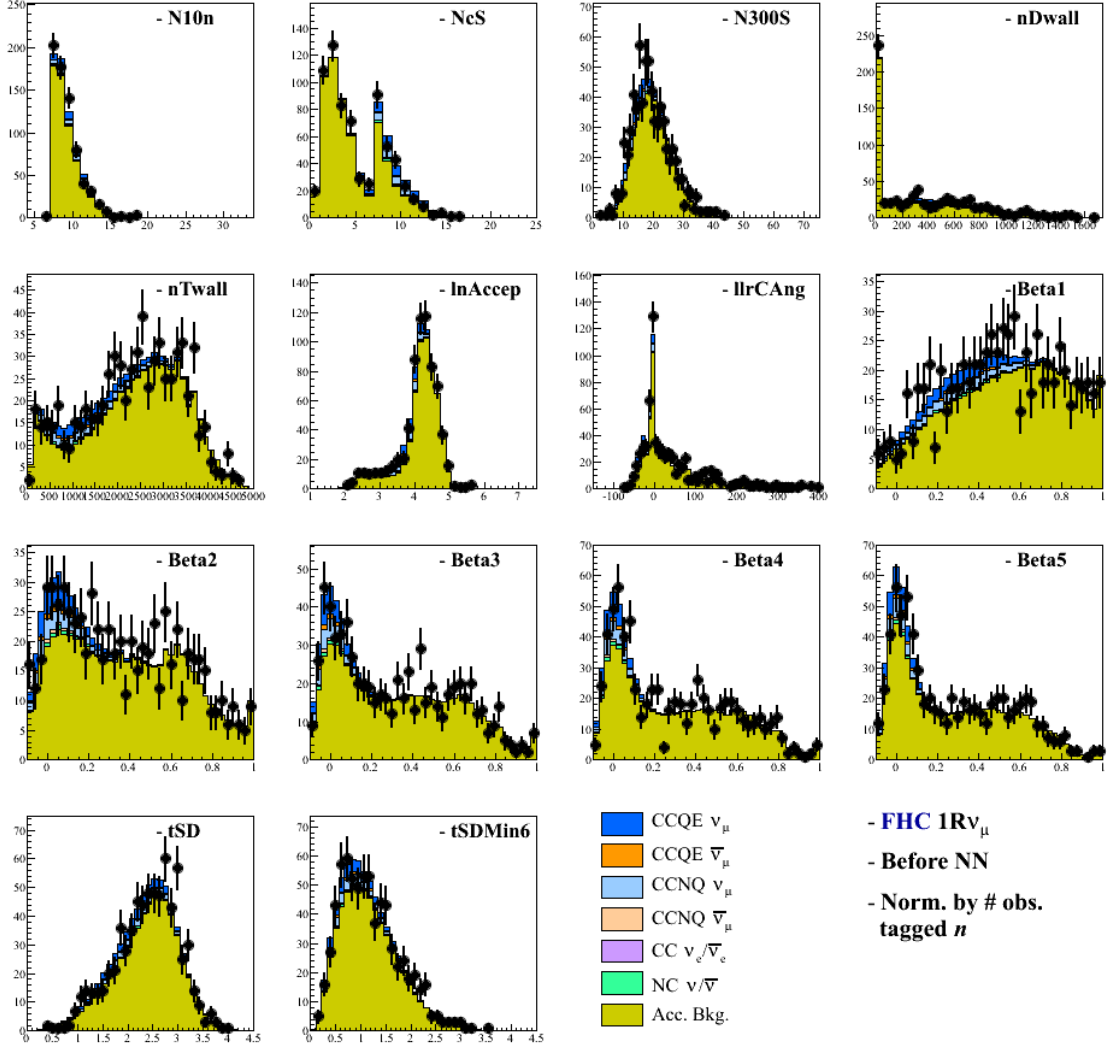
Figure B.1: Distributions of the NN input variables before the NN classification (i.e. just after the primary selection) for the Runs 1-9 FHC $1R\nu_\mu$ sample in comparison to the corresponding MC disributions. All the MC distributions are normalized by the number of observed neutron candidates.

Figure B.2: Distributions of the NN input variables after the NN classification for the Runs 1-9 FHC 1Rν_μ sample in comparison to the corresponding MC disributions. All the MC distributions are normalized by the number of observed tagged neutrons.
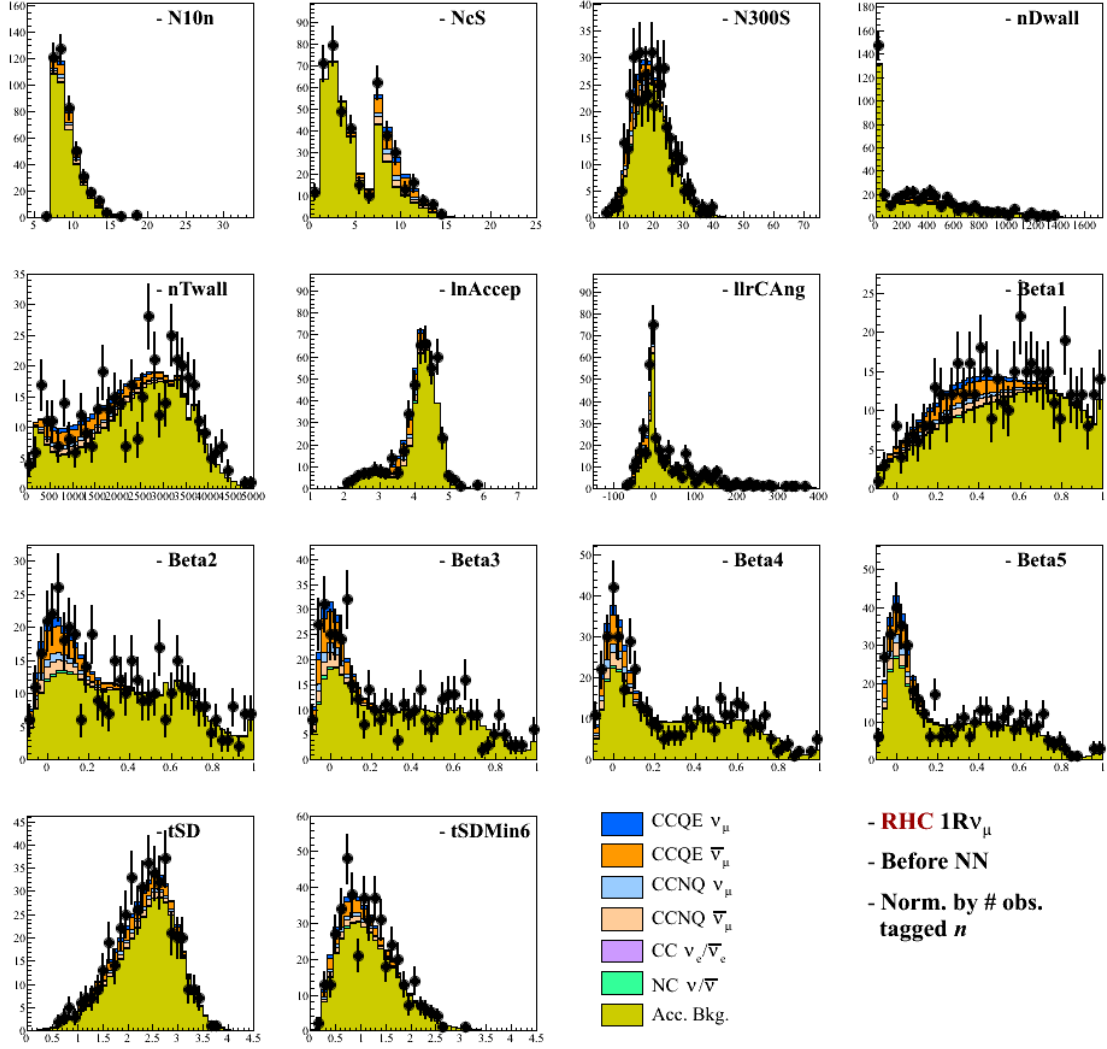
Figure B.3: Distributions of the NN input variables before the NN classification (i.e. just after the primary selection) for the Runs 1-9 RHC $1R\nu_\mu$ sample in comparison to the corresponding MC disributions. All the MC distributions are normalized by the number of observed neutron candidates.

Figure B.4: Distributions of the NN input variables after the NN classification for the Runs 1-9 RHC 1Rν_μ sample in comparison to the corresponding MC disributions. All the MC distributions are normalized by the number of observed tagged neutrons.

Appendix C

True neutrino energy spectra

In Chapter 8, mean neutron multiplicity as a function of reconstructed muon transverse momentum P_t is measured. Distribution of true neutrino energy is different among the different P_t regions. Figure C.1 to C.2 show the distribution of true neutrino energy for each P_t bin for the FHC and RHC $1R\nu_\mu$ samples, respectively.
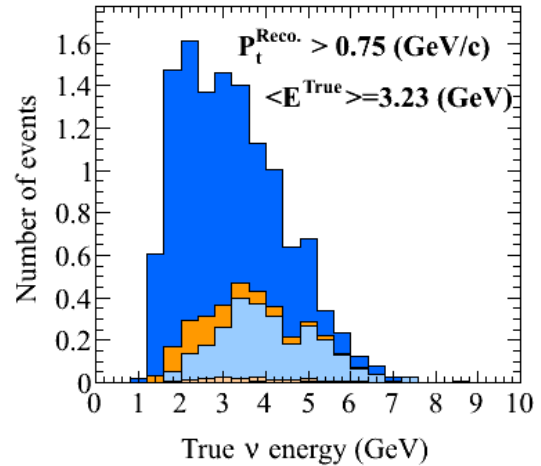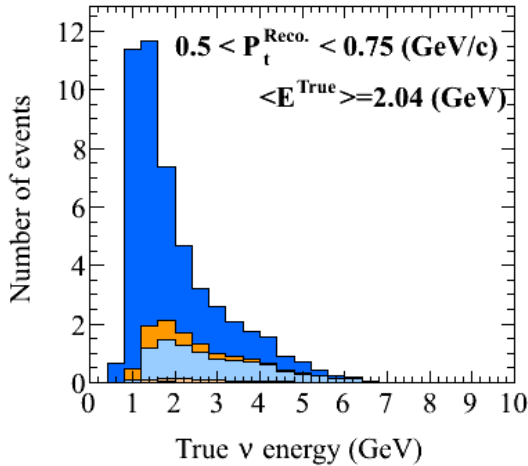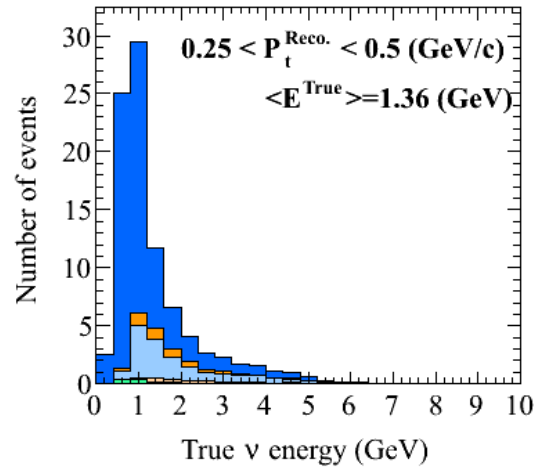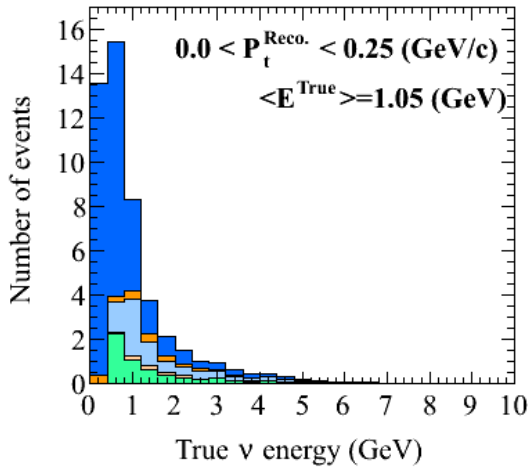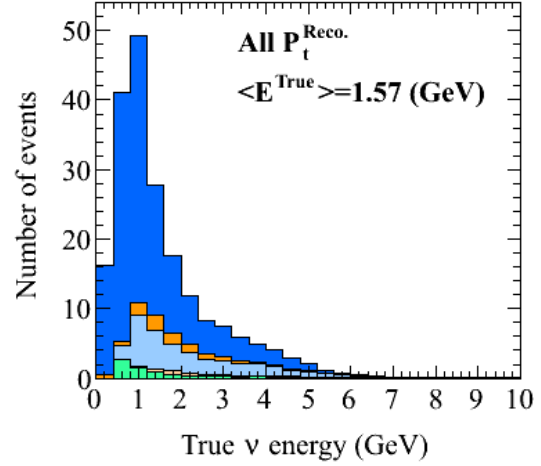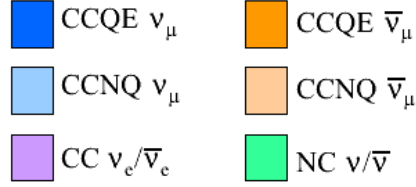
Figure C.1: Distributions of true neutrino energy for each reconstructed muon transverse momentum of the FHC 1Rν_μ sample. The bin edges of the transverse momentum is summarized in Table 8.13.
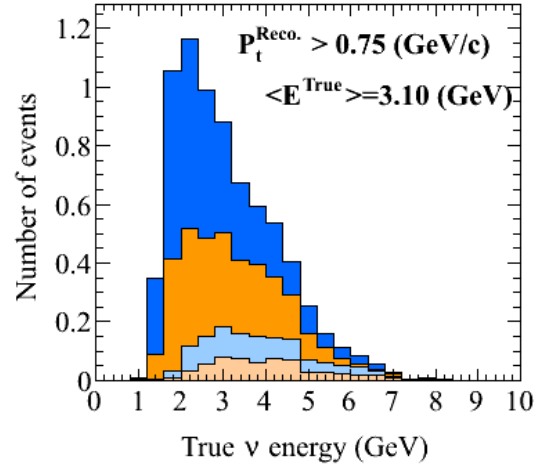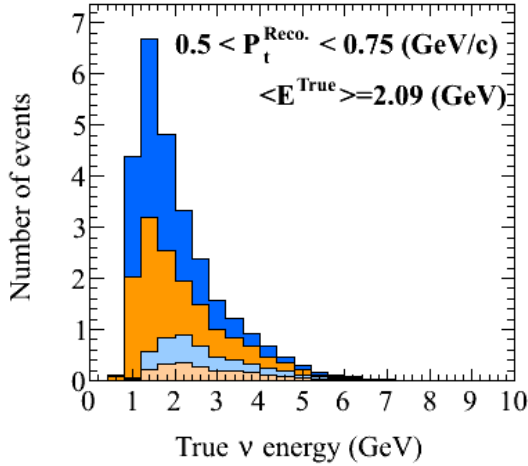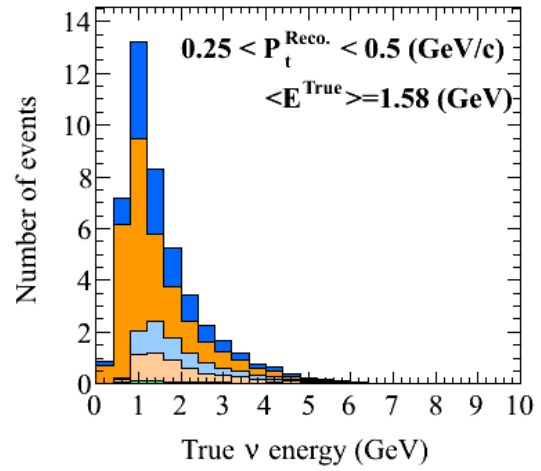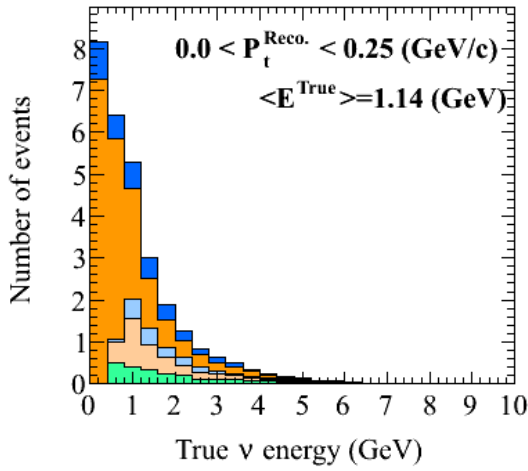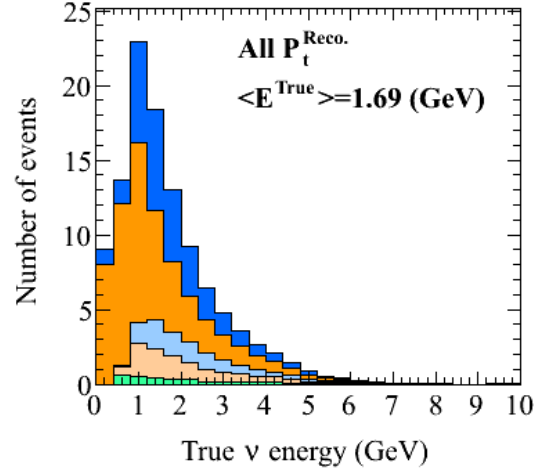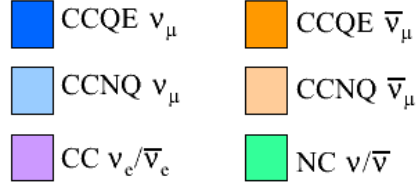
Figure C.2: Distributions of true neutrino energy for each reconstructed muon transverse momentum of the RHC 1Rν_μ sample. The bin edges of the transverse momentum is summarized in Table 8.13.